





Heterogeen geïntegreerde III-V-op-silicium golflengte-afstembare  
DFB- en DBR-lasers

Heterogeneously Integrated III-V-on-Silicon Wavelength-Tunable  
DFB and DBR Lasers

Sören Dhoore

Promotoren: prof. dr. ir. G. Morthier, prof. dr. ir. G. Roelkens  
Proefschrift ingediend tot het behalen van de graad van  
Doctor in de ingenieurswetenschappen: fotonica



Vakgroep Informatietechnologie  
Voorzitter: prof. dr. ir. B. Dhoedt  
Faculteit Ingenieurswetenschappen en Architectuur  
Academiejaar 2018 - 2019

ISBN 978-94-6355-177-9  
NUR 950, 959  
Wettelijk depot: D/2018/10.500/95



Universiteit Gent  
Faculteit Ingenieurswetenschappen en Architectuur  
Vakgroep Informatietechnologie

**Promotoren:**

prof. dr. ir. Geert Morthier  
prof. dr. ir. Günther Roelkens

**Examencommissie:**

prof. dr. ir. Daniël De Zutter (voorzitter)	Universiteit Gent
prof. dr. ir. Geert Morthier (promotor)	Universiteit Gent
prof. dr. ir. Günther Roelkens (promotor)	Universiteit Gent
prof. dr. ir. Johan Bauwelinck (secretaris)	Universiteit Gent
prof. dr. ir. Dries Van Thourhout	Universiteit Gent
prof. dr. ir. Filip Beunis	Universiteit Gent
prof. dr. Xaveer J. M. Leijtens	Technische Universiteit Eindhoven
dr. ir. Yannick De Koninck	Interuniversitair Micro Elektronica Centrum

Universiteit Gent  
Faculteit Ingenieurswetenschappen en Architectuur  
Vakgroep Informatietechnologie  
Technologiepark Zwijnaarde 15, B-9052 Gent, België

Proefschrift tot het behalen van de graad van  
Doctor in de ingenieurswetenschappen: fotonica  
Academiejaar 2018-2019



# Dankwoord

*Finita la commedia.* Deze gevleugelde woorden werden me ooit ingegeven door een leerkracht Frans en betekenen vrij vertaald zoveel als *de klucht is over*. Een doctoraat vergelijken met een klucht is hier geenszins de bedoeling en zou de waarheid oneer aandoen. Maar net als in een klucht kenden de voorbije 4 jaar voornamelijk leuke en memorabele momenten. En daarbij is het op zijn plaats om heel wat mensen te bedanken.

Vooreerst wil ik graag mijn promotoren Geert en Gunther bedanken. Geert, ik vond het de voorbije 4 jaar zeer aangenaam samenwerken en heb je nonsense communicatie en open-door policy altijd erg gewaardeerd. Hopelijk kunnen we in de toekomst nog geregeld samenwerken! Gunther, bedankt voor je originele invalshoeken op het gebied van III-V/Si lasers (of was het nu III-V/Ge/Si?) maar evenzeer bedankt voor de alomtegenwoordige Club/Buffalo-grapjes.

Ook de andere professoren van de Photonics Research Group ben ik dank verschuldigd. Roel, voor het uitbouwen van een ijzersterke internationale onderzoeksgroep en de trigger gegeven te hebben om de weg van de fotonica in te slaan. Peter, voor het pogen de verjaardags- en koffiepauzetradities in stand te houden en voor je vaak droge maar geniale grappen (“*Let’s raise the level of this presentation a bit.*”). Wim, voor je sterke leiding in het MEGAchip-project. Je woordgrapjes kan ik af en toe ook wel smaken. Bart, voor het opmerken van intriges die anderen al eens over het hoofd zouden zien. *District 9* bekijk ik volgende week! Nicolas, voor het uitklaren waarom Nederlands dan toch geen wereldtaal is. Dries, voor je to-the-point-aanpak en voor de persoonlijke thuisafgifte van de CR-wachtgsm.

Many thanks I owe to my office mates, for making room 130.034 the most fun office in the iGent building. Alejandro, thanks for the daily portion of humour, life contemplations and paella/tapas/fries discussions. Just don’t press *Sluiten*. Mahmoud, your positive mood always sets the tone! “*En je spreekt Nederlands nu!*” Xiaomin, I appreciate your *je m’en fous* spirit. I’m still not afraid of your signature feint though. Irfan – *best out of 3* – good luck with your photoshoot! Javad, your long-distance shots are legendary! Nicolas, please leave your white holes for what they are. Haolan, you made the right choice. Sorry for the mystery calls.

Verder dank ik graag nog: Anton, om regelmatig eens langs te komen. Altijd fijn en je lach werkt aanstekelijk! Frédéric, Carré of toch maar Plansjee? Kasper, bedankt voor je hero-alignmentinzichten (ofwel chance) en opmerkelijke telefoongesprekken. Andreas, bedankt voor je West-Vlaamse grappen en grollen. Althans, af en toe eens. Koen, het squashen was zeer fijn (maar toch verkies ik tennis). Alvast veel succes in de VS! Pieter, nu je bij *imec* werkt, vermoed ik dat het wel goed komt met die technische bagage.

I also want to thank the star players from the Infrared Devils football team (in no particular order): Clemens, Daan, Jeroen, Isaac, Alexandros, Ahmed, Kristof, Camiel, Stijn ( $\times 2$ ), Gilles, Yufei, Jing. Now we're out of the cup league, we can fully focus on the competition. The title is within reach!

Special thanks also go to: Ashim and Nuria, the Hawaii experience was great! Ali, good luck and enjoy the muesli! Sulakshna, once one of the *Sulakshna* songs will make for a great hit! Grigorij, sometimes it's all a bit of a dark forest to me. Chiara, maybe we'll meet again in Leuven (by night). Abdul, your positivism and life views always make for an interesting conversation. Lukas, one day we can go cycling together. Next summer I am definitely going to buy that bike. Nayyera, thanks for (not always) singing along with me. Yuting, thank you for always giving in to my PL requests. Also the former colleagues I want to thank: Sam, Rodica (*"in particular"*), Saurav (*"It's in the trailer!"*), Alfonso (I quit), Jan-Willem, Amin (*"Any news?"*), Leili, Sarvagya, Ashwyn.

I would also like to thank all other doctoral and postdoctoral researchers of the Photonics Research Group: Laurens ( $\times 2$ ), Xiangfeng, Hong, Emmanuel, Jesper, Bahawal, Artur, Xiaoning, Andrew, Floris, Chupao, Zuyang, Alessio, Chonghuai, Cenk, Sanja, Khannan, Antonio, Ivo, Paul, Nina, Sarah, Jochem, Mattias, Ewoud, Mi, Yufei, Yinghao, Iman, Banafsheh, Naidi, Joan, Muhammad, Yanlu, Fabio, Ana, Christos, Zheng, Eva, Kamal.

Graag dank ik ook nog de mensen van de CR. Liesbet, de SEM/FIB-sessies brengen altijd raad. Steven, je processing-kennis blijft verbazen. Muhammad, thanks for the nice EBL/SOI collaboration. But, what are you saying? Bedankt ook aan: Ilse V.R., voor snelle dossierafhandeling en leuke chitchat. Kristien, voor meer van dat. Ilse M., voor je excellente filmtips en stadslooppaanmoedigingen.

Een doctoraat afronden is natuurlijk niet louter het resultaat van de voorbije 4 jaar aan onderzoek maar gaat een stuk verder terug in de tijd. En daar hebben heel wat mensen toe bijgedragen, in het bijzonder familie en vrienden. Een welgemeende dank aan allen! Uiteraard is een speciale vermelding voor mijn ouders op zijn plaats. Papa en mama, dank jullie voor de warmte waarin Kjell en ik zijn opgegroeid en voor de absolute steun bij alles wat we deden, lieten en nog steeds doen en laten. Kjell, een betere broer had ik me niet kunnen wensen!

Ten slotte dank ik graag mijn vriendin Lydia. Liefste schat, jou leren kennen was zonder twijfel de belangrijkste gebeurtenis van afgelopen jaren. Ik

ben ontzettend gelukkig met jou en hoop dat we samen een fantastische toekomst tegemoet gaan!

*Gent, december 2018*  
*Sören Dhoore*



# Table of Contents

<b>Dankwoord</b>	<b>i</b>
<b>Samenvatting</b>	<b>xxvii</b>
<b>Summary</b>	<b>xxxv</b>
<b>1 Introduction</b>	<b>1</b>
1.1 Optical interconnects in data centers . . . . .	1
1.1.1 Optical burst and packet switching . . . . .	2
1.2 Remote sensing applications . . . . .	4
1.2.1 Frequency-modulated continuous-wave LIDAR . . . . .	5
1.3 Trace-gas sensing and spectroscopy . . . . .	6
1.4 Silicon photonic integrated circuits . . . . .	6
1.5 Heterogeneous III-V-on-silicon integration . . . . .	7
1.5.1 Integration approaches . . . . .	8
1.5.2 VCSELs vs DFB and DBR lasers . . . . .	9
1.5.3 Thermally tunable III-V-on-silicon lasers . . . . .	9
1.5.4 Electronically tunable III-V-on-silicon lasers . . . . .	10
1.6 Tunable laser diodes – state-of-the art . . . . .	10
1.7 Outline . . . . .	13
1.8 List of publications . . . . .	15
1.8.1 International peer-reviewed journals . . . . .	15
1.8.2 International conference proceedings . . . . .	16
1.8.3 National conference proceedings . . . . .	17
References . . . . .	18
<b>2 Fundamentals of tunable laser diodes</b>	<b>25</b>
2.1 Introduction . . . . .	25
2.2 Laser basics . . . . .	26
2.2.1 Introduction . . . . .	26
2.2.2 Wave propagation in periodic structures . . . . .	27
2.2.3 FP and DBR lasers . . . . .	29
2.2.4 DFB lasers . . . . .	29
2.3 Electro-optical aspects of laser diodes . . . . .	31
2.3.1 Heterojunctions and quantum wells . . . . .	31

---

2.3.2	Carrier transport – diffusion and drift . . . . .	32
2.3.3	Carrier generation and recombination . . . . .	32
2.3.4	Optical gain . . . . .	35
2.3.5	Optical loss mechanisms . . . . .	36
2.3.6	Laser rate equations . . . . .	36
2.4	Electronic wavelength control . . . . .	37
2.4.1	The free-carrier plasma dispersion effect . . . . .	37
2.4.2	Application of an electric field . . . . .	39
2.4.3	Thermal tuning . . . . .	40
2.5	Characteristics of tunable laser diodes . . . . .	40
2.5.1	Wavelength tuning range and accuracy . . . . .	40
2.5.2	Side-mode suppression ratio . . . . .	41
2.5.3	Linewidth . . . . .	42
2.6	Extending the wavelength tuning range . . . . .	42
2.6.1	The Vernier principle . . . . .	42
2.6.2	Sampled grating reflectors . . . . .	42
2.6.3	Design rules for wide tuning of SG-based lasers . . . . .	45
2.7	Native III-V versus III-V-on-silicon lasers . . . . .	46
2.7.1	Optical confinement . . . . .	46
2.7.2	Grating coupling coefficient . . . . .	46
2.7.3	Thermal properties . . . . .	47
2.8	Epitaxial layer stacks used in this work . . . . .	47
2.9	Conclusion . . . . .	47
	References . . . . .	50
<b>3</b>	<b>Fabrication of heterogeneously integrated tunable lasers</b>	<b>53</b>
3.1	Introduction . . . . .	53
3.2	Laser fabrication . . . . .	54
3.2.1	Lithographic mask design . . . . .	54
3.2.2	SOI and III-V processing . . . . .	56
3.2.3	Fabrication issues and fixes . . . . .	60
3.2.4	Final fabrication results . . . . .	61
3.3	Electron-beam lithography and reactive ion etching of SOI circuits . . . . .	62
3.3.1	Electron-beam lithography . . . . .	63
3.3.2	Lithographic mask design . . . . .	63
3.3.3	EBL process flow . . . . .	64
3.3.4	RIE of SOI circuits . . . . .	65
3.3.5	Fabrication and characterization results . . . . .	66
3.3.6	Bonding on the SOI chips . . . . .	69
3.4	Conclusion . . . . .	69
	References . . . . .	70

---

<b>4</b>	<b>Electronically tunable DFB lasers on silicon</b>	<b>71</b>
4.1	Introduction . . . . .	71
4.2	Tunable twin-guide (TTG-) DFB laser . . . . .	72
4.2.1	Transversely integrated laser structure . . . . .	72
4.2.2	Design aspects . . . . .	74
4.2.3	Fabrication . . . . .	83
4.2.4	Static laser characteristics . . . . .	84
4.2.5	Dynamic laser characteristics . . . . .	87
4.3	Sampled grating (SG-) TTG-DFB laser . . . . .	92
4.3.1	Characterization . . . . .	92
4.4	SG-DFB laser . . . . .	93
4.4.1	Design aspects . . . . .	93
4.4.2	Fabrication . . . . .	96
4.4.3	Characterization . . . . .	97
4.5	Conclusion . . . . .	101
	References . . . . .	103
<b>5</b>	<b>Electronically tunable DBR lasers on silicon</b>	<b>107</b>
5.1	Introduction . . . . .	107
5.2	Thermally tunable TTG-DBR laser . . . . .	108
5.2.1	Design aspects . . . . .	108
5.2.2	Fabrication . . . . .	111
5.2.3	Static laser characteristics . . . . .	114
5.3	Electronically tunable TTG-DBR laser . . . . .	116
5.3.1	Laser structure . . . . .	117
5.3.2	Optimization of the tuning layer thickness . . . . .	117
5.3.3	Optimization of the cladding layer thickness . . . . .	118
5.3.4	Mode profiles for the optimized structure . . . . .	118
5.4	Conclusion . . . . .	118
	References . . . . .	120
<b>6</b>	<b>Discretely tunable lasers on silicon based on filtered optical feedback</b>	<b>121</b>
6.1	Introduction . . . . .	121
6.2	Design aspects . . . . .	122
6.2.1	Laser structure . . . . .	122
6.2.2	SOA design . . . . .	123
6.2.3	AWG filter design . . . . .	123
6.2.4	DBR design . . . . .	125
6.2.5	Simulation of the wavelength switching behavior . . . . .	126
6.3	Fabrication . . . . .	129
6.4	Static laser characteristics . . . . .	129
6.5	Dynamic laser characteristics . . . . .	133
6.5.1	Small-signal characteristics . . . . .	133
6.5.2	Large-signal characteristics . . . . .	133

---

6.5.3	Wavelength switching characteristics . . . . .	135
6.6	Conclusion . . . . .	137
	References . . . . .	138
<b>7</b>	<b>Adiabatic tapered coupler for transfer printing</b>	<b>141</b>
7.1	Introduction . . . . .	141
7.1.1	Process flow for transfer printing . . . . .	142
7.1.2	Adiabatic tapered coupler for transfer printing . . . . .	143
7.2	Coupler design . . . . .	144
7.2.1	Technology platforms and simulation tools . . . . .	144
7.2.2	Coupling mechanism . . . . .	144
7.2.3	Coupling structure . . . . .	145
7.2.4	Optimization of Coupling Section 1 . . . . .	145
7.2.5	Optimization of Coupling Section 2 . . . . .	148
7.2.6	Optimization of Coupling Section 3 . . . . .	149
7.2.7	Overall coupling structure – lateral misalignment tolerance . . . . .	152
7.3	Other alignment-tolerant couplers . . . . .	153
7.4	Conclusion . . . . .	154
	References . . . . .	155
<b>8</b>	<b>Conclusion and prospects</b>	<b>157</b>
8.1	Conclusion . . . . .	157
8.2	Prospects . . . . .	158

# List of Figures

1	Elektronisch golflengte-afstembare TTG-DFB-laser. <b>(a)</b> SEM/FIB dwarsdoorsnede-beeld van een gefabriceerde laser; <b>(b)</b> Gesuperponeerde laserspectra bij verschillende afstemstromen; <b>(c)</b> Oogdiagram bij 12.5 Gbit/s NRZ-OOK directe modulatie; <b>(d)</b> Golflengteschakelkarakteristieken. . . . . xxviii
2	Thermisch golflengte-afstembare TTG-DBR-laser. <b>(a)</b> Optische microscoopafbeelding van een gefabriceerde chip; <b>(b)</b> Gesuperponeerde laserspectra bij verschillende fase- en Bragg-afstemstromen. . . . . xxix
3	Golflengte-selecteerbare laser op basis van gefilterde optische feedback. <b>(a)</b> Oogdiagrammen bij 12.5 Gbit/s NRZ-OOK directe modulatie voor elk golflengte-kanaal; <b>(b)</b> Golflengteschakelkarakteristieken voor het schakelen tussen twee naburige kanalen. xxx
4	Illustratie van heterogene integratie door middel van transferprinten. Het diagram toont een typisch actief silicium-fotonica integratieplatform. Een lokale opening in de back-end stapel bevat een geprefabriceerde III-V coupon. . . . . xxxi
5	Koppelingsefficiëntie voor de ontworpen adiabatisch getaperde koppelaar versus laterale misalignering. . . . . xxxii
6	Electronically tunable TTG-DFB laser. <b>(a)</b> SEM/FIB cross-sectional image of a fabricated laser; <b>(b)</b> Superimposed laser spectra at different tuning currents; <b>(c)</b> Eye diagram at 12.5 Gbit/s NRZ-OOK direct modulation; <b>(d)</b> Wavelength switching characteristics. . . . . xxxvi
7	Thermally tunable TTG-DBR laser. <b>(a)</b> Optical microscope image of the fabricated chip; <b>(b)</b> Superimposed laser spectra for different Phase and Bragg currents. . . . . xxxvii
8	Wavelength-selectable laser based on filtered optical feedback. <b>(a)</b> Eye diagrams at 12.5 Gbit/s NRZ-OOK direct modulation of each wavelength channel; <b>(b)</b> Wavelength switching characteristics for switching between two neighboring channels. . . . . xxxviii

---

9	Illustration of sparse heterogeneous integration through transfer printing. The schematic shows a typical active silicon photonic integration platform. A local opening in the back-end stack contains a processed III-V device coupon. . . . .	xxxix
10	Coupling efficiency of the designed adiabatic tapered coupler versus lateral alignment offset. . . . .	xl
1.1	Global data center IP traffic growth. Estimations indicate that by the end of 2021 the annual global data center IP traffic will reach 20.6 ZB, up from 6.8 ZB in 2016. Graphic is reproduced from [2]. . . . .	2
1.2	An optical packet switch forwarding module using TWCs and an AWGR. Incoming optical packets arrive at any wavelength. A fast tunable laser as part of the TWC is rapidly tuned to the desired forwarding wavelength. The $N \times N$ cyclic AWGR passively routes the optical packets to the desired physical output port (depending on the chosen forwarding wavelength). Graphic is reproduced from [9]. . . . .	4
1.3	Operation principle of a frequency-modulated continuous-wave (FMCW) LIDAR system. A sawtooth-like frequency modulated laser beam is sent simultaneously to an object and a reference mirror. From the superimposed reflected signals the distance to the object can be determined. Graphic is reproduced from [5]. . . . .	5
1.4	Optical microscope image of a silicon photonic integrated circuit wire-bonded on a printed circuit board. Image taken from [35]. . . . .	7
1.5	Schematic overview of different heterogeneously integrated laser structures. (a) VCSEL; (b) DFB laser; (c) DBR laser. . . . .	10
2.1	Power reflection as a function of $\kappa L$ at the Bragg wavelength ( $\Delta\beta = 0$ ) in a grating reflector. . . . .	28
2.2	Laser operation. (a) Heterogeneously integrated Fabry-Pérot (FP) laser; (b) Heterogeneously integrated Distributed Bragg reflector (DBR) laser. . . . .	30
2.3	Energy diagram for heterojunctions and quantum wells, with indication of the conduction band energy ( $E_C$ ), valence band energy ( $E_V$ ) and Fermi level ( $E_F$ ). . . . .	31
2.4	Band diagrams for $p$ -type and $n$ -type semiconductor-metal contacts. . . . .	33
2.5	Overview of the different radiative and non-radiative recombination processes in a semiconductor. . . . .	34

2.6	Free-carrier plasma dispersion effect for InGaAsP, InP and Si. (a) Carrier-induced refractive index changes ( $-\Delta n_R$ ); (b) Carrier-induced absorption changes ( $\Delta\alpha$ ); (c) $-\Delta n_R/\Delta n_I$ as a function of carrier density. . . . .	38
2.7	Illustration of the quantum-confined Stark effect (QCSE). (a) No electric field applied; (b) Electric field applied. By application of an electric field to a QW structure, the band edges become inclined and the wavefunctions get displaced with respect to each other. This leads to a reduction of the effective bandgap and a modification of the refractive index. . . . .	39
2.8	Different types of wavelength tuning. (a) Continuous; (b) Discontinuous; (c) Quasi-continuous. . . . .	41
2.9	Working principle of a Vernier caliper. The caliper contains a fixed main scale and a movable Vernier scale. Both scales exhibit slightly different pitches. From the main scale the rough measurement value can be read, whereas increased accuracy can be reached through the Vernier scale. . . . .	43
2.10	Simulated SG reflection spectrum for two different sampling duty cycles. Grating parameters are $\Lambda = 240$ nm, $\Lambda_S = 80$ $\mu\text{m}$ and $L = 720$ $\mu\text{m}$ . (a) $D_{SG} = 10\%$ ; (b) $D_{SG} = 20\%$ . . . . .	44
2.11	Schematic of a heterogeneously integrated SG-DBR laser, with two SG reflectors. Both reflectors exhibit a comb-like reflection spectrum with different peak spacing. The peak spacing for Reflector 1 and Reflector 2 is proportional to $1/\Lambda_{S1}$ and $1/\Lambda_{S2}$ , respectively. . . . .	45
3.1	Lithographic mask design for a set of TTG-DFB and SG-TTG-DFB lasers. . . . .	55
3.2	Fabrication process flow for TTG-DFB lasers. . . . .	57
3.3	Undesired undercut after wet etching. (a) In the $p$ -InGaAs contact layer; (b) In the active and tuning layer. . . . .	60
3.4	Dependence of the mesa profile on the III-V crystal orientation. (a) Christmas tree profile (wrong); (b) V-groove profile (correct). . . . .	60
3.5	Definition of the tuning taper through ICP etching. . . . .	61
3.6	Optical microscope image of a fabricated chip with a set of TTG-DFB and SG-TTG-DFB lasers. . . . .	62
3.7	Introduction of waveguide imperfections at stitching boundaries of the 500 $\mu\text{m}$ by 500 $\mu\text{m}$ EBL write fields. . . . .	64
3.8	EBL and RIE for the fabrication of single-mode SOI rib waveguides. (a) Cross-sectional view of the waveguide structure after development; (b) Cross-sectional view of the waveguide structure after RIE. . . . .	65
3.9	Estimation of the waveguide loss through a set of “grating coupler in – waveguide – grating coupler out” test structures. . . . .	66

---

3.10	E-beam fabrication of a set of sidewall-corrugated gratings (with a grating length of $150\ \mu\text{m}$ and a grating period of $250\ \text{nm}$ ). (a) SEM image of a grating with a sidewall corrugation of $300\ \text{nm}$ ; (b) SEM image of a grating with a sidewall corrugation of $700\ \text{nm}$ ; (c) Reflection spectra. . . . .	67
3.11	E-beam fabrication of a top-etched grating. (a) SEM image of a waveguide connected to the grating; (b) SEM image of the enlarged grating and indication of the geometrical dimensions. . . . .	68
3.12	E-beam fabrication of a photonic crystal structure on a $220\ \text{nm}$ SOI die. (a) SEM image of the full structure, with several input and output waveguides connected to the photonic crystal cavity; (b) SEM image of the enlarged photonic crystal cavity. . . . .	68
4.1	TTG-DFB laser structure. (a) 3D schematic; (b) Cross-sectional view. Through carrier injection into the tuning layer, the effective index of the optical mode can be modified, in turn modifying the laser wavelength. . . . .	73
4.2	Overview of the different figures of merit in the TTG-DFB laser design. The transverse confinement factor in the silicon waveguide $\Gamma_{\text{Si}}$ is strongly linked with the grating coupling coefficient $\kappa$ . . . . .	76
4.3	Optimization of the TTG-DFB laser design. Influence of the tuning layer thickness $t_{\text{T}}$ and DVS-BCB thickness $t_{\text{DVS-BCB}}$ on (a) the confinement factor in the tuning layer $\Gamma_{\text{T}}$ ; (b) the confinement factor in the active layer $\Gamma_{\text{A}}$ ; (c) the grating coupling coefficient $\kappa$ . . . . .	77
4.4	Simulated optical mode profile for the chosen TTG-DFB laser design (at $1550\ \text{nm}$ , TE polarization). The mode is nicely distributed over the active, tuning and silicon waveguide layer, with very strong confinement in the tuning layer ( $\Gamma_{\text{T}} = 23.7\%$ ). . . . .	78
4.5	Bragg grating design. (a) Influence of $t_{\text{DVS-BCB}}$ on $\kappa$ for the chosen epitaxial layer stack ( $t_{\text{T}} = 190\ \text{nm}$ ); (b) $\kappa \cdot L$ versus $L$ . Typically $1 < \kappa \cdot L < 3$ is taken as rule-of-thumb in the design of DFB lasers. . . . .	79
4.6	TCAD simulation of the electron density profile upon carrier injection into the tuning layer. . . . .	80
4.7	Adiabatic tapered coupler in the TTG-DFB laser design. (a) Schematic (top view); (b) Simulated intensity distribution for the optimized structure (side view). . . . .	82
4.8	Adiabatic tapered coupler for the TTG-DFB laser structure. (a) Influence of $L_2$ on the coupling efficiency; (b) Influence of the InP taper tip width on the coupling efficiency and power reflection for $L_2 = 180\ \mu\text{m}$ . . . . .	83

4.9	TTG-DFB laser fabrication. (a) SEM image of a set of fabricated devices with different Bragg grating lengths; (b) SEM/FIB image of the laser cross-section taken in the middle of the structure. . . . .	84
4.10	TTG-DFB laser characterization. (a) LIV characteristics (waveguide-coupled output power); (b) Laser spectrum at a gain current of 90 mA and zero tuning bias. . . . .	85
4.11	TTG-DFB laser tuning characteristics. (a) Superimposed laser spectra upon tuning at a gain current of 90 mA; (b) Wavelength and SMSR versus tuning current. . . . .	86
4.12	Measurement setup to characterize the small- and large-signal modulation response of the TTG-DFB laser. . . . .	88
4.13	Small-signal modulation response of the TTG-DFB laser at 70 mA and 90 mA DC gain current and zero tuning bias (curves have been smoothed). . . . .	89
4.14	Large-signal modulation response of the TTG-DFB laser at 90 mA DC gain current and zero tuning bias under 10 Gbit/s and 12.5 Gbit/s NRZ-OOK direct modulation of the gain current. . . . .	89
4.15	Measurement setup to characterize the small- and large-signal wavelength modulation response of the TTG-DFB laser. . . . .	90
4.16	Wavelength switching characteristics of the TTG-DFB laser. (a) Small-signal wavelength modulation response; (b) Large-signal time-domain characteristic upon switching. . . . .	91
4.17	SG-TTG-DFB laser characterization. LIV characteristics (waveguide-coupled output power). . . . .	92
4.18	SG-TTG-DFB laser spectra at a fixed DC gain current of 300 mA. . . . .	94
4.19	3D layout of the SG-DFB laser. The front and back SG have a slightly different periodicity to exploit the Vernier effect for wide wavelength tuning. . . . .	95
4.20	Superimposed simulated reflection spectra for the two sampled gratings of the SG-DFB laser. . . . .	96
4.21	SEM/FIB image of the fabricated SG-DFB laser. (a) Transverse cross-sectional view; (b) Longitudinal cross-sectional view. . . . .	97
4.22	LIV characteristics of the SG-DFB laser. (a) IV curves; (b) LI curves (fiber-coupled output power). . . . .	98
4.23	Tuning characteristics of the SG-DFB laser. (a) Laser wavelength versus $I_{\text{front}}$ and $I_{\text{back}}$ ; (b) Fiber-coupled output power versus $I_{\text{front}}$ and $I_{\text{back}}$ . . . . .	99
4.24	(a) Superimposed laser spectra; (b) Fiber-coupled output power and SMSR at the different wavelength channels. . . . .	100
5.1	3D schematic of the InP-on-silicon TTG-DBR laser structure.	108

---

5.2	Sidewall-corrugated silicon grating. (a) Design on the lithographic mask with $L = 300 \mu\text{m}$ , $W = 1 \mu\text{m}$ , $\Delta W = 300 \text{ nm}$ and $\Lambda = 250 \text{ nm}$ . (b) SEM image of the fabricated structure. For clarity the passive InP tuning waveguide is not shown. (c) Simulated reflection spectra for the precompensated design and the fabricated structure (post-litho). . . . .	110
5.3	InP-to-silicon adiabatic tapered coupler. (a) Coupling efficiency for the first and second taper section as a function of taper length. (b) Coupling efficiency and power reflection for the first and second taper section as a function of InP taper tip width for a total taper length of $130 \mu\text{m}$ . . . . .	111
5.4	(a) Optical mode profile in the phase and Bragg section. (b) Optical mode profile in the gain section. (c) Optical microscope image of the fabricated laser device. . . . .	112
5.5	Facet of a thermally tunable TTG-DBR laser fabricated by means of a FIB cut. . . . .	112
5.6	Static laser characteristics of the thermally tunable TTG-DBR laser. (a) LI characteristic (waveguide-coupled output power); (b) Optical spectrum for a Gain current of 120 mA. In both graphs the Phase and Bragg section are unbiased. . . . .	113
5.7	Laser wavelength as a function of Bragg current at a Gain current of 120 mA. The Phase current is varied between 0 mA and 24 mA. Both currents are swept in steps of 1 mA. The inset shows a close-up around 1571 nm, illustrating the continuous tuning nature. . . . .	114
5.8	(a) Laser wavelength as a function of the Phase current. (b) Superimposed laser spectra for different Phase and Bragg currents. In both graphs the Gain current is 120 mA and the Bragg current is varied between 0 mA and 70 mA. The current step is chosen such that the peak wavelength spacing is 0.5 nm (also see Fig. 5.7). . . . .	115
5.9	Cross-sectional view of the improved TTG-DBR laser layout in the phase and Bragg section. . . . .	116
5.10	Optimization of the tuning layer thickness. Influence of $t_T$ on (a) the confinement factor in the tuning layer $\Gamma_T$ and on (b) the grating coupling coefficient $\kappa$ . . . . .	117
5.11	Optimization of the cladding layer thickness. Influence of $t_{\text{InP}}$ on the modal loss, with assumption of a Ni/Ge/Au metallurgy. . . . .	118
5.12	Illustration of the optical mode profiles in the gain and Bragg section for the optimized TTG-DBR laser design (at 1550 nm, TE polarization). . . . .	119
6.1	Schematic of the filtered feedback tunable laser structure. . . . .	122

6.2	AWG design. (a) Simulation of the AWG filter transmission; (b) SEM image of the AWG; (c) SEM image of the AWG (zoom on the star coupler region). . . . .	124
6.3	Characterization of the stand-alone AWG after complete laser device processing. . . . .	125
6.4	DBR design. (a) Peak reflectance as a function of number of grating periods ( $\Lambda = 252$ nm, duty cycle = 50%); (b) Reflection spectra for $\text{DBR}_{\text{FF}}$ , $\text{DBR}_{\text{Out}}$ and $\text{DBR}_{\text{HR}}$ . . . . .	126
6.5	Relationship between the filtered feedback strength $\gamma$ and the amplification in the SOA gate $A_{\text{Gate}}$ , for different values of $R_{\text{DBR}_{\text{FF}}}$ . . . . .	127
6.6	Simulation of the wavelength switching behavior. (a) Time-domain characteristics when $\gamma_1$ and $\gamma_2$ are periodically and complementary switched between $0 \text{ ns}^{-1}$ and $10 \text{ ns}^{-1}$ ; (b) Dependence of the switching time on feedback phase $\phi_2$ ( $\phi_1 = 0$ ); (c) Dependence of the switching time on the feedback strength $\gamma$ ( $\phi_1 = \phi_2 = 0$ ). . . . .	128
6.7	Optical microscope image of the fabricated device. Naming of the different currents and contact pads for characterization are indicated. The upper contact pads are used for static characterization whereas the lower contact pads are used for dynamic characterization. . . . .	130
6.8	Static laser characteristics (with unbiased gates). (a) LI curves at different substrate temperatures (fiber-coupled output power); (b) Dependence of the threshold current on the substrate temperature. . . . .	131
6.9	Static laser characteristics. (a) Laser spectrum when the gates are left unbiased; (b) Superimposed laser spectra when the gates are appropriately biased above transparency; (c) Dependence of the laser wavelength on the gate current (only data points with an SMSR $> 35$ dB are shown). . . . .	132
6.10	Dynamic laser characteristics. (a) Small-signal modulation response for $I_{\text{Gain}} = 80$ mA and $I_{\text{G1}} = 28$ mA (curve has been smoothed); (b) Eye diagrams for all four different wavelength channels under 12.5 Gbit/s direct modulation (back-to-back); (c) Bit error rate versus received power under 10 Gbit/s and 12.5 Gbit/s direct modulation (Channel 1, back-to-back). . . . .	134
6.11	Schematic of the optical setup to measure the wavelength switching characteristics. . . . .	135
6.12	Wavelength switching characteristics. (a) Switching from Gate 1 to Gate 2; (b) Switching from Gate 3 to Gate 4. . . . .	136

- 
- 7.1 Illustration of sparse heterogeneous integration through transfer printing. The schematic shows a typical active silicon photonic integration platform. A local opening in the back-end stack contains a processed III-V device coupon. . . . . 142
- 7.2 Process flow for transfer printing a III-V patterned device onto a silicon target substrate. **(a)** III-V source wafer; **(b)** Patterning of device and release layer; **(c)** Definition of tethers for device anchoring; **(d)** Removal of release layer; **(e)** Device pick-up from source; **(f)** Device release on target. . . . 143
- 7.3 Schematic of the adiabatic tapered coupler. **(a)** 3D view; **(b)** Projected cross-sectional view with indication of the different layers; **(c)** Top view with cross-sectional views along the coupling structure. . . . . 146
- 7.4 Optimization of Coupling Section 1. **(a)** Schematic of Coupling Section 1; **(b)** Schematic of the interface at the end of Coupling Section 1; **(c)** Transmission at the interface at the end of Coupling Section 1 versus width of the  $n$ -InP rib waveguide for different thicknesses of the  $n$ -InP bottom cladding,  $w_{\text{III-V tip}} = 400$  nm; **(d)** Optimum choice of the  $n$ -InP rib waveguide width versus thickness of the  $n$ -InP bottom cladding; **(e)** Taper coupling efficiency versus taper length for different values of the III-V taper tip width,  $t_{n\text{-clad}} = 900$  nm and  $w_{n\text{-clad, start}} = 3$   $\mu\text{m}$ ; **(f)** Taper coupling efficiency versus III-V taper tip width for  $L_1 = 150$   $\mu\text{m}$ ,  $t_{n\text{-clad}} = 900$  nm and  $w_{n\text{-clad, start}} = 3$   $\mu\text{m}$ . . . . . 147
- 7.5 Optimization of Coupling Section 2. **(a)** Schematic of Coupling Section 2; **(b)** Taper coupling efficiency versus taper length for different values of the InP waveguide end width. . . 149
- 7.6 Optimization of Coupling Section 3. **(a)** Schematic of Coupling Section 3; **(b)** Schematic of interface at the end of Coupling Section 3; **(c)** Transmission at the interface at the end of Coupling Section 3 versus width of the silicon waveguide for different values of the III-V taper tip width,  $t_{\text{DVS-BCB}} = 50$  nm; **(d)** Transmission at the interface at the end of Coupling Section 3 versus width of the silicon waveguide for different values of the III-V taper tip width,  $t_{\text{DVS-BCB}} = 150$  nm; **(e)** Transmission at the interface at the end of Coupling Section 3 versus III-V taper tip width for different values of the DVS-BCB thickness,  $w_{\text{silicon}} = 2$   $\mu\text{m}$ ; **(f)** Taper coupling efficiency versus taper length for different values of the DVS-BCB thickness,  $w_{\text{silicon}} = 2$   $\mu\text{m}$ ,  $w_{\text{IM}} = 1.1$   $\mu\text{m}$ . . . . 150

---

7.7	Overall coupling structure. (a) Coupling efficiency versus length of Coupling Section 3 ( $L_3$ ) for different lateral alignment offsets and values of the III-V taper tip width; (b) Coupling efficiency versus lateral alignment offset for different values of the III-V taper tip width, $L_3 = 255 \mu\text{m}$ . . . . .	151
7.8	Overall coupling structure. Light propagation from the III-V waveguide to the SOI waveguide in the overall coupling structure for $w_{\text{III-V tip}} = 400 \text{ nm}$ . Mode profiles along the coupler are indicated as well. . . . .	152
7.9	Wavelength dependence of the coupler efficiency for the overall optimized coupling structure with $n\text{-InP}$ intermediate waveguide, $w_{\text{III-V tip}} = 400 \text{ nm}$ . . . . .	153



# List of Tables

1.1	Heterogeneously integrated tunable laser diodes – state-of-the-art. . . . .	12
2.1	Epitaxial layer stack – amplifier. . . . .	48
2.2	Epitaxial layer stack – tunable twin-guide (TTG). . . . .	49
4.1	Injection current and laser wavelength for the channels shown in Fig. 4.24. . . . .	101
7.1	Detailed III-V epitaxial layer stack. The refractive index (RI) values are at 1550 nm. . . . .	145



# List of Acronyms

## A

AC	Alternating Current
AWG	Arrayed Waveguide Grating
AWGR	Arrayed Waveguide Grating Router

## B

BER	Bit Error Rate
BOX	Buried Oxide
BW	Bandwidth

## C

CMOS	Complementary Metal-Oxide-Semiconductor
CW	Continuous-Wave

## D

DBR	Distributed Bragg Reflector
DC	Direct Current
DDE	Delay Differential Equation
DFB	Distributed Feedback
DI	Deionized
DVS-BCB	Divinylsiloxane-Bis-Benzocyclobutene

**E**

EBL	Electron-Beam Lithography
EDFA	Erbium-Doped Fiber Amplifier
EME	Eigenmode Expansion
ER	Extinction Ratio

**F**

FBMS	Fixed Beam Moving Stage
FCA	Free-Carrier Absorption
FCD	Free-Carrier Plasma Dispersion
FEC	Forward Error Correction
FIB	Focused Ion Beam
FM	Frequency Modulation
FP	Fabry-Pérot
FPR	Free Propagation Region
FSR	Free Spectral Range
FWHM	Full Width at Half Maximum

**G**

GC	Grating Coupler
GSG	Ground-Signal-Ground
GSGSG	Ground-Signal-Ground-Signal-Ground

**H**

HWHM	Half Width at Half Maximum
HD	Hard Decision

**I**

ICP	Inductively Coupled Plasma
-----	----------------------------

---

IP	Internet Protocol
IPA	Iso-Propylalcohol
IVBA	Intervalence Band Absorption

**L**

LD	Laser Diode
LI	Light-Current
LIDAR	Light Detection And Ranging
LIV	Light-Current-Voltage

**M**

MBMS	Modulated Beam Moving Stage
MEMS	Microelectromechanical Systems
MPW	Multi-Project Wafer
MQW	Multiple Quantum Wells

**N**

N/A	Not Applicable
NID	Not Intentionally Doped
N/S	Not Specified
NRZ	Non-Return-to-Zero

**O**

OBS	Optical Burst Switching
OOK	On-Off-Keying
OPS	Optical Packet Switching
OSA	Optical Spectrum Analyzer
OTF	Optical Tunable Filter

**P**

PECVD	Plasma-Enhanced Chemical Vapor Deposition
PIC	Photonic Integrated Circuit
PL	Photoluminescence
PPG	Pulse-Pattern Generator
PR	Photoresist
PRBS	Pseudorandom Binary Sequence

## Q

QCSE	Quantum-Confined Stark Effect
------	-------------------------------

## R

RADAR	Radio Detection And Ranging
RF	Radio Frequency
RI	Refractive Index
RIE	Reactive Ion Etching
RT	Rise Time

## S

SCH	Separate Confinement Heterostructure
SEM	Scanning Electron Microscope
SG	Sampled Grating
SMF	Single-Mode Optical Fiber
SMSR	Side-Mode Suppression Ratio
SOA	Semiconductor Optical Amplifier
SOI	Silicon-On-Insulator
SRH	Shockley-Read-Hall

## T

TCAD	Technology Computer-Aided Design
TE	Transverse Electric
TLM	Transmission Line Model
TM	Transverse Magnetic

TMM	Transfer Matrix Method
TP	Transfer Printing
TTG	Tunable Twin-Guide
TWC	Tunable Wavelength Converter

**U**

UG	Uniform Grating
UV	Ultraviolet

**V**

VCSEL	Vertical-Cavity Surface-Emitting Laser
VNA	Vector Network Analyzer

**W**

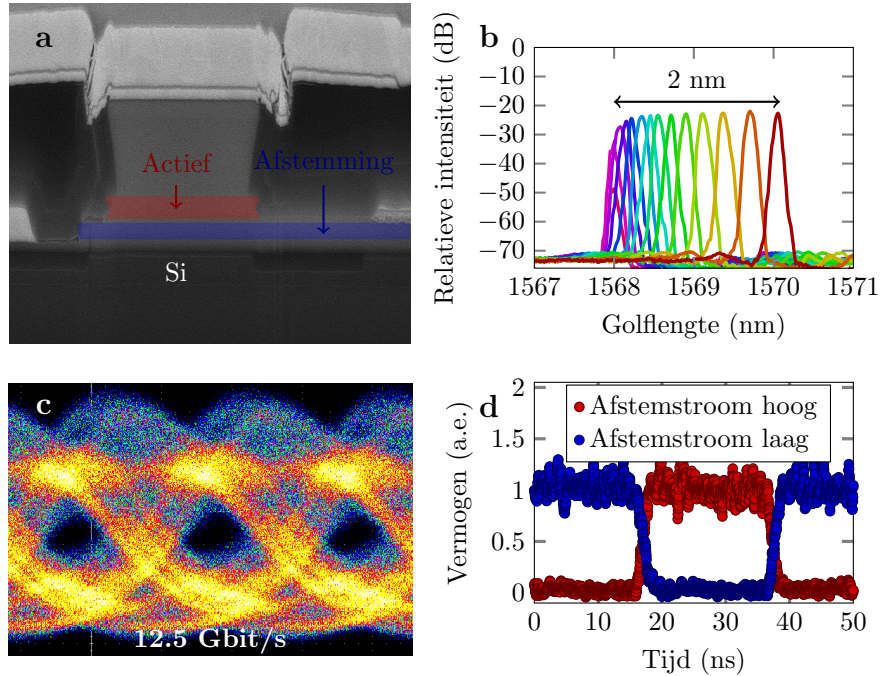
WDM	Wavelength-Division Multiplexing
-----	----------------------------------



# Samenvatting

**I**N dit werk wordt de realisatie nagestreefd van elektronisch golflengte-afstembare lasers die heterogeen geïntegreerd zijn op een silicium-fotonica platform.

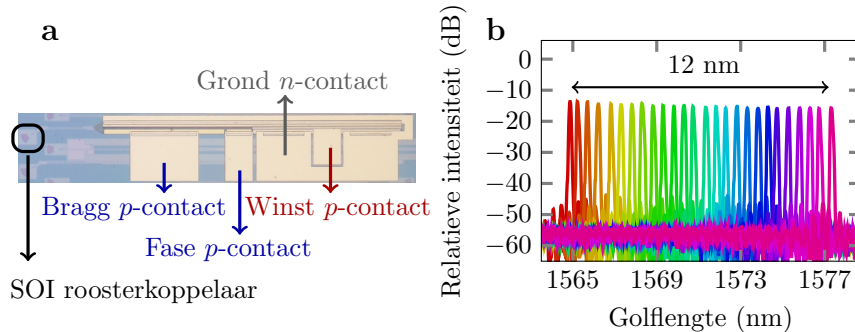
De voorbije twintig jaar hebben internettechnologieën een ongelooflijk snelle groei gekend. Sociale netwerken, video-on-demand-diensten en cloud computing zijn slechts enkele toepassingen die hebben geleid tot een enorme toename van de hoeveelheid dataverkeer en -opslag wereldwijd. Deze trend lijkt niet snel te zullen stoppen en heeft specifieke implicaties voor datacenteromgevingen, waar steeds complexere en frequentere communicatie tussen de gebruikte servers vereist is. Aangezien het internetprotocol (IP)-verkeer van een inherent burst-achtige aard is, zijn optisch burst- en pakketschakelen naar voren gebracht als haalbare oplossing om te voldoen aan de strenge bandbreedtevereisten. Mogelijke implementaties van dergelijke burst- of pakketschakelsystemen zijn typisch gebaseerd op golflengte-afstembare lasers met nanoseconde schakelsnelheden in combinatie met passieve optische routers (AWGR's). De meest veelbelovende manier om snel-afstembare lasers te realiseren is gebaseerd op elektronische golflengtecontrole, waarbij geïnjecteerde ladingsdragers leiden tot een verandering in brekingsindex en een daaruitvolgende golflengteverschuiving. Omdat nauwe integratie met elektronische systemen gunstig is voor de laseraansturing, is CMOS-compatible optische technologie hoogst wenselijk. In de afgelopen jaren is het silicium-op-isolator (SOI)-platform een uitstekende CMOS-compatibele kandidaat gebleken. Vanwege zijn indirecte bandkloof is silicium echter niet geschikt voor de realisatie van efficiënte actieve componenten zoals laserdiodes. Heterogene III-V-op-silicium integratietechnologie, waarbij een III-V epitaxiale laagstapeling geïntegreerd wordt op een SOI-golfgeleidercircuit, heeft evenwel zijn sporen verdiend als alternatief. In dit werk worden verschillende III-V-op-silicium heterogeen geïntegreerde elektronisch afstembare laserstructuren op basis van adhesieve divinylsiloxaan-bis-benzocyclobuteen (DVS-BCB)-binding onderzocht.



**Figuur 1:** Elektronisch golflengte-afstembare TTG-DFB-laser. (a) SEM/FIB dwarsdoorsnede-beeld van een gefabriceerde laser; (b) Gesuperponeerde laserspectra bij verschillende afstemstromen; (c) Oogdiagram bij 12.5 Gbit/s NRZ-OOK directe modulatie; (d) Golflengteschakelkarakteristieken.

## Golflengte-afstembare twin-guide DFB- en DBR-lasers

Een golflengte-afstembare twin-guide (TTG) III-V epitaxiale laagstapeling bestaat uit een actieve laag (met meerdere kwantumputten) en een afstemlaag, beiden met hun omringende bekleding- en contactlagen. Wanneer een TTG epitaxiale laagstapeling geïntegreerd wordt bovenop een SOI-golfgelidercircuit, kan men een heterogeen geïntegreerde afstembare verdeelde terugkoppeling (DFB)- of gedistribueerde Bragg-reflector (DBR)-laser realiseren. De verticale integratie van een actieve en een afstemlaag maakt een bijna onafhankelijke controle van het laservermogen en de lasergolflengte mogelijk. Aangezien het afstemmechanisme gebaseerd is op de injectie van ladingsdragers, is de afstemsnelheid inherent snel. In dit werk worden vier TTG-gebaseerde laserstructuren geïntegreerd op silicium in beschouwing genomen.



**Figuur 2:** Thermisch golflengte-afstembare TTG-DBR-laser. (a) Optische microscopieafbeelding van een gefabriceerde chip; (b) Gesuperponeerde laserspectra bij verschillende fase- en Bragg-afstemstromen.

### TTG-DFB-laser

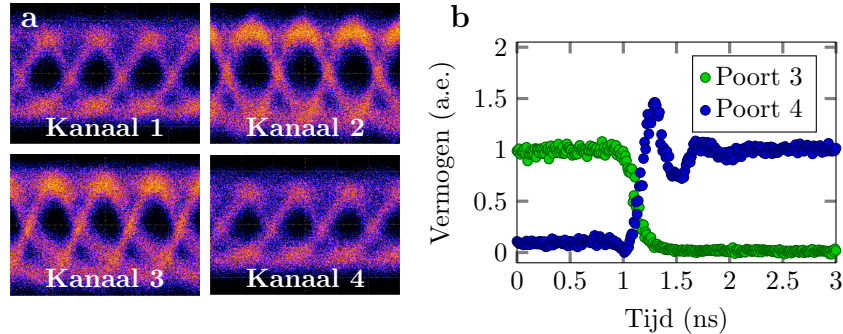
De eerste laserstructuur is een TTG-DFB-laser die elektronische golflengte-afstemming mogelijk maakt. De structuur bevat een  $\lambda/4$  in-fase-verschoven silicium Bragg-rooster dat gedistribueerde terugkoppeling voorziet. Figuur 1(a) toont een SEM/FIB dwarsdoorsnede-beeld van een gefabriceerde laser. Een elektronisch afstembereik van 2 nm wordt aangetoond met een enkele afstemstroom. Continue-golf (CW)-monomode laserwerking met een zijmode-onderdrukingsverhouding (SMSR) groter dan 44 dB over het afstembereik wordt verkregen. De afstemresultaten worden weergegeven in Fig. 1(b). Dynamische metingen tonen werking aan bij 12.5 Gbit/s non-return-to-zero aan-uit (NRZ-OOK) directe modulatie. Dit wordt geïllustreerd in Fig. 1(c). De gemeten schakeltijd is ongeveer 3 nanoseconden, met een dynamisch afstemmingsrendement van 0.13 nm/mA. De golflengteschakelkarakteristieken worden weergegeven in Fig. 1(d).

### SG-TTG-DFB-laser

Door gebruik te maken van bemonsterde roosters in plaats van uniforme Bragg-roosters, hebben we ook een bemonsterd rooster (SG-) TTG-DFB-laser gerealiseerd. Het gebruik van bemonsterde roosters kan het afstembereik vergroten door middel van het Vernier-principe. In dit geval tonen we golflengte-afstemming aan over zes afzonderlijke supermodes, met een totaal afstembereik van 8 nm.

### Thermisch golflengte-afstembare TTG-DBR-laser

Deze laserstructuur wordt geïmplementeerd als een DBR-laser met drie secties en bestaat uit een versterkings-, fase- en Bragg-sectie. In de verster-

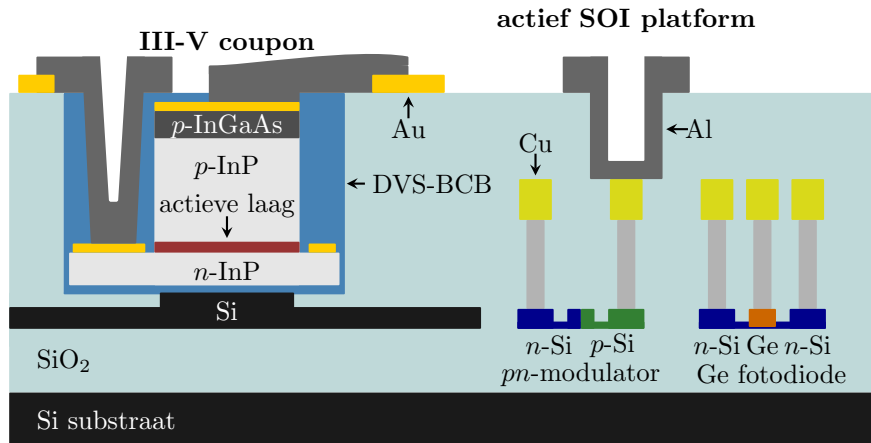


**Figuur 3:** Golfengte-selecteerbare laser op basis van gefilterde optische feedback. (a) Oogdiagrammen bij 12.5 Gbit/s NRZ-OOK directe modulatie voor elk golfengte-kanaal; (b) Golfengteschakelkarakteristieken voor het schakelen tussen twee naburige kanalen.

kingssectie wordt geen stroom geïnjecteerd in de afstemlaag. In de fase- en Bragg-sectie wordt de actieve laag verwijderd. Ladingsdragers kunnen geïnjecteerd worden om de lasergolfengte af te stemmen. In principe is een DBR-laser voordelig ten opzichte van een DFB-structuur omdat men de individuele longitudinale lasersecties afzonderlijk kan optimaliseren. In onze demonstratie is de golfengte-afstemming hoofdzakelijk thermisch, met een continu afstembereik groter dan 12 nm. De afstemlaag fungeert dus eerder als verwarmingselement, wat leidt tot een roodverschuiving van de lasergolfengte bij stroominjectie. Figuur 2(a) toont een optische microscopafbeelding van de gefabriceerde chip, met vermelding van de verschillende contacten. De gesuperponeerde laserspectra bij verschillende fase- en Bragg-afstemstromen worden getoond in Fig. 2(b).

### Elektronisch golfengte-afstembare TTG-DBR-laser

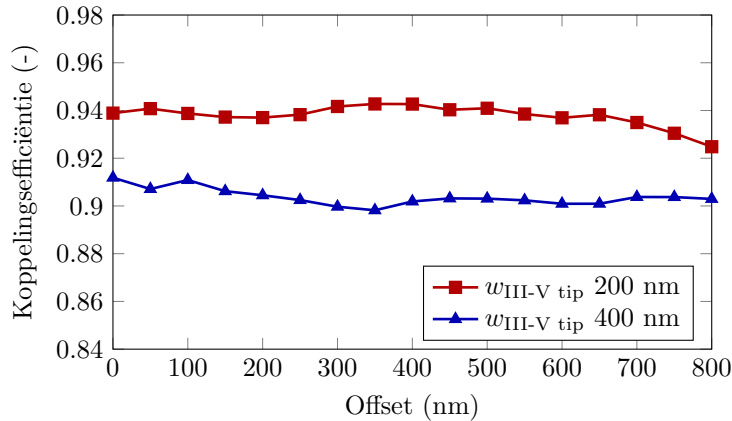
De hiervoor vernoemde thermisch afstembare TTG-DBR-laser vertoont geen netto elektronisch afstemmingseffect. Dit komt omdat er geen geoptimaliseerde TTG epitaxiale laagstapel werd gebruikt. Door optimalisatie van de TTG laagstapel en door gebruik te maken van een dikke afstemlaag en zeer dikke  $n$ -InP bekleding, wordt echter verwacht dat het afstemgedrag aanzienlijk kan verbeteren. In dit werk wordt zo'n geoptimaliseerd ontwerp voorgesteld. We merken hierbij op dat men ook bij deze laserstructuur het golfengte-afstembereik kan vergroten door gebruik te maken van bemonsterde roosters.



**Figuur 4:** Illustratie van heterogene integratie door middel van transferprinten. Het diagram toont een typisch actief silicium-fotonica integratieplatform. Een lokale opening in de back-end stapel bevat een geprefabriceerde III-V coupon.

## Golflengte-selecteerbare laser op basis van gefilterde optische terugkoppeling

Hoewel de op TTG-gebaseerde laserstructuren veelbelovend zijn, lijden ze onder zelfverhittingseffecten bij stroominjectie, wat het afstembereik en de afstemsnelheid beperkt. Bovendien is de groei van een TTG-epitaxiale laagstapel complexer dan die van een standaard epitaxiale versterkersstapel. Daarom hebben we een alternatieve laserstructuur onderzocht, waarbij gefilterde optische terugkoppeling gebruikt wordt om monomodaal gedrag en golflengte-selectiviteit te bekomen. Door middel van een optische filter (AWG) en een stel korte optische halfgeleiderversterkers (SOA's) in het terugkoppelpad van de externe caviteiten van de laserstructuur, kan zeer snelle golflengte-schakeling worden bereikt. Als proof-of-principle tonen we een laser met vier golflengte-kanalen aan. CW-monomodale laserwerking wordt eenvoudig bereikt wanneer de juiste stroom in de SOA-poorten wordt geïnjecteerd. 12.5 Gbit/s NRZ-OOK directe modulatie voor elk golflengte-kanal wordt aangetoond en het schakelen tussen twee kanalen kan in minder dan een nanoseconde. Figuur 3(a) toont de overeenkomstige oogdiagrammen. De golflengteschakelkarakteristieken voor het schakelen tussen twee naburige kanalen worden getoond in Fig. 3(b).



**Figuur 5:** Koppelingsefficiëntie voor de ontworpen adiabatisch getaperde koppelaar versus laterale misalignering.

## De weg naar transferprinten

Opdat de integratie van III-V-op-silicium op een massaal parallelle manier kan worden uitgevoerd, wordt transferprinten (TP) gezien als een zeer aantrekkelijke methode. De heilige graal van het combineren van gefabriceerde actieve III-V-componenten zoals versterkers en (afstembare) DFB- en DBR-lasers op een actief silicium-fotonica platform lijkt haalbaar in de nabije toekomst door middel van de transferprint-methode. Een illustratie daarvan wordt getoond in Fig. 4. Een belangrijke uitdaging bij TP is de relatief grote afwijking die ontstaat tussen de III-V-componenten en het silicium-doelwit tijdens het printen. Daarom wordt een adiabatisch getaperde koppelaar voorgesteld en ontworpen die zeer tolerant is voor misalignering en daarbij compatibel blijft met courante componentarchitecturen. De koppelingsefficiëntie voor de ontworpen koppelaar bereikt waarden boven 90%, zelfs voor een relatief grote laterale misalignering van 800 nm (zie Fig. 5). Dit is een significante verbetering in vergelijking met typische koppelaars, die over het algemeen een aligneringsnauwkeurigheid beter dan 300 nm vereisen. De koppelaar is met name geschikt voor componenten met een zeer dikke bekleedingslaag, waarvan de voorgestelde TTG-DBR-laser het beste voorbeeld is.

## Besluit

In dit doctoraatsonderzoek zijn verschillende elektronisch afstembare lasers op silicium ontwikkeld en experimenteel onderzocht. De aangetoonde lasers worden verwacht toepassing te vinden in toekomstige flexibele optische net-

werkarchitecturen en kunnen een aantrekkelijke oplossing zijn bij gebruik in optische burst- of pakketschakelsystemen in datacenternetwerken.



# Summary

**I**<sup>N</sup> *this work, the realization of electronically wavelength-tunable lasers heterogeneously integrated on a silicon photonics platform is pursued.*

In the past twenty years, internet technologies have known an incredibly fast growth. Social networking, video-on-demand services and cloud computing are only a few applications that have led to a massive increment in the amount of data traffic and storage worldwide. This trend is not stopping anytime soon and has particular implications in data center environments, where increasingly complex and frequent communication between the employed servers will be required. As the Internet Protocol (IP) traffic is of an inherent bursty nature, optical burst and packet switching network architectures have been put forward as a viable solution to keep up with the stringent bandwidth requirements. Envisioned implementations of such optical burst or packet switching systems are often based on fast wavelength-tunable lasers with nanosecond switching speeds in combination with passive arrayed waveguide grating routers (AWGRs). The most promising way to realize fast tunable lasers is based on electronic wavelength control, where injected carriers lead to a refractive index and consecutive wavelength shift, thereby exploiting the free-carrier plasma dispersion (FCD) effect. As close integration with electronic systems is beneficial for laser driver operation, complementary metal-oxide-semiconductor (CMOS) compatible optical technology is highly desirable. In recent years, the silicon-on-insulator (SOI) platform has proven to be an excellent CMOS-compatible candidate. However, because of its indirect bandgap, silicon is not suited for the realization of efficient active devices such as laser diodes. Heterogeneous III-V-on-silicon integration technology, in which a III-V epitaxial layer stack is integrated on top of an SOI waveguide circuit, has therefore made its mark to overcome this shortcoming. In this work, several III-V-on-silicon heterogeneously integrated electronically tunable laser structures based on adhesive divinylsiloxane-bis-benzocyclobutene (DVS-BCB) bonding are investigated.

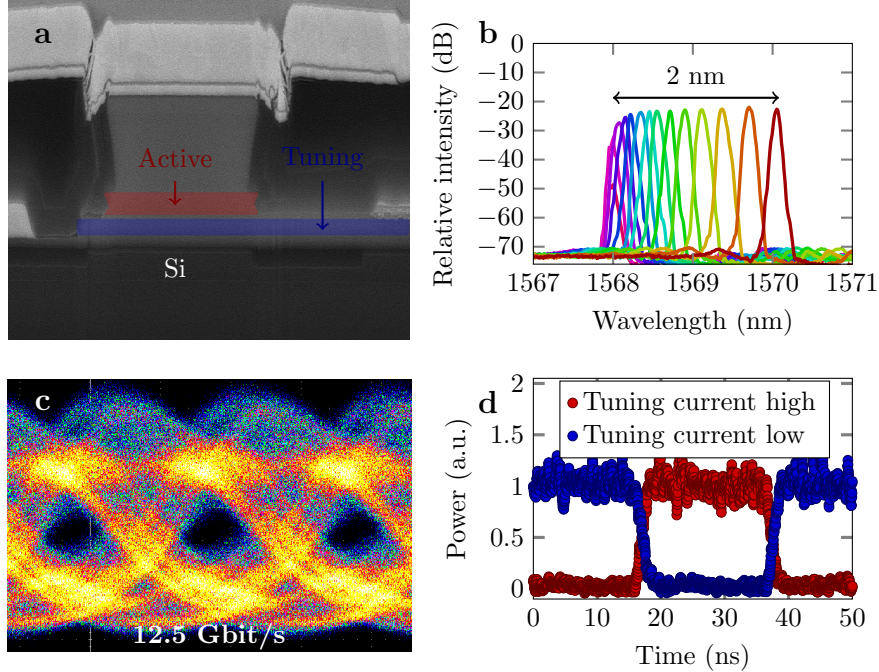


**Figure 6:** Electronically tunable TTG-DFB laser. (a) SEM/FIB cross-sectional image of a fabricated laser; (b) Superimposed laser spectra at different tuning currents; (c) Eye diagram at 12.5 Gbit/s NRZ-OOK direct modulation; (d) Wavelength switching characteristics.

## Tunable twin-guide DFB and DBR lasers

A tunable twin-guide (TTG) III-V epitaxial layer stack consists of an active layer (with multiple quantum wells) and a tuning layer, both with their surrounding cladding and contact layers. When a TTG epitaxial layer stack is integrated on top of an SOI waveguide circuit, a heterogeneously integrated tunable distributed feedback (DFB) or distributed Bragg reflector (DBR) laser can be realized. The vertical integration of an active and a tuning layer allows close to independent control of the laser power and wavelength. As the tuning mechanism is carrier-injection based, the tuning speed is inherently fast. In this work, four TTG-based laser structures integrated on silicon are considered.

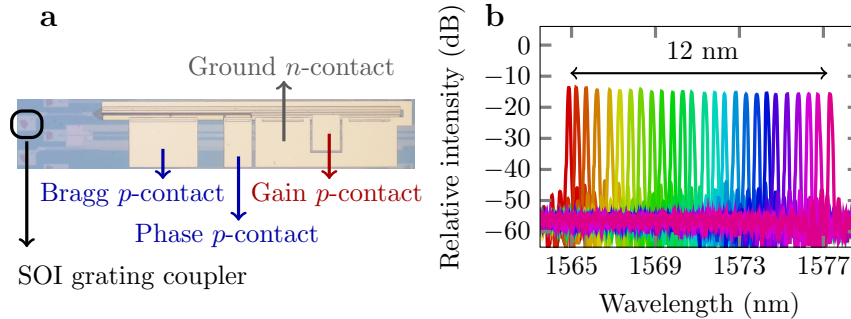


**Figure 7:** Thermally tunable TTG-DBR laser. (a) Optical microscope image of the fabricated chip; (b) Superimposed laser spectra for different Phase and Bragg currents.

### TTG-DFB laser

The first considered laser structure is a TTG-DFB laser that allows for electronic wavelength tuning. A  $\lambda/4$  phase-shifted Bragg grating is implemented in the silicon device layer to provide distributed feedback. Figure 6(a) shows an SEM/FIB cross-sectional image of a fabricated laser device. A 2 nm electronic wavelength tuning range is demonstrated with a single tuning current. Continuous-wave (CW) single-mode laser operation with a side-mode suppression ratio (SMSR) larger than 44 dB across the tuning range is obtained. The wavelength tuning characteristics are shown in Fig. 6(b). Dynamic measurements indicate back-to-back operation at 12.5 Gbit/s upon non-return-to-zero on-off-keying (NRZ-OOK) direct modulation. This is indicated in Fig. 6(c). The measured wavelength switching time is about 3 nanoseconds, with a dynamic tuning efficiency of 0.13 nm/mA. The wavelength switching characteristics are shown in Fig. 6(d).

### SG-TTG-DFB laser

Through use of sampled gratings instead of uniform Bragg gratings, a sampled grating (SG-) TTG-DFB laser has been realized as well. The use of sampled gratings can extend the wavelength tuning range through exploitation of the Vernier principle. In our case wavelength tuning over six distinct supermodes has been demonstrated, with a total tuning range of 8 nm.

### Thermally tunable TTG-DBR laser

This laser structure is implemented as a three-section DBR laser and consists of a gain, phase and Bragg section. In the gain section the tuning layer is left unbiased. In the phase and Bragg section, the active layer is

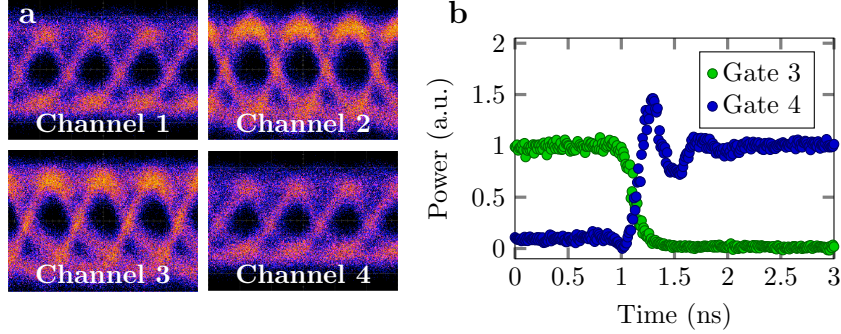


**Figure 8:** Wavelength-selectable laser based on filtered optical feedback. (a) Eye diagrams at 12.5 Gbit/s NRZ-OOK direct modulation of each wavelength channel; (b) Wavelength switching characteristics for switching between two neighboring channels.

removed. Carriers can be injected to tune the laser wavelength. In principle, a DBR laser is advantageous over a DFB structure as the individual longitudinal laser sections can be separately optimized. In our demonstration, wavelength tuning is mainly thermal, with a continuous wavelength tuning range larger than 12 nm. The tuning layer basically acts as a heater and leads to a redshift of the laser wavelength upon current injection. Figure 7(a) shows an optical microscope image of the fabricated chip, with indication of the different contacts. The superimposed laser spectra are shown in Fig. 7(b).

### Electronically tunable TTG-DBR laser

The aforementioned thermally tunable TTG-DBR laser exhibits no net electronic tuning effect. This is because no optimized TTG epitaxial layer stack was used. Through an optimization of the TTG stack and by making use of a thick tuning layer and very thick  $n$ -InP cladding the tuning behavior is expected to significantly improve. In this work, such an optimized design is presented. Note that here the overall wavelength tuning range can also be extended through use of sampled gratings.

## Wavelength-selectable laser based on filtered optical feedback

Although the TTG-based laser structures are promising, they suffer from self-heating effects upon carrier injection, which limits the wavelength tuning range and speed. Moreover, the growth of a TTG epitaxial layer stack is more complex than that of a standard amplifier stack. We have therefore

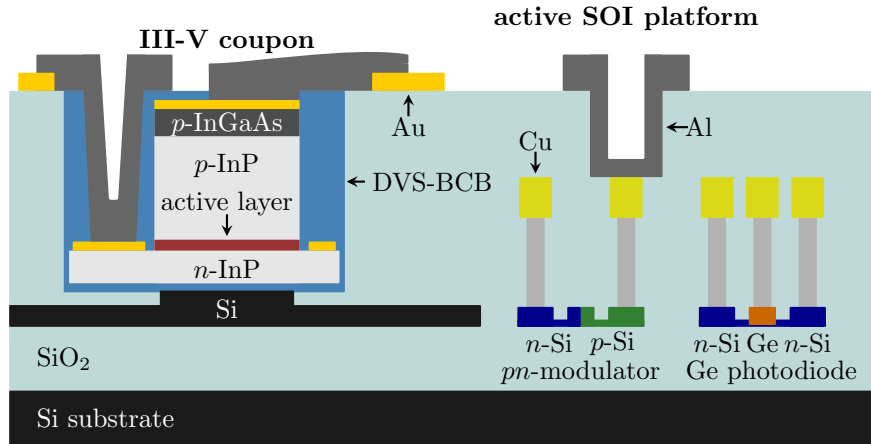


**Figure 9:** Illustration of sparse heterogeneous integration through transfer printing. The schematic shows a typical active silicon photonic integration platform. A local opening in the back-end stack contains a processed III-V device coupon.

investigated an alternative laser structure, where filtered optical feedback is used as a way to achieve single-mode laser operation and wavelength selectivity. By means of an arrayed waveguide grating (AWG) and a set of short semiconductor optical amplifiers (SOAs) in the feedback path of the external cavities of the laser structure, very fast wavelength switching can be achieved. As proof-of-principle a four-channel laser has been demonstrated. CW single-mode laser operation is readily achieved when the SOA gates are appropriately biased. 12.5 Gbit/s NRZ-OOK direct modulation for each wavelength channel is demonstrated and wavelength switching can occur in less than one nanosecond. Figure 8(a) shows the corresponding eye diagrams whereas the wavelength switching characteristics for switching between two neighboring channels are shown in Fig. 8(b).

## The road towards transfer printing

For III-V-on-silicon integration to be deployable in a massively parallel fashion, transfer printing (TP) is considered to be a very attractive solution. The holy grail of combining processed active III-V devices such as amplifiers and (tunable) DFB and DBR lasers on an active silicon photonics platform seems attainable in the near future through use of the TP technique. An example implementation is shown in Fig. 9. One important difficulty in TP is the relatively large misalignment introduced between the III-V devices and the silicon target during printing. Therefore an adiabatic tapered coupler is proposed and designed that is highly tolerant for alignment offsets

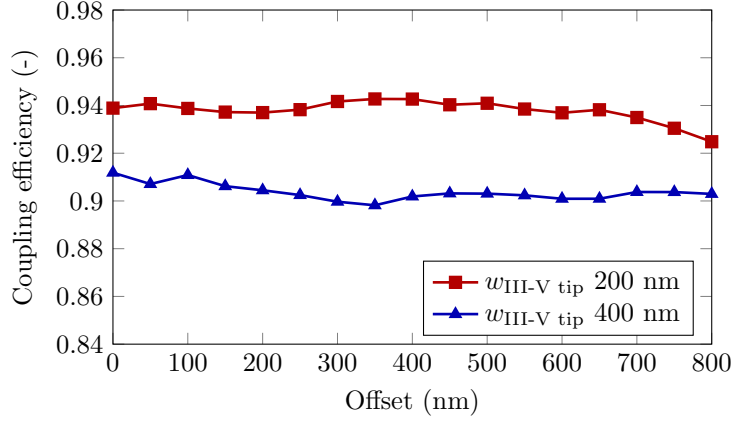


**Figure 10:** Coupling efficiency of the designed adiabatic tapered coupler versus lateral alignment offset.

and that remains compatible with common device architectures. The coupling efficiency for the designed coupler reaches values above 90%, even for a large lateral alignment offset of 800 nm (see Fig. 10). This is a significant improvement as compared to typical coupling structures, which generally require a lateral alignment accuracy better than 300 nm. The coupling structure is especially suited for devices with a very thick cladding layer, of which the proposed TTG-DBR laser is the best example.

## Conclusion

In this doctoral research, several electronically tunable lasers on silicon have been developed and experimentally investigated. The demonstrated laser devices are expected to find application in future flexible optical network architectures and can be an attractive solution for use in optical burst or packet switching systems in data center networks.

# 1

## Introduction

**L**ASER diodes have been around for quite some time. Their unique spectral properties, small size and mass-producibility make them indispensable for data transmission and data storage applications. Also for other emerging applications such as medical imaging and remote sensing they are essential. Electronic wavelength control gives laser diodes additional functionality that is required to keep up with modern and future application requirements, especially in data center environments. In this introduction chapter the driver behind the research in this PhD project is outlined.

### Contents

---

1.1	Optical interconnects in data centers . . . . .	1
1.2	Remote sensing applications . . . . .	4
1.3	Trace-gas sensing and spectroscopy . . . . .	6
1.4	Silicon photonic integrated circuits . . . . .	6
1.5	Heterogeneous III-V-on-silicon integration . . . . .	7
1.6	Tunable laser diodes – state-of-the art . . . . .	10
1.7	Outline . . . . .	13
1.8	List of publications . . . . .	15
	References . . . . .	18

---

### 1.1 Optical interconnects in data centers

Since the advent of the World Wide Web in the early nineties, internet technologies have known an incredibly fast development. Social network-

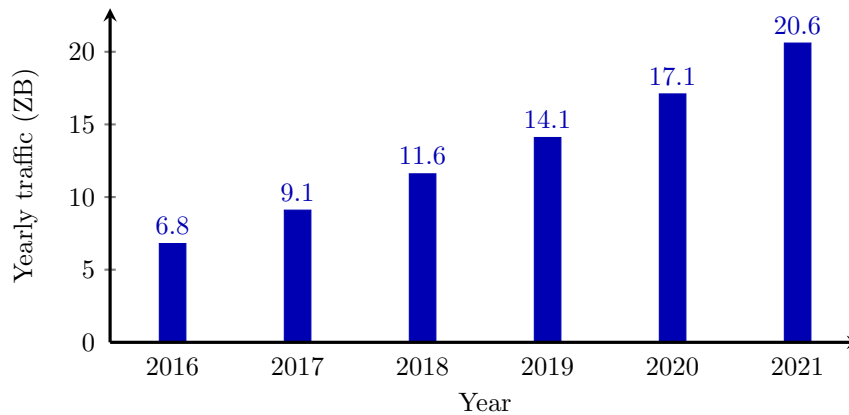


**Figure 1.1:** Global data center IP traffic growth. Estimations indicate that by the end of 2021 the annual global data center IP traffic will reach 20.6 ZB, up from 6.8 ZB in 2016. Graphic is reproduced from [2].

ing, video-on-demand services, cloud computing and other web applications have led to an enormous increase in the amount of data traffic and storage worldwide [1]. This is particularly reflected in data center environments, where complex and frequent communication between the employed servers is required. An illustration of this is given in Fig. 1.1, which shows the global data center Internet Protocol (IP) traffic growth. It is estimated that by the end of 2021 the annual global data center IP traffic will reach 20.6 Zettabytes (ZB), up from 6.8 ZB in 2016 [2]. In order to sustain this increasing demand for bandwidth, response speed and data storage, even more powerful data centers will be required, with very fast optical interconnects between the servers. Reducing the delay in delivering packets to and from the cloud is also crucial to keep up with today's advanced services and for companies' revenues. In line with this, power consumption in data centers remains a challenging issue to be addressed. In 2015, data center power consumption accounted for about 3 percent of the global electricity supply and for about 2 percent of total greenhouse gas emissions [3]. It is obvious that such high power consumption creates an economic and ecological driver for interconnection schemes with high bandwidth, low latency and low power consumption.

### 1.1.1 Optical burst and packet switching

In classical optical circuit-switched networks, optical paths are set up between source and destination and maintained for a relatively long time period. This is not very efficient in terms of bandwidth utilization, especially when the network is dominated by packet-based IP traffic. As data center traffic has such a bursty nature, the interest in more efficient and flexible

interconnect architectures using optical burst or packet switching has been renewed [4]. Such network configurations do not simply involve laser tuning to a new wavelength and transmitting data for a short time period. They must also deal with the complex problem of reliably delivering data from end-to-end and for all users. Successful implementation therefore goes well beyond the transmitter technology itself. Optical burst switching (OBS) allows to transmit bursts of traffic with a connection being set up end-to-end for the duration of a burst, without buffering. Typical burst durations are on the order of 100  $\mu$ s to 100 ms [5]. In optical packet switching (OPS) the user data is transmitted in optical packets, which are switched entirely in the optical domain, without power-hungry optical-to-electrical conversions. In contrast to OBS, OPS is designed as today's packet networks, in which each optical packet carries its routing information with it. OPS requires optical buffering, however, and still remains technologically difficult. Nevertheless, several optical burst and packet switching architectures have been proposed already. Many of them are rather complex and optimized to achieve high throughput, good delay performance and low wiring complexity. An optical packet switch needs to read header information of each incoming optical packet (input interfacing), perform fast switching from input to output (forwarding) and replace the header information with the new routing information (output interfacing). Buffering is also required to deal with contention when packets request to enter (exit) the same input (output) port simultaneously. At the core of the optical packet switch lies the switch technology, capable of fast data reconfiguration to support a continuous stream of packets with small interpacket gaps. A 40 byte packet at 10 Gbit/s corresponds for instance with a packet duration of 32 ns. If we assume a guard time of 10% of the packet duration, this means that the switch must be able to reconfigure in less than 3.2 ns. At higher bitrates even sub-nanosecond switching times are required. Switch implementations based on fast tunable wavelength converters (TWCs) and arrayed waveguide grating routers (AWGRs) are most likely to meet such stringent demands [6, 7]. A simple example of how this could be implemented is shown in Fig. 1.2. Incoming optical packets arrive at any wavelength. A fast tunable laser as part of a TWC is rapidly tuned to the desired forwarding wavelength. This forwarding wavelength can for instance be used to choose the physical output port of the AWGR, to which the optical packet is passively routed. Since AWGRs do not have good scalability, the interconnection of multiple AWGRs is typically preferred over a single large AWGR. The feasibility of optical packet switching as networking technique hence greatly depends on the availability of high-speed and fast tunable optical transmitters with nanosecond switching times and good power efficiency [8].

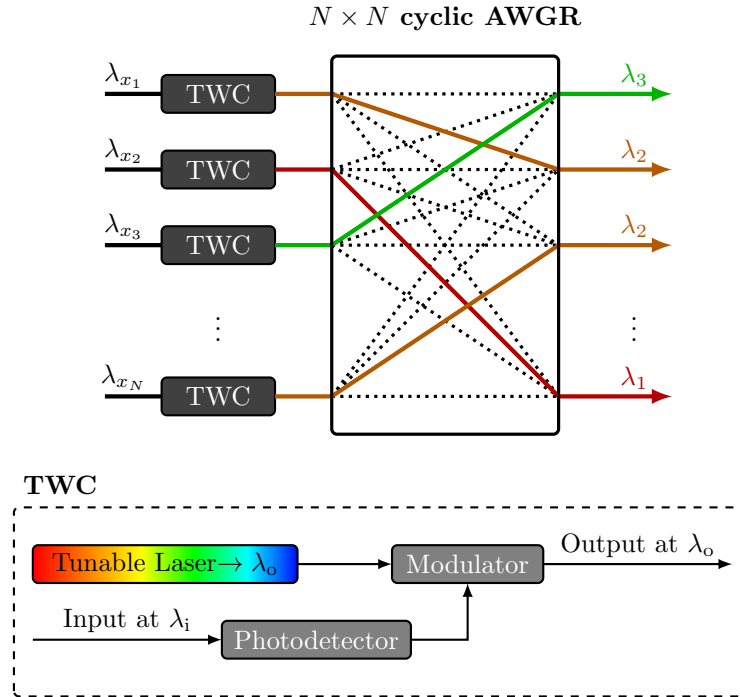


**Figure 1.2:** An optical packet switch forwarding module using TWCs and an AWGR. Incoming optical packets arrive at any wavelength. A fast tunable laser as part of the TWC is rapidly tuned to the desired forwarding wavelength. The  $N \times N$  cyclic AWGR passively routes the optical packets to the desired physical output port (depending on the chosen forwarding wavelength). Graphic is reproduced from [9].

## 1.2 Remote sensing applications

Very recently, remote sensing systems have attracted an enormous interest by the automotive industry for use in self-driving cars. Every year, more than one million people die in road-related incidents [10]. Often the fatalities can be attributed to human error and autonomous vehicles are envisioned to overcome this issue. It is no surprise that the required sensor technology has to meet very stringent demands in terms of size, cost, effectiveness and safety and is not yet at a maturity level for widespread deployment. Nowadays, remote non-contact distance sensing in cars relies on cameras, classical Radio Detection and Ranging (RADAR) at 80 GHz or Light Detection and Ranging (LIDAR) [11]. Generally a combination of the three methods is used. LIDAR systems can be implemented with several mechanically rotating lasers and receivers on the vehicle's roof. This approach is, however, not suited for long-term reliability because of the moving parts and puts a

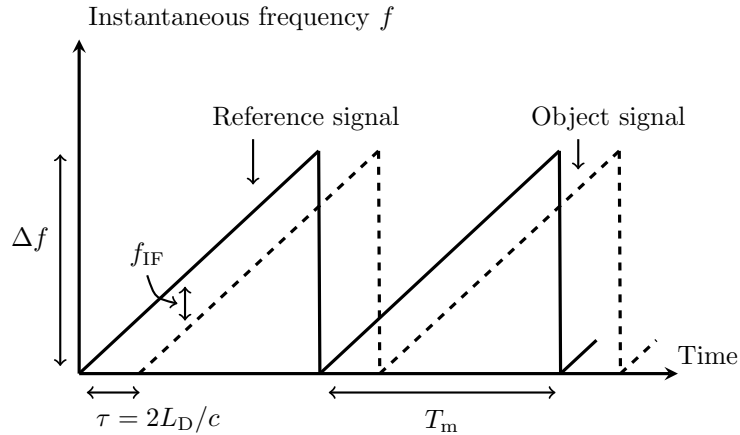


**Figure 1.3:** Operation principle of a frequency-modulated continuous-wave (FMCW) LIDAR system. A sawtooth-like frequency modulated laser beam is sent simultaneously to an object and a reference mirror. From the superimposed reflected signals the distance to the object can be determined. Graphic is reproduced from [5].

limitation on the size and cost of the sensing system. Recent academic and industrial efforts have pushed forward the development of LIDAR systems that are faster and more reliable. Examples include the use of Microelectromechanical Systems (MEMS) sensors [12, 13] and optical phased arrays for beam steering [14, 15]. Very often LIDAR systems also require a large number of lasers and detectors, which again poses limits on the scalability, cost and size. The use of a single, fast tunable laser can therefore play another important role in addressing the aforementioned hurdles.

### 1.2.1 Frequency-modulated continuous-wave LIDAR

An example of a LIDAR technique with good sensitivity and resolution that makes use of a single tunable laser diode is so-called frequency-modulated continuous-wave (FMCW) LIDAR [16–18]. Its operation principle is illustrated in Fig. 1.3. The instantaneous frequency  $f$  of a continuously tunable laser diode is periodically shifted by an amount  $\Delta f$ , through application of a sawtooth-like tuning current. This signal is sent simultaneously to an object and a reference mirror after which the reflected signals are superimposed and detected by a  $p$ - $i$ - $n$  photodetector. An optical isolator with excellent isolation (e.g.  $> 50$  dB) is used to avoid deterioration of the laser operation by the reflected signal. Because of the time-dependent instantaneous frequency  $f$  and path difference  $L_D$ , the two signals exhibit different instantaneous frequencies ( $f_1$  and  $f_2$ , respectively) when incident on the photodetector. Exactly this frequency difference (denoted as  $f_{IF} = |f_2 - f_1|$ ,

in accordance with the intermediate frequency in heterodyne detection) is detected in the photodiode. In the case of a linear ramp with period  $T_m$ , the intermediate frequency is proportional to the delay time  $\tau = 2L_D/c$ :

$$f_{\text{IF}} = \Delta f \frac{\tau}{T_m}. \quad (1.1)$$

By an appropriate choice of both  $\Delta f$  and  $T_m$ , very small delay times ( $\sim$  ps) may be measured, without the need for high-speed electronics. In practice, the frequency is measured indirectly through a direct measurement of the phase of the signal at the detector over a relatively long time (approaching the period  $T_m$ ).

### 1.3 Trace-gas sensing and spectroscopy

Wavelength-tunable laser diodes are also very useful for gas-monitoring systems using absorption spectroscopy [19, 20]. This requires the gas under consideration to exhibit sufficiently strong absorption lines in the available wavelength tuning range and with spectral linewidths smaller than the tuning range. In the 1520 nm to 1570 nm wavelength range, widely tunable sampled grating distributed Bragg reflector (SG-DBR) lasers have been successfully used to detect for instance  $\text{H}_2\text{S}$ ,  $\text{C}_2\text{H}_2$  and  $\text{CO}_2$  [21]. Around 1580 nm, in-situ measurements of CO,  $\text{H}_2\text{O}$  and temperature have been performed during combustion [22]. It is noted, however, that most molecules exhibit strong absorption lines in the mid-infrared. Only very recently, tunable lasers based on the GaSb material platform have been used for sensitive molecule and gas detection measurements in the  $1.7 \mu\text{m} - 2.5 \mu\text{m}$  wavelength range [23, 24].

### 1.4 Silicon photonic integrated circuits

A photonic integrated circuit (PIC) combines multiple optical elements on a single chip and typically consists of a substrate on which a low- and high-refractive index material layer are grown or deposited. Structures are defined in the high-refractive index material and can guide light between different elements on the chip. The low-refractive index material acts as buffer layer to avoid optical leakage to the substrate. Over the years PICs have been demonstrated in a wide range of material systems and platforms, each with their obvious (dis)-advantages. The silicon photonics or silicon-on-insulator (SOI) platform has become one of the most promising platforms and consists of a silicon substrate (wafer diameter up to 300 mm), a thermal silicon oxide layer (thickness 1 to 3  $\mu\text{m}$ ) and a silicon device layer (typical thickness 220 nm or 400 nm). The index contrast between the silicon and its surroundings is very high ( $\Delta n \approx 2$  at 1550 nm), which results

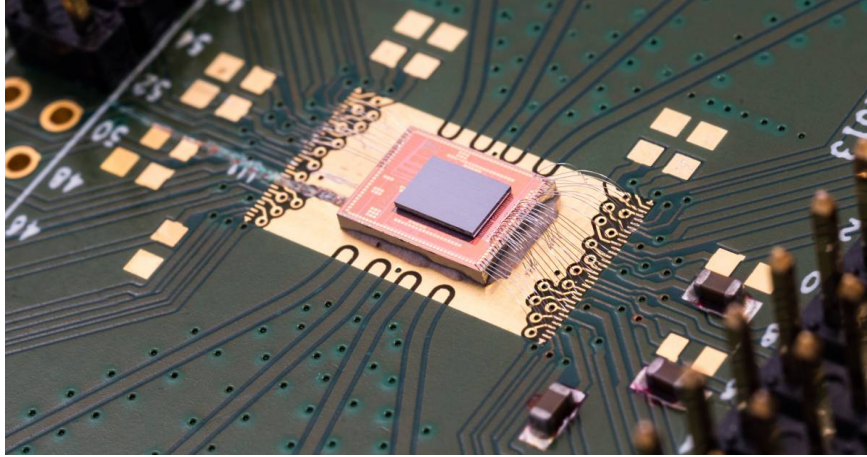


**Figure 1.4:** Optical microscope image of a silicon photonic integrated circuit wire-bonded on a printed circuit board. Image taken from [35].

in highly confined waveguide modes and which allows for tight integration with waveguide radii of only a few  $\mu\text{m}$ . Excellent passive functionality with small footprint is therefore the key asset of the silicon photonics platform: high-confinement low-loss waveguides [25, 26], grating couplers [27], Bragg gratings [28], high-Q ring resonators [29] and arrayed waveguide gratings (AWGs) [30] have been successfully demonstrated on SOI. Through the introduction of selective material doping and the epitaxial growth of germanium also active components can be realized. Examples include injection- and depletion-based modulators [31, 32] and high-speed photodetectors [33]. An example of a silicon photonic integrated circuit wire-bonded on a printed circuit board is shown in Fig. 1.4. It is no surprise that silicon photonics has reached a level of maturity that is required for high-volume commercial applications [34].

## 1.5 Heterogeneous III-V-on-silicon integration

An important problem of the silicon photonics platform is the lack of an on-chip light source [36]. Silicon has an indirect bandgap and therefore does not allow efficient light generation, let alone laser operation. In the past decade there has therefore been considerable interest in the area of heterogeneous (or hybrid) III-V-on-silicon integration, where III-V lasers are integrated on passive SOI PICs, with light outcoupling to a silicon waveguide [37–39]. In this way laser sources can be effectively combined with high-performing silicon components on the same chip.

### 1.5.1 Integration approaches

Different heterogeneous integration approaches exist, ranging from high-maturity low-density heterogeneous bonding to low-maturity high-density direct epitaxial growth. A non-exhaustive overview of the most common integration techniques is presented below [40].

#### Direct and adhesive bonding

In die-to-wafer or wafer-to-wafer bonding, an unprocessed III-V die or wafer is bonded upside-down on a fully patterned SOI wafer. Afterwards the III-V substrate is removed and the remaining III-V sheet patterned and etched in the standard way. Typically a distinction is made between direct and adhesive bonding [41]. Direct bonding makes use of Van der Waals forces between the silicon and III-V to bond both substrates. Adhesive bonding makes use of an adhesive polymer (typically DVS-BCB) to bond the substrates together. The latter has the advantage that the requirements on surface cleanliness are more relaxed as compared to the former. It however also slightly deteriorates the heat sinking properties. Both bonding techniques are commonly used today and have achieved a high level of maturity. Adhesive bonding will be the technique of choice for the realization of III-V-on-silicon lasers in this PhD project.

#### Transfer printing

Although reliable, bonding is not very efficient in terms of III-V material usage. Commonly the area covered by III-V components in heterogeneously integrated devices is only a small fraction of the total circuit area. The seemingly simple technique of transfer printing allows to transfer thin-film components from a source to a target substrate. It is thought to be an enabling method for cost-effective integration of III-V material or devices onto target SOI PICs, while maintaining high throughput and scalability. It should in principle also allow for sparse integration of III-V devices onto full platform SOI PICs comprising a thick back-end stack. Although transfer printing is not used as integration technique in the course of this PhD project, the presented devices are inherently compatible with the transfer printing approach.

#### Direct epitaxial growth

A further step forward in the efficiency increase of III-V material and cost reduction is direct epitaxial III-V growth on silicon. However, the large mismatch in lattice constant (8% for InP/Si) makes it extremely difficult to grow III-V materials defect-free on silicon. Threading dislocations generated during growth are detrimental for device operation and can substantially decrease device performance over time. Although laser devices based on

direct III-V growth on silicon have been demonstrated [42, 43], the low-maturity of current direct epitaxial growth techniques has impeded their consideration for this PhD project.

### 1.5.2 VCSELs vs DFB and DBR lasers

So far 850 nm multimode vertical-cavity surface-emitting lasers (VCSELs) have been the light sources of choice for short-reach interconnects in data centers, mainly owing to their low threshold current, high power efficiency and large direct modulation bandwidth [44–46]. They are however not suited for wavelength-division multiplexing (WDM) nor do they allow fast wavelength switching. The output power and the side-mode suppression ratio (SMSR) of VCSELs is also limited such that for high bitrate interconnects over longer distances in data center networks they are getting replaced by single-mode edge-emitting distributed feedback (DFB) and distributed Bragg reflector (DBR) lasers. A schematic overview of the typical structure of heterogeneously integrated VCSELs, DFB and DBR lasers is shown in Fig. 1.5. In the case of DFB lasers, optical feedback is distributed along the laser cavity through use of a Bragg grating. In DBR lasers, a Bragg grating is implemented at one or at both sides of the laser cavity. The grating acts as a wavelength-selective filter and allows for single-mode laser operation. Typically the laser design is matched for operation at 1310 nm or 1550 nm, the wavelength with lowest material dispersion and lowest material loss in optical fibers, respectively. Suitable active materials that can be used to provide gain at these wavelengths are generally based on InP ternary and quaternary epitaxial layer stacks with InGaAsP or InGaAlAs. Because of their abundance in many optical communication systems, it is no surprise that native III-V DFB and DBR lasers with splendid performance exist. Fixed-wavelength DFB lasers with optical output powers as high as 100 mW, low threshold currents around 5 mA and large modulation bandwidths above 20 GHz have been shown by several research groups and are even commercially available [47–49]. More recently, similar and even outperforming DFB and DBR lasers heterogeneously integrated on silicon have been demonstrated as well [50, 51].

### 1.5.3 Thermally tunable III-V-on-silicon lasers

Also more complex, wavelength tunable III-V-on-silicon lasers have been presented already. The research has mainly been directed towards thermally tunable lasers since these types typically yield a narrow emission linewidth and thus small phase noise, a feature which is essential for coherent optical communication [52]. State-of-the art thermally tunable lasers are based on double-ring configurations with Sagnac loop mirrors [53]. Although useful for an abundance of applications, even beyond optical communication, their

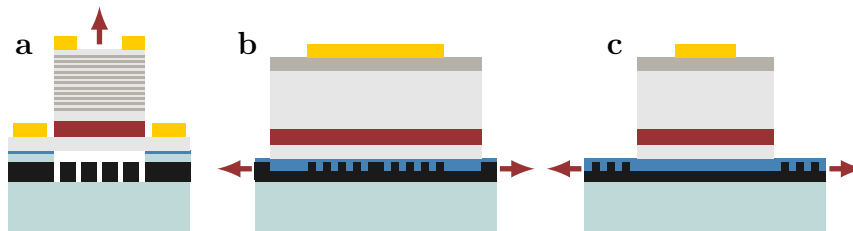


**Figure 1.5:** Schematic overview of different heterogeneously integrated laser structures. (a) VCSEL; (b) DFB laser; (c) DBR laser.

tuning speed is too low (switching times  $\sim 10 \mu\text{s}$ ) to find application in optical packet switching systems.

#### 1.5.4 Electronically tunable III-V-on-silicon lasers

Electronically tunable lasers on the other hand do allow fast tuning but are more difficult to implement on SOI. One of the reasons is that the free-carrier plasma dispersion effect used to realize fast electronic tuning is about a factor 10 weaker for silicon than for typical InP/InGaAsP compounds [54]. The first electronically tunable laser on silicon was presented shortly after the first III-V-on-silicon DFB laser. With a sampled grating (SG-) DBR laser, discrete wavelength tuning was realized. Using quantum well intermixing, passive longitudinal grating sections with different bandgaps were created, allowing current injection to tune the laser wavelength [55]. Tuning was, however, discrete and only two supermodes were addressed because of the limited electronic effect. More recently, an integrated MOS capacitor formed between a heavily doped InGaAsP and doped silicon waveguide layer into the cavity allowed electronic wavelength control [56]. The approach has the advantage of low thermal chirp and power consumption. The demonstrated tuning range was limited to 0.4 nm, however, and single-mode laser operation was barely demonstrated across the tuning range. In recent work [57], a fast tunable laser was demonstrated based on double-ring silicon resonators with lateral *p-i-n* junctions. Fast switching was limited to neighboring channels, however, owing to silicon's weak plasma dispersion effect.

## 1.6 Tunable laser diodes – state-of-the art

An overview of the state of the art of tunable lasers is presented in Table 1.1. The main static laser characteristics are provided. As the overall tuning range depends on whether or not the Vernier effect has been exploited, the number of wavelength-selective reflectors is mentioned as well. We note that

only heterogeneously integrated lasers are considered as a comparison with native III-V lasers will be presented in Chapter 2.

**Table 1.1:** Heterogeneously integrated tunable laser diodes – state-of-the-art.

<b>Name</b>	<b>Tuning</b>	<b>Range (nm)</b>	<b># Reflectors</b>	<b>P<sub>out</sub> (mW)</b>	<b>Inst.</b>	<b>Ref.</b>
single-ring	Electronic	0.4 cont.	1	N/S	HP Labs	[56]
SG-DBR	Electronic	13 discr.	2	1 at 20°C	UCSB	[55]
double-ring	Electronic/Thermal	45 discr.	2	1.8 at 20°C	III-V Lab	[57]
single-ring	Thermal	8 cont.	1	10 at 20°C	UGent	[58]
double-ring	Thermal	40 cont.	2	3.3 at 10°C	UCSB	[59]
double-ring	Thermal	40 cont.	2	1 at 20°C	UGent	[60]
AWG	Switching	4 ch. discr.	N/A	0.3 at 17°C	UCSB	[61]
SG-DFB	Electronic/Thermal	55 discr.	2	10 at 20°C	UGent	[62]
UG-DBR	Thermal	12 cont.	1	0.4 at 20°C	UGent	[63]
AWG	Filtered feedback	4 ch. discr.	N/A	4 at 20°C	UGent	[64]
UG-DFB	Electronic	2 cont.	1	3 at 20°C	UGent	[65]

## 1.7 Outline

This work consists of eight chapters, of which the content is summarized below.

In Chapter 2 the basic concepts of electronically tunable laser diodes are discussed. Wave propagation in periodic structures is highlighted and a short comparison between common grating-based structures is presented. Afterwards electro-optical aspects of laser diodes are discussed, together with the concept of electronic wavelength control for tunable laser diodes. The Vernier principle and the concept of sampled gratings are presented as part of a route to extend the wavelength tuning range. The chapter concludes with a comparison of native III-V and III-V-on-silicon lasers and the presentation of the two epitaxial layer stacks that are used in this work. It forms the foundation for the research results discussed in the subsequent chapters.

Chapter 3 presents the details of the fabrication process used for the realization of the heterogeneously integrated tunable lasers discussed in this work. It also contains a part on process development of electron-beam lithography and reactive ion etching of SOI circuits. Initial characterization results of some passive devices are discussed as well.

In Chapter 4 the core work of this PhD project is addressed. An extensive discussion is presented on the design, fabrication and characterization of electronically tunable DFB lasers. In total three different DFB laser structures are discussed.

Chapter 5 contains a discussion on electronically tunable DBR lasers. The first part is about thermal wavelength tuning with a TTG-DBR laser. The second part is about an optimized TTG-DBR laser design which should allow for an even wider electronic tuning range than what was achieved with the TTG-DFB laser. It also forms the basis for the discussion on the future work.

In Chapter 6 a laser structure based on filtered optical feedback and the standard amplifier epitaxial layer stack is discussed. Design, fabrication and characterization aspects are presented. The laser is a good alternative for the TTG-based laser structures and can enable sub-nanosecond wavelength switching.

Chapter 7 describes the extensive design of an adiabatic tapered coupler that is highly tolerant towards lateral misalignment between the III-V and silicon waveguide in heterogeneously integrated active devices. The presented coupler may particularly be useful for transfer printing of III-V-on-silicon amplifiers and some of the tunable laser structures described in this

work.

Finally the conclusions of this work are formulated in Chapter 8. Also future prospects are shortly discussed.

## 1.8 List of publications

This PhD thesis has led to a number of publications in international peer-reviewed journals. Much of the work has also been presented at national and international conferences. An overview of the research output is given below.

### 1.8.1 International peer-reviewed journals

1. K. Van Gasse, L. Bogaert, L. Breyne, J. Van Kerrebrouck, **S. Dhoore**, C. Op de Beeck, A. Katumba, C.Y. Wu, H. Li, J. Verbist, A. Rahim, A. Abbasi, B. Moeneclaeys, Z. Wang, H. Chen, J. Van Campenhout, X. Yin, B. Kuyken, G. Morthier, J. Bauwelinck, G. Torfs, and G. Roelkens, “Analog radio-over-fiber transceivers based on III-V-on-silicon photonics,” *IEEE Photonics Technology Letters* (invited) 30(21), 1818–1821 (2018). <https://doi.org/10.1109/LPT.2018.2867930>
2. **S. Dhoore**, A. Rahim, G. Roelkens, and G. Morthier, “12.5 Gbit/s discretely tunable InP-on-silicon filtered feedback laser with sub-nanosecond wavelength switching times,” *Optics Express* 26(7), 8059–8068 (2018). <https://doi.org/10.1364/OE.26.008059>
3. J. Zhang, Y. Li, **S. Dhoore**, G. Morthier, and G. Roelkens, “Unidirectional, widely-tunable and narrow-linewidth heterogeneously integrated III-V-on-silicon laser,” *Optics Express* 25(6), 7092–7100 (2017). <https://doi.org/10.1364/OE.25.007092>
4. **S. Dhoore**, G. Roelkens, and G. Morthier, “III-V-on-silicon three-section DBR laser with over 12 nm continuous tuning range,” *Optics Letters* 42(6), 1121–1124 (2017). <https://doi.org/10.1364/OL.42.001121>
5. A. Rahim, E. Ryckeboer, A. Subramanian, S. Clemmen, B. Kuyken, A. Dhakal, A. Raza, A. Hermans, M. Muneeb, **S. Dhoore**, Y. Li, U. Dave, P. Bienstman, N. Le Thomas, G. Roelkens, D. Van Thourhout, P. Helin, S. Severi, X. Rottenberg, and R. Baets, “Expanding the silicon photonics portfolio with silicon nitride photonic integrated circuits,” *Journal of Lightwave Technology* 35(4), 639–649 (2017). <https://doi.org/10.1109/JLT.2016.2617624>
6. **S. Dhoore**, L. Li, A. Abbasi, G. Roelkens, and G. Morthier, “Demonstration of a discretely tunable III-V-on-silicon sampled grating DFB laser,” *IEEE Photonics Technology Letters* 28(21), 2343–2346 (2016). <https://doi.org/10.1109/LPT.2016.2593983>
7. **S. Dhoore**, S. Uvin, D. Van Thourhout, G. Morthier, and G. Roelkens, “Novel adiabatic tapered couplers for active III-V/SOI devices fabri-

cated through transfer printing,” *Optics Express* 24(12), 12976–12990 (2016). <https://doi.org/10.1364/OE.24.012976>

8. G. Roelkens, A. Abbasi, P. Cardile, U. Dave, A. De Groote, Y. De Koninck, **S. Dhoore**, X. Fu, A. Gassenq, N. Hattasan, Q. Huang, S. Kumari, S. Keyvaninia, B. Kuyken, L. Li, P. Mechet, M. Muneeb, D. Sanchez, H. Shao, T. Spuesens, A. Subramanian, S. Uvin, M. Tassaert, K. Van Gasse, J. Verbist, R. Wang, Z. Wang, J. Zhang, J. Van Campenhout, Y. Xin, J. Bauwelinck, G. Morthier, R. Baets, and D. Van Thourhout, “III-V-on-silicon photonic devices for optical communication and sensing,” *Photonics (invited)* 2(3), 969–1004 (2015). <https://doi.org/10.3390/photonics2030969>

### 1.8.2 International conference proceedings

1. **S. Dhoore**, A. Köninger, R. Meyer, G. Roelkens, and G. Morthier, “Electronically tunable DFB laser on silicon,” *International Semiconductor Laser Conference (ISLC)*, United States (2018).
2. **S. Dhoore**, G. Roelkens, and G. Morthier, “InP-on-silicon electronically tunable lasers,” *International Conference on Transparent Optical Networks (ICTON)* (invited), Romania (2018).
3. **S. Dhoore**, A. Rahim, G. Roelkens, and G. Morthier, “III-V-on-silicon filtered feedback discretely tunable laser with nanosecond switching times,” *Conference on Lasers and Electro-Optics (CLEO)*, United States (2018).
4. **S. Dhoore**, G. Roelkens, and G. Morthier, “Towards fast tunable InP-on-SOI laser diodes,” *European Semiconductor Laser Workshop (ESLW)*, Denmark (2017).
5. **S. Dhoore**, G. Roelkens, and G. Morthier, “Heterogeneously integrated III-V/SOI DBR laser with over 7 nm continuous wavelength tuning range,” *European Conference on Integrated Optics (ECIO)*, The Netherlands (2017).
6. **S. Dhoore**, G. Roelkens, and G. Morthier, “Discretely tunable III-V/SOI SG-DFB laser,” *IEEE Photonics Society Benelux Symposium*, Belgium (2016).
7. **S. Dhoore**, L. Li, A. Abbasi, G. Roelkens, and G. Morthier, “Demonstration of a discretely tunable III-V/SOI sampled grating distributed feedback laser,” *IEEE Photonics Conference (IPC)*, United States (2016).
8. **S. Dhoore**, G. Roelkens, and G. Morthier, “Design of an electronically tunable laser diode integrated on the SOI platform,” *IEEE Photonics Society Benelux Symposium*, Belgium (2015).

### 1.8.3 National conference proceedings

1. **S. Dhoore**, A. Köninger, R. Meyer, G. Roelkens, and G. Morthier, “Electronically tunable DFB laser on silicon,” ePIXfab Silicon Photonics Summer School, Belgium (2018).
2. **S. Dhoore**, A. Abbasi, J. Zhang, K. Van Gasse, M. Shahin, G. Roelkens, and G. Morthier, “InP-on-silicon lasers for optical communication,” FEA Research Symposium, Belgium (2017).

## References

- [1] Q. Zhang, L. Cheng, and R. Boutaba, “Cloud computing: state-of-the-art and research challenges,” *Journal of Internet Services and Applications* **1**(1), 7–18 (2010).
- [2] C. V. Networking, “Cisco global cloud index: forecast and methodology, 2016-2021. White paper,” Cisco Public (2018).
- [3] T. Bawden, “Global warming: data centres to consume three times as much energy in next decade, experts warn,” *The Independent* **23** (2016).
- [4] C. Kachris, K. Kanonakis, and I. Tomkos, “Optical interconnection networks in data centers: recent trends and future challenges,” *IEEE Communications Magazine* **51**(9), 39–45 (2013).
- [5] J. Buus, M.-C. Amann, and D. J. Blumenthal, *Tunable laser diodes and related optical sources* (Wiley-Interscience New York, 2005).
- [6] D. J. Blumenthal, B.-E. Olsson, G. Rossi, T. E. Dimmick, L. Rau, M. Masanovic, O. Lavrova, R. Doshi, O. Jerphagnon, J. E. Bowers, V. Kaman, L. A. Coldren, and J. Barton, “All-optical label swapping networks and technologies,” *Journal of Lightwave Technology* **18**(12), 2058–2075 (2000).
- [7] J. Gripp, M. Duelk, J. E. Simsarian, A. Bhardwaj, P. Bernasconi, O. Laznicka, and M. Zirngibl, “Optical switch fabrics for ultra-high-capacity IP routers,” *Journal of Lightwave Technology* **21**(11), 2839 (2003).
- [8] M. Chen, H. Jin, Y. Wen, and V. C. Leung, “Enabling technologies for future data center networking: a primer,” *IEEE Network* **27**(4), 8–15 (2013).
- [9] T. Segawa, Y. Muranaka, and R. Takahashi, “High-speed optical packet switching for photonic datacenter networks,” *NTT Technical Review* **14**(1), 1–7 (2016).
- [10] W. H. Organization, “Global status report on road safety 2015,” (2015).
- [11] Editorial, “LiDAR drives forward,” *Nature Photonics* (2018).
- [12] G. A. Kumar, A. K. Patil, R. Patil, S. S. Park, and Y. H. Chai, “A LiDAR and IMU integrated indoor navigation system for UAVs and its application in real-time pipeline classification,” *Sensors* **17**(6), 1268 (2017).

- 
- [13] D. Wang, S. Strassle, A. Stainsby, Y. Bai, S. Koppal, and H. Xie, “A compact 3D lidar based on an electrothermal two-axis MEMS scanner for small UAV,” in *Laser Radar Technology and Applications XXIII*, vol. 10636, p. 106360G (International Society for Optics and Photonics, 2018).
- [14] C. V. Poulton, A. Yaacobi, D. B. Cole, M. J. Byrd, M. Raval, D. Vermeulen, and M. R. Watts, “Coherent solid-state LIDAR with silicon photonic optical phased arrays,” *Optics Letters* **42**(20), 4091–4094 (2017).
- [15] S. Chung, H. Abediasl, and H. Hashemi, “A monolithically integrated large-scale optical phased array in silicon-on-insulator CMOS,” *IEEE Journal of Solid-State Circuits* **53**(1), 275–296 (2018).
- [16] A. Dieckmann, “FMCW-LIDAR with tunable twin-guide laser diode,” *Electronics Letters* **30**(4), 308–309 (1994).
- [17] D. Pierrottet, F. Amzajerdian, L. Petway, B. Barnes, G. Lockard, and M. Rubio, “Linear FMCW laser radar for precision range and vector velocity measurements,” *MRS Online Proceedings Library Archive* **1076** (2008).
- [18] P. Feneyrou, L. Leviandier, J. Minet, G. Pillet, A. Martin, D. Dolfi, J.-P. Schlotterbeck, P. Rondeau, X. Lacondemine, A. Rieu, *et al.*, “Novel development for FMCW LIDAR,” in *Applications of Lasers for Sensing and Free Space Communications*, pp. SM3H–2 (Optical Society of America, 2018).
- [19] D. M. Sonnenfroh and M. G. Allen, “Observation of CO and CO 2 absorption near 1.57  $\mu\text{m}$  with an external-cavity diode laser,” *Applied Optics* **36**(15), 3298–3300 (1997).
- [20] R. Nagai, K. Tei, and S. Yamaguchi, “Absorption line measurement of  $^{12}\text{C}^{18}\text{O}_2$  using a broadly tunable DFB laser diode array,” in *Lasers and Electro-Optics Pacific Rim (CLEO-PR), 2017 Conference on*, pp. 1–2 (IEEE, 2017).
- [21] K. Boylan, V. Weldon, D. McDonald, J. O’Gorman, and J. Hegarty, “Sampled grating DBR laser as a spectroscopic source in multigas detection at 1.52–1.57  $\mu\text{m}$ ,” *IEEE Proceedings-Optoelectronics* **148**(1), 19–24 (2001).
- [22] J. J. Nikkari, J. M. Di Iorio, and M. J. Thomson, “In situ combustion measurements of CO, H<sub>2</sub>O, and temperature with a 1.58- $\mu\text{m}$  diode laser and two-tone frequency modulation,” *Applied Optics* **41**(3), 446–452 (2002).

- 
- [23] R. Wang, A. Malik, I. Šimonytė, A. Vizbaras, K. Vizbaras, and G. Roelkens, “Compact GaSb/silicon-on-insulator  $2.0 \times \mu\text{m}$  widely tunable external cavity lasers,” *Optics Express* **24**(25), 28,977–28,986 (2016).
- [24] A. Vizbaras, I. Šimonytė, A. Miasojedovas, A. Trinkūnas, T. Bučiūnas, M. Greibus, G. Naujokaitė, N. Torcheboeuf, S. Droz, D. Boiko, *et al.*, “Swept-wavelength lasers based on GaSb gain-chip technology for non-invasive biomedical sensing applications in the  $1.7\text{--}2.5 \mu\text{m}$  wavelength range,” *Biomedical Optics Express* **9**(10), 4834–4849 (2018).
- [25] P. Dumon, W. Bogaerts, V. Wiaux, J. Wouters, S. Beckx, J. V. Campenhout, D. Taillaert, B. Luyssaert, P. Bienstman, D. V. Thourhout, and R. Baets, “Low-loss SOI photonic wires and ring resonators fabricated with deep UV lithography,” *IEEE Photonics Technology Letters* **16**(5), 1328–1330 (2004).
- [26] Y. A. Vlasov and S. J. McNab, “Losses in single-mode silicon-on-insulator strip waveguides and bends,” *Optics Express* **12**(8), 1622–1631 (2004).
- [27] D. Taillaert, F. Van Laere, M. Ayre, W. Bogaerts, D. Van Thourhout, P. Bienstman, and R. Baets, “Grating couplers for coupling between optical fibers and nanophotonic waveguides,” *Japanese Journal of Applied Physics* **45**(8R), 6071 (2006).
- [28] X. Wang, W. Shi, H. Yun, S. Grist, N. A. Jaeger, and L. Chrostowski, “Narrow-band waveguide Bragg gratings on SOI wafers with CMOS-compatible fabrication process,” *Optics Express* **20**(14), 15,547–15,558 (2012).
- [29] J. Niehusmann, A. Vörckel, P. H. Bolivar, T. Wahlbrink, W. Henschel, and H. Kurz, “Ultrahigh-quality-factor silicon-on-insulator microring resonator,” *Optics Letters* **29**(24), 2861–2863 (2004).
- [30] T. Fukazawa, F. Ohno, and T. Baba, “Very compact arrayed-waveguide-grating demultiplexer using Si photonic wire waveguides,” *Japanese Journal of Applied Physics* **43**(5B), L673 (2004).
- [31] Q. Xu, S. Manipatruni, B. Schmidt, J. Shakya, and M. Lipson, “12.5 Gbit/s carrier-injection-based silicon micro-ring silicon modulators,” *Optics Express* **15**(2), 430–436 (2007).
- [32] A. Liu, L. Liao, D. Rubin, H. Nguyen, B. Ciftcioglu, Y. Chetrit, N. Izhaky, and M. Paniccia, “High-speed optical modulation based on carrier depletion in a silicon waveguide,” *Optics Express* **15**(2), 660–668 (2007).

- [33] L. Chen and M. Lipson, “Ultra-low capacitance and high speed germanium photodetectors on silicon,” *Optics Express* **17**(10), 7901–7906 (2009).
- [34] P. D. Dobbelaere, A. Dahl, A. Mekis, B. Chase, B. Weber, B. Welch, D. Foltz, G. Armijo, G. Masini, G. McGee, G. Wong, J. Balardeta, J. Dotson, J. Schramm, K. Hon, K. Khauv, K. Robertson, K. Stechschulte, K. Yokoyama, L. Planchon, L. Tullgren, M. Eker, M. Mack, M. Peterson, N. Rudnick, P. Milton, P. Sun, R. Bruck, R. Zhou, S. Denton, S. Fath-pour, S. Gloeckner, S. Jackson, S. Pang, S. Sahni, S. Wang, S. Yu, T. Pinguet, Y. D. Koninck, Y. Chi, and Y. Liang, “Advanced silicon photonics technology platform leveraging a semiconductor supply chain,” in *2017 IEEE International Electron Devices Meeting (IEDM)*, pp. 34.1.1–34.1.4 (2017).
- [35] “Silicon photonics integration at imec,” (2018). URL <https://www.imec-int.com/en/integrated-silicon-photonics>.
- [36] R. Soref, “The past, present, and future of silicon photonics,” *IEEE Journal of Selected Topics in Quantum Electronics* **12**(6), 1678–1687 (2006).
- [37] G. Duan, C. Jany, A. L. Liepvre, A. Accard, M. Lamponi, D. Make, P. Kaspar, G. Levaufre, N. Girard, F. Lelarge, J. Fedeli, A. Descos, B. B. Bakir, S. Messaoudene, D. Bordel, S. Menezo, G. de Valicourt, S. Keyvaninia, G. Roelkens, D. V. Thourhout, D. J. Thomson, F. Y. Gardes, and G. T. Reed, “Hybrid III–V on silicon lasers for photonic integrated circuits on silicon,” *IEEE Journal of Selected Topics in Quantum Electronics* **20**(4), 158–170 (2014).
- [38] G. Roelkens, L. Liu, D. Liang, R. Jones, A. Fang, B. Koch, and J. Bowers, “III-V/silicon photonics for on-chip and intra-chip optical interconnects,” *Laser & Photonics Reviews* **4**(6), 751–779 (2010).
- [39] T. Komljenovic, M. Davenport, J. Hulme, A. Y. Liu, C. T. Santis, A. Spott, S. Srinivasan, E. J. Stanton, C. Zhang, and J. E. Bowers, “Heterogeneous silicon photonic integrated circuits,” *Journal of Lightwave Technology* **34**(1), 20–35 (2016).
- [40] Z. Wang, A. Abbasi, U. Dave, A. Groote, S. Kumari, B. Kunert, C. Merckling, M. Pantouvaki, Y. Shi, B. Tian, K. Gasse, J. Verbist, R. Wang, W. Xie, J. Zhang, Y. Zhu, J. Bauwelinck, X. Yin, Z. Hens, J. Campenhout, B. Kuyken, R. Baets, G. Morthier, D. Thourhout, and G. Roelkens, “Novel light source integration approaches for silicon photonics,” *Laser & Photonics Reviews* **11**(4), 1700,063 (2017).
- [41] G. Roelkens, A. Abassi, P. Cardile, U. Dave, A. de Groote, Y. de Koninck, S. Dhoore, X. Fu, A. Gassenq, N. Hattasan, Q. Huang, S. Kumari,

- S. Keyvaninia, B. Kuyken, L. Li, P. Mechet, M. Muneeb, D. Sanchez, H. Shao, T. Spuesens, A. Z. Subramanian, S. Uvin, M. Tassaert, K. van Gasse, J. Verbist, R. Wang, Z. Wang, J. Zhang, J. van Campenhout, X. Yin, J. Bauwelinck, G. Morthier, R. Baets, and D. van Thourhout, “III-V-on-silicon photonic devices for optical communication and sensing,” *Photonics* **2**(3), 969–1004 (2015).
- [42] A. Y. Liu, C. Zhang, J. Norman, A. Snyder, D. Lubyshev, J. M. Fastenau, A. W. Liu, A. C. Gossard, and J. E. Bowers, “High performance continuous wave 1.3  $\mu\text{m}$  quantum dot lasers on silicon,” *Applied Physics Letters* **104**(4), 041,104 (2014).
- [43] Z. Wang, B. Tian, M. Pantouvaki, W. Guo, P. Absil, J. Van Campenhout, C. Merckling, and D. Van Thourhout, “Room-temperature InP distributed feedback laser array directly grown on silicon,” *Nature Photonics* **9**(12), 837 (2015).
- [44] M. Ortsiefer, B. Kögel, J. Roskopf, and C. Neumeyr, “Long wavelength high speed VCSELs for long haul and data centers,” in *Optical Fiber Communication Conference*, pp. W4C–2 (Optical Society of America, 2014).
- [45] J. A. Tatum, D. Gazula, L. A. Graham, J. K. Guenter, R. H. Johnson, J. King, C. Kocot, G. D. Landry, I. Lyubomirsky, A. N. MacInnes, E. M. Shaw, K. Balemarthy, R. Shubochkin, D. Vaidya, M. Yan, and F. Tang, “VCSEL-Based Interconnects for Current and Future Data Centers,” *Journal of Lightwave Technology* **33**(4), 727–732 (2015).
- [46] F. Karinou, C. Prodaniuc, N. Stojanovic, M. Ortsiefer, A. Daly, R. Hohenleitner, B. Kögel, and C. Neumeyr, “Directly PAM-4 Modulated 1530-nm VCSEL Enabling 56 Gb/s/ $\lambda$  Data-Center Interconnects,” *IEEE Photonics Technology Letters* **27**(17), 1872–1875 (2015).
- [47] M. Poirier, M. Boudreau, Y.-M. Lin, R. Narayan, C. Chen, X. Hong, R. Olson, X. Liu, M. Gokhale, J. Y. Ma, and M. Eshelman, “InP integrated coherent transmitter for 100 Gb/s DP-QPSK transmission,” in *Optical Fiber Communication Conference*, p. Th4F.1 (Optical Society of America, 2015).
- [48] S. Lange, S. Wolf, J. Lutz, L. Altenhain, R. Schmid, R. Kaiser, M. Schell, C. Koos, and S. Randel, “100 GBd intensity modulation and direct detection with an InP-based monolithic DFB laser Mach-Zehnder modulator,” *Journal of Lightwave Technology* **36**(1), 97–102 (2018).
- [49] “Photonic integration at Oclaro,” (2018). URL <https://www.oclaro.com/technology/photonic-integration/>.

- [50] A. Abbasi, B. Moeneclaey, J. Verbist, X. Yin, J. Bauwelinck, G.-H. Duan, G. Roelkens, and G. Morthier, "Direct and electroabsorption modulation of a III-V-on-silicon DFB laser at 56 Gb/s," *IEEE Journal of Selected Topics in Quantum Electronics* **23**(6), 1–7 (2017).
- [51] T. Fujii, K. Takeda, N.-P. Diamantopoulos, E. Kanno, K. Hasebe, H. Nishi, R. Nakao, T. Kakitsuka, and S. Matsuo, "Heterogeneously integrated membrane lasers on Si substrate for low operating energy optical links," *IEEE J. Sel. Topics Quantum Electron.* **24**(1) (2018).
- [52] G. P. Agrawal, *Fiber-optic communication systems*, vol. 222 (John Wiley & Sons, 2012).
- [53] T. Komljenovic, L. Liang, R.-L. Chao, J. Hulme, S. Srinivasan, M. Davenport, and J. E. Bowers, "Widely-Tunable Ring-Resonator Semiconductor Lasers," *Applied Sciences* **7**(7), 732 (2017).
- [54] G. T. Reed, G. Mashanovich, F. Y. Gardes, and D. Thomson, "Silicon optical modulators," *Nature Photonics* **4**(8), 518 (2010).
- [55] M. N. Sysak, J. O. Anthes, D. Liang, J. E. Bowers, O. Raday, and R. Jones, "A hybrid silicon sampled grating DBR tunable laser," in *Group IV Photonics, 2008 5th IEEE International Conference on*, pp. 55–57 (IEEE, 2008).
- [56] D. Liang, X. Huang, G. Kurczveil, M. Fiorentino, and R. Beausoleil, "Integrated finely tunable microring laser on silicon," *Nature Photonics* **10**(11), 719 (2016).
- [57] T. Veroleet, A. Gallet, X. Pommared, J. Decobert, D. Make, J.-G. Provost, M. Fournier, C. Jany, S. Olivier, A. Shen, and G. Duan, "Hybrid III-V on silicon fast and widely tunable laser based on rings resonators with PIN junctions," in *Asia Communications and Photonics Conference* (IEEE, 2018).
- [58] S. Keyvaninia, G. Roelkens, D. V. Thourhout, C. Jany, M. Lamponi, A. L. Liepvre, F. Lelarge, D. Make, G.-H. Duan, D. Bordel, and J.-M. Fedeli, "Demonstration of a heterogeneously integrated III-V/SOI single wavelength tunable laser," *Optics Express* **21**(3), 3784–3792 (2013).
- [59] J. Hulme, J. Doylend, and J. Bowers, "Widely tunable Vernier ring laser on hybrid silicon," *Optics Express* **21**(17), 19,718–19,722 (2013).
- [60] J. Zhang, Y. Li, S. Dhoore, G. Morthier, and G. Roelkens, "Unidirectional, widely-tunable and narrow-linewidth heterogeneously integrated III-V-on-silicon laser," *Optics Express* **25**(6), 7092–7100 (2017).

- [61] G. Kurczveil, M. J. Heck, J. D. Peters, J. M. Garcia, D. Spencer, and J. E. Bowers, “An integrated hybrid silicon multiwavelength AWG laser,” *IEEE Journal of Selected Topics in Quantum Electronics* **17**(6), 1521–1527 (2011).
- [62] S. Dhoore, L. Li, A. Abbasi, G. Roelkens, and G. Morthier, “Demonstration of a discretely tunable III-V-on-silicon sampled grating DFB laser,” *IEEE Photonics Technology Letters* **28**(21), 2343–2346 (2016).
- [63] S. Dhoore, G. Roelkens, and G. Morthier, “III-V-on-silicon three-section DBR laser with over 12 nm continuous tuning range,” *Optics Letters* **42**(6), 1121–1124 (2017).
- [64] S. Dhoore, A. Rahim, G. Roelkens, and G. Morthier, “12.5 Gbit/s discretely tunable InP-on-silicon filtered feedback laser with subnanosecond wavelength switching times,” *Optics Express* **26**(7), 8059–8068 (2018).
- [65] S. Dhoore, A. Königer, R. Meyer, G. Roelkens, and G. Morthier, “Electronically tunable DFB laser on silicon,” in *International Semiconductor Laser Conference* (IEEE, 2018).

# 2

## Fundamentals of tunable laser diodes

**T**HIS chapter covers some essential concepts on the working principle of tunable laser diodes. No completeness nor rigor is aspired and emphasis is put on the discussion of electronically tunable lasers.

### Contents

---

2.1	Introduction . . . . .	25
2.2	Laser basics . . . . .	26
2.3	Electro-optical aspects of laser diodes . . . . .	31
2.4	Electronic wavelength control . . . . .	37
2.5	Characteristics of tunable laser diodes . . . . .	40
2.6	Extending the wavelength tuning range . . . . .	42
2.7	Native III-V versus III-V-on-silicon lasers . . . . .	46
2.8	Epitaxial layer stacks used in this work . . . . .	47
2.9	Conclusion . . . . .	47
	References . . . . .	50

---

### 2.1 Introduction

It is expected that in many future optical network architectures tunable laser diodes (LDs) will play a crucial role [1, 2]. Extra flexibility, functionality and performance are commonly known advantages as compared to

fixed-wavelength single-mode lasers [3, 4]. Ideally, the added value of tunability should affect the laser characteristics as little as possible and ease of tuning and stability should be kept in mind in the choice of laser structure.

In this chapter basic concepts of LDs are discussed and the concept of electronic wavelength control is introduced. The operation principle of sampled gratings is briefly discussed and an overview of the different epitaxial layer stacks used in this work is given.

## 2.2 Laser basics

### 2.2.1 Introduction

Laser operation requires two main ingredients: a cavity and optical gain. A cavity is usually formed by two reflectors, whereas optical gain is achieved by means of stimulated emission through current injection into the active layer. Lasing occurs when the cavity round trip gain is unity: the optical field is reproduced after one round trip in the cavity. The gain current for which this resonance condition is met first is the so-called threshold current. Above threshold gain clamping occurs and the extra injected carriers are converted into photons through stimulated emission. These photons partly contribute to the optical output power and are partly absorbed or scattered. The gain clamping mechanism has important consequences for the limited laser tunability based on carrier injection in standard laser structures. The laser operation wavelength is determined by the resonance condition: the cavity round trip gain is unity and the round trip phase  $\phi(\lambda)$  is an integer multiple of  $2\pi$ . The gain condition can be expressed as [5]:

$$\Gamma_A g_A(\lambda) - \alpha_i - \alpha_m(\lambda) = 0, \quad (2.1)$$

where  $g_A$  is the gain of the active medium,  $\Gamma_A$  is the confinement factor of the optical mode in the active layer,  $\alpha_i$  is the internal loss and  $\alpha_m$  the mirror loss. The phase condition involves the cavity length  $L$  and the effective refractive index of the optical mode  $n_{\text{eff}} = n_{\text{eff,R}} + jn_{\text{eff,I}}$ :

$$\phi(\lambda) = 2k_0 n_{\text{eff,R}} L = \frac{4\pi n_{\text{eff,R}} L}{\lambda_m} = 2\pi m \implies \lambda_m = \frac{2n_{\text{eff,R}} L}{m}, \quad (2.2)$$

with  $k_0 = 2\pi/\lambda_0$  the free-space propagation constant ( $\lambda_0$  is the free-space wavelength) and  $m$  the order of the cavity mode. The solution determines a number of longitudinal cavity modes for which lasing can occur. Laser operation will start first for the cavity mode that reaches the gain condition (2.1) first. This is the cavity mode that experiences the lowest mirror losses. Wavelength tuning can be done through a change in the phase condition or a change of the wavelength with the lowest mirror loss. Both conditions depend on  $n_{\text{eff,R}}$  and have to be changed simultaneously when

continuous wavelength tuning is desired. The mirror loss can be made wavelength dependent through the introduction of grating or ring resonator structures in the laser cavity [6]. As a significant number of laser structures in this work are based on gratings, a concise discussion on grating structures is presented in the following section.

### 2.2.2 Wave propagation in periodic structures

A grating is in essence a periodic modulation of the physical medium (and hence effective index of the optical mode) through which an optical wave travels. At each discontinuity the wave will partly be transmitted and partly be reflected. The reflections can build up constructively in a narrow wavelength range around the so-called Bragg wavelength  $\lambda_B = 2n_{\text{eff,R}}\Lambda$ , with  $\Lambda$  the grating period. Gratings have been extensively studied and can be described in numerous ways, for instance through the Fresnel approach [7] or by means of the transfer matrix method (TMM) [8]. Here a short derivation based on coupled-mode theory [4, 9] will set the thoughts.

We start from the scalar wave equation of the electric field  $E$ , given by:

$$\frac{d^2 E}{dz^2} + [n(z)k_0]^2 E = 0, \quad (2.3)$$

where  $z$  is the propagation direction and where all transverse and lateral variations are neglected. For simplicity, the periodic modulation of the effective index is assumed to be sinusoidal and given by:

$$n(z) = n_{\text{eff,R}} + \frac{\Delta n}{2} \cos(2\beta_0 z), \quad (2.4)$$

where  $n_{\text{eff,R}}$  is the average effective index and  $\beta_0 = \pi/\Lambda$ . Hence we can write:

$$[n(z)k_0]^2 = \left[ n_{\text{eff,R}}^2 + n_{\text{eff,R}}\Delta n \cos(2\beta_0 z) + \frac{(\Delta n)^2}{4} \cos^2(2\beta_0 z) \right] k_0^2 \quad (2.5)$$

$$\approx [n_{\text{eff,R}}^2 + n_{\text{eff,R}}\Delta n \cos(2\beta_0 z)] k_0^2, \quad (2.6)$$

thereby neglecting second order variations of  $n(z)$ . If we furthermore write the propagation constant in the grating as  $\beta = n_{\text{eff,R}}k_0$  and introduce the grating coupling coefficient  $\kappa \equiv \pi\Delta n/2\lambda_0$ , we can rewrite (2.6) as:

$$[n(z)k_0]^2 = \beta^2 + 4\beta\kappa \cos(2\beta_0 z). \quad (2.7)$$

When operating close to the Bragg wavelength ( $\Delta\beta \equiv \beta - \beta_0 \ll \beta_0$ ) the electric field can be written as the superposition of two counterpropagating waves:

$$E(z) = E^{\text{R}}(z) \exp(-j\beta_0 z) + E^{\text{L}}(z) \exp(j\beta_0 z), \quad (2.8)$$

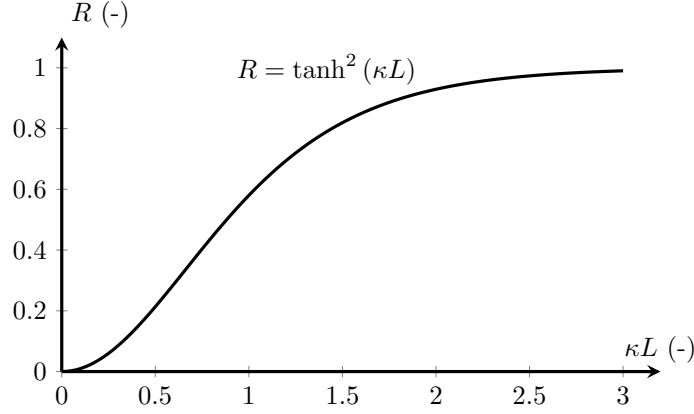


**Figure 2.1:** Power reflection as a function of  $\kappa L$  at the Bragg wavelength ( $\Delta\beta = 0$ ) in a grating reflector.

with  $E^R(z)$  and  $E^L(z)$  two slowly varying functions. By inserting (2.7) and (2.8) in (2.3), neglecting second derivatives of  $E^R$  and  $E^L$  (as they are smaller than the terms with first derivatives) and using  $\Delta\beta \ll \beta_0$ , the following set of coupled-mode equations is obtained:

$$\frac{dE^R}{dz} + j\Delta\beta E^R = -j\kappa E^L \quad (2.9)$$

$$\frac{dE^L}{dz} - j\Delta\beta E^L = j\kappa E^R. \quad (2.10)$$

When there is no coupling ( $\kappa = 0$ ), the equations become decoupled and the trivial solution

$$E(z) = E^R(0) \exp(-j\beta z) + E^L(0) \exp(j\beta z) \quad (2.11)$$

is obtained, which represents a pair of independent plane waves with constant amplitude travelling in the  $+z$  and  $-z$  direction, respectively. In the more general case ( $\kappa \neq 0$ ), the solution to the coupled-mode equations is given by:

$$E^R(z) = \left[ \cosh(\gamma z) - \frac{j\Delta\beta}{\gamma} \sinh(\gamma z) \right] E^R(0) - \frac{j\kappa}{\gamma} \sinh(\gamma z) E^L(0) \quad (2.12)$$

$$E^L(z) = \left[ \cosh(\gamma z) + \frac{j\Delta\beta}{\gamma} \sinh(\gamma z) \right] E^R(0) + \frac{j\kappa}{\gamma} \sinh(\gamma z) E^L(0), \quad (2.13)$$

with

$$\gamma^2 = \kappa^2 - \Delta\beta^2. \quad (2.14)$$

For a grating with length  $L$  and a right-propagating incident wave ( $E^L(L) = 0$ ) the field reflection  $r$  is given by:

$$r = \frac{E^L(0)}{E^R(0)} = \frac{-j\kappa \sinh(\gamma L)}{\gamma \cosh(\gamma L) + j\Delta\beta \sinh(\gamma L)}. \quad (2.15)$$

The power reflection  $R = |r|^2$  is maximum for  $\Delta\beta = 0$ , which is exactly at the Bragg wavelength.  $R$  is then given by:

$$R = \tanh^2(\kappa L) \quad (\Delta\beta = 0). \quad (2.16)$$

This is illustrated in Fig. 2.1. For  $\kappa L$  values of about 0.7, the power reflection is similar to the typical reflectivity of a cleaved facet in conventional LDs.

### 2.2.3 FP and DBR lasers

Many semiconductor laser configurations exist, all with their respective advantages and disadvantages. Figure 2.2 shows the simplified operation for two common types, a heterogeneously integrated Fabry-Pérot (FP) laser and a distributed Bragg reflector (DBR) laser. A FP laser consists of an active medium with two broadband reflectors that make up the cavity. Many longitudinal modes are supported within the gain bandwidth of the active medium. Typically the realization of a FP laser is the first step in the development of more advanced laser structures because of its relative ease of fabrication. FP lasers are however not suited for most optical communication links because of their multimode nature. In a DBR laser, a narrowband Bragg reflector is incorporated at one side of the laser structure that enables the laser to operate in a single longitudinal mode. By changing the temperature of the Bragg reflector (e.g. through the use of heaters) or by injecting carriers in the Bragg section, the Bragg wavelength can be shifted and the laser wavelength tuned.

### 2.2.4 DFB lasers

Distributed feedback (DFB) lasers have a Bragg grating incorporated along with the active medium. This makes fabrication generally easier (only a single regrowth step is required in the case of native III-V lasers) but makes the description a bit more complex as compared to their DBR counterparts. Most telecom lasers operating at 1310 nm and 1550 nm are DFB lasers, because of their low cost, straightforward fabrication and good static and dynamic characteristics. It is therefore no surprise that DFB lasers with additional functionality such as (electronic) wavelength tunability can be of great interest for the telecommunications industry [9].

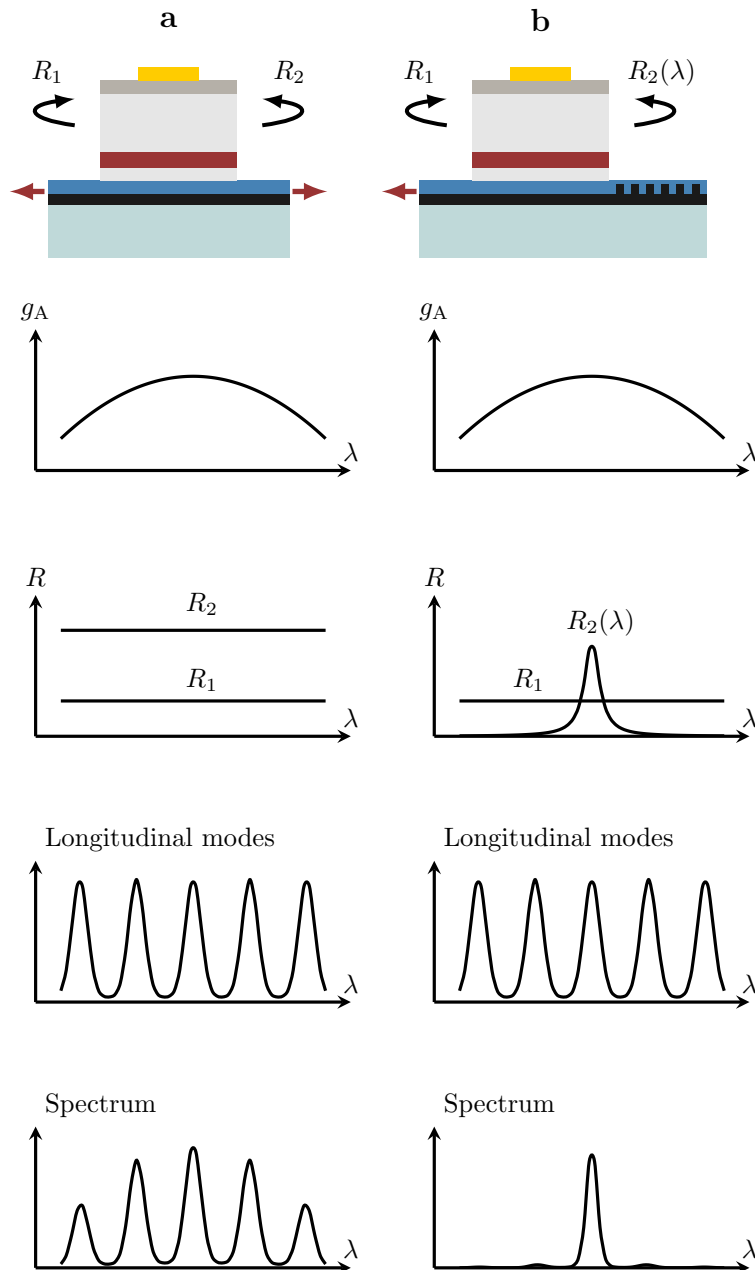


**Figure 2.2:** Laser operation. (a) Heterogeneously integrated Fabry-Pérot (FP) laser; (b) Heterogeneously integrated Distributed Bragg reflector (DBR) laser.

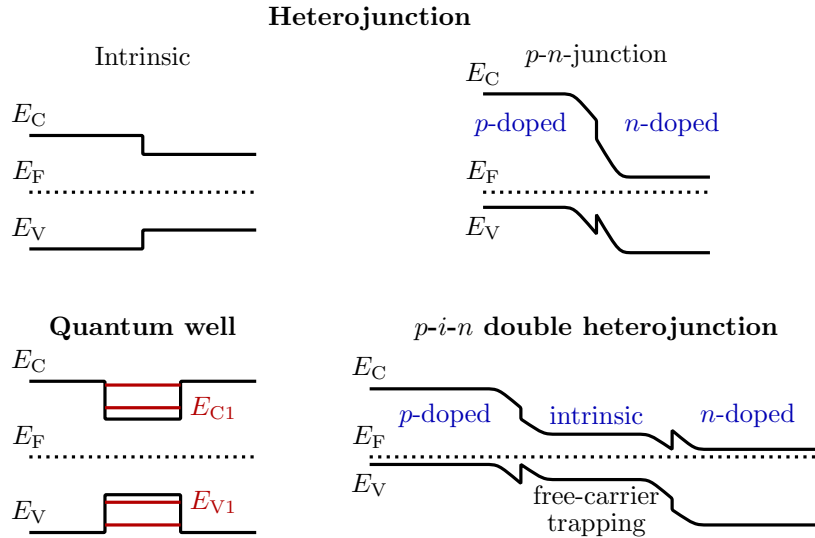


**Figure 2.3:** Energy diagram for heterojunctions and quantum wells, with indication of the conduction band energy ( $E_C$ ), valence band energy ( $E_V$ ) and Fermi level ( $E_F$ ).

## 2.3 Electro-optical aspects of laser diodes

Optical gain in a LD is provided through carrier injection into the active layer of the III-V medium and the resulting stimulated emission process. For this to work it is crucial that injected carriers are injected in an efficient way and that they are trapped inside the active layer. It turns out that a double-heterojunction is an excellent electrical confinement structure that also happens to provide optical confinement. Exactly both properties have effectively contributed to the successful realization of LDs and led to the Nobel Prize in Physics awarded to H. Kroemer and Z. I. Alferov in 2000 [10, 11].

### 2.3.1 Heterojunctions and quantum wells

A heterojunction is the interface that is formed when two semiconductors with different bandgaps are brought together. Through engineering of the band diagram by appropriate doping, an energy barrier for electrons and holes can be created [12]. When two heterojunctions (a so-called double heterojunction) are used in such way that the middle material has the smallest bandgap, electron and hole confinement in both directions is possible. This then allows for efficient pumping of the middle material. A special type of heterojunctions are quantum wells. They are only a few nm thick such that

only certain energy levels for the trapped carriers in the well are allowed (cfr. the solutions of the Schrödinger equation). The width of the quantum well determines the lowest allowed energy level such that the bandgap can be engineered by means of a change in the epitaxial layer stack geometry. Another advantage of quantum wells as compared to bulk material is their staircase-like density of states vs energy function which leads to a larger differential gain  $dg/dN$ . Note that also quantum wire and quantum dot structures exist, with an even larger theoretical differential gain. Technology-wise they are however not as mature as the quantum well counterparts and are not further considered in this work. A schematic overview of the energy diagrams for heterojunctions and quantum wells is shown in Fig. 2.3.

### 2.3.2 Carrier transport – diffusion and drift

Several carrier transport mechanisms play an important role in a semiconductor. When the carrier density profile is not uniform, carriers will diffuse in order to achieve an equilibrium state. The current as a result of carrier diffusion is described by Fick's law [13] and given by:

$$J_n = -D_n \nabla N \quad \text{and} \quad J_p = -D_p \nabla P, \quad (2.17)$$

where  $N$  is the electron density,  $P$  the hole density and  $D_n$  and  $D_p$  are the diffusion constants for electrons and holes, respectively. The latter are governed by the Einstein relation:

$$D_n = \frac{\mu_n k_B T}{q} \quad \text{and} \quad D_p = \frac{\mu_p k_B T}{q}, \quad (2.18)$$

where  $\mu_n$  and  $\mu_p$  are the mobilities for electrons and holes, respectively. Apart from diffusion currents, also drift currents are present. They are the result from the electric field  $E$  that pushes and pulls carriers towards a certain direction. The drift currents for electrons ( $J_n$ ) and holes ( $J_p$ ) are expressed by:

$$J_n = -q\mu_n N E \quad \text{and} \quad J_p = q\mu_p P E. \quad (2.19)$$

### 2.3.3 Carrier generation and recombination

Carriers can be generated either through optical or electrical pumping. Optical pumping is theoretically relevant and often used in early device demonstrations. In practice, however, mostly electrically pumped devices attract interest.

#### *p-i-n* heterojunctions

As already mentioned, a *p-i-n* heterojunction is generally used for current injection, as it provides good electrical confinement. The *p-i-n* stack forms

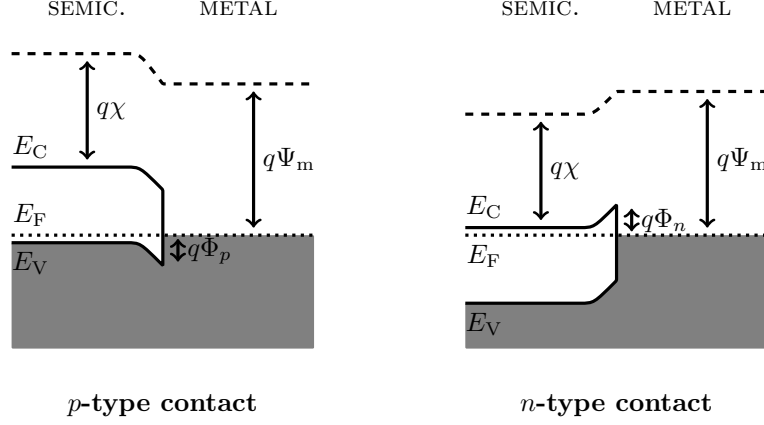


**Figure 2.4:** Band diagrams for  $p$ -type and  $n$ -type semiconductor-metal contacts.

a diode and can have interesting properties. The intrinsic region contains quantum wells to trap injected carriers and to provide gain. Through proper doping, low electrical resistance can be achieved at the  $p$ -doped and  $n$ -doped side. Typically, lower doping is chosen towards the middle of the structure, where the optical mode resides. This is to avoid optical losses due to free-carrier absorption (see Section 2.3.5).

### Ohmic contacts

Ideally, the metal contacts at the  $p$ -doped and  $n$ -doped side of the heterojunction exhibit Ohmic behavior. This means that the voltage-current relationship across the metal contact is linear, with small resistance. This is not trivial and can be engineered through proper selection of the used metallurgies. In the ideal case no potential barrier for the injected carriers has to be overcome. For an ideally terminated semiconductor, the height of the potential barrier  $q\Phi_n$  and  $q\Phi_p$  for an  $n$ -type and  $p$ -type contact, respectively, can be calculated through:

$$q\Phi_n = q\Psi_M - q\chi - q\Delta\Phi \quad (2.20)$$

$$q\Phi_p = E_G - q\Psi_M + q\chi - q\Delta\Phi, \quad (2.21)$$

where  $\Psi_M$  is the metal work function,  $\chi$  the semiconductor affinity,  $E_G$  the bandgap of the semiconductor and  $\Delta\Phi$  the barrier-lowering potential (which is related to the applied electric field). Equations (2.20) and (2.21) indicate that in order to obtain a low barrier height in an  $n$ -type contact, the metal work function should be as close as possible to the electron affinity. For a  $p$ -type contact the metal work function should be larger, as also the semiconductor bandgap comes into play. Note that for a non-ideally terminated

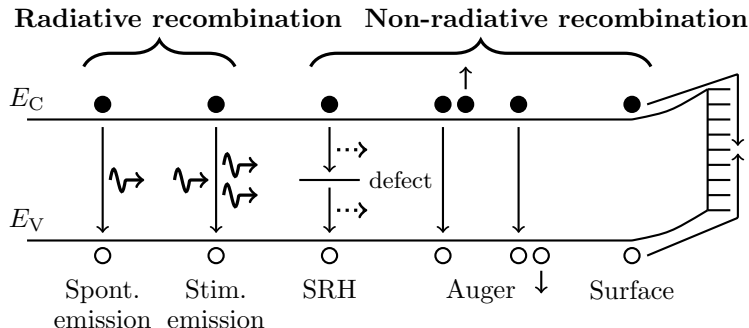


**Figure 2.5:** Overview of the different radiative and non-radiative recombination processes in a semiconductor.

semiconductor with surface states at the interface, this does not hold. The surface states then fully determine the band bending, such that the metal work function does not influence the barrier height anymore. This is referred to as Fermi level pinning and only through very high doping levels the resistance can be decreased [14].

### Radiative recombination

Carriers can be annihilated through radiative recombination, which means that a photon is generated upon electron-hole recombination. An important distinction between spontaneous and stimulated emission exists.

**Spontaneous emission** Spontaneous emission involves the generation of a photon when an electron and a hole recombine in a “natural” way. The generated photon has an energy that corresponds to the bandgap energy of the particular semiconductor. The spontaneous emission rate  $R_{sp}$  is given by:

$$R_{sp} = BN^2, \quad (2.22)$$

where  $B$  is the spontaneous emission coefficient.

**Stimulated emission** In stimulated emission a photon is generated through the recombination of an electron and a hole, with the process being triggered by the presence of another photon. The generated photon is an exact replica of the stimulating photon. The process forms the basis for optical gain and laser operation.

### Non-radiative recombination

In non-radiative recombination no photon is generated (or at least not with photon energies close to the bandgap energy) upon electron-hole recom-

ination. Non-radiative recombination processes are dominant in indirect bandgap materials such as silicon but also play an important role in direct bandgap III-V materials.

**Shockley-Read-Hall recombination** Shockley-Read-Hall (SRH) recombination refers to annihilation of an electron-hole pair through the assistance of a defect in the semiconductor. The defect sits within the semiconductor bandgap and traps the free carrier before it recombines non-radiatively. The SRH recombination rate  $R_{\text{SRH}}$  is given by:

$$R_{\text{SRH}} = \frac{N}{\tau_c}, \quad (2.23)$$

where  $\tau_c$  is the free-carrier non-radiative lifetime. III-V materials tend to suffer less from SRH recombination, as their growth quality is generally very good.

**Auger recombination** Auger recombination involves three free carriers. In the process, an electron-hole pair recombines, thereby transferring the released energy to another electron or hole that is then excited within its energy band. The Auger recombination rate  $R_{\text{Auger}}$  is given by:

$$R_{\text{Auger}} = CN^3, \quad (2.24)$$

where  $C$  is the Auger recombination coefficient. It has to be noted that Auger recombination is strongly temperature dependent, such that often a more complex description is used (where  $C$  is temperature dependent). Auger recombination is especially important in regions with high carrier densities.

**Surface recombination** At the semiconductor surface interface, so-called dangling bonds can be formed that result in traps. These traps act as non-radiative recombination centers. Surface recombination is described through the recombination velocity and strongly material dependent. It tends to be more of a problem in GaAs material systems than in InP/InGaAsP materials.

### 2.3.4 Optical gain

When light is incident on a direct bandgap semiconductor material, two competing processes come into play. An incoming photon can be absorbed through so-called band-to-band absorption whereby an electron in the conduction band is created. The other option is for the incoming photon to stimulate the recombination of an electron in the conduction band with a hole in the valence band, thereby creating an extra photon through stimulated emission. In order to have net gain, the amount of electrons in the

valence band available for absorption needs to be smaller than the amount of electrons in the conduction band. This carrier density distribution is often referred to as population inversion and leads to net optical gain, needed for e.g. laser operation. Fermi's golden rule provides a way to calculate the gain and absorption in a semiconductor material. An extensive description can e.g. be found in [5].

### 2.3.5 Optical loss mechanisms

#### Free-carrier absorption

In free-carrier absorption (FCA), carriers in the conduction or valence band are excited to a higher energy level within their band by an incident photon. As the valence band actually consists of three different bands (i.e. a heavy-hole, light-hole and split-off band), vertical transitions within the valence band are possible. This means that no phonon in the process is needed, leading to an undesired larger efficiency. It also explains why FCA losses are larger due to holes than due to electrons. The FCA loss can be expressed as:

$$\alpha_{\text{FCA}} = k_n N + k_p P, \quad (2.25)$$

where  $k_n \approx 1.5 \cdot 10^{-18} \text{ cm}^2$  and  $k_p \approx 40 \cdot 10^{-18} \text{ cm}^2$  for InP/InGaAsP at 1550 nm [15].

#### Metal absorption

Metals don't exhibit a bandgap between valence and conduction band and have therefore a very strong light absorption at any arbitrary wavelength around 1550 nm. This leads to a tradeoff where metals are put close enough to the injection structure to decrease the series resistance, but far enough away from the optical mode to decrease optical absorption losses.

#### Scattering

Scattering losses result from imperfect waveguide fabrication. Scattering generally occurs at rough material interfaces and is especially a problem in high-index contrast platforms, such as SOI. Rib-waveguide instead of wire-waveguide configurations can reduce the scattering loss but are not always suited for e.g. compact ring resonator structures. Because of the lower index contrast, silicon nitride platforms generally suffer less from scattering losses [16].

### 2.3.6 Laser rate equations

In order to describe the interplay between carriers and photons in the laser cavity, the laser rate equations are commonly used. They are a powerful

tool to model both the static and dynamic behavior of the laser. For a laser operating in single-mode, the rate equations are given by [5, 17]:

$$\frac{dN}{dt} = \eta_i \frac{I}{qV} - (R_{\text{sp}} + R_{\text{nr}}) - v_g g N_p \quad (2.26)$$

$$\frac{dN_p}{dt} = \left[ \Gamma v_g g - \frac{1}{\tau_p} \right] N_p + \Gamma \beta_{\text{sp}} R_{\text{sp}}, \quad (2.27)$$

where  $N$  is the carrier density,  $N_p$  the photon density,  $I$  the injection current,  $V$  the volume of the active region,  $\eta_i$  the injection efficiency,  $\Gamma$  the confinement factor in the active layer,  $g$  the gain per length unit,  $v_g$  the group velocity of the optical mode and  $\tau_p$  the photon lifetime in the cavity.  $R_{\text{nr}}$  is the non-radiative recombination rate and takes into account the non-radiative recombination processes discussed in Section 2.3.3.  $\beta_{\text{sp}}$  is the spontaneous emission factor and is defined as the fraction of the total spontaneous emission coupled into the laser mode. The steady-state solutions to the laser rate equations are found by setting the time derivatives to zero ( $dN/dt = 0$  and  $dN_p/dt = 0$ ).

## 2.4 Electronic wavelength control

Generally, three different physical mechanisms can be used to tune the laser wavelength: injection of free carriers, application of an electric field and changing the temperature.

### 2.4.1 The free-carrier plasma dispersion effect

The free-carrier plasma dispersion (FCD) effect essentially involves the refractive index change  $\Delta n = \Delta n_{\text{R}} + j\Delta n_{\text{I}}$  caused by the injection of an electron-hole plasma into a semiconductor [4]. In the common case of carrier injection  $N = P$  into an undoped tuning region that has a bandgap energy much larger than the photon energy, the real part of the refractive index change is given by [4]:

$$\Delta n_{\text{R}} = -\frac{e^2 \lambda^2}{8\pi^2 c^2 n \epsilon_0} \left( \frac{1}{m_n^*} + \frac{1}{m_p^*} \right) N = \beta_{\text{plasma}} N, \quad (2.28)$$

where  $n$  is the unperturbed refractive index of the semiconductor and  $m_n^*$  and  $m_p^*$  the effective masses of the injected electrons and holes, respectively. The imaginary part of the refractive index is also changed and yields an additional optical loss given by:

$$\Delta \alpha = -2k_0 \Delta n_{\text{I}} = \frac{e^3 \lambda^2}{4\pi^2 c^3 n \epsilon_0} \left( \frac{1}{m_n^{*2} \mu_n} + \frac{1}{m_p^{*2} \mu_p} \right) N = k_{\text{plasma}} N. \quad (2.29)$$

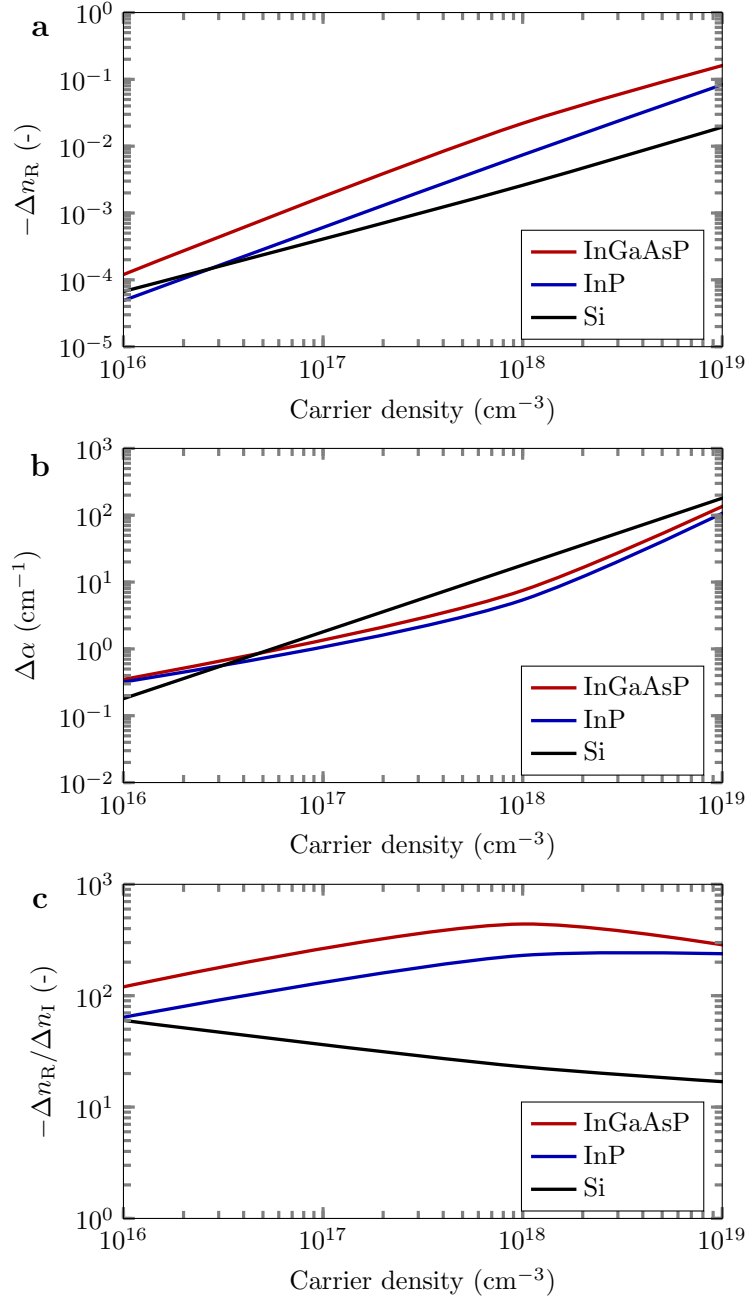


**Figure 2.6:** Free-carrier plasma dispersion effect for InGaAsP, InP and Si. (a) Carrier-induced refractive index changes ( $-\Delta n_R$ ); (b) Carrier-induced absorption changes ( $\Delta\alpha$ ); (c)  $-\Delta n_R/\Delta n_I$  as a function of carrier density.

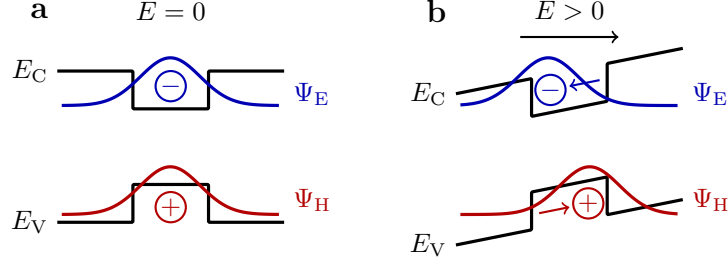


**Figure 2.7:** Illustration of the quantum-confined Stark effect (QCSE). (a) No electric field applied; (b) Electric field applied. By application of an electric field to a QW structure, the band edges become inclined and the wavefunctions get displaced with respect to each other. This leads to a reduction of the effective bandgap and a modification of the refractive index.

Note that in addition to FCD, the injection of electron-hole plasma modifies the spectral shape of the band-to-band optical absorption due to bandgap shrinkage and band filling, which leads to an additional refractive index change. In order to assess the suitability for wavelength tuning, the carrier-induced refractive index and absorption changes of InGaAsP (bandgap wavelength  $\lambda = 1400$  nm), InP and Si are calculated. A similar approach as outlined in [18] is followed. The calculation results are shown in Fig. 2.6. At a carrier density  $N = P = 10^{18} \text{ cm}^{-3}$ , the refractive index change of InGaAsP is an order of magnitude larger than for Si. Meanwhile, the carrier-induced absorption change is about half the absorption change of Si. Fig. 2.6(c) shows the ratio of the refractive index change  $\Delta n_R$  to the absorption coefficient change  $\Delta n_I$  as a function of carrier density.  $-\Delta n_R/\Delta n_I$  is significantly higher in InGaAsP than that in InP and Si, which makes InGaAsP ideal for wavelength tuning based on FCD with relatively low optical loss.

### 2.4.2 Application of an electric field

Also through application of an electric field the refractive index can be modified. In bulk semiconductors this is referred to as the Franz-Keldysh effect [19] and relatively weak in common III-V materials ( $-1.68 \cdot 10^{-10} \text{ cm/V}$  [20]). However, enhanced refractive index changes may be achieved in MQW structures by exploiting the so-called quantum-confined Stark effect (QCSE) [21]. In QCSE, a MQW structure is placed in a reverse-biased  $p$ - $n$  junction, such that the applied electric field influences the refractive index. This is illustrated in Fig. 2.7. The application of an electric field leads to an inclination of the band edges and a relative displacement between the wavefunctions for electrons and holes in a single QW. This reduces the energy difference between the lowest-order wavefunctions in the valence and

conduction band such that the effective bandgap is reduced and the refractive index is modified. The refractive index changes are typically of the order  $10^{-3}$  to  $10^{-2}$ , depending on how closely the bandgap wavelength of the MQW structure used for tuning, matches the laser wavelength [22]. The main advantage of tuning based on the QCSE is the fact that no current flows such that heat generation does not occur. There is also no carrier lifetime that limits the tuning speed, such that tuning is only limited by parasitic capacitances. However, in addition to relatively small refractive index changes, the optical confinement in the MQW structures is low as compared to bulk semiconductor structures. Consequently, the largest tuning ranges have so far been achieved through FCD.

### 2.4.3 Thermal tuning

The refractive index of III-V materials exhibits a very strong temperature dependence. A well-known rule of thumb for InGaAsP/InP lasers operating around 1550 nm is that the emission wavelength increases with temperature at a rate of approximately 0.1 nm/K [23]. This corresponds to a temperature coefficient  $dn_R/dT = 2 \cdot 10^{-4} \text{ K}^{-1}$ . Carrier injection and recombination processes in case of FCD cause heating of the device such that FCD is inherently associated with parasitic thermal tuning. As the wavelength change because of FCD and self-heating have opposite signs, they compensate each other to a certain extent. This puts the ultimate limit to the wavelength tuning range achievable through carrier injection. At low tuning currents, FCD is dominant and the refractive index decreases. For larger tuning currents, however, the thermal tuning efficiency becomes larger than the carrier-induced tuning efficiency.

## 2.5 Characteristics of tunable laser diodes

### 2.5.1 Wavelength tuning range and accuracy

The wavelength tuning range is one of the important characteristics of a tunable laser. Three different types of tuning can generally be distinguished: continuous, discontinuous and quasi-continuous tuning (see Fig. 2.8).

#### Continuous tuning

In continuous tuning, the laser wavelength can be changed in a smooth way with a single tuning current and in arbitrarily small steps. Tuning ranges are generally limited (with record continuous tuning of 13 nm for twin-guide lasers [24]) and usually smaller than a few 100 GHz [25].

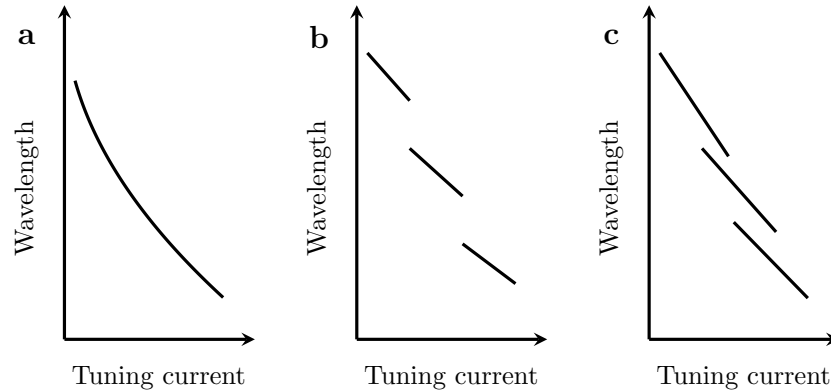


**Figure 2.8:** Different types of wavelength tuning. (a) Continuous; (b) Discontinuous; (c) Quasi-continuous.

### Discontinuous tuning

In a discontinuous tuning scheme, sudden, discontinuous wavelength changes are possible. In this case wavelength tuning is not limited by the tunability of a single longitudinal mode but rather by the tunability of the minimum roundtrip loss. A natural limit is set by the bandwidth of the gain material in the laser. This can be larger than 100 nm and discontinuous tuning ranges of more than 100 nm have readily been demonstrated [26, 27].

### Quasi-continuous tuning

Quasi-continuous tuning involves at least two tuning currents and is achieved by combining overlapping continuous ranges in order to get full wavelength coverage over a wide range. Wavelength control can be quite challenging in this case, as two or more control parameters have to be changed simultaneously to set the laser wavelength. Usually use is made of driver electronics and a look-up table to set the laser wavelength and output power. Some feedback control can be applied to improve the accuracy and stability of the emission wavelength [28].

## 2.5.2 Side-mode suppression ratio

The spectral purity of a laser is quantified through the side-mode suppression ratio (SMSR) and defined as the ratio of the power in the dominant laser mode and the power in the strongest side-mode. It is usually expressed in decibel (dB). For telecommunication applications, an SMSR larger than 30 dB is generally required.

### 2.5.3 Linewidth

The spectral linewidth is another important laser characteristic, especially for coherent optical communication systems that make use of heterodyne detection. Such systems require a linewidth below a few MHz. In direct detection the allowed linewidth is at least one order of magnitude larger. For tunable lasers the linewidth strongly depends on the tuning mechanism. Thermal and electric-field induced wavelength tuning have negligible effects on the laser linewidth. In carrier-induced wavelength tuning, however, strong linewidth broadening is observed [29]. The origin of the increased laser linewidth is attributed to the shot noise in the tuning section(s) upon carrier injection. Indeed, carrier injection and recombination lead to fluctuations in the carrier density and accompanied fluctuations in the refractive index and loss. This causes a fluctuation of the instantaneous laser wavelength and hence a broadening of the laser linewidth.

## 2.6 Extending the wavelength tuning range

Through heating or carrier injection the achievable change in refractive index is limited to about  $10^{-3}$ . This in turn limits the change in effective index and hence the wavelength tuning range. Luckily this can be extended through the Vernier principle.

### 2.6.1 The Vernier principle

The principle of a Vernier caliper is illustrated in Fig. 2.9 [4]. The caliper contains a fixed main scale and a movable Vernier scale. A shift of one scale by a certain amount leads to a bigger shift of the point where the two scales coincide. In this way the measurement accuracy can be increased as compared to a uniformly divided measurement scale. Similarly, this principle can be used in tunable laser structures with two reflectors to enhance the laser wavelength shift upon tuning of one reflector. Both reflectors should therefore exhibit a comb-like reflection characteristic with slightly different comb pitches.

### 2.6.2 Sampled grating reflectors

A sampled grating (SG) reflector exhibits a comb-like reflection spectrum with different reflection peaks and constant peak spacing [5]. A SG can be described as a uniform grating (UG) with grating period  $\Lambda$  that is multiplied by a sampling function with period  $\Lambda_S$ . The sampling duty cycle is defined as  $D_{SG} = \Lambda_G/\Lambda_S$ , where  $\Lambda_G = N\Lambda$  and  $N$  the number of remaining periods of the original UG. In order to get a basic understanding of the shape of the reflection spectrum of a SG, coupled-mode theory is used once more. It can be shown that every spatial Fourier component of the refractive index

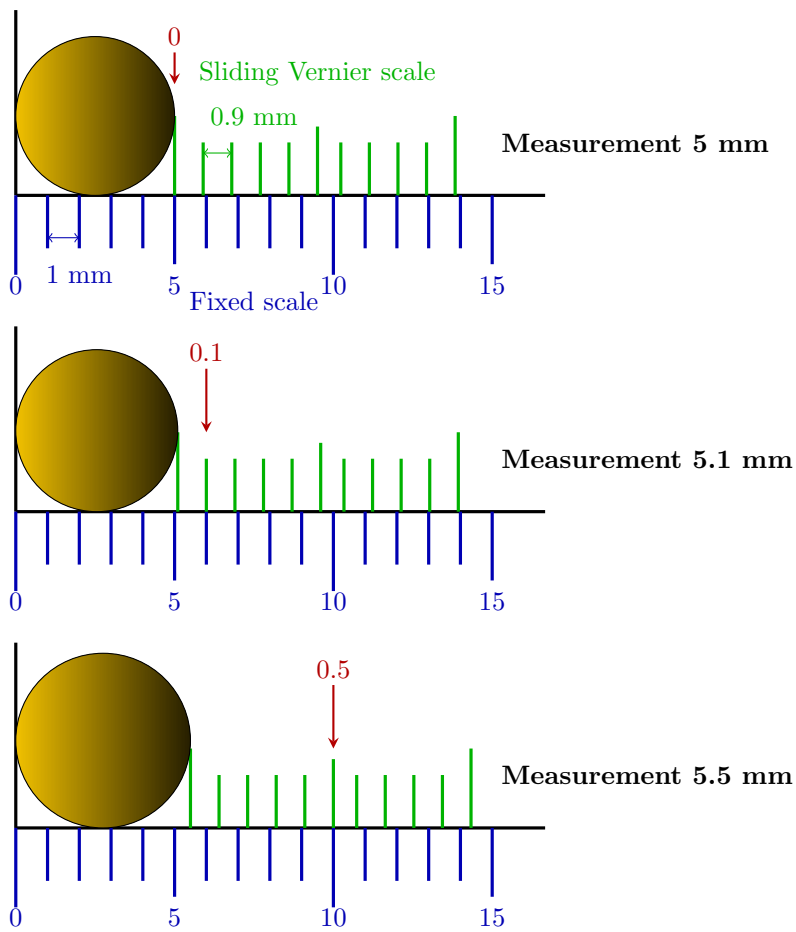
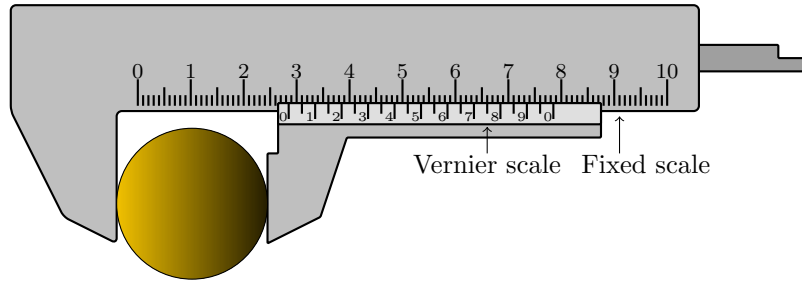


**Figure 2.9:** Working principle of a Vernier caliper. The caliper contains a fixed main scale and a movable Vernier scale. Both scales exhibit slightly different pitches. From the main scale the rough measurement value can be read, whereas increased accuracy can be reached through the Vernier scale.

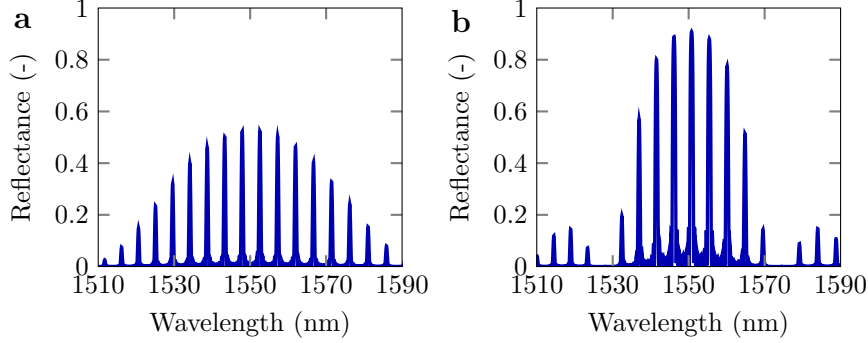


**Figure 2.10:** Simulated SG reflection spectrum for two different sampling duty cycles. Grating parameters are  $\Lambda = 240$  nm,  $\Lambda_S = 80$   $\mu\text{m}$  and  $L = 720$   $\mu\text{m}$ . (a)  $D_{\text{SG}} = 10\%$ ; (b)  $D_{\text{SG}} = 20\%$ .

modulation leads to a peak in the reflection spectrum of the SG. The spatial Fourier components are found by convolving the Fourier transform of the UG with the Fourier transform of the sampling function. We remark that a UG has a single Fourier component with coupling coefficient  $\kappa$  at spatial frequency  $1/\Lambda$  (and which corresponds to the Bragg wavelength  $\lambda_B$ ). The sampling function can be written as:

$$F(z) = \begin{cases} 1, & m\Lambda_S < z < m\Lambda_S + \Lambda_G \\ 0, & m\Lambda_S + \Lambda_G < z < (m+1)\Lambda_S, \end{cases} \quad (2.30)$$

with  $m$  an integer. The amplitudes of the Fourier components then follow from:

$$F_k = \frac{1}{\Lambda_S} \int_0^{\Lambda_S} F(z) \exp\left(-j\frac{2\pi k}{\Lambda_S} z\right) dz \quad (2.31)$$

$$= \frac{\Lambda_G}{\Lambda_S} \frac{\sin(\pi k \Lambda_G / \Lambda_S)}{\pi k \Lambda_G / \Lambda_S} \exp\left(-j\frac{\pi k \Lambda_G}{\Lambda_S}\right). \quad (2.32)$$

The convolution of both Fourier transforms has peaks centered at  $1/\Lambda$ , with constant peak spacing  $1/\Lambda_S$ . As is clear from Eq. (2.32), the envelope of the reflection spectrum is a sinc-function, with decreasing reflectance when deviating from the Bragg wavelength. Reflection peaks far from the Bragg wavelength may not be useful for laser operation because of a too low reflectance. Generally, the envelope of the reflection spectrum becomes broader with decreasing  $D_{\text{SG}}$ . This can be exploited to address more reflection peaks with similar reflectivity. However, this comes at the expense of a lower overall reflectivity of the peaks, which also decreases with decreasing  $D_{\text{SG}}$ . This is illustrated in Fig. 2.10 and follows from the fact that the

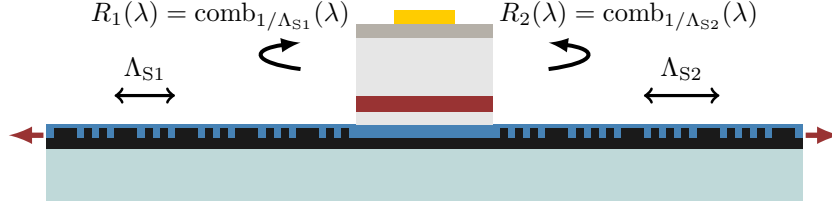


**Figure 2.11:** Schematic of a heterogeneously integrated SG-DBR laser, with two SG reflectors. Both reflectors exhibit a comb-like reflection spectrum with different peak spacing. The peak spacing for Reflector 1 and Reflector 2 is proportional to  $1/\Lambda_{S1}$  and  $1/\Lambda_{S2}$ , respectively.

coupling coefficients at the peak wavelengths equal the product of the coupling coefficient  $\kappa$  for the UG with the Fourier components of the sampling function  $F_k$  [30]:

$$\kappa_k = \kappa F_k. \quad (2.33)$$

Figure 2.11 shows a schematic of a heterogeneously integrated SG-DBR laser, where two SG reflectors with different sampling period define the laser cavity.

### 2.6.3 Design rules for wide tuning of SG-based lasers

#### Quasi-continuous tuning

Full wavelength coverage is usually desired when deploying widely tunable lasers, especially in sensing applications. Quasi-continuous (with full wavelength coverage) is possible when the reflector peak spacing is smaller than the continuous tuning range of a single reflector.

#### Maximization of the tuning range

The tuning range of widely tunable lasers is limited by the gain bandwidth and the repeat mode spacing of the combined reflector (i.e. the product of the reflection spectra of the individual reflectors). The gain bandwidth depends on the gain material and generally increases with increasing carrier density. This means that a higher threshold current and higher optical losses will allow for a larger tuning range, at the expense of a reduced efficiency. The repeat mode spacing of the combined reflector is determined by the difference in sampling period of the individual reflectors and given by:

$$\text{FSR} = \frac{\lambda^2}{n_{\text{eff,R}} |\Lambda_{S1} - \Lambda_{S2}|}. \quad (2.34)$$

This suggests that a large tuning range may be obtained by choosing the difference in peak spacing of the two reflectors very small (with  $\Lambda_{S1} \approx$

$\Lambda_{S2}$ ). However, it has to be ensured that the difference in peak spacing is larger than the spectral width of an individual reflection peak. Generally a compromise must be made between a small sampling duty cycle, a small difference in sampling period and a small grating coupling coefficient for a large tuning range on one hand and a large sampling duty cycle and a large grating coupling coefficient for a low threshold current on the other hand.

### Maximization of the side-mode suppression

In order to achieve a large SMSR, the peak spacing difference has to be sufficiently larger than the peak width. Moreover, the envelope of the reflection spectra needs to be sufficiently flat over the tuning range as to obtain good side-mode suppression. Finally the length of both sampled grating reflectors is preferably equal, with a  $\lambda/4$  phase shift in the middle of the cavity. When the phase shift is not in the middle of the cavity, the SMSR will decrease. Generally a 5% difference in reflector length is tolerable [31].

## 2.7 Native III-V versus III-V-on-silicon lasers

In Chapter 1 the drivers for the realization of heterogeneously integrated lasers have been highlighted. However, it remains true that many good native III-V lasers exist and that research towards such laser devices is very much ongoing. A concise comparison between native III-V lasers and III-V-on-silicon lasers therefore seems in place.

### 2.7.1 Optical confinement

In native InP/InGaAsP devices, the refractive index contrast between core and cladding is generally much lower ( $\Delta n \approx 0.5$  at 1550 nm) than for III-V-on-silicon devices, where the high index contrast between the silicon device and BOX layer can be exploited. This has important consequences, as the optical confinement factor plays an important role in the compactness of the laser devices. More importantly, it has a strong influence on the direct modulation bandwidth and other output characteristics of the laser. Through a proper choice of the silicon waveguide width, the confinement factor in the silicon device and the III-V layer can easily be controlled. This has for instance enabled the realization of amplifiers with high gain and high saturation power heterogeneously integrated on silicon [32].

### 2.7.2 Grating coupling coefficient

The grating coupling coefficient in DFB and DBR lasers has important implications for the laser threshold and direct modulation bandwidth of the laser. Therefore, a relatively large grating coupling coefficient is generally

desired. In III-V-on-silicon DFB lasers, grating coupling coefficients larger than  $1500 \text{ cm}^{-1}$  have been reported [33].

### 2.7.3 Thermal properties

A major drawback of heterogeneously integrated lasers is the presence of the BOX layer in the SOI platform. The BOX is needed to prevent optical leakage to the silicon substrate but has a very low thermal conductivity and prevents good heat sinking of the laser devices. Moreover, commonly DVS-BCB is used as overcladding for planarization purposes, which has equally bad heat sinking properties. In native InP/InGaAsP laser devices, no BOX layer is present and the InP cladding does have a good thermal conductivity.

## 2.8 Epitaxial layer stacks used in this work

In this work, two epitaxial layer stacks are used. The first one is a rather standard stack, commonly used for heterogeneously integrated amplifiers, FP and fixed-wavelength DFB lasers. The details are presented in Table 2.1. The second stack is a so-called tunable twin-guide (TTG) layer stack, which has an additional passive tuning layer and surrounding cladding layers. The latter will unsurprisingly form the starting point for the TTG-based laser structures. The details are presented in Table 2.2. Note that some thicknesses are presented as variables, which will be properly assigned in the discussion of the corresponding laser structures.

## 2.9 Conclusion

In this chapter, a brief introduction to tunable laser diodes has been presented. Most emphasis is put on the discussion of Bragg gratings (both uniform and sampled) as they play a significant role in the laser structures discussed in the remainder of this thesis. The details of the epitaxial layer stacks used in this work will form the starting point for the respective laser designs.

**Table 2.1:** Epitaxial layer stack – amplifier.

Layer no.	Type	Periods	Material	PL wavelength ( $\mu\text{m}$ )	Thickness (nm)	Doping ( $\text{cm}^{-3}$ )	Doping type
Substrate	-	-	InP	-	-	-	<i>n</i>
1	-	-	InP	-	50	-	NID
2	Etch stop	-	InGaAs	-	100	-	NID
3	Sacrificial	-	InP	-	100	-	NID
4	Contact	-	InGaAs	-	300	$3 \cdot 10^{19}$	<i>p</i>
5	Cladding	-	InP	-	1500	$1 \cdot 10^{18}$	<i>p</i>
6	Cladding	-	InP	-	10	-	NID
7	SCH	-	InGaAsP	1.17	100	-	NID
8	MQW (well)	6	InGaAsP	1.52	8	-	NID
9	MQW (barrier)	5	InGaAsP	1.17	10	-	NID
10	SCH	-	InGaAsP	1.17	100	-	NID
11	Cladding	-	InP	-	200	$5 \cdot 10^{18}$	<i>n</i>
12	Sacrificial	-	InGaAs	-	100	-	NID

**Table 2.2:** Epitaxial layer stack – tunable twin-guide (TTG).

Layer no.	Type	Periods	Material	PL wavelength ( $\mu\text{m}$ )	Thickness (nm)	Doping ( $\text{cm}^{-3}$ )	Doping type
Substrate	-	-	InP	-	-	-	$n$
1	-	-	InP	-	50	-	NID
2	Etch stop	-	InGaAs	-	100	-	NID
3	Sacrificial	-	InP	-	100	-	NID
4	Contact	-	InGaAs	-	300	$3 \cdot 10^{19}$	$p$
5	Cladding	-	InP	-	1200	$1 \cdot 10^{18}$	$p$
6	Cladding	-	InP	-	10	-	NID
7	SCH	-	InGaAsP	1.17	100	-	NID
8	MQW (well)	6	InGaAsP	1.52	8	-	NID
9	MQW (barrier)	5	InGaAsP	1.17	10	-	NID
10	SCH	-	InGaAsP	1.17	100	-	NID
11	Cladding	-	InP	-	$t_{\text{InP}}$	$5 \cdot 10^{18}$	$n$
12	Tuning	-	InGaAsP	1.40	$t_{\text{T}}$	-	NID
13	Cladding	-	InP	-	50	$1 \cdot 10^{18}$	$p$
14	Contact	-	InGaAsP	1.30	$t_{\text{C}}$	$5 \cdot 10^{18}$	$p$
15	Sacrificial	-	InP	-	100	-	NID

## References

- [1] S. Bindhaiq, A. S. M. Supa, N. Zulkifli, A. B. Mohammad, R. Q. Shaddad, M. A. Elmagzoub, and A. Faisal, “Recent development on time and wavelength-division multiplexed passive optical network (TWDM-PON) for next-generation passive optical network stage 2 (NG-PON2),” *Optical Switching and Networking* **15**, 53–66 (2015).
- [2] N. Ryan, M. Todd, T. Farrell, A. Lavin, P.-J. Rigole, B. Corbett, B. Roycroft, and J.-P. Engelstaedter, “A 10Gbps optical burst switching network incorporating ultra-fast (5ns) wavelength switched tunable laser sources,” in *International Conference on Space Optics ICSSO 2008*, vol. 10566, p. 1056616 (International Society for Optics and Photonics, 2017).
- [3] K. Kobayashi and I. Mito, “Single frequency and tunable laser diodes,” *Journal of Lightwave Technology* **6**(11), 1623–1633 (1988).
- [4] J. Buus, M.-C. Amann, and D. J. Blumenthal, *Tunable laser diodes and related optical sources* (Wiley-Interscience New York, 2005).
- [5] L. A. Coldren, S. W. Corzine, and M. L. Mashanovitch, *Diode lasers and photonic integrated circuits*, vol. 218 (John Wiley & Sons, 2012).
- [6] H. Ghafouri-Shiraz, *Distributed feedback laser diodes and optical tunable filters* (John Wiley & Sons, 2004).
- [7] R. Baets and G. Roelkens, *Microphotonics* (Ghent University, 2013).
- [8] J. Hong, W. Huang, and T. Makino, “On the transfer matrix method for distributed-feedback waveguide devices,” *Journal of Lightwave Technology* **10**(12), 1860–1868 (1992).
- [9] G. Morthier and P. Vankwikelberge, *Handbook of distributed feedback laser diodes* (Artech House, 2013).
- [10] H. Kroemer, “Nobel Lecture: Quasielectric fields and band offsets: teaching electrons new tricks,” *Reviews of Modern Physics* **73**(3), 783 (2001).
- [11] Z. I. Alferov, “Nobel Lecture: The double heterostructure concept and its applications in physics, electronics, and technology,” *Reviews of Modern Physics* **73**(3), 767 (2001).
- [12] S. O. Kasap, *Principles of electronic materials and devices*, vol. 2 (McGraw-Hill New York, 2006).
- [13] S. M. Sze, *Semiconductor devices: physics and technology* (John Wiley & Sons, 2008).

- [14] A. G. Baca and C. I. Ashby, *Fabrication of GaAs devices*, 6 (IET, 2005).
- [15] J. Piprek, *Semiconductor optoelectronic devices: introduction to physics and simulation* (Elsevier, 2013).
- [16] A. Rahim, E. Ryckeboer, A. Z. Subramanian, S. Clemmen, B. Kuyken, A. Dhakal, A. Raza, A. Hermans, M. Muneeb, S. Dhoore, Y. Li, U. Dave, P. Bienstman, N. L. Thomas, G. Roelkens, D. V. Thourhout, P. Helin, S. Severi, X. Rottenberg, and R. Baets, “Expanding the silicon photonics portfolio with silicon nitride photonic integrated circuits,” *Journal of Lightwave Technology* **35**(4), 639–649 (2017).
- [17] G. Morthier, R. Schatz, and O. Kjebon, “Extended modulation bandwidth of DBR and external cavity lasers by utilizing a cavity resonance for equalization,” *IEEE Journal of Quantum Electronics* **36**(12), 1468–1475 (2000).
- [18] J.-H. Han, F. Boeuf, J. Fujikata, S. Takahashi, S. Takagi, and M. Takekawa, “Efficient low-loss InGaAsP/Si hybrid MOS optical modulator,” *Nature Photonics* **11**(8), 486 (2017).
- [19] S. L. Chuang and S. L. Chuang, “Physics of Optoelectronic Devices,” (1995).
- [20] J. Faist and F.-K. Reinhart, “Phase modulation in GaAs/AlGaAs double heterostructures. II. Experiment,” *Journal of Applied Physics* **67**(11), 7006–7012 (1990).
- [21] H. Yamamoto, M. Asada, and Y. Suematsu, “Electric-field-induced refractive index variation in quantum-well structure,” *Electronics Letters* **21**(13), 579–580 (1985).
- [22] J. Zucker, I. Bar-Joseph, B. Miller, U. Koren, and D. Chemla, “Quaternary quantum wells for electro-optic intensity and phase modulation at 1.3 and 1.55  $\mu\text{m}$ ,” *Applied Physics Letters* **54**(1), 10–12 (1989).
- [23] J. Hong, M. Cyr, H. Kim, S. Jatar, C. Rogers, D. Goodchild, and S. Clements, “Cascaded strongly gain-coupled (SGC) DFB lasers with 15-nm continuous-wavelength tuning,” *IEEE Photonics Technology Letters* **11**(10), 1214–1216 (1999).
- [24] M.-C. Amann, “Broad-band wavelength-tunable twin-guide lasers,” *Optoelectronics-Devices and Technologies* **10**(1), 27–38 (1995).
- [25] M.-C. Amann and W. Thulke, “Continuously tunable laser diodes: Longitudinal versus transverse tuning scheme,” *IEEE Journal on Selected Areas in Communications* **8**(6), 1169–1177 (1990).

- 
- [26] Y. Tohmori, Y. Yoshikuni, H. Ishii, F. Kano, T. Tamamura, Y. Kondo, and M. Yamamoto, “Broad-range wavelength-tunable superstructure grating (SSG) DBR lasers,” *IEEE Journal of Quantum Electronics* **29**(6), 1817–1823 (1993).
- [27] P.-J. Rigole, S. Nilsson, L. Backbom, T. Klinga, J. Wallin, B. Stalnacke, E. Berglind, and B. Stoltz, “Access to 20 evenly distributed wavelengths over 100 nm using only a single current tuning in a four-electrode monolithic semiconductor laser,” *IEEE Photonics Technology Letters* **7**(11), 1249–1251 (1995).
- [28] G. Sarlet, G. Morthier, and R. Baets, “Control of widely tunable SSG-DBR lasers for dense wavelength division multiplexing,” *Journal of Lightwave Technology* **18**(8), 1128 (2000).
- [29] Y. Kotaki and H. Ishikawa, “Spectral characteristics of a three-section wavelength-tunable DBR laser,” *IEEE Journal of Quantum Electronics* **25**(6), 1340–1345 (1989).
- [30] G. Sarlet, *Tunable laser diodes for WDM communication—methods for control and characterisation* (2001).
- [31] M. Usami, S. Akiba, and K. Utaka, “Asymmetric  $\lambda/4$ -shifted In-GaAsP/InP DFB lasers,” *IEEE Journal of Quantum Electronics* **23**(6), 815–821 (1987).
- [32] M. L. Davenport, S. Skendžić, N. Volet, J. C. Hulme, M. J. Heck, and J. E. Bowers, “Heterogeneous silicon/III–V semiconductor optical amplifiers,” *IEEE Journal of Selected Topics in Quantum Electronics* **22**(6), 78–88 (2016).
- [33] S. Matsuo and T. Kakitsuka, “Low-operating-energy directly modulated lasers for short-distance optical interconnects,” *Advances in Optics and Photonics* **10**(3), 567–643 (2018).

# 3

## Fabrication of heterogeneously integrated tunable lasers

**I**N this chapter most aspects concerning the fabrication of heterogeneously integrated tunable laser diodes are discussed. Mainly III-V processing details are given but also the in-house fabrication of SOI waveguide circuits by means of electron-beam lithography is covered.

### Contents

---

<b>3.1</b>	<b>Introduction</b>	<b>53</b>
<b>3.2</b>	<b>Laser fabrication</b>	<b>54</b>
<b>3.3</b>	<b>Electron-beam lithography and reactive ion etching of SOI circuits</b>	<b>62</b>
<b>3.4</b>	<b>Conclusion</b>	<b>69</b>
	<b>References</b>	<b>70</b>

---

### 3.1 Introduction

A big part of this PhD project is concerned with the fabrication of different heterogeneously integrated laser structures. Although the adhesive bonding integration technology is well established, in itself it does not plainly lead to high-quality laser devices. Optimization of each SOI and III-V postprocessing step is also of utmost importance. Moreover, novel laser structures involve optimization steps tailored to these specific layouts. In this PhD

project, bonding and III-V postprocessing are carried out using the clean-room facilities at Ghent University.

## 3.2 Laser fabrication

The realization of heterogeneously integrated lasers is not straightforward and depends a great deal on successful fabrication. This can be achieved not only through good cleanroom skills and processing experience, but in the first place through careful lithographic contact mask design. In this section the latter is primarily discussed, after which the details are given on the SOI and III-V processing.

### 3.2.1 Lithographic mask design

A set of lithographic masks is required to postprocess the III-V layers on top of the SOI waveguide circuit of interest. This set not only contains the actual laser structures but also a number of test and alignment structures to assess the fabrication quality during the process and to allow for fine structural alignment, respectively. Figure 3.1 shows a typical mask layout with indication of the different laser and test structures:

**1. Laser devices** The main laser structures, typically positioned in the center of the die. The lasers have a  $250\ \mu\text{m}$  spacing, which allows relatively easy routing of the metal pads in the last fabrication step. Typically different structural parameters such as grating period, grating length and mesa width are varied from laser to laser. Nevertheless it is made sure that grating couplers are vertically aligned to facilitate optical characterization.

**2. Alignment markers** Consist of crosses and Vernier rectangles. The former allow for coarse alignment, whereas the latter can account for very precise alignment. Typically the first lithographic step is most crucial in terms of alignment accuracy, as it involves the positioning of the III-V structures with respect to the underlying SOI structures. Obviously, the further the markers are spaced from each other, the more accurate alignment can be done. As rule of thumb a vertical and horizontal spacing of at least  $15\ \text{mm}$  leads to good translational and angular alignment.

**3. TLM structures** Test structures to assess the quality of the metal contacts during and after fabrication. Based on the transmission line model (TLM) an estimation of the contact resistance can be extracted. During the fabrication process the structures can also assist to determine whether or not a certain hard mask layer has been completely removed.

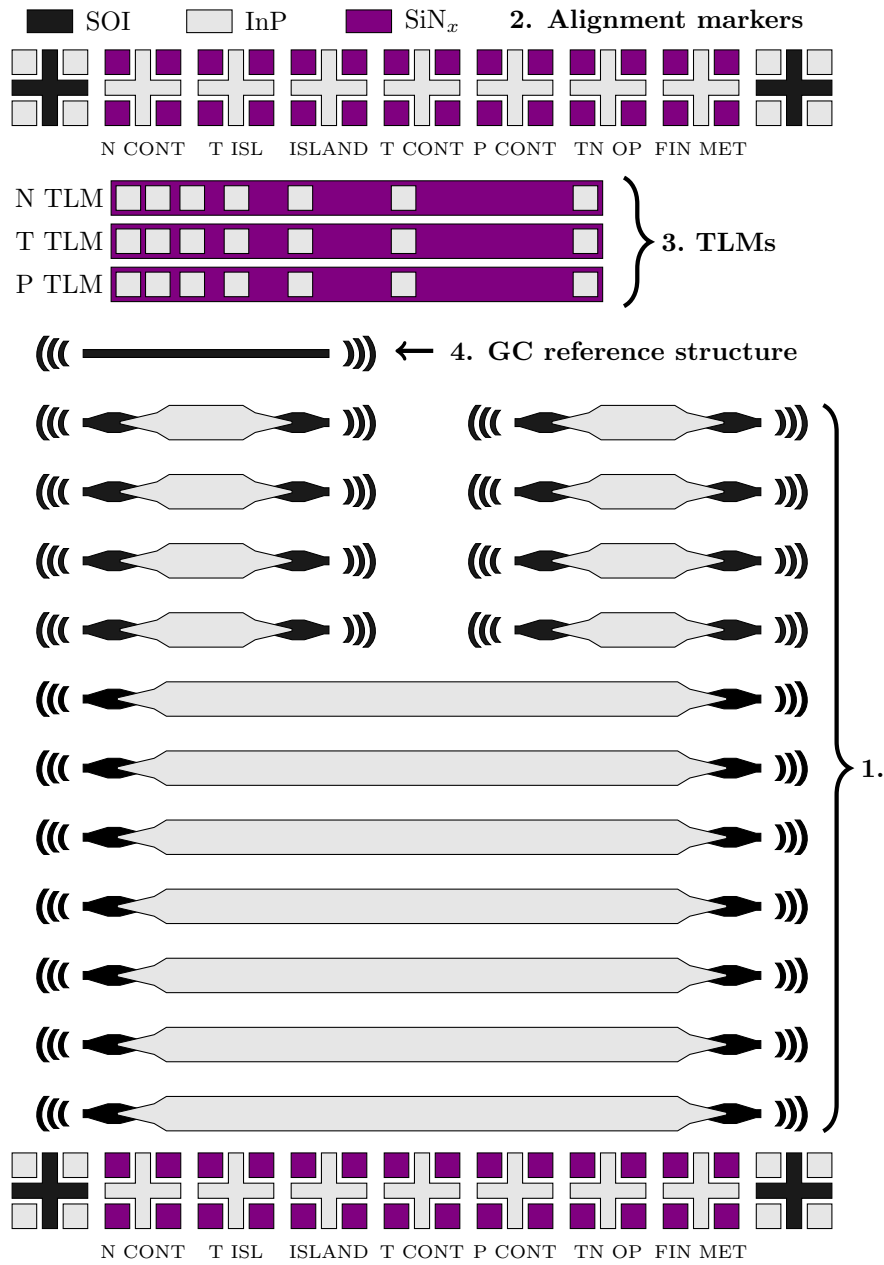


**Figure 3.1:** Lithographic mask design for a set of TTG-DFB and SG-TTG-DFB lasers.

**4. Reference structures** Simple “grating coupler in – waveguide – grating coupler out” structures. From these structures the grating coupler efficiency can be extracted and hence also the waveguide-coupled output power from the laser devices. For an accurate estimation it is crucial that the test structures are positioned as close as possible to the laser devices of interest, as also the grating couplers are affected by the different etching steps.

### 3.2.2 SOI and III-V processing

An overview of the fabrication process flow is presented in Fig. 3.2.

#### Surface preparation

**III-V die** A die is cleaved from the III-V wafer in suitable dimensions. Typically such a die is a 9 mm × 8 mm rectangle. The asymmetry allows to easily recognize the major flat direction, which is also the direction of the waveguide structures. Before bonding, the top sacrificial layers are removed to be able to start the processing from a clean surface. Afterwards a very thin ( $\sim 10$  nm) SiO<sub>x</sub> layer is deposited by means of plasma-enhanced chemical vapor deposition (PECVD), which greatly enhances the adhesion between the III-V die and DVS-BCB.

**SOI die** An SOI die is cleaved from a multi-project wafer (MPW). Protective photoresist (PR) is removed with acetone, iso-propylalcohol (IPA) and deionized (DI) water. Afterwards the sample is thoroughly cleaned in microwave oxygen plasma for 15 minutes. This not only removes remaining polymers from the SOI die but also oxidizes the surface, which again enhances the adhesion with DVS-BCB. Subsequently a diluted DVS-BCB solution is spincoated at 3000 rpm on the SOI die. Mesitylene is used for dilution, where for a 40 nm bonding layer thickness a 1:8 DVS-BCB:mesitylene dilution is needed. The sample is then baked at 150°C on a hotplate for 15 minutes after which the sample is gradually cooled down to 70°C.

#### Adhesive bonding & III-V substrate removal (I)

**Adhesive bonding** For the actual bonding the III-V die is flipped upside down and placed on the DVS-BCB containing SOI die. A set of pyrex carrier wafers is used to keep the III-V and SOI die in place. The whole is then loaded in the bonding machine. The chamber is pumped to vacuum and the sample stage heated to 150°C. Afterwards force is applied to the III-V/SOI die set while the temperature is gradually increased to 250°C. In order to fully cure the DVS-BCB adhesive layer the temperature is kept fixed at 250°C for 1 hour after which it is slowly cooled down to finalize the bonding process.

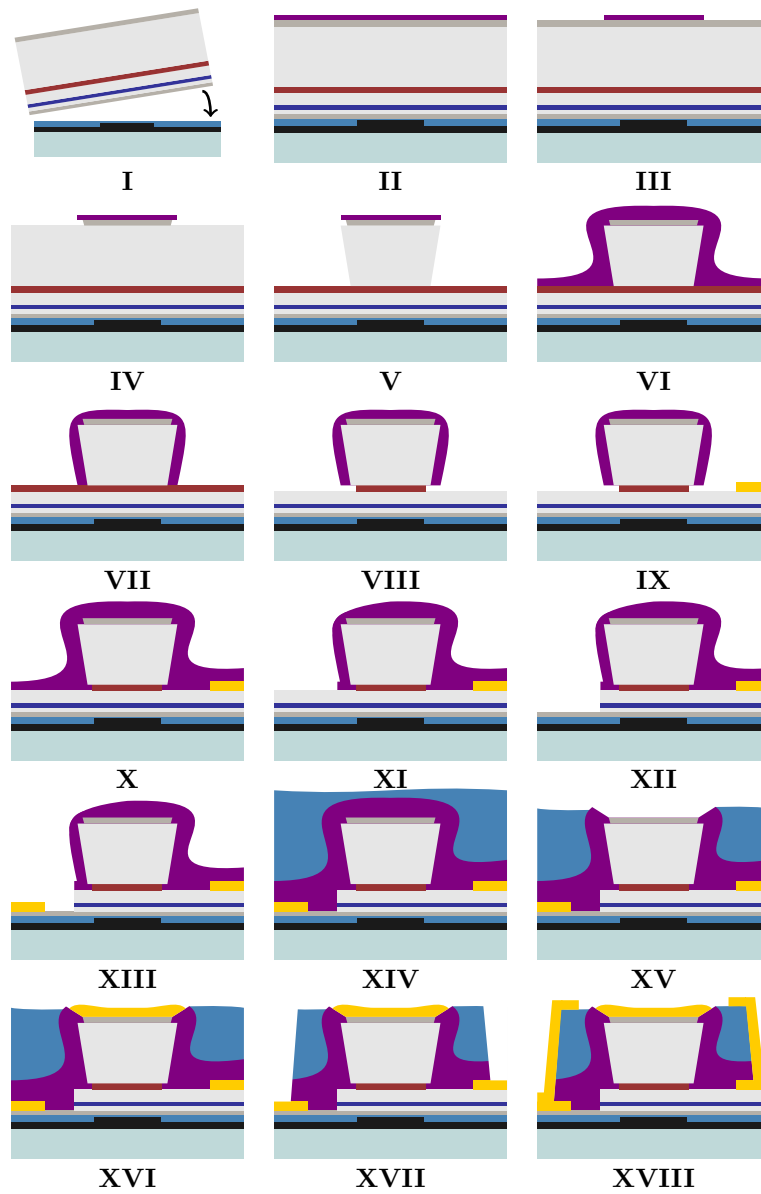


Figure 3.2: Fabrication process flow for TTG-DFB lasers.

**III-V substrate removal** After bonding the III-V/SOI die is unloaded from the bonding machine and placed in a 1:4 DI water:HCl solution at 40°C–50°C to remove the InP substrate. A pair of InGaAs/InP layers underneath the InP substrate act as etch stop layers. After about 10 minutes the complete InP substrate is removed. The 1:4 DI water:HCl solution is optimized to prevent so-called “ears” from appearing at the sides of the bonded III-V die. Finally the InGaAs and InP etch stop layers are removed with 1:1:18 H<sub>2</sub>SO<sub>4</sub>:H<sub>2</sub>O<sub>2</sub>:DI water and pure HCl, respectively.

### Mesa & MQW definition

For the definition of the mesa the *p*-InGaAs layer is structured by means of inductively coupled plasma (ICP) etching. Therefore a 200 nm thick SiN<sub>x</sub> layer that acts as hard mask is initially deposited on top of the surface via PECVD (**II**). After patterning of the SiN<sub>x</sub> layer through optical contact lithography, the hard mask is defined through reactive ion etching (RIE) (**III**). Afterwards the InGaAs layer is etched through by means of an 8-cycle ICP etch (**IV**). The remainder of the InP layer is then etched with 1:1 HCl:DI water (**V**). A stirrer is used during the process. The wet etch results in a V-shape, which is beneficial for the adiabatic tapered coupler used to couple light from the InP waveguide to the underlying silicon waveguide. Subsequently a 200 nm thick SiN<sub>x</sub> layer is deposited via PECVD (**VI**) after which the structure is etched via RIE (**VII**). The SiN<sub>x</sub> layer protects the *p*-InGaAs contact layer during etching of the MQWs. The latter are etched through a combination of ICP etching and wet etching with 1:1:10 H<sub>2</sub>SO<sub>4</sub>:H<sub>2</sub>O<sub>2</sub>:DI water (**VIII**). Care must be taken to prevent a too large undercut of the MQWs.

### *n*-type ground contact metallization

The *n*-type ground contact structures are defined through an image-reversal optical contact lithography step (**IX**). A 30:20:50 nm Ni:Ge:Au + 40:200 nm Ti:Au metallurgy is used. The extra Ti:Au improves the protection of the contact during a later via definition step.

### Tuning waveguide definition

The tuning waveguide is defined through ICP etching of the *n*-InP, InGaAsP tuning and *p*-InP layer. Therefore a 200 nm thick SiN<sub>x</sub> layer is deposited via PECVD (**X**), patterned via optical contact lithography and etched via RIE (**XI**). Afterwards the ICP etching is performed (**XII**). Through profilometer measurements it is checked that the *p*-InGaAsP contact layer is reached.

### ***p*-type tuning contact metallization**

The *p*-type tuning contact structures are also defined through an image-reversal optical contact lithography step (XIII). A 40:500 nm Ti:Au metallurgy is used. The large thickness of the Au equalizes the step height as compared to the *n*-type ground contact and improves the protection of the contact during a later via definition step.

### **Island definition**

During the island definition the individual laser structures are electrically isolated from each other. The islands are patterned through optical contact lithography after which the bottom *p*-type InGaAsP contact layer is etched with 1:1:18 H<sub>2</sub>SO<sub>4</sub>:H<sub>2</sub>O<sub>2</sub>:DI water. A linear taper is formed at the ends of the laser structures to maximize coupling from the III-V to the silicon waveguide and to reduce back reflections.

### **Passivation & planarization**

In order to passivate the sample a 300 nm thick SiN<sub>x</sub> layer is deposited through PECVD. Afterwards an undiluted DVS-BCB layer is spincoated to planarize the sample (XIV). A typical 50 nm topography is achieved. The planarized sample is then etched back through RIE (XV). The 300 nm thick SiN<sub>x</sub> layer above the *p*-type InGaAs contact layer is removed through RIE as well.

### ***p*-type active contact metallization**

Another image-reversal optical contact lithography step is used to define the *p*-type active contact (XVI). A 40:150 nm Ti:Au metallurgy is used. A short (~ 10 seconds) 1:1:18 H<sub>2</sub>SO<sub>4</sub>:H<sub>2</sub>O<sub>2</sub>:DI water dip after lithography removes any oxidized layer and ensures good contact.

### **Via definition**

Openings are then defined in the sample to reach the *n*-type ground contact and *p*-type tuning contact. The DVS-BCB material and underlying SiN<sub>x</sub> layer are removed through RIE (XVII).

### **Pad metallization**

Finally the metal contact pads are defined through optical contact lithography (XVIII). Typically the pads are defined in a ground-signal-ground (GSG) configuration to allow for high-speed characterization of the laser devices.

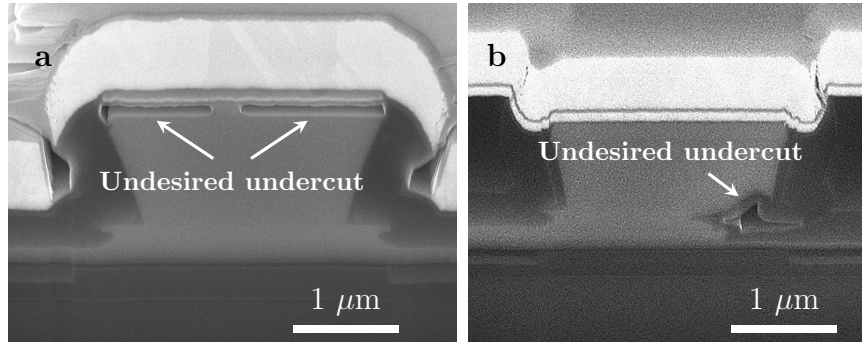


**Figure 3.3:** Undesired undercut after wet etching. (a) In the  $p$ -InGaAs contact layer; (b) In the active and tuning layer.

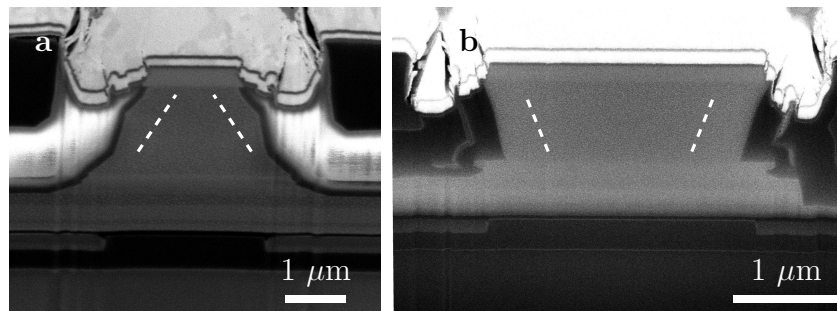


**Figure 3.4:** Dependence of the mesa profile on the III-V crystal orientation. (a) Christmas tree profile (wrong); (b) V-groove profile (correct).

### 3.2.3 Fabrication issues and fixes

Sometimes (or actually, quite often) the fabrication process does not evolve as planned and leads to issues that decrease device performance or even hamper its final realization. Luckily most of the time different approaches can be found to overcome these issues. Some encountered problems and their fixes are discussed here.

#### Undercut of the InGaAs contact layer

During MQW wet etching the  $p$ -InGaAs layer has to be protected to prevent a strong undercut. Indeed the etch rate of InGaAs is actually higher than the etch rate of InGaAsP in a piranha solution. An SEM/FIB image of a fabrication run in which the contact layer was not protected, is shown in Fig. 3.3(a).

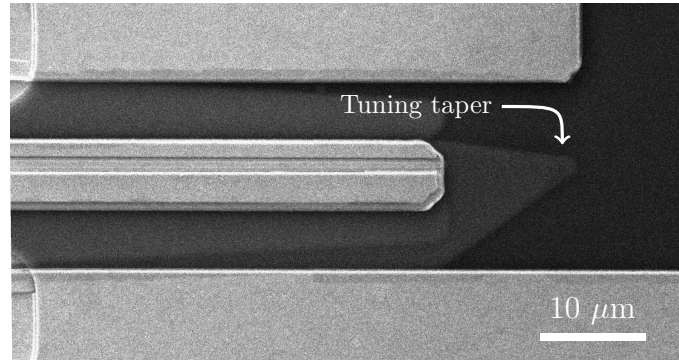


**Figure 3.5:** Definition of the tuning taper through ICP etching.

### Undercut of the active and tuning layer

Initial attempts to define the tuning waveguide made use of HCl and piranha wet etching to remove the InP and InGaAsP layers. This led, however to a very strong undercut of the active and tuning layer, as shown in Fig. 3.3(b) and prevented laser operation. By making use of ICP etching instead, a much more directional definition can be achieved. Disadvantage is that selectivity of the etch is lower and care has to be taken to not remove too much of the bottom InGaAsP contact layer as this dramatically increases the resistance of the tuning contact.

### V-groove versus Christmas tree shape of the mesa

When the III-V die is oriented  $90^\circ$  with respect to the proper orientation, no V-shape is obtained after definition of the mesa but rather a Christmas tree shape. This is illustrated in Fig. 3.4. Although the convention of alignment with the major flat is typically maintained, sometimes the convention can differ.

### Bad definition of the tuning taper

Similarly, wet etching affects the definition of the tuning taper at the end of the laser structure. Sometimes the taper is almost completely removed after a long wet etch. Again ICP etching can overcome this problem. An example of a rather well-defined tuning taper is shown in Fig. 3.5.

## 3.2.4 Final fabrication results

An optical microscope image of the final state of a fabricated chip with TTG-DFB and SG-TTG-DFB lasers is shown in Fig. 3.6. The fabrication results for the specific laser devices will be presented in the respective chapters.

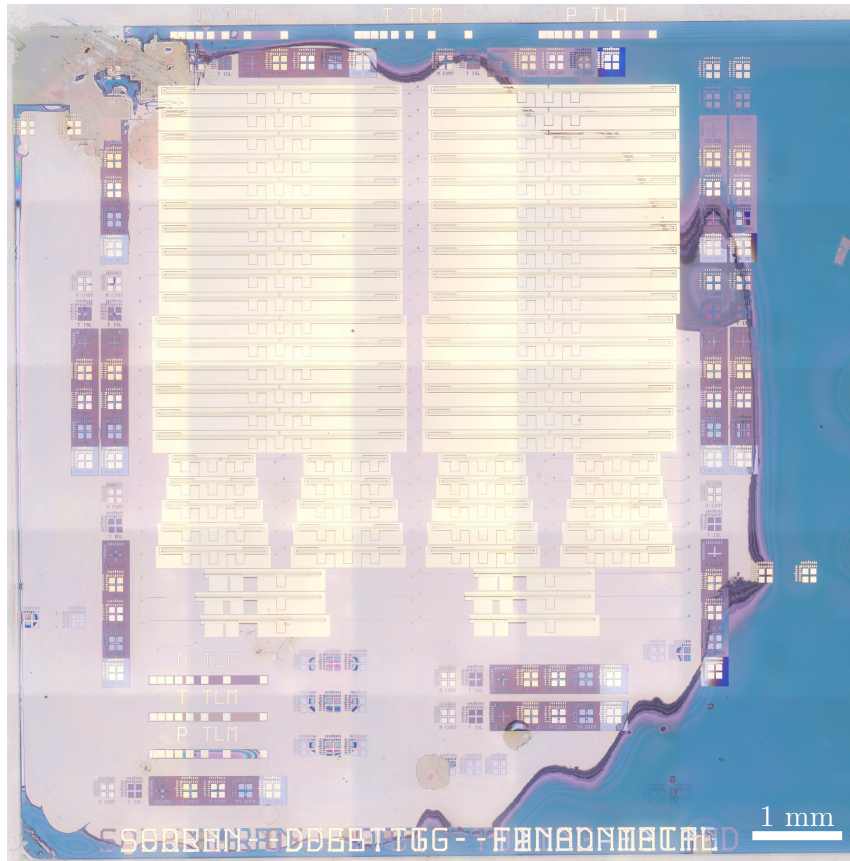


**Figure 3.6:** Optical microscope image of a fabricated chip with a set of TTG-DFB and SG-TTG-DFB lasers.

### 3.3 Electron-beam lithography and reactive ion etching of SOI circuits

In this work, most SOI waveguide circuits were fabricated in a CMOS pilot-line at *imec*. However, for faster prototyping of devices effort has been put in the development of a fabrication process that involves the in-house Voyager electron-beam lithography tool from Raith [1]. Here a short introduction on electron-beam lithography is presented, after which the main fabrication results are highlighted.

### 3.3.1 Electron-beam lithography

Electron-beam lithography (e-beam lithography or EBL) allows to define structures by scanning a focused beam of electrons on an electron-sensitive film (resist). The electron beam changes the solubility of the resist and enables selective removal of either the exposed or non-exposed regions of the resist by immersing it in an appropriate solvent solution (development). The Voyager EBL tool allows operation with electron acceleration voltages up to 50 kV with a maximum write field area of 500  $\mu\text{m}$  by 500  $\mu\text{m}$ . The system has advanced automation capabilities (e.g. autofocus and write-field alignment) and can be used for wafers with a diameter up to 8 inch. As compared to standard optical lithography, EBL can typically obtain a much higher resolution because of the extremely short De Broglie wavelength. However, the achievable resolution also greatly depends on and is mainly limited by the type and thickness of resist, the substrate, the acceleration voltage and the operating conditions. Several key parameters are commonly used to identify the EBL process. Electron dose ( $\mu\text{C}/\text{cm}^2$ ) is the charge per unit area needed to induce a desired chemical response in the resist. Area dwell time defines the writing time of the electron beam at a certain position on the sample. Step size and line spacing are geometric parameters that define the distance between two subsequent dots and the distance between two subsequent dot lines, respectively. The electron dose is given by

$$\text{Electron dose} = \frac{\text{Beam current} \cdot \text{Area dwell time}}{\text{Step size} \cdot \text{Line spacing}}, \quad (3.1)$$

where the Beam current can be directly measured from the EBL system. Our purpose is to develop an EBL and subsequent RIE process for SOI with a 400 nm thick silicon device layer and 180 nm etch depth.

### 3.3.2 Lithographic mask design

Similarly as for the contact mask design for laser fabrication, the importance of careful EBL mask design cannot be underestimated. In the early development stage, “grating coupler in – waveguide – grating coupler out” test structures are written to assess the performance of the grating couplers and the waveguide loss for different EBL parameters. Although the test structures can be written within 1 write field, laser structures are typically much longer than 500  $\mu\text{m}$ , which makes that the laser structures encompasses several write fields. This can lead to so-called stitching errors (see Fig. 3.7), which is detrimental when it occurs in the laser cavity. Stitching errors can be minimized by careful optimization through the Voyager software but are nevertheless always present. Luckily positive lithography merely leads to hanging or ear-like side structures and do not interrupt the waveguides contrary to negative lithography. Another way to minimize the stitching error is by locating the boundaries of the write field at very wide

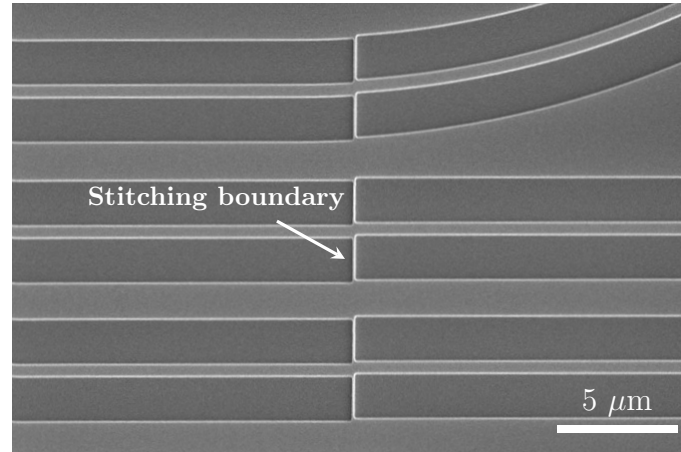


**Figure 3.7:** Introduction of waveguide imperfections at stitching boundaries of the  $500\ \mu\text{m}$  by  $500\ \mu\text{m}$  EBL write fields.

waveguides, such that the relative error and scattering losses become lower. Finally, use can be made of the fixed beam moving stage (FBMS) mode, which is especially suited for writing very long and narrow structures of arbitrary curvature. The mode is however not suited for the definition of grating structures and is not considered here.

### 3.3.3 EBL process flow

The EBL process starts with spincoating of the e-beam resist on the clean SOI die. The positive tone AR-P 6200.09 resist is used and has similar performance in terms of resolution and etch resistance as the more commonly used ZEP520A resist. As a rule of thumb we target a resist thickness that is about twice the desired etch depth. The resist is therefore spincoated at 1500 rpm for 1 minute and has a thickness of around 340 nm to 360 nm. After a short bake at  $150^\circ\text{C}$  for 1 minute, a thin layer of water-soluble Elektra 92 is spincoated on the SOI die at 2000 rpm for 1 minute. The latter is a conductive polymer and reduces charging effects that could defocus the electron beam and that would lead to a deteriorated pattern definition. In the initial development phase, a set of test exposures are done to determine the optimum electron dose. After exposure the sample is therefore immersed in DI water to remove the Elektra 92 layer. Afterwards, the sample is developed with *n*-amylacetate for 1 minute. Subsequently, IPA is used to stop the development. The test structures are then examined under the optical microscope and through SEM. It turns out that an electron dose of  $160\ \mu\text{C}/\text{cm}^2$  with a step size of 5 nm gives the most satisfying pattern definition. The used e-beam aperture mode is LC – 60 and corresponds with a

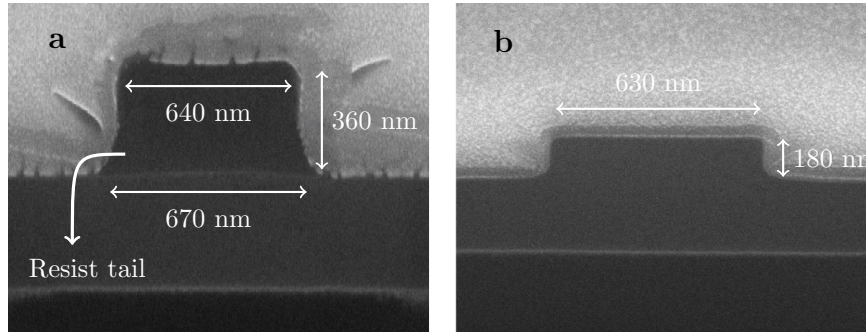


**Figure 3.8:** EBL and RIE for the fabrication of single-mode SOI rib waveguides. (a) Cross-sectional view of the waveguide structure after development; (b) Cross-sectional view of the waveguide structure after RIE.

beam spot size of 7 nm in the center of the write field. An SEM/FIB image of a fabricated single-mode rib waveguide structure (with a target waveguide width of 650 nm) after development of the e-beam resist is shown in Fig. 3.8(a). A small resist tail is observed at the sides of the waveguide pattern. This tail is removed through a very short (10 sec.)  $O_2$  plasma in the RIE tool prior to etching.

### 3.3.4 RIE of SOI circuits

The 180 nm partial etch of the silicon device layer is done through RIE. A mixture of  $CF_4$ ,  $H_2$  and  $SF_6$  is used, which is inspired by an in-house developed etching process for silicon nitride and germanium. A power of 210 W, a pressure of 20 mTorr with gas flow parameters 100 sccm for  $CF_4$ , 7 sccm for  $H_2$  and 3 sccm for  $SF_6$  are used, respectively. The etch rate is around 50 nm per minute, both for the e-beam resist and the silicon. Note that the actual etch rate varies strongly with time, as power in the etch chamber has to build up. It also depends on the preconditioning of the chamber. In order to get an idea of the actual etch depth before the resist is stripped, a simple trick can be used. A soft scratch in the resist is made, after which the remaining resist thickness and the full structure thickness are measured with the profilometer. From this thickness difference the actual etch depth is estimated. Typically the actual etch depth is overestimated by 10 nm. After etching, the sample is kept in the RIE chamber to remove the remaining resist with  $O_2$  plasma. An SEM/FIB image of a single-mode rib SOI waveguide structure after RIE is shown in Fig. 3.8(b). The shape is well on target, although the waveguide is slightly narrower than targeted. However, this can be compensated for in the mask design.

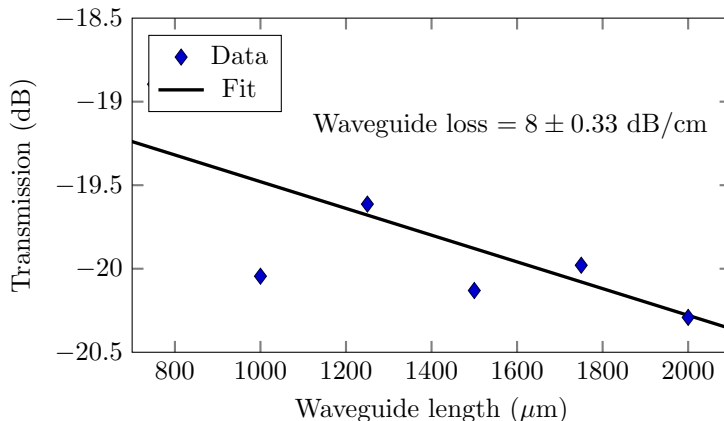


**Figure 3.9:** Estimation of the waveguide loss through a set of “grating coupler in – waveguide – grating coupler out” test structures.

### 3.3.5 Fabrication and characterization results

#### Single-mode rib waveguides

From the “grating coupler in – waveguide – grating coupler out” test structures, a rough estimation of the waveguide loss is extracted through the cutback method and a set of different waveguide lengths. These characterization results are shown in Fig. 3.9. A waveguide loss of about 8 to 11 dB/cm is obtained. This is high as compared to rib waveguides fabricated at *imec* by means of deep UV lithography (with waveguide losses smaller than 1 dB/cm), but is sufficient for our purpose to define laser structures. Also note that modest waveguide lengths are used in the test structures, as the waveguide lengths have to fit within one write field. This as to prevent any unknown loss from stitching errors. The waveguide loss can be reduced through a resist reflow step before RIE to smoothen the structures. This, however, is unsuited when gratings are part of the structures. As already mentioned, the FBMS mode can be used as well to obtain a lower waveguide loss. Currently, in-house e-beam fabrication of rib SOI waveguides by means of the FBMS mode gives a waveguide loss around 2 dB/cm. This clearly shows that most of the waveguide loss can be attributed to the e-beam writing rather than the RIE process. A promising way to go is therefore to define all long waveguide structures with the FBMS mode and the grating structures with the normal writing mode. Some e-beam tools also feature a modulated beam moving stage (MBMS) mode, which is very suited for writing low-loss waveguide and grating structures, without stitching errors.

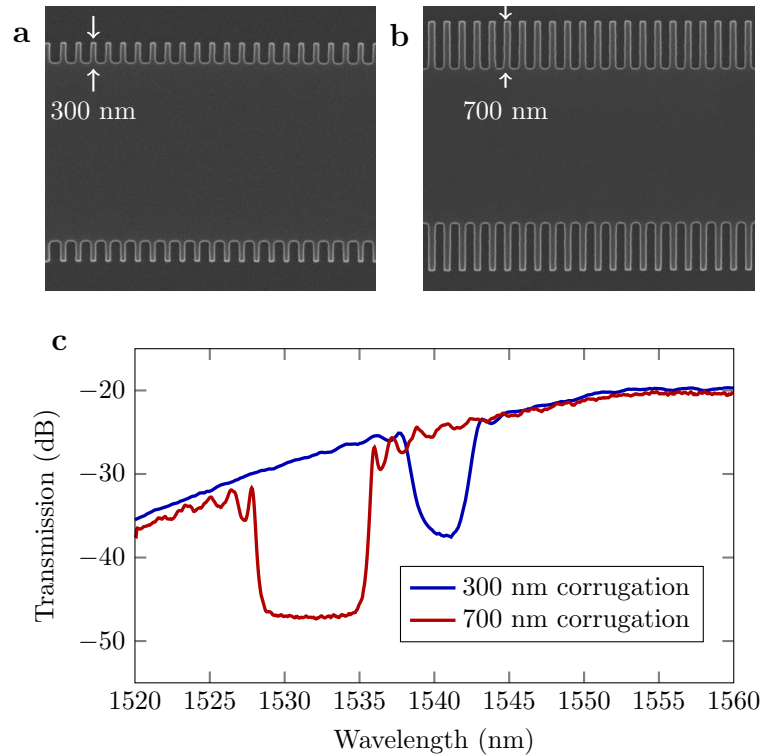


**Figure 3.10:** E-beam fabrication of a set of sidewall-corrugated gratings (with a grating length of  $150\ \mu\text{m}$  and a grating period of  $250\ \text{nm}$ ). (a) SEM image of a grating with a sidewall corrugation of  $300\ \text{nm}$ ; (b) SEM image of a grating with a sidewall corrugation of  $700\ \text{nm}$ ; (c) Reflection spectra.

### Sidewall-corrugated gratings

A different set of passive test structures defined with EBL are sidewall-corrugated grating reflectors. These structures are useful for the realization of single-mode DBR lasers. SEM images of the fabricated structures (with different corrugation depths, a grating length of  $150\ \mu\text{m}$  and grating period  $250\ \text{nm}$ ) are shown in Figs. 3.10(a) and (b). The rectangular corrugation teeth are well-defined, without clear sinusoidal corrugation pattern. The corresponding reflection spectra are shown in Fig. 3.10(c). The obtained extinction ratio (ER) is  $10\ \text{dB}$  and for a  $300\ \text{nm}$  corrugation depth the reflection spectrum is sufficiently narrowband to be useful in single-mode DBR laser structures. Note that the effective index of the optical mode in the grating with a  $700\ \text{nm}$  corrugation depth is slightly lower than for the  $300\ \text{nm}$  corrugation depth case, which explains the slightly different Bragg wavelength. The estimated grating coupling coefficient is  $60\ \text{cm}^{-1}$  and

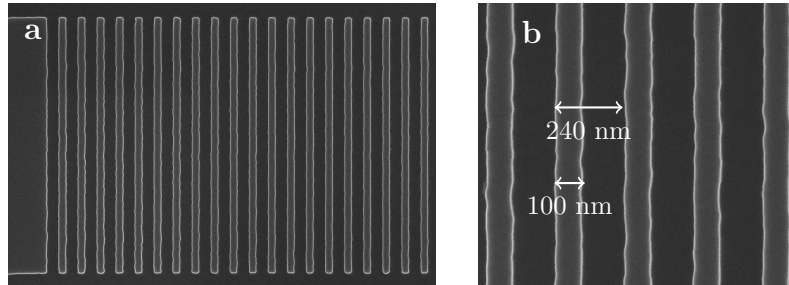


**Figure 3.11:** E-beam fabrication of a top-etched grating. (a) SEM image of a waveguide connected to the grating; (b) SEM image of the enlarged grating and indication of the geometrical dimensions.

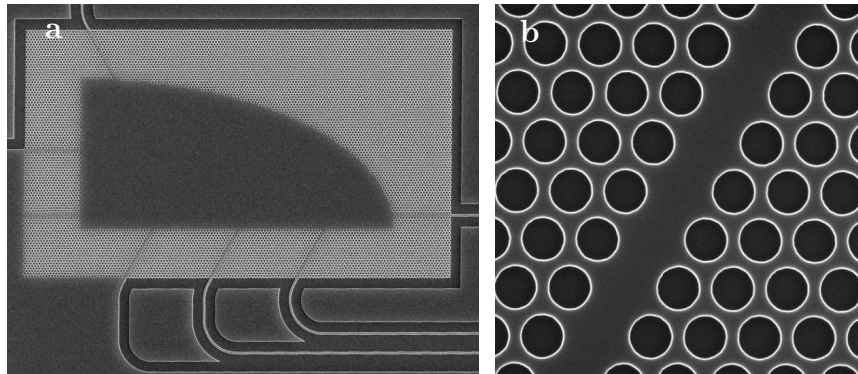


**Figure 3.12:** E-beam fabrication of a photonic crystal structure on a 220 nm SOI die. (a) SEM image of the full structure, with several input and output waveguides connected to the photonic crystal cavity; (b) SEM image of the enlarged photonic crystal cavity.

$225 \text{ cm}^{-1}$  for the 300 nm and 700 nm corrugation depth case, respectively.

### Top-etched gratings

Figure 3.11 shows an SEM image of a fabricated top-etched Bragg grating. Again, the structure is well-defined. On the mask a 50% grating duty cycle is used. Clearly, the grating lines are narrower than targeted. This can be attributed to slight overdevelopment after EBL. To compensate for this, a duty cycle of 65% on the mask can be used. As may be expected from EBL, the fabricated grating period is perfectly on target. The top-etched gratings with a grating period around 240 nm are the most commonly used structures for heterogeneously integrated III-V-on-silicon DFB lasers at 1550 nm.

### Structures on the 220 nm SOI platform

Finally, the same etching process has also been used to successfully fabricate fully etched silicon waveguides and photonic crystal structures on the 220 nm SOI platform. Some example SEM images are shown in Fig. 3.12. Currently effort is put in further optimization of the fabrication process.

### 3.3.6 Bonding on the SOI chips

One difficulty to integrate III-V material on top of the e-beam-defined SOI structures is the fact that the SOI chips are not planarized. Usually *imec* SOI wafers are planarized with remaining side-oxide, such that adhesive bonding is relatively straightforward. Successful adhesive bonding on air-clad SOI chips (defined through EBL) highly depends on the local density of the SOI structures and the thickness of the adhesive DVS-BCB layer. A way to ensure good adhesive bonding is to prevent very large etched areas (without patterning) on the SOI die. In our fabrication runs, successfully bonded III-V-on-silicon devices with DVS-BCB thicknesses lower than 30 nm have been achieved.

## 3.4 Conclusion

This chapter has covered the different aspects concerned with the fabrication of the TTG-based laser structures presented in this work. The detailed fabrication process flow has been presented and a few fabrication issues and fixes have been discussed. Process development of electron-beam lithography and reactive ion etching to realize SOI waveguide and grating structures have been covered as well. The latter can be very useful for short-term demonstration of novel heterogeneously integrated laser structures in a research environment.

## References

- [1] “Raith nanofabrication, dedicated electron beam lithography,” (2017).  
URL <https://www.raith.com/>.

# 4

## Electronically tunable DFB lasers on silicon

**T**HIS chapter is based on [1] and [2] and covers the core work of this PhD project. Design, fabrication and characterization aspects of electronically tunable DFB lasers on silicon are presented.

### Contents

---

4.1	Introduction . . . . .	71
4.2	Tunable twin-guide (TTG-) DFB laser . . . . .	72
4.3	Sampled grating (SG-) TTG-DFB laser . . . . .	92
4.4	SG-DFB laser . . . . .	93
4.5	Conclusion . . . . .	101
	References . . . . .	103

---

### 4.1 Introduction

Distributed feedback (DFB) lasers are among the most used and most suited laser types for optical communication. This stems from the fact that they are generally easier in terms of fabrication as compared to their DBR-like counterparts and the fact that they typically exhibit a large direct modulation bandwidth. In 2008 the first DFB laser with outcoupling to a silicon waveguide was realized [3]. Since then, more heterogeneously integrated DFB laser devices have been successfully demonstrated, with excellent static and dynamic characteristics. Threshold currents as low as

10 mA [4], waveguide-coupled output powers of tens of mW [5] and direct modulation up to 56 Gbit/s [6] are state-of-the art specifications.

Although fixed-wavelength DFB lasers are useful on their own for many applications, the lack of (electronic) tunability inherently limits their applicability in advanced communication architectures. In this chapter we will discuss several heterogeneously integrated electronically tunable DFB laser structures. Devices based on the tunable twin-guide (TTG) and the standard amplifier InP/InGaAsP epitaxial layer stack are presented.

## 4.2 Tunable twin-guide (TTG-) DFB laser

The structure of a TTG-DFB laser is schematically shown in Fig. 4.1(a). A cross-sectional view of the laser structure is shown in Fig. 4.1(b). The structure consists of a TTG membrane that is integrated on top of an SOI waveguide circuit that contains a  $\lambda/4$  phase-shifted Bragg grating. The latter provides optical feedback and justifies the DFB name designation. The TTG membrane (see Table 2.2 for the detailed epitaxial layer stack) constitutes two double heterojunctions with an  $n$ -type separation layer that electronically decouples the active layer and the tuning layer, such that gain and wavelength can be controlled independently. Through electron and hole injection into the tuning layer, the effective index of the optical mode can be modified, in turn modifying the laser wavelength. Due to the electronic tuning nature (based on FCD), tuning speeds are intrinsically high, with expected wavelength switching times on the order of nanoseconds. Moreover, as the TTG-DFB laser is an example of a transversely integrated laser structure, inherent continuous wavelength tunability can be provided. How this works, is shortly discussed in the next section. Afterwards, the design, fabrication and characterization of the laser devices is presented.

### 4.2.1 Transversely integrated laser structure

Consider a hypothetical single-mode DFB laser of which the length can be easily stretched or compressed. Starting from an initial laser length  $L_1$  and grating period  $\Lambda_1$  the laser is for instance expanded to length  $L_2$  and grating period  $\Lambda_2$ . It is clear that the stretching factor is equal for both the laser length and the grating period, such that:

$$\frac{L_2}{L_1} = \frac{\Lambda_2}{\Lambda_1}. \quad (4.1)$$

Although the laser wavelength is determined by the Bragg wavelength and proportional to the grating period (which increases with stretching), the number of half-wavelengths fitting in the laser cavity (i.e. the mode number  $N$ ) remains constant during stretching. Hence, laser operation in the same

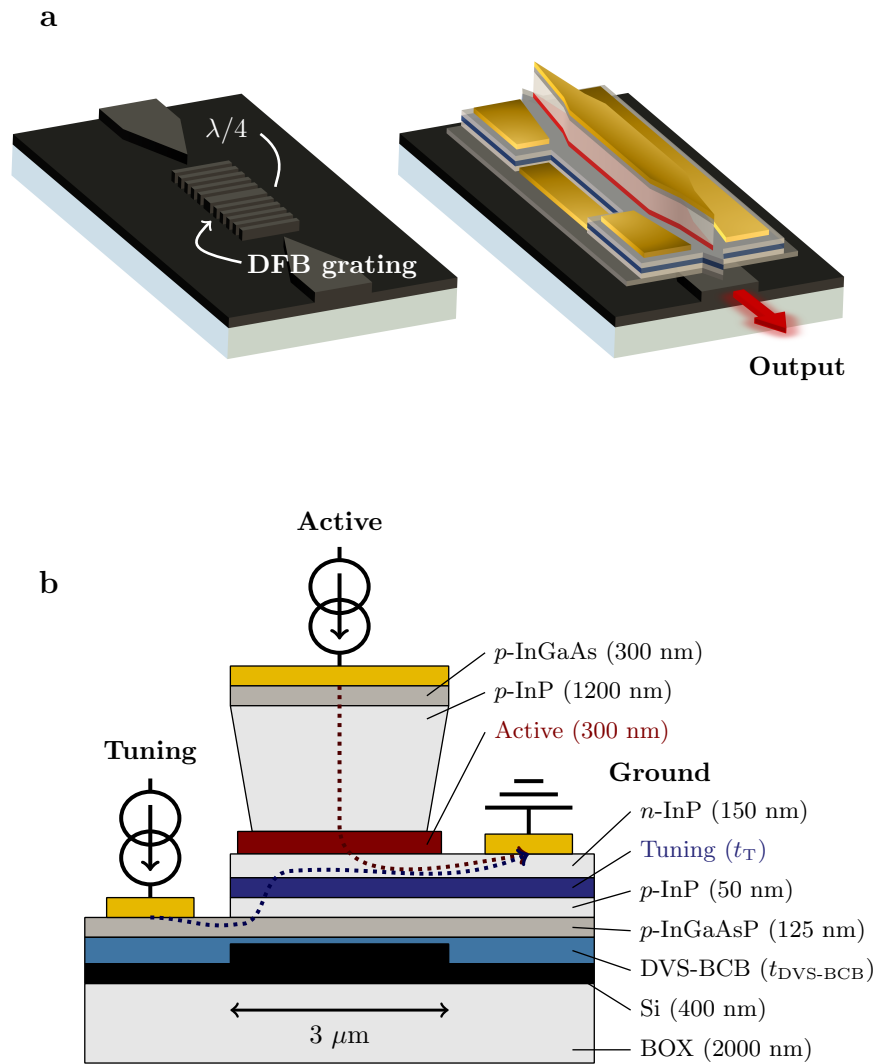


**Figure 4.1:** TTG-DFB laser structure. (a) 3D schematic; (b) Cross-sectional view. Through carrier injection into the tuning layer, the effective index of the optical mode can be modified, in turn modifying the laser wavelength.

longitudinal mode is achieved although the wavelength is increased. Wavelength tuning is thus continuous, without the appearance of mode hops. The same principle holds for a TTG-DFB laser, where not the geometrical length is stretched but rather the optical laser length is tuned through carrier injection into the tuning layer of the TTG stack. If we assume the laser to operate at the Bragg wavelength  $\lambda_B$  we then have:

$$\lambda = \lambda_B = 2\Lambda n_{\text{eff,R}}. \quad (4.2)$$

The total roundtrip phase  $\phi$  for the laser light is given by:

$$\phi = 2\beta L = \frac{4\pi n_{\text{eff,R}}}{\lambda} L. \quad (4.3)$$

Using (4.2) this can also be expressed as:

$$\phi = 2\pi \frac{L}{\Lambda}. \quad (4.4)$$

The latter clearly shows that the total roundtrip phase and, hence, the mode number  $N = \phi/2\pi = L/\Lambda$  remains constant during tuning of the laser wavelength (given by (4.2)). Since tuning is inherently continuous in a TTG-DFB laser, no separate phase section is needed. This as opposed to longitudinally integrated tunable laser structures such as DBR lasers.

### 4.2.2 Design aspects

As might be clear from the rather complex TTG epitaxial layer stack, careful laser design is required to find the sweet spot in the extensive design space. This design contains (to a certain extent) an optimization of the epitaxial layer stack and the optimum parameters of the Bragg grating. As will become clear, the thickness of the adhesive DVS-BCB bonding layer (and the influence of its variation) will also play an important role in the laser design.

#### Laser cross section

As main design target the overlap of the optical mode with the different layers in the TTG stack has to be optimized so to minimize the laser threshold and maximize the optical output power. On top of that, the mode should have significant overlap with the tuning layer and the silicon waveguide to ensure efficient tuning and sufficient distributed feedback, respectively. In a first design stage, there are therefore four figures of merit considered:

- The transverse confinement factor in the active layer –  $\Gamma_A$
- The transverse confinement factor in the tuning layer –  $\Gamma_T$
- The transverse confinement factor in the bottom contact layer –  $\Gamma_C$

- The grating coupling coefficient  $\kappa$  of the Bragg grating.

The transverse confinement factor of the optical mode is defined as the overlap integral [7]:

$$\Gamma_i = \frac{\int_i \text{Re}[(\mathbf{E} \times \mathbf{H}^*) \cdot \mathbf{u}_z] dx dy}{\int_{\text{Total}} \text{Re}[(\mathbf{E} \times \mathbf{H}^*) \cdot \mathbf{u}_z] dx dy}, \quad (4.5)$$

with  $i = \{A, T, C\}$ . In essence, it is a measure for the light-matter interaction in that particular layer.  $\Gamma_A$  is related to the transverse modal gain  $g_m$  through:

$$g_m = \Gamma_A g, \quad (4.6)$$

where  $g$  is the gain of the active medium.  $\Gamma_T$  is directly proportional to the tuning efficiency through:

$$\frac{\Delta \lambda_B}{\Delta N} = \Gamma_T \frac{\lambda_B}{n_g} \frac{dn_T}{dN}, \quad (4.7)$$

where  $n_g$  is the group index,  $\lambda_B$  the Bragg wavelength,  $n_T$  the refractive index of InGaAsP in the tuning layer and  $N$  the carrier density. As the bottom contact layer is heavily  $p$ -doped, it significantly contributes to the modal loss, given by:

$$\alpha_m = \Gamma_C \alpha_{\text{FCA}}. \quad (4.8)$$

The choice for  $p$ -InGaAsP instead of  $p$ -InGaAs as material for the bottom contact layer is prompted by the former's lower absorption loss, with the obvious trade-off of a larger contact resistance. Related to that, we note that the top  $p$ -InGaAs contact layer exhibits a very strong optical loss. However, because of the large 1200 nm  $p$ -InP separation, the optical mode has very weak overlap with the contact layer and its contribution to the overall modal loss may be neglected.

The grating coupling coefficient represents the strength of the coupling between the forward and backward propagating wave in the grating and is a measure for the reflection per unit length ( $\text{cm}^{-1}$ ). For the case of a uniform rectangular grating,  $\kappa$  may be calculated from [7]:

$$\kappa = 2 \left( \frac{n_{\text{eff, Si}} - n_{\text{eff, no Si}}}{\lambda_B} \right) \sin(m\pi D) \quad (\text{weak-grating approximation}), \quad (4.9)$$

where  $n_{\text{eff, Si}}$  and  $n_{\text{eff, no Si}}$  are the effective indices in the unetched and etched parts of the grating, respectively.  $D$  is the grating duty cycle and  $m$  the grating order. It is clear that for a first order grating ( $m = 1$ ) and a second order grating ( $m = 2$ ) the optimum duty cycle is  $D = 50\%$  and  $D = 25\%$  (or  $75\%$ ), respectively. Typically, one opts for first order gratings as they do not suffer from higher-order radiation losses.

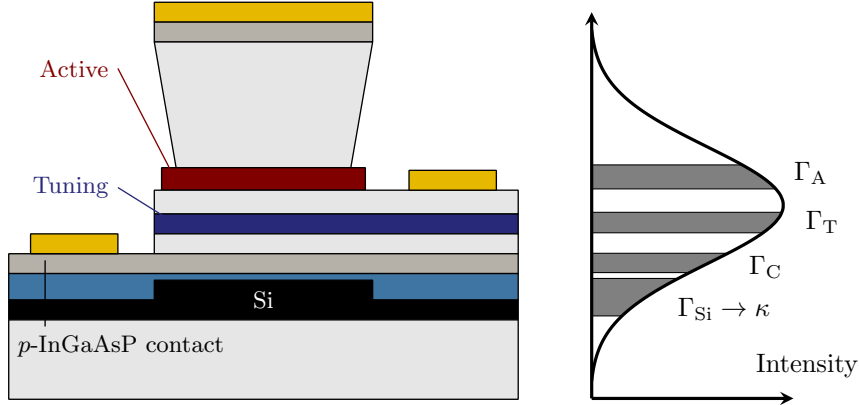


**Figure 4.2:** Overview of the different figures of merit in the TTG-DFB laser design. The transverse confinement factor in the silicon waveguide  $\Gamma_{\text{Si}}$  is strongly linked with the grating coupling coefficient  $\kappa$ .

Optical properties are studied using Fimmwave and MODE Solutions, mode solvers from Photon Design [8] and Lumerical [9], respectively. Waveguide modes and the corresponding  $\Gamma_A$ ,  $\Gamma_T$ ,  $\Gamma_C$  and  $\kappa$  are calculated for different values of the tuning layer thickness  $t_T$  and the DVS-BCB thickness  $t_{\text{DVS-BCB}}$ . Other parameters are initially kept fixed, both for reduction of design complexity and ease of epitaxial growth. The  $p$ -InGaAsP contact layer thickness  $t_C = 125$  nm. The width of the laser mesa and silicon grating is also kept constant, at  $3 \mu\text{m}$ . Narrower mesas can lead to larger injection efficiencies but typically suffer from larger waveguide losses and vice versa. The silicon grating has a total thickness of 400 nm with an etch depth of 180 nm. Figure 4.2 gives a schematic overview of the different considered figures of merit in the laser design. In Fig. 4.3 the simulation results are shown. From Fig. 4.3(a) it is obvious that a larger  $t_T$  results in a larger  $\Gamma_T$ , with little dependence on  $t_{\text{DVS-BCB}}$ . A different story follows from the two other contour plots. A larger  $t_{\text{DVS-BCB}}$  leads to a larger  $\Gamma_A$  and lower  $\kappa$ , respectively. This is as expected, as a larger spacing between the active layer and silicon waveguide leads to a reduced modal overlap with the silicon grating and hence lower grating coupling coefficient. For  $t_{\text{DVS-BCB}} > 50$  nm,  $t_T$  has a relatively large impact on  $\Gamma_A$ . If we target a  $\kappa > 100 \text{ cm}^{-1}$  and  $\Gamma_A > 7\%$ , we end up in the region  $40 \text{ nm} < t_{\text{DVS-BCB}} < 60 \text{ nm}$ .  $t_T$  can be chosen as large as possible, although  $\Gamma_A$  and  $\kappa$  start to decrease for  $t_T > 200$  nm. We therefore choose  $t_T = 190$  nm to account for some fluctuations in the epitaxial growth and target a  $t_{\text{DVS-BCB}} = 50$  nm as initial design parameters. The corresponding figures of merit are  $\Gamma_A = 7.4\%$ ,  $\Gamma_T = 23.7\%$ ,  $\Gamma_C = 4.3\%$  and  $\kappa = 115 \text{ cm}^{-1}$ . The optical mode profile is nicely distributed over the

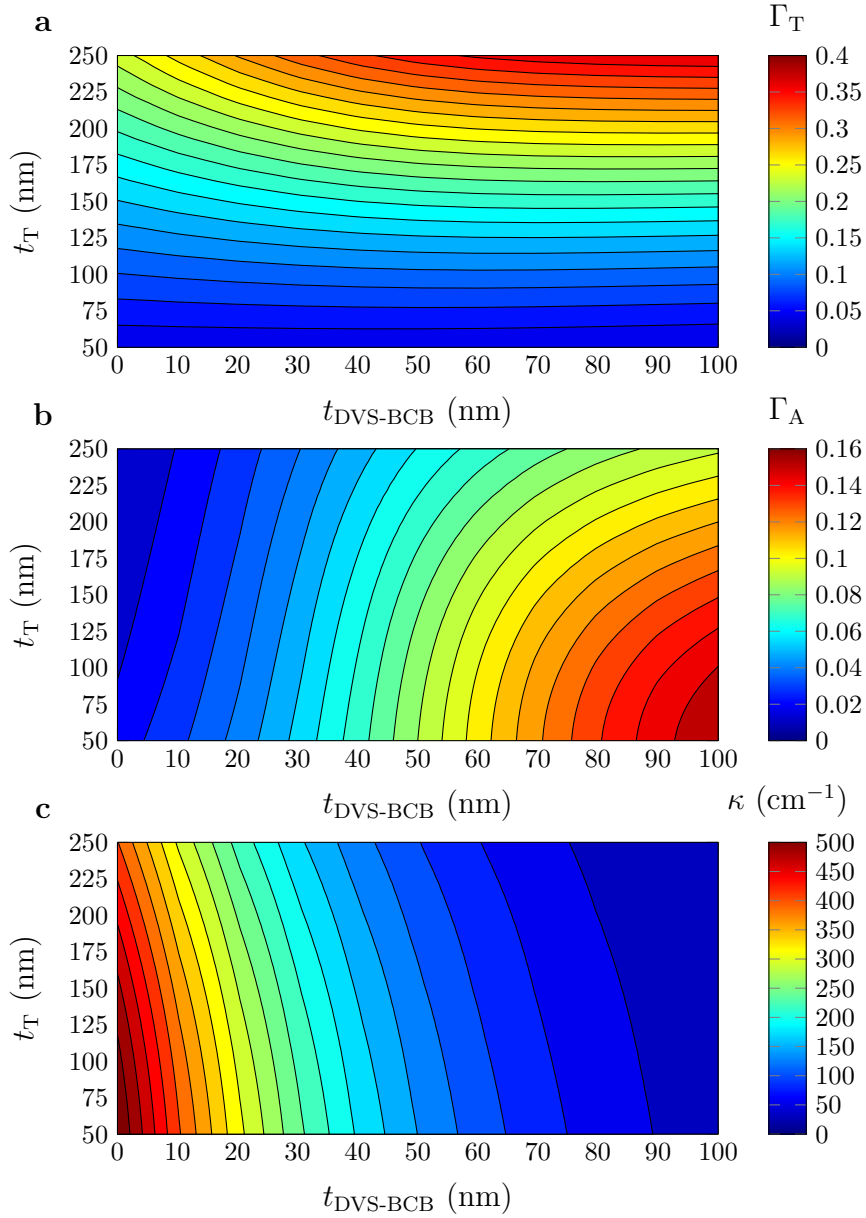


**Figure 4.3:** Optimization of the TTG-DFB laser design. Influence of the tuning layer thickness  $t_T$  and DVS-BCB thickness  $t_{\text{DVS-BCB}}$  on (a) the confinement factor in the tuning layer  $\Gamma_T$ ; (b) the confinement factor in the active layer  $\Gamma_A$ ; (c) the grating coupling coefficient  $\kappa$ .

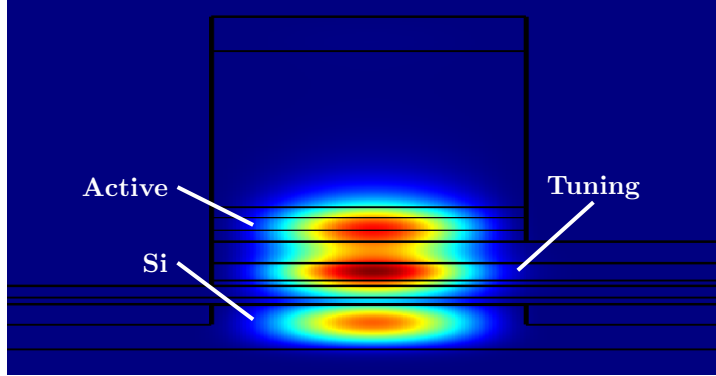


**Figure 4.4:** Simulated optical mode profile for the chosen TTG-DFB laser design (at 1550 nm, TE polarization). The mode is nicely distributed over the active, tuning and silicon waveguide layer, with very strong confinement in the tuning layer ( $\Gamma_T = 23.7\%$ ).

different layers of interest and is shown in Fig. 4.4 for the particular design.

### Bragg grating

A first-order Bragg grating is chosen for the DFB laser. The  $\lambda/4$  phase shift in the middle of the structure breaks the modal degeneracy and ensures single-mode laser operation. The grating period  $\Lambda$  is 240 nm, which corresponds to a Bragg wavelength of 1570 nm ( $n_{\text{eff}} \approx 3.27$ ). As was already clear from Fig. 4.3(c),  $t_{\text{DVS-BCB}}$  has a strong influence on the grating coupling coefficient  $\kappa$ . Figure 4.5(a) shows its influence on  $\kappa$ , specifically for the chosen design. Commonly in DFB lasers the  $\kappa \cdot L$  product (with  $L$  the grating length) is taken as figure of merit to assess and predict several laser characteristics. Typically  $1 < \kappa \cdot L < 3$  is taken as design target. Lower  $\kappa \cdot L$  values makes it hard for the device to exhibit laser operation whereas higher  $\kappa \cdot L$  values can lead to overcoupling and spatial-hole burning effects [10]. Nevertheless have very high  $\kappa \cdot L$  values been reported in several successful III-V-on-silicon laser device demonstrations [11]. This is because a large  $\kappa$  results in a low threshold current  $I_{\text{th}}$ , which can enable a large direct modulation bandwidth. This follows from [10]:

$$2\pi f_r = \sqrt{\frac{\Gamma_A v_g dg/dN}{qV_A}} (I - I_{\text{th}}), \quad (4.10)$$

where  $f_r$  is the relaxation oscillation frequency,  $v_g$  is the group velocity of the laser mode,  $\Gamma_A dg/dN$  is the differential modal gain,  $q$  the elementary electron charge and  $V_A$  the active volume. Lowering the  $\kappa \cdot L$  product through a

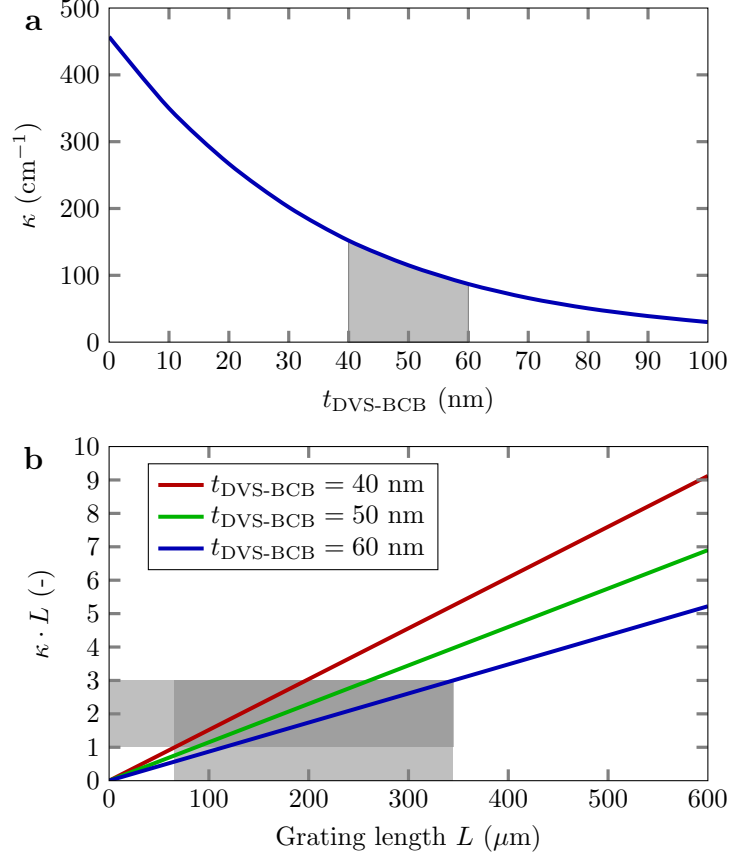


**Figure 4.5:** Bragg grating design. (a) Influence of  $t_{\text{DVS-BCB}}$  on  $\kappa$  for the chosen epitaxial layer stack ( $t_{\text{T}} = 190$  nm); (b)  $\kappa \cdot L$  versus  $L$ . Typically  $1 < \kappa \cdot L < 3$  is taken as rule-of-thumb in the design of DFB lasers.

decrease in the grating length is also not always desired, as it increases the thermal resistance. For our laser design a  $\kappa \cdot L \approx 3$  is targeted, with rather a slightly larger than slightly lower value. All considerations taken into account, a total Bragg grating length of at least  $300 \mu\text{m}$  seems desirable (see Fig. 4.5(b)). This choice also tackles the uncertainty on  $t_{\text{DVS-BCB}}$ . In any case a sweep with different grating lengths is carried out in each fabrication run.

### Electrical considerations

In the TTG-DFB laser, the laser wavelength is tuned through carrier injection into the tuning layer. As the structure is asymmetric, it is not

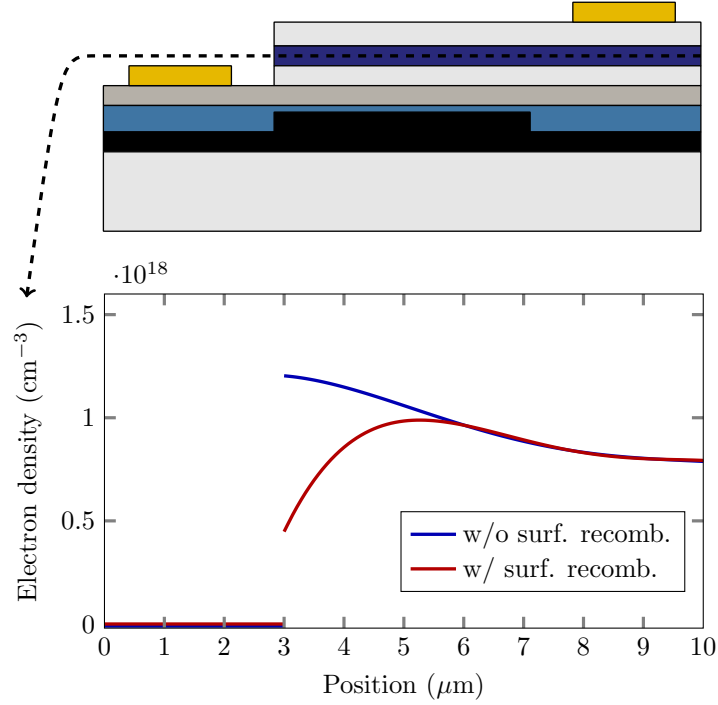


**Figure 4.6:** TCAD simulation of the electron density profile upon carrier injection into the tuning layer.

necessarily guaranteed that the carrier density will be large where the optical mode resides. In order to get a better understanding of the electrical properties, the structure is simulated through Atlas Technology Computer-Aided Design (TCAD) software from Silvaco [12]. Note that no complete time-consuming simulation is aspired here, but rather a qualitative and semi-quantitative approach is taken.

The Atlas software contains many standard models to describe the electrical behavior and solves Poisson's equation, the continuity equations and the drift and diffusion equations (2.17) and (2.19). Poisson's equation is given by [13]:

$$\nabla \cdot (\epsilon \nabla \psi) = -\rho \quad (4.11)$$

and relates the electrostatic potential  $\psi$  to the space charge density  $\rho$ .  $\epsilon$  is the dielectric permittivity. The continuity equations are given by [13]:

$$\frac{\partial N}{\partial t} = \frac{1}{q} \nabla \cdot \mathbf{J}_n + G_n - R_n \quad (4.12)$$

$$\frac{\partial P}{\partial t} = \frac{1}{q} \nabla \cdot \mathbf{J}_p + G_p - R_p \quad (4.13)$$

These equations in essence express that the local change in carrier density equals the sum of the change in current flow and the local generation or recombination of carriers. As the tuning layer is terminated closely where the optical mode resides, the structure is simulated for the case when surface recombination is zero and for the case when surface recombination is present. The simulated electron density profile along the lateral position in the tuning layer is shown in Fig. 4.6. The profile indicates a pile-up of carriers towards the left hand side of the laser mesa. Since the waveguide mode is mainly concentrated centrally under the mesa, this leads to a misalignment between waveguide mode and the carrier concentration in the tuning layer and, hence, to a reduced tuning efficiency. When surface recombination is taken into account, the profile has a maximum that is already closer to the center of the waveguide mode. However, this highly depends on the value of the surface recombination velocity, which is generally not large in InP and InGaAsP ( $v_s \leq 10^4$  cm/s [14]). The pile up of carriers on the left hand side of the structure is intuitively understood by considering that the path of least resistance between the ground and tuning electrode is the path with the smallest fraction in the less conductive  $p$ -type layers (the mobility of electrons is larger than the mobility of holes). Using an  $n$ - $p$ - $n$  structure instead of a  $p$ - $n$ - $p$  structure is no solution. The lossy  $p$ -type contact layer would then have maximum overlap with the waveguide mode and the carriers would pile up near the right hand side of the structure, even further away from the optical mode.

### Coupling structure

In order to efficiently couple light from the InP waveguide to the underlying silicon waveguide, an adiabatic tapered coupler is used [15–17]. By varying the waveguide dimensions along the coupling structure, the effective indices of the fundamental local modes of the unperturbed waveguides (i.e. the InP and silicon waveguide) can be increased or decreased. In this way the optical mode is gradually coupled from one waveguide to another. At the intermediate phase-matching point the energy of the optical mode is equally distributed over both waveguides. If the spatial waveguide variations occur gradual enough, no light is coupled to higher-order modes and the tapering is said to be adiabatic. Inspired by the coupling structure used in fixed-wavelength InP-on-silicon DFB lasers [5], we propose a taper structure as shown in Fig. 4.7. The coupling structure consists of three parts. In the

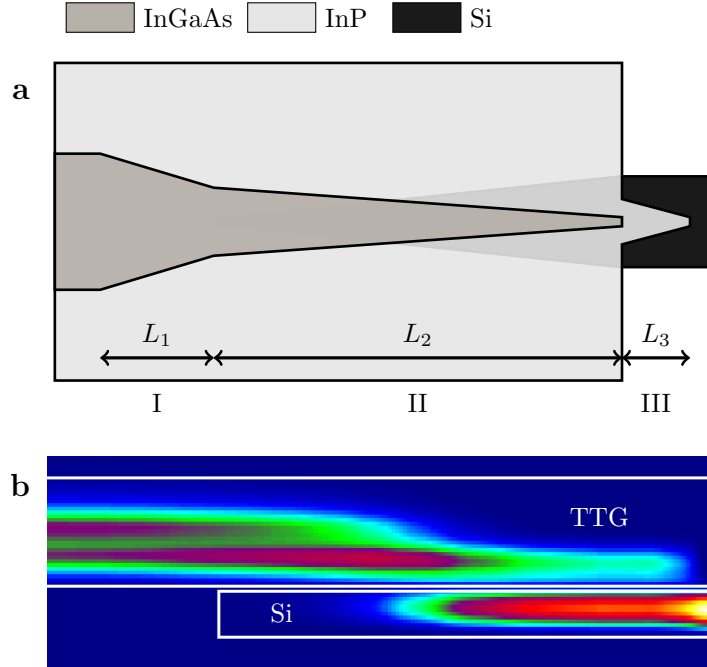


**Figure 4.7:** Adiabatic tapered coupler in the TTG-DFB laser design. (a) Schematic (top view); (b) Simulated intensity distribution for the optimized structure (side view).

first part (I), the InP waveguide is tapered down from  $3 \mu\text{m}$  to  $1.5 \mu\text{m}$  over a length  $L_1 = 50 \mu\text{m}$ . As the mode remains confined in the InP waveguide, the taper length can be rather short. In the second part (II) the InP waveguide is further tapered down, whereas the silicon waveguide is tapered up. Here the actual mode transition occurs, such that the adiabatic taper length will be longer than the first part ( $L_2 \gg L_1$ ). In the third part (III) the tuning waveguide is tapered down (over a short length  $L_3 = 20 \mu\text{m}$ ) to minimize reflections at the end of the coupling structure. Figure 4.8(a) shows the simulated coupling efficiency as a function of  $L_2$  for different InP taper tip widths. For  $L_2 > 110 \mu\text{m}$  the taper is adiabatic, with the coupling efficiency determined by the InP taper tip width. For a relatively wide InP taper tip of  $800 \text{ nm}$  some ripple is seen, which indicates non-perfect adiabaticity as the mode is partly moving up and down between the InP and silicon waveguide as a function of taper length. In order to account for some robustness with respect to misalignment during optical contact lithography,  $L_2 = 180 \mu\text{m}$  is chosen. The influence of the InP taper tip width on the coupling efficiency and power reflection for  $L_2 = 180 \mu\text{m}$  is shown in Fig. 4.8(b). The coupling efficiency stays above 75%, even for InP taper tips as wide as  $800 \text{ nm}$ .

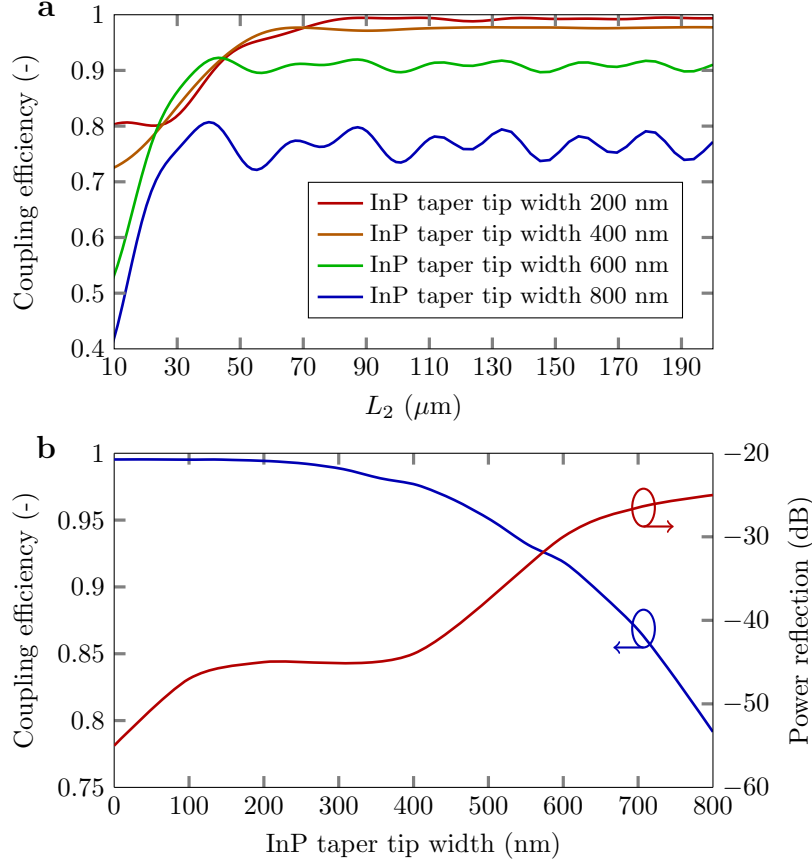


**Figure 4.8:** Adiabatic tapered coupler for the TTG-DFB laser structure. (a) Influence of  $L_2$  on the coupling efficiency; (b) Influence of the InP taper tip width on the coupling efficiency and power reflection for  $L_2 = 180 \mu\text{m}$ .

However and more importantly, in order to keep the power reflection below -30 dB, an InP taper tip width below 600 nm is needed. This is important to prevent gaps in the wavelength tuning curves [18].

### 4.2.3 Fabrication

The details of the fabrication process are extensively described in Chapter 3. E-beam lithography is chosen for the definition of the SOI waveguide structures. Figure 4.9(a) shows an SEM image of a set of fabricated TTG-DFB lasers with different Bragg grating lengths after the final metallization step. The metallization pads have a  $100 \mu\text{m}$  pitch in a ground-signal-ground (GSGSG) configuration. This is compatible with common

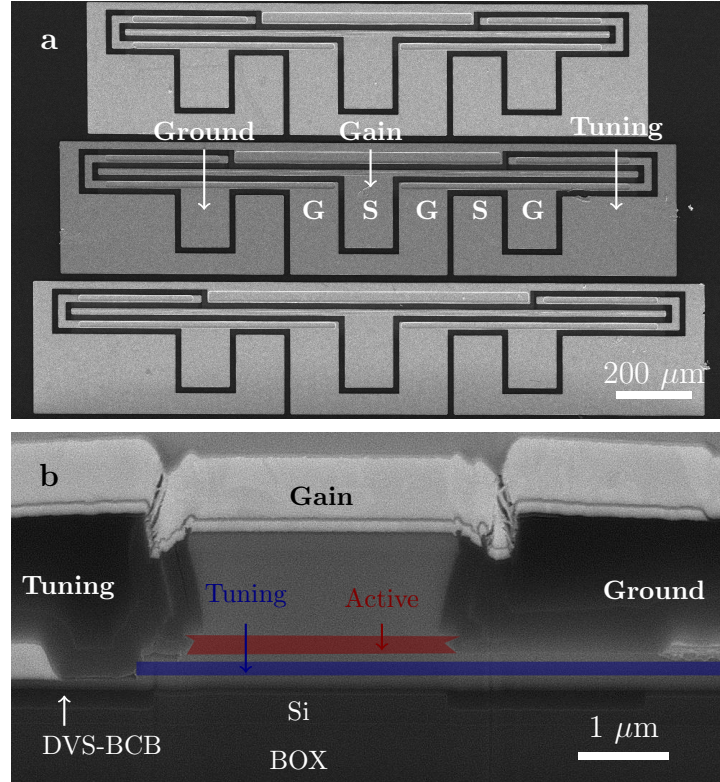


**Figure 4.9:** TTG-DFB laser fabrication. (a) SEM image of a set of fabricated devices with different Bragg grating lengths; (b) SEM/FIB image of the laser cross-section taken in the middle of the structure.

electrical high-speed probes and allows to carry out burst-mode experiments, where both the gain and tuning current are modulated at relatively high speed. An SEM/FIB image of the cross section in the middle of one of the lasers is shown in Fig. 4.9(b), with indication of the different metal contacts and the active and tuning layer. Fabrication is very well on target, with  $t_{\text{DVS-BCB}} \approx 40$  nm and a relatively small spacing between the tuning/ground contact and the laser mesa of 1 to 2  $\mu\text{m}$ .

#### 4.2.4 Static laser characteristics

The laser device is characterized on a temperature-controlled stage. A reflectionless SOI grating coupler [19] is used to couple the laser output to a single-mode optical fiber (SMF). An HP 8153A power meter is used to measure the optical output power. Two Keithley2400 current sources allow

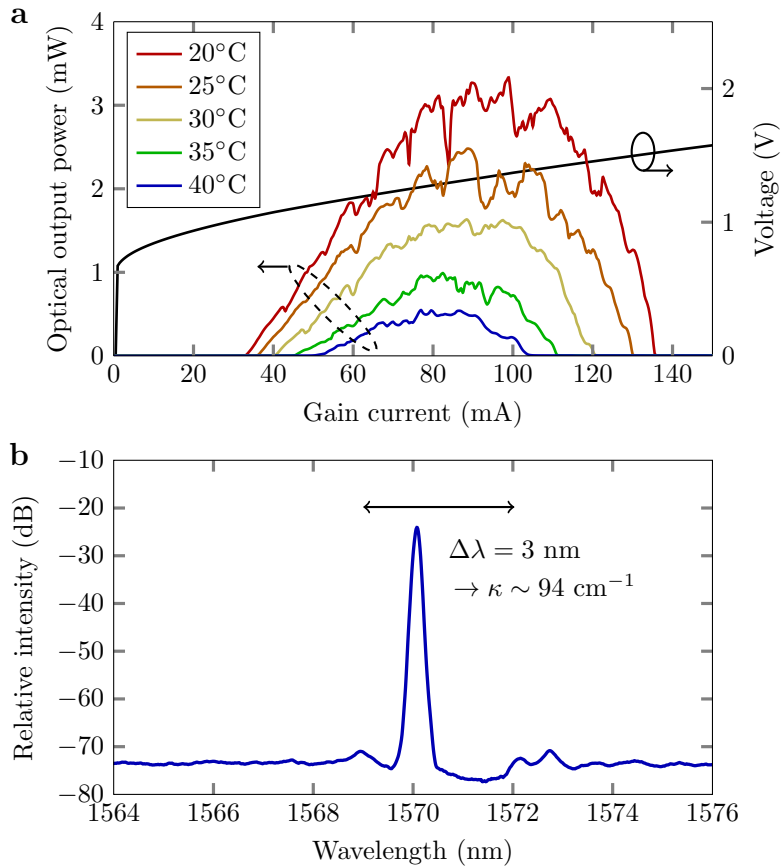


**Figure 4.10:** TTG-DFB laser characterization. (a) LIV characteristics (waveguide-coupled output power); (b) Laser spectrum at a gain current of 90 mA and zero tuning bias.

to control the gain and tuning current. Optical spectra are measured with an HP optical spectrum analyzer (OSA) at a resolution of 80 pm.

### LIV curves and laser spectrum

The light-current-voltage (LIV) characteristics at different temperatures for a device with a  $350 \mu\text{m}$  long Bragg grating are shown in Fig. 4.10(a). At  $20^\circ\text{C}$  the threshold current is 33 mA. The maximum fiber-coupled output power is 0.1 mW, which corresponds to a waveguide-coupled output power of about 3 mW, given the relatively large grating coupler loss ( $\sim 15 \text{ dB}$ ) at the laser wavelength. The laser spectrum at zero tuning bias is shown in Fig. 4.10(b). Single-mode laser operation is achieved with an SMSR of

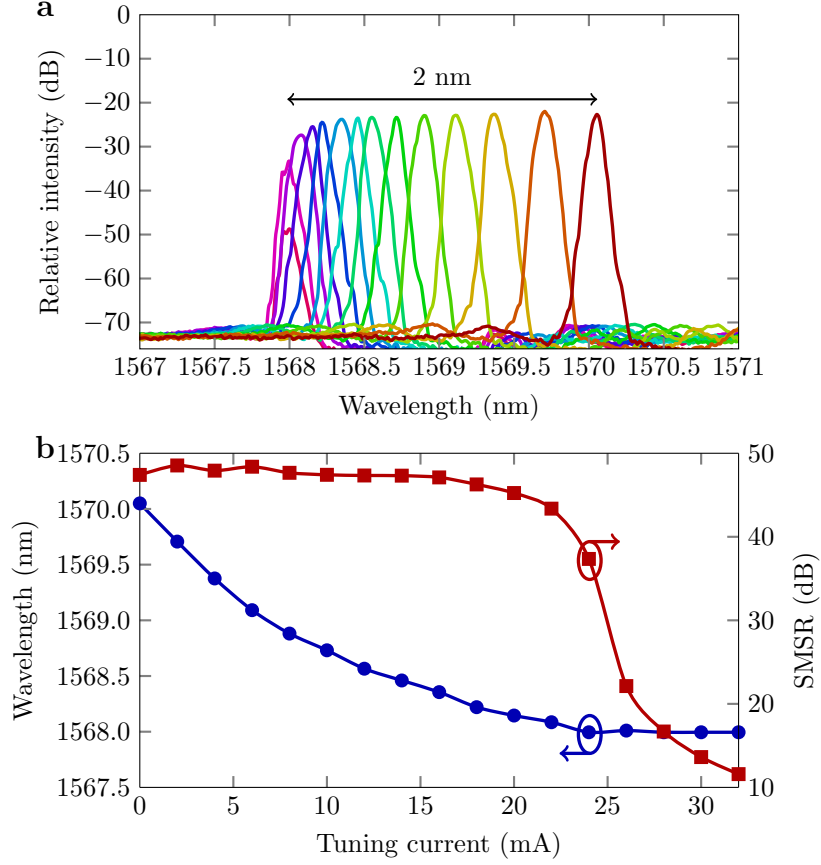


**Figure 4.11:** TTG-DFB laser tuning characteristics. (a) Superimposed laser spectra upon tuning at a gain current of 90 mA; (b) Wavelength and SMSR versus tuning current.

47 dB. From the width of the stopband, the grating coupling coefficient  $\kappa$  of the TTG-DFB laser can be estimated through:

$$\Delta\lambda = \frac{\lambda_B^2}{n_{\text{eff}}\pi L} \sqrt{(\kappa L)^2 + \pi^2}. \quad (4.14)$$

As  $\Delta\lambda = 3$  nm, a  $\kappa = 94$  cm<sup>-1</sup> is obtained. This is not large as compared to fixed-wavelength DFB lasers but corresponds rather well with the simulation results. Note that this yields  $\kappa L = 3.29$ .

### Tuning characteristics

Fig. 4.11(a) shows the superimposed laser spectra for different tuning currents at a fixed gain current of 90 mA. Continuous wavelength tuning is possible over a total tuning range of 2 nm. Single-mode laser operation is achieved, with an SMSR that remains larger than 44 dB across the tuning range (Fig. 4.11(b)). With native III-V TTG-DFB lasers, a much larger tuning range of about 8 nm was demonstrated [20]. The reason for the large discrepancy is twofold: firstly, the thermal resistance of heterogeneously integrated lasers is larger than the thermal resistance of native III-V devices. This is mainly due to the presence of the BOX layer and the DVS-BCB overcladding that is used. Secondly, the asymmetric geometry of the TTG structure can lead to a misalignment of the carrier density profile and the optical mode (as discussed before) but also results in significant lateral carrier diffusion, away from the optical mode.

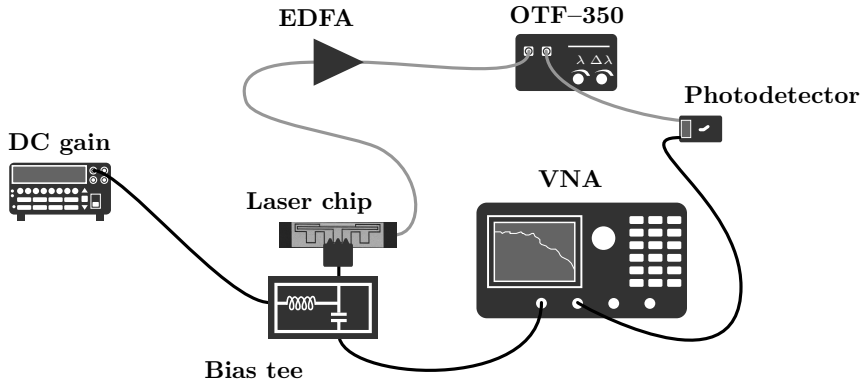
### 4.2.5 Dynamic laser characteristics

The dynamic laser characteristics show how well the laser device behaves under dynamic, (relatively) high-speed modulation of the gain and tuning current. They can typically be subdivided in small-signal and large-signal modulation characteristics. Under small-signal modulation, the laser current is fixed at a certain direct current (DC) bias, on which a low-amplitude alternating current (AC) is superimposed. Afterwards the transfer function response is measured at different modulation frequencies. In large-signal modulation, the gain or tuning current is modulated with a large-amplitude rectangular pulse train. The measurement generally mimics the application of the laser in real-life systems.

#### Small-signal modulation of the gain current

The measurement setup to characterize the small-signal modulation characteristics of the laser is shown in Fig. 4.12 (upper part). A small-amplitude radio frequency (RF) signal from a Keysight PNA-X N5247A Vector Network Analyzer (VNA) is combined with a DC gain current bias using a bias tee. With a 100  $\mu\text{m}$  pitch high-speed ground-signal-ground (GSG) electrical probe the combined signal is connected to the gain contact of the laser. The output from the laser is amplified with an Erbium-Doped Fiber Amplifier (EDFA) and sent through a Santec OTF-350 tunable bandpass filter to filter out amplified noise. The response is detected with a 40 GHz Discovery Semiconductors *p-i-n* photodiode, of which the output is connected to the network analyzer. The small-signal response is shown in Fig. 4.13. The 3 dB bandwidth at 70 mA and 90 mA DC bias is 6 GHz and 7 GHz, respectively. Such bandwidth should in principle allow for direct modulation above 10 Gbit/s.

### Small-signal modulation – gain current



### Large-signal modulation – gain current

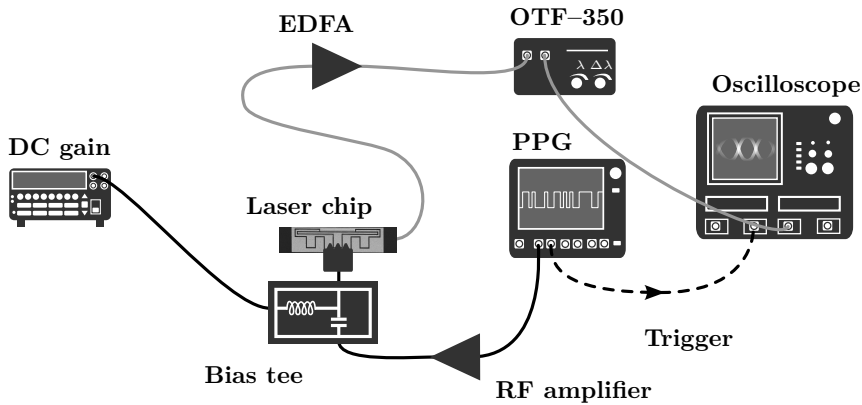


**Figure 4.12:** Measurement setup to characterize the small- and large-signal modulation response of the TTG-DFB laser.

### Large-signal modulation of the gain current

For the large-signal modulation characterization of the laser, the measurement setup in Fig. 4.12 (bottom part) is used. An electrical non-return-to-zero on-off-keying (NRZ-OOK) pseudorandom binary stream (PRBS) is generated by means of an Anritsu MP2100A pulse-pattern generator (PPG) at different bitrates. The maximum available 0.8 V<sub>pp</sub> RF voltage swing is amplified by a tunable electrical RF amplifier to allow for larger voltage swings. The DC gain current is kept fixed at 90 mA. Eye diagrams are measured by means of a Tektronix DSA 8300 sampling oscilloscope with built-in receiver. Open eye diagrams are obtained up to 12.5 Gbit/s, al-

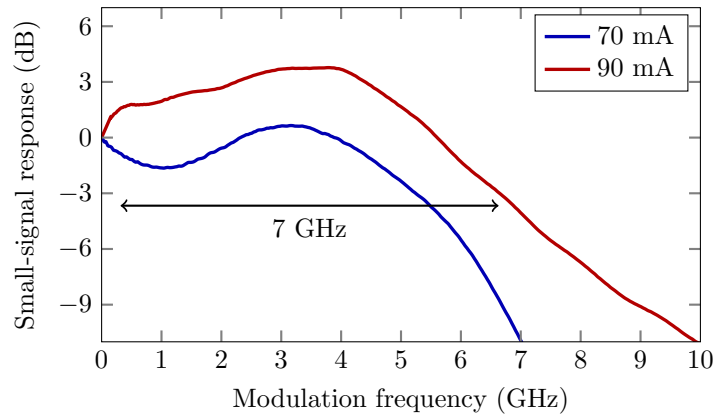


**Figure 4.13:** Small-signal modulation response of the TTG-DFB laser at 70 mA and 90 mA DC gain current and zero tuning bias (curves have been smoothed).

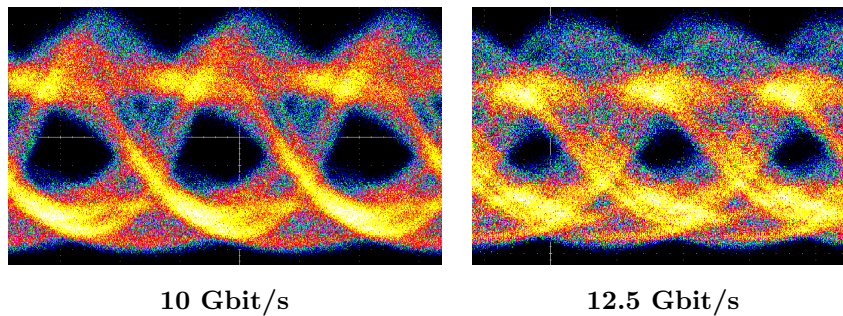


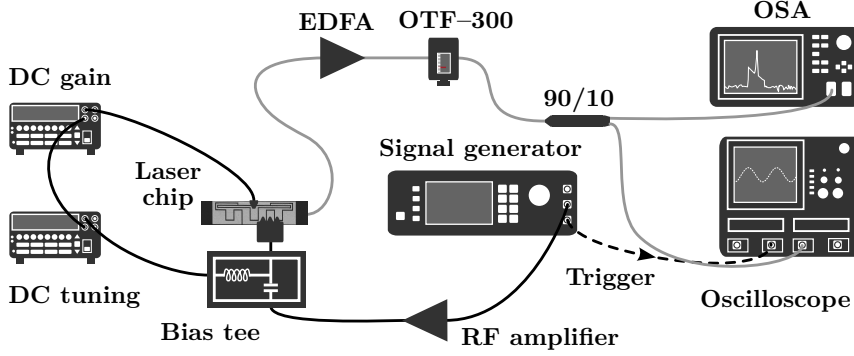
**Figure 4.14:** Large-signal modulation response of the TTG-DFB laser at 90 mA DC gain current and zero tuning bias under 10 Gbit/s and 12.5 Gbit/s NRZ-OOK direct modulation of the gain current.

though operation seems to be at the edge of the device bandwidth. The eye diagrams at 10 Gbit/s and 12.5 Gbit/s are shown in Fig. 4.14.

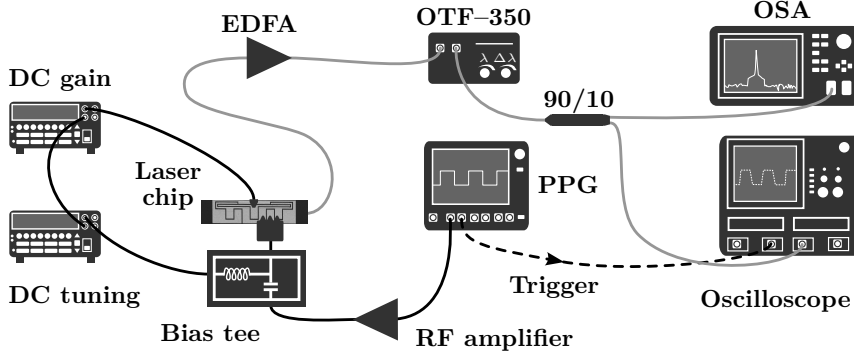
#### Small-signal modulation of the tuning current

Figure 4.15 (upper part) shows the measurement setup to characterize the small-signal wavelength modulation behavior of the laser. The tuning current is modulated with a sinusoidal voltage at small amplitude (50 mV) and at different modulation frequencies. The DC tuning current is fixed at 2 mA and the laser peak is positioned at the edge of the transmission response of a Santec OTF-300 filter with a transmission slope of 16.67 dB/nm. From the OTF characteristic, the IV tuning curve and the detected mod-

### Small-signal modulation – tuning current



### Large-signal modulation – tuning current



**Figure 4.15:** Measurement setup to characterize the small- and large-signal wavelength modulation response of the TTG-DFB laser.

ulation response, the tuning efficiency can be calculated (nm/mA). The measured characteristic is shown in Fig. 4.16(a). For low modulation frequencies the tuning efficiency is 0.13 nm/mA. The obtained 3 dB bandwidth is 125 MHz. In good approximation the relationship between the system bandwidth (BW) and the rise time (RT) is given by [21]:

$$\text{BW}(\text{GHz}) = \frac{0.35}{\text{RT}(\text{ns})}. \quad (4.15)$$

From the obtained BW we hence find an estimated RT of 2.8 ns.

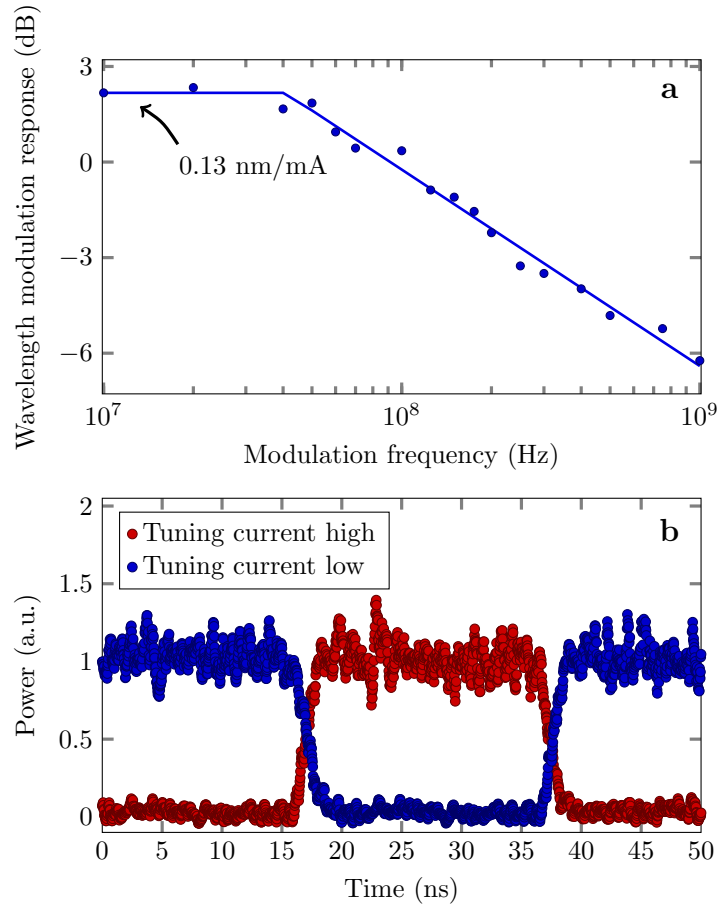


**Figure 4.16:** Wavelength switching characteristics of the TTG-DFB laser. (a) Small-signal wavelength modulation response; (b) Large-signal time-domain characteristic upon switching.

### Large-signal modulation of the tuning current

In order to get a confirmation of the exact wavelength switching time, an Anritsu PPG is now used to modulate the tuning current at large amplitude. The characterization setup is shown in Fig. 4.15 (bottom part). The light output from the laser device is initially amplified by an EDFA and sent through a Santec OTF-350 tunable bandpass filter, such that the laser peak periodically falls within and outside of the filter passband. A 90/10 splitter is used to couple 90% and 10% of the light to a Tektronix DSA 8300 sampling oscilloscope with built-in receiver and an Anritsu MS9740A OSA, respectively. The OSA monitoring allows to appropriately tune the center

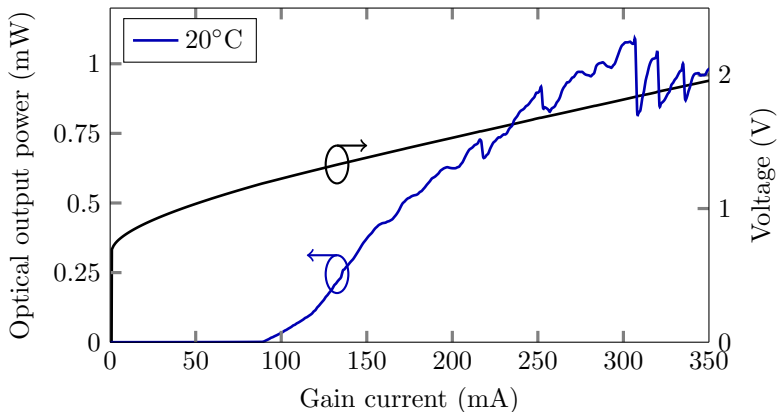


**Figure 4.17:** SG-TTG-DFB laser characterization. LIV characteristics (waveguide-coupled output power).

wavelength and bandwidth of the filter whereas the time-dependent power levels are monitored with the oscilloscope. A 20 ns periodic rectangular 0.9 V ( $\sim 0$  mA) – 1.5 V ( $\sim 20$  mA) pulse train is used. The wavelength switching characteristics are shown in Fig. 4.16(b). The rise and fall time are about 3 ns. This matches very well with the estimated value from the small-signal wavelength modulation response and is within the targeted wavelength tuning speed for the laser to find application in optical packet switching systems.

### 4.3 Sampled grating (SG-) TTG-DFB laser

The use of a uniform Bragg grating inherently limits the wavelength tuning range. By making use of two sampled gratings with different sampling periods the Vernier effect can be exploited to extend the tuning range, as explained in Chapter 2. A set of sampled grating (SG-) TTG-DFB lasers is fabricated on the same chip as the TTG-DFB lasers with uniform gratings. As the expected continuous tuning range is not large, a design is chosen with sampled gratings that exhibit a merely 2.5 nm and 3 nm peak spacing.

#### 4.3.1 Characterization

##### LIV curves

The LIV characteristics are shown in Fig. 4.17 at a heatsink temperature of 20°C. The laser threshold is 93 mA. A maximum waveguide-coupled output power of 1 mW is obtained. The ripple for gain currents above 300 mA is attributed to mode hopping.

### Tuning characteristics

Laser spectra for different tuning current in the front and back reflector ( $I_{T1}$  and  $I_{T2}$ , respectively) at a fixed DC gain current of 300 mA are shown in Fig. 4.18. The overall tuning range is around 8 nm and the SMSR remains within 30 and 40 dB. The tuning range is relatively low and may be related to the low grating coupling coefficient. It is also noted that not all wavelengths within the the tuning range are addressable and optimization is needed to extend the tuning range and to demonstrate quasi-continuous tuning.

## 4.4 SG-DFB laser

From the previous section, it is clear that the use of a TTG epitaxial layer stack in SG-based laser structures is far from trivial as the grating coupling coefficient is relatively low and the experimentally demonstrated tuning range rather limited. Also with the standard amplifier epitaxial layer stack from Table 2.1 a SG-DFB laser can be created, albeit with less independent control of power and wavelength. A wider tuning range can much more easily be achieved though. Such a laser structure is considered here.

### 4.4.1 Design aspects

The 3D layout of the SG-DFB laser structure is schematically shown in Fig 4.19. The structure consists of an InP/InGaAsP gain region that is integrated on top of an SOI waveguide circuit by means of adhesive DVS-BCB bonding. In this case the SOI waveguide structures are fabricated in a CMOS pilot-line at *imec*. Once more, the silicon device layer thickness is 400 nm with an etch depth of 180 nm. The sampled gratings in the silicon device layer have a slightly different sampling period ( $\Lambda_{S1}$  and  $\Lambda_{S2}$ ) in order to exhibit a comb-like reflection spectrum with slightly different periodicity. In this design  $\Lambda_{S1}$  and  $\Lambda_{S2}$  are chosen as 72  $\mu\text{m}$  (10 sampling periods) and 80  $\mu\text{m}$  (9 sampling periods), respectively. The total cavity length is 1440  $\mu\text{m}$ . The second order gratings are 3.5  $\mu\text{m}$  wide and have a period of 480 nm with a duty cycle of 75%, which corresponds to a Bragg wavelength of 1565 nm ( $n_{\text{eff}} \approx 3.26$ ). Second order gratings are used as they have been proven superior to the first order gratings in this particular *imec* fabrication run. Both sampled gratings have a sampling duty cycle  $D_{\text{SG}}$  of 10%, which ensures a sufficiently flat envelope of the reflection spectrum. This is needed to obtain a high side mode suppression across the entire tuning range.

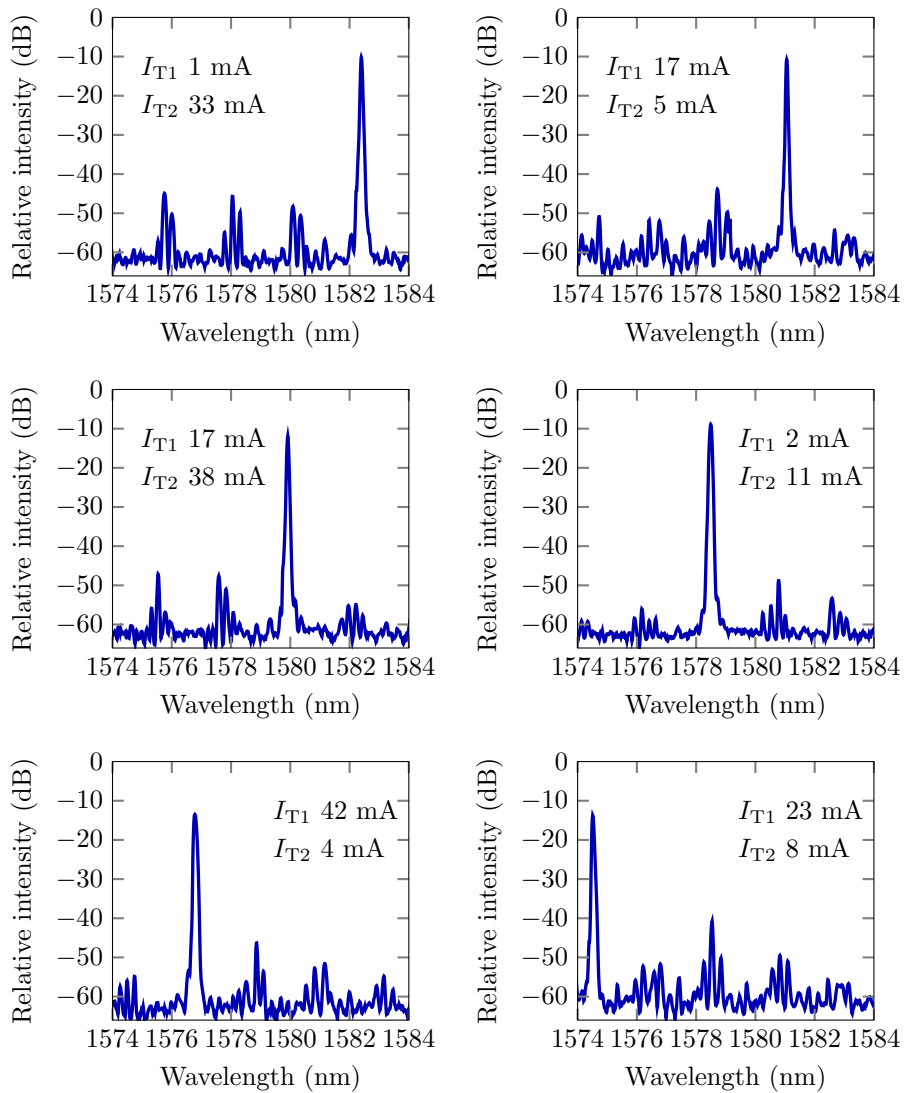


**Figure 4.18:** SG-TTG-DFB laser spectra at a fixed DC gain current of 300 mA.

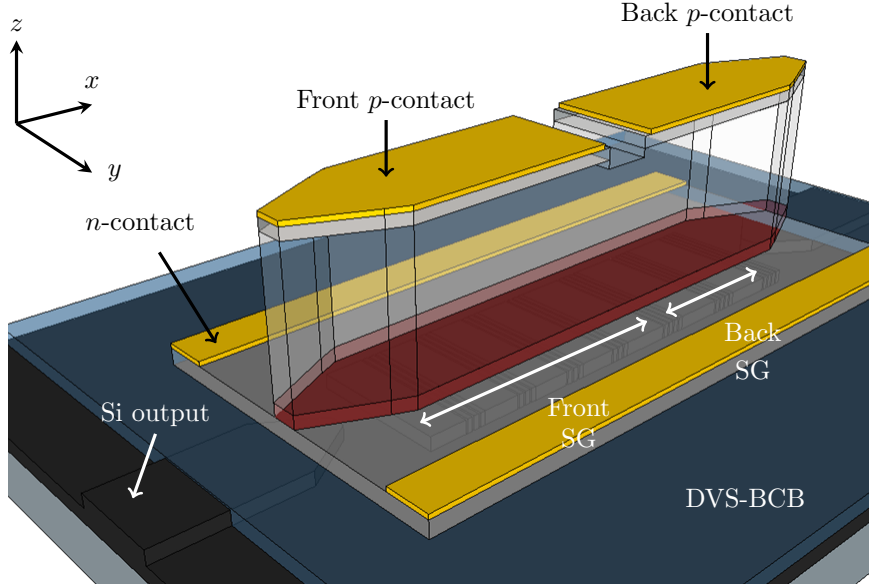


**Figure 4.19:** 3D layout of the SG-DFB laser. The front and back SG have a slightly different periodicity to exploit the Vernier effect for wide wavelength tuning.

### Sampled gratings

Figure 4.20 shows the superimposed simulated reflection spectra for both sampled gratings of the SG-DFB laser. The simulations are based on the TMM [7] and optical mode calculations with Fimmwave. The front grating reflector has a designed free spectral range ( $\text{FSR}_{\text{front}}$ ) of 5 nm. For the back grating reflector the designed free spectral range ( $\text{FSR}_{\text{back}}$ ) is 4.5 nm. The small difference in FSR of 0.5 nm creates a Vernier effect and allows for wide wavelength tuning. The limitation on the tuning range is set by the repeat mode spacing ( $\text{FSR}_{\text{repeat}}$ ) and can be estimated from [22]

$$\text{FSR}_{\text{repeat}} = \frac{\text{FSR}_{\text{front}} \cdot \text{FSR}_{\text{back}}}{|\text{FSR}_{\text{front}} - \text{FSR}_{\text{back}}|} = 45 \text{ nm}. \quad (4.16)$$

In order to achieve quasi-continuous tuning with full wavelength coverage, the change in effective index upon carrier injection should be large enough to directly tune over at least the mode spacing of a single reflector, i.e. over  $\text{FSR}_{\text{back}} = 4.5 \text{ nm}$ .

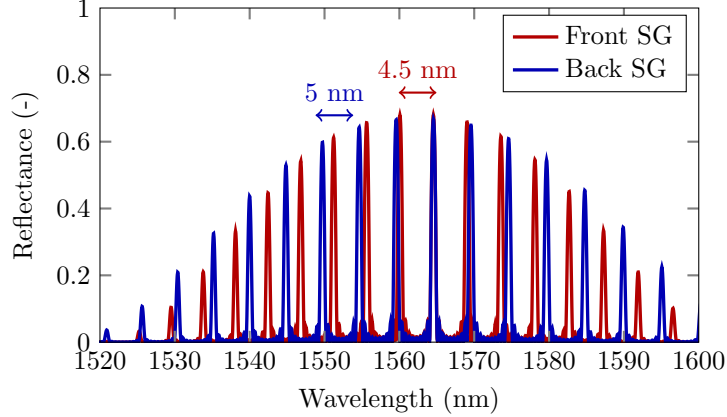


**Figure 4.20:** Superimposed simulated reflection spectra for the two sampled gratings of the SG-DFB laser.

### Coupling structure

In order to efficiently couple the light from the InP region to the silicon output waveguides a double adiabatic tapered coupler, as described in [16], is used. The total InP taper length is  $200 \mu\text{m}$  and consists of two parts. In the first part the InP waveguide is tapered down from  $3 \mu\text{m}$  to  $1 \mu\text{m}$  whereas the second part tapers from  $1 \mu\text{m}$  to a taper tip of  $600 \text{ nm}$ . The underlying silicon rib waveguide tapers from  $300 \text{ nm}$  to  $2 \mu\text{m}$  over a length of  $150 \mu\text{m}$ .

### 4.4.2 Fabrication

The fabrication of the SG-DFB laser is more straightforward than for TTG-based lasers and similar to the fabrication process of a standard InP-on-silicon DFB laser. Therefore details are not repeated here, but we refer to [5, 23] for more details. The  $p$ -contact consists of two individual contacts that allow close to independent current injection in the two SG sections. Figures 4.21(a) and 4.21(b) show a transverse, respectively, longitudinal cross-sectional SEM/FIB image of the fabricated SG-DFB laser device, captured in the center of the laser cavity. The laser mesa has a V-groove shape, which is realised through wet etching of the  $p$ -InP cladding layer. This increases the optical confinement factor in the MQWs (12% confinement factor in the 6 quantum wells) and realizes narrow taper tips. The total DVS-BCB bonding layer thickness is  $40 \text{ nm}$ , which gives rise to a relatively large effective grating coupling constant  $\kappa_{\text{eff}} = \kappa \cdot D_{\text{SG}}$  that (based on simulations with the measured laser structure dimensions) is estimated to be  $31.8 \text{ cm}^{-1}$ .

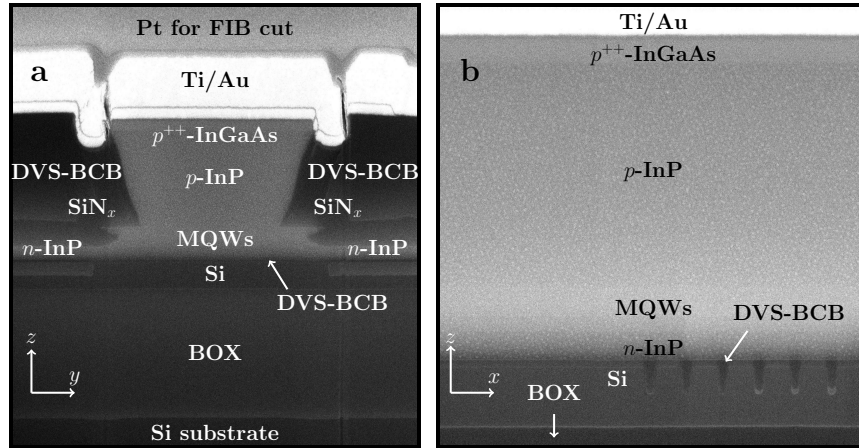


**Figure 4.21:** SEM/FIB image of the fabricated SG-DFB laser. (a) Transverse cross-sectional view; (b) Longitudinal cross-sectional view.

#### 4.4.3 Characterization

As already mentioned in Chapter 2, two counteracting effects come into play upon carrier injection. FCD (fast,  $\sim$  ns) induces a decrease in the refractive index due to an increase in the carrier density. As the carrier density is clamped above threshold only a limited change in carrier density can typically be achieved through current injection in the active layer. However, since the laser structure constitutes two sections, significant relative changes in the carrier density are possible through appropriate current variation in a push-pull manner. Self-heating (slow,  $\sim$  ms) on the other hand increases the refractive index. The presence of the BOX layer in heterogeneously integrated III-V-on-silicon devices prevents efficient heat sinking and leads to devices with large thermal resistance. Based on thermal simulations with COMSOL the thermal resistance of the SG-DFB laser can be estimated to be 124 K/W.

#### LIV curves

Characterization of the laser device is done at a heatsink temperature of  $10^\circ\text{C}$ . Through a standard fiber-to-chip SOI grating coupler light is coupled from the laser to a SMF. The measured fiber-to-chip coupling loss is 9 dB at 1550 nm and decreases monotonically, with a coupling loss of 18 dB at 1600 nm. Using a current source and three electrical DC probes the front ( $I_{\text{front}}$ ) and back ( $I_{\text{back}}$ ) SG sections of the laser are independently biased. The series resistance of both laser sections ( $dV/dI_{\text{front}}$  and  $dV/dI_{\text{back}}$ ) is

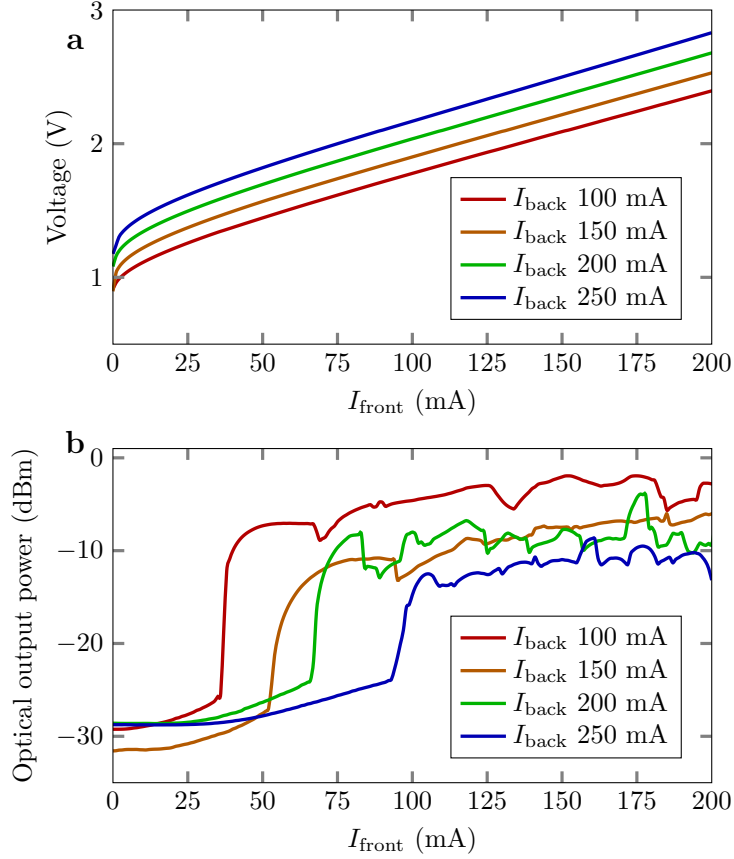


**Figure 4.22:** LIV characteristics of the SG-DFB laser. (a) IV curves; (b) LI curves (fiber-coupled output power).

$6 \Omega$ . The resistance between the two  $p$ -contacts is  $250 \Omega$ , which is not very high and which can be attributed to the non-ideal isolation through FIB. The LIV characteristics of the SG-DFB laser are shown in Fig. 4.22. Thereby  $I_{\text{front}}$  is swept while  $I_{\text{back}}$  is kept constant. At  $(I_{\text{front}}, I_{\text{back}}) = (175 \text{ mA}, 100 \text{ mA})$  the fiber-coupled output power is  $-1.94 \text{ dBm}$ . The threshold current increases with increasing  $I_{\text{back}}$  because of heating and deteriorated overlap of the reflection peaks of both reflectors upon current injection. For uniform pumping ( $I_{\text{front}} = I_{\text{back}}$ ) the total threshold current is  $90 \text{ mA}$ . The ripples in the LI characteristics are attributed to mode hopping.

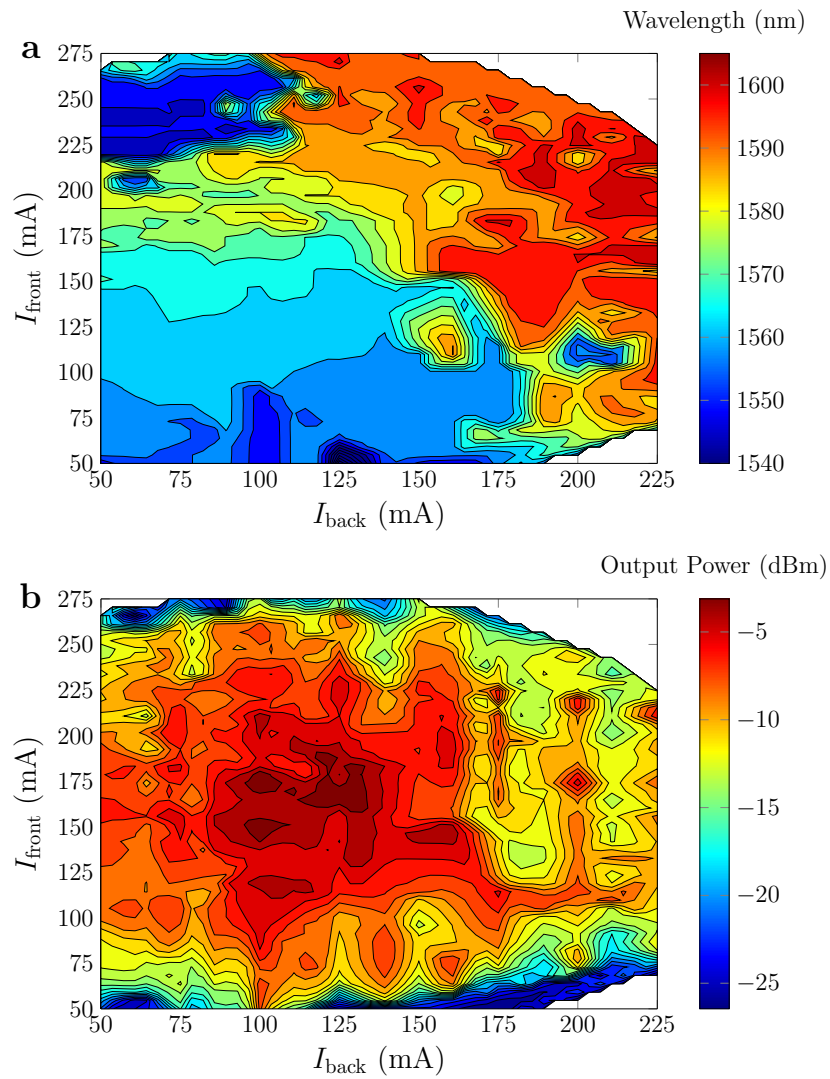


**Figure 4.23:** Tuning characteristics of the SG-DFB laser. (a) Laser wavelength versus  $I_{\text{front}}$  and  $I_{\text{back}}$ ; (b) Fiber-coupled output power versus  $I_{\text{front}}$  and  $I_{\text{back}}$ .

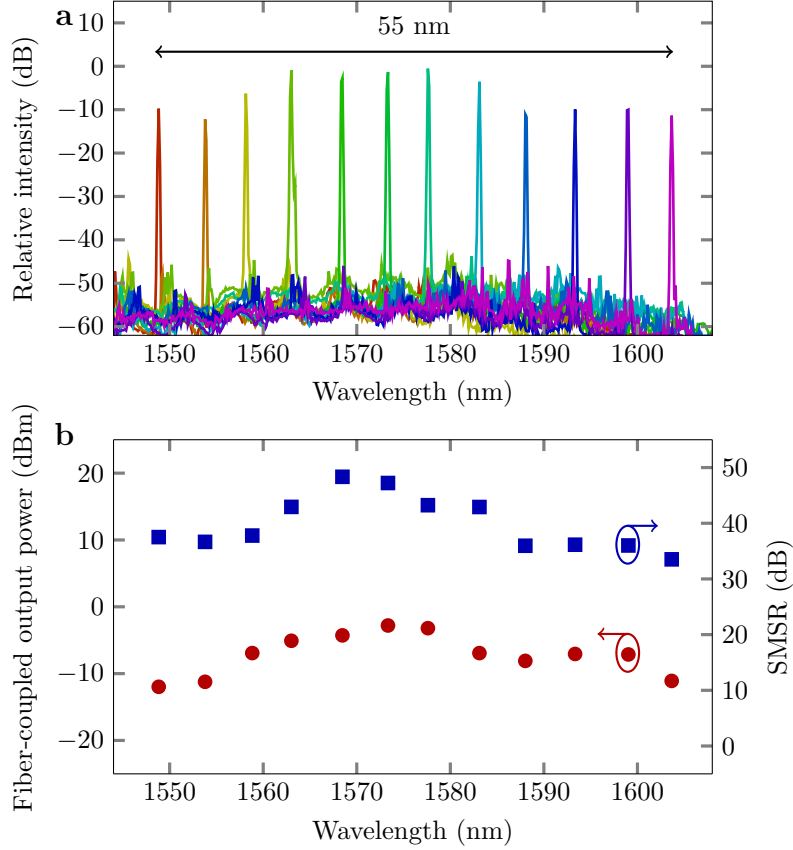


**Figure 4.24:** (a) Superimposed laser spectra; (b) Fiber-coupled output power and SMSR at the different wavelength channels.

### Tuning characteristics

Figures 4.23(a) and 4.23(b) show the laser wavelength and fiber-coupled output power versus  $I_{\text{front}}$  and  $I_{\text{back}}$ . Generally the laser wavelength increases with total injection current  $I_{\text{tot}} = I_{\text{front}} + I_{\text{back}}$  due to a dominant heating effect. At a total injection current  $I_{\text{tot}} = 275$  mA the fiber-coupled output power reaches maximum values between  $-3$  dBm and  $-1.8$  dBm. Hence the maximum output power in the silicon waveguide can be estimated to be about 15 dBm. This yields a (single-sided) wall-plug efficiency of 4%. At larger injection currents the power drops again due to local heating. Figure 4.24(a) shows the superimposed laser spectra across the wavelength tuning range. Laser operation occurs from 1547 nm to 1603 nm, at a discrete number of wavelengths. The spacing between these wavelength channels is 5 nm and corresponds with the designed peak spacing, as dis-

**Table 4.1:** Injection current and laser wavelength for the channels shown in Fig. 4.24.

Channel	$I_{\text{front}}$ (mA)	$I_{\text{back}}$ (mA)	$I_{\text{tot}}$ (mA)	$\lambda$ (nm)
1	50	235	285	1548.83
2	90	265	355	1553.79
3	140	80	220	1558.14
4	100	135	235	1563.01
5	115	170	285	1568.47
6	125	185	310	1573.34
7	100	210	310	1577.60
8	150	220	370	1583.11
9	160	245	405	1588.02
10	180	115	295	1593.34
11	160	165	325	1599.03
12	225	160	385	1603.66

cussed in Section 4.4.1. Table 4.1 shows the injection current and lasing wavelength for the different channels shown in Fig. 4.24(a). Around each wavelength channel about 1.5 nm continuous tuning is possible. All channels operate in single-mode regime with an SMSR ranging from 33 dB to 48 dB. The fiber-coupled output power varies from  $-12$  dBm to  $-2.8$  dBm. This is illustrated in Fig. 4.24(b), which shows the fiber-coupled output power and SMSR for the different wavelength channels. The variation in the fiber-coupled output power is due to the variation of the total current for all wavelength channels and due to the influence of the grating coupler response. Also note that the overall wavelength tuning range of 55 nm is larger than the predicted 45 nm. This may be attributed to the limited bandwidth of the gain spectrum (that red shifts at high injection currents). In this way laser operation is most likely to occur near the gain peak, with good suppression of the repeat modes at shorter wavelengths.

## 4.5 Conclusion

In this chapter several heterogeneously integrated tunable DFB lasers have been discussed. With the TTG-DFB laser, the most important results have been achieved. Nanosecond fast wavelength switching, a tuning range of 2 nm and direct modulation up to 12.5 Gbit/s is readily demonstrated. The SG-TTG-DFB laser shows a promising path to reach wide tunability but has to be improved further to reach this goal. Optimization of design, fabrication and epitaxial layer growth is therefore essential. Finally an alternative SG-DFB laser has been discussed as well. This laser is tunable over a wide wavelength range of 55 nm in discrete steps of 5 nm and has the

advantage a standard amplifier epitaxial layer stack can be used. Due to the limited achievable change in carrier density upon current injection and the large thermal impedance of the device, however, no quasi-continuous nor fast tuning could be obtained.

## References

- [1] S. Dhoore, L. Li, A. Abbasi, G. Roelkens, and G. Morthier, “Demonstration of a discretely tunable III-V-on-silicon sampled grating DFB laser,” *IEEE Photonics Technology Letters* **28**(21), 2343–2346 (2016).
- [2] S. Dhoore, A. Königer, R. Meyer, G. Roelkens, and G. Morthier, “Electronically tunable DFB laser on silicon,” in *International Semiconductor Laser Conference* (IEEE, 2018).
- [3] A. W. Fang, E. Lively, Y.-H. Kuo, D. Liang, and J. E. Bowers, “A distributed feedback silicon evanescent laser,” *Optics Express* **16**(7), 4413–4419 (2008).
- [4] C. Zhang, S. Srinivasan, Y. Tang, M. J. Heck, M. L. Davenport, and J. E. Bowers, “Low threshold and high speed short cavity distributed feedback hybrid silicon lasers,” *Optics Express* **22**(9), 10,202–10,209 (2014).
- [5] S. Keyvaninia, S. Verstuyft, L. V. Landschoot, F. Lelarge, G.-H. Duan, S. Messaoudene, J. M. Fedeli, T. D. Vries, B. Smalbrugge, E. J. Geluk, J. Bolk, M. Smit, G. Morthier, D. V. Thourhout, and G. Roelkens, “Heterogeneously integrated III-V/silicon distributed feedback lasers,” *Optics Letters* **38**(24), 5434–5437 (2013).
- [6] A. Abbasi, B. Moeneclaey, J. Verbist, X. Yin, J. Bauwelinck, G.-H. Duan, G. Roelkens, and G. Morthier, “Direct and electroabsorption modulation of a III-V-on-silicon DFB laser at 56 Gb/s,” *IEEE Journal of Selected Topics in Quantum Electronics* **23**(6), 1–7 (2017).
- [7] L. A. Coldren, S. W. Corzine, and M. L. Mashanovitch, *Diode lasers and photonic integrated circuits*, vol. 218 (John Wiley & Sons, 2012).
- [8] “Fimmwave: a powerful waveguide mode solver,” (2017). URL <https://www.photond.com/>.
- [9] “Lumerical MODE Solutions – comprehensive optical waveguide design environment,” (2017). URL <https://www.lumerical.com/tcad-products/mode/>.
- [10] G. Morthier and P. Vankwikelberge, *Handbook of distributed feedback laser diodes* (Artech House, 2013).
- [11] S. Matsuo and T. Kakitsuka, “Low-operating-energy directly modulated lasers for short-distance optical interconnects,” *Advances in Optics and Photonics* **10**(3), 567–643 (2018).
- [12] “Silvaco device simulation framework,” (2017). URL <https://www.silvaco.com/>.

- 
- [13] S. O. Kasap, *Principles of electronic materials and devices*, vol. 2 (McGraw-Hill New York, 2006).
- [14] D. Nolte, “Surface recombination, free-carrier saturation, and dangling bonds in InP and GaAs,” *Solid-State Electronics* **33**(2), 295–298 (1990).
- [15] X. Sun, H.-C. Liu, and A. Yariv, “Adiabaticity criterion and the shortest adiabatic mode transformer in a coupled-waveguide system,” *Optics Letters* **34**(3), 280–282 (2009).
- [16] M. Lamponi, S. Keyvaninia, C. Jany, F. Poingt, F. Lelarge, G. de Valicourt, G. Roelkens, D. V. Thourhout, S. Messaoudene, J.-M. Fedeli, and G. H. Duan, “Low-threshold heterogeneously integrated InP/SOI lasers with a double adiabatic taper coupler,” *IEEE Photonics Technology Letters* **24**(1), 76–78 (2012).
- [17] Q. Huang, J. Cheng, L. Liu, Y. Tang, and S. He, “Ultracompact tapered coupler for the Si/III–V heterogeneous integration,” *Applied Optics* **54**(14), 4327–4332 (2015).
- [18] R. Todt and M.-C. Amann, “Influence of facet reflections on monolithic widely tunable laser diodes,” *IEEE Photonics Technology Letters* **17**(12), 2520–2522 (2005).
- [19] D. Vermeulen, Y. De Koninck, Y. Li, E. Lambert, W. Bogaerts, R. Baets, and G. Roelkens, “Reflectionless grating couplers for Silicon-on-Insulator photonic integrated circuits,” *Optics Express* **20**(20), 22,278–22,283 (2012).
- [20] M.-C. Amann and W. Thulke, “Continuously tunable laser diodes: Longitudinal versus transverse tuning scheme,” *IEEE Journal on Selected Areas in Communications* **8**(6), 1169–1177 (1990).
- [21] L. R. Rabiner and B. Gold, “Theory and application of digital signal processing,” Englewood Cliffs, NJ, Prentice-Hall, Inc., 1975. 777 p. (1975).
- [22] S. Matsuo and T. Segawa, “Microring-resonator-based widely tunable lasers,” *IEEE Journal of Selected Topics in Quantum Electronics* **15**(3), 545–554 (2009).
- [23] G. Roelkens, A. Abassi, P. Cardile, U. Dave, A. de Groot, Y. de Koninck, S. Dhoore, X. Fu, A. Gassenq, N. Hattasan, Q. Huang, S. Kumari, S. Keyvaninia, B. Kuyken, L. Li, P. Mechet, M. Muneeb, D. Sanchez, H. Shao, T. Spuesens, A. Z. Subramanian, S. Uvin, M. Tassaert, K. van Gasse, J. Verbist, R. Wang, Z. Wang, J. Zhang, J. van Campenhout, X. Yin, J. Bauwelinck, G. Morthier, R. Baets, and D. van Thourhout,

“III-V-on-silicon photonic devices for optical communication and sensing,” *Photonics* **2**(3), 969–1004 (2015).



# 5

## Electronically tunable DBR lasers on silicon

**T**HIS chapter summarizes the work on electronically tunable DBR lasers on silicon and is based on [1] and [2]. In the first part, experimental results for a demonstrated tunable laser device with a nonoptimal TTG epitaxial layer stack are presented. The second part covers the general design and optimization of the TTG epitaxial layer to realize an electronically tunable DBR laser with large tuning efficiency.

### Contents

---

5.1	Introduction . . . . .	107
5.2	Thermally tunable TTG-DBR laser . . . . .	108
5.3	Electronically tunable TTG-DBR laser . . . . .	116
5.4	Conclusion . . . . .	118
	References . . . . .	120

---

### 5.1 Introduction

Conventional DFB lasers have attracted most interest among existing laser structures because of their ease of fabrication. To a large extent, this remains true for heterogeneously integrated lasers as no regrowth nor quantum well intermixing processes are needed. However, DBR laser types offer other important advantages such as ease of tuning and the suitability for separate

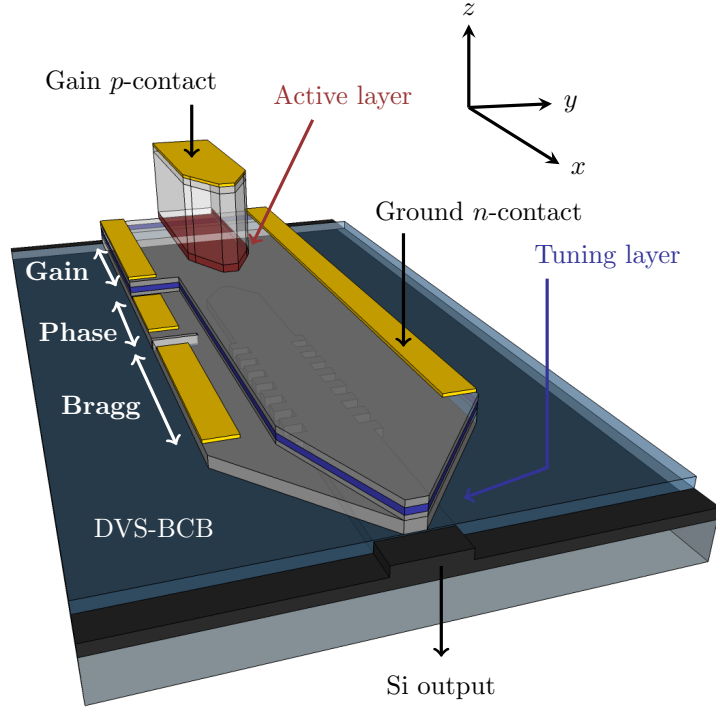


**Figure 5.1:** 3D schematic of the InP-on-silicon TTG-DBR laser structure.

optimization of each longitudinal laser section. In this chapter, a DBR laser structure based on the TTG epitaxial layer stack is discussed. In the first section, simulation and experimental results for an unoptimized stack with thin tuning layer ( $t_T = 100$  nm) are presented. In the second section simulations resulting in an optimized stack are presented. The realization of a TTG-DBR laser with the optimized stack can be part of the future work after this PhD project.

## 5.2 Thermally tunable TTG-DBR laser

### 5.2.1 Design aspects

#### Laser structure

A 3D schematic of the laser structure is shown in Fig. 5.1. The laser consists of a passive silicon waveguide circuit on which a TTG membrane is heterogeneously integrated. In this case  $t_C = 100$  nm and  $t_T = 100$  nm. The

laser cavity is formed by a broadband reflecting facet (reflectance  $\sim 30\%$ ) and a highly reflective DBR mirror (peak reflectance  $> 90\%$ ). The latter is implemented as a first-order sidewall-corrugated waveguide grating [3, 4] defined in the silicon device layer. The silicon waveguide structures are fabricated in a CMOS pilot-line at *imec* through deep UV lithography and have a 400 nm-thick silicon device layer with an etch depth of 180 nm. The DBR's weak sidewall-corrugation provides a narrowband spectral reflection characteristic to ensure single-mode laser operation. Ring resonator configurations do offer high spectral purity but do not easily allow for a large free spectral range (FSR) due to minimum bend radii requirements. They are therefore not considered as suitable option for incorporation in this laser structure. Three longitudinal sections can be discerned in the laser structure: a gain, a phase and a Bragg section. In the gain section current is injected into the active layer to provide optical gain. The tuning layer is left unbiased. In the phase and Bragg section the active layer is removed during fabrication and current is injected into the tuning layer to modify the effective index of the optical mode, similarly as for the TTG-DFB laser.

### Silicon grating design

For the design of the silicon waveguide grating, MODE Solutions, a commercial mode solver from Lumerical [5], is used. By anticipating lithographic fabrication errors, the design is precompensated by providing a stronger grating corrugation width  $\Delta W$  (see Fig. 5.2(a)) on the mask. A similar method is described in [6], where a reduction of the grating coupling strength by a factor 3 is reported as a rule-of-thumb for a standard single-mode 220 nm $\times$ 450 nm silicon waveguide. Figures 5.2(a) and (b) show the silicon grating design and the fabricated structure, respectively. The grating coupling strength  $\kappa$  is estimated from  $\kappa = 2\Delta\bar{n}/\lambda_0$ , where  $\bar{n}$  represents the difference in effective index for the fundamental mode considered in the wide and narrow waveguide, respectively.  $\lambda_0$  is the free-space wavelength. The simulated reflection spectra for the precompensated design and the fabricated structure are shown in Fig. 5.2(c). The  $\kappa$  is significantly reduced from 900 cm $^{-1}$  to 70 cm $^{-1}$ , resulting in a targeted reflection characteristic with a 3 dB bandwidth  $\Delta\lambda$  of only 1 nm.

### Coupling structure

In order to efficiently couple light from the InP waveguide to the output silicon waveguide an adiabatic tapered coupler is used. The InP waveguide and the silicon waveguide are inversely tapered down. In the first section the active InP waveguide is tapered down from 3  $\mu\text{m}$  to 1.5  $\mu\text{m}$  over a short length of 30  $\mu\text{m}$ . In the second section the InP waveguide is further tapered down to a narrow taper tip. The silicon waveguide is tapered up from 200 nm to 1  $\mu\text{m}$ . Note that the total thickness of the tuning layer and

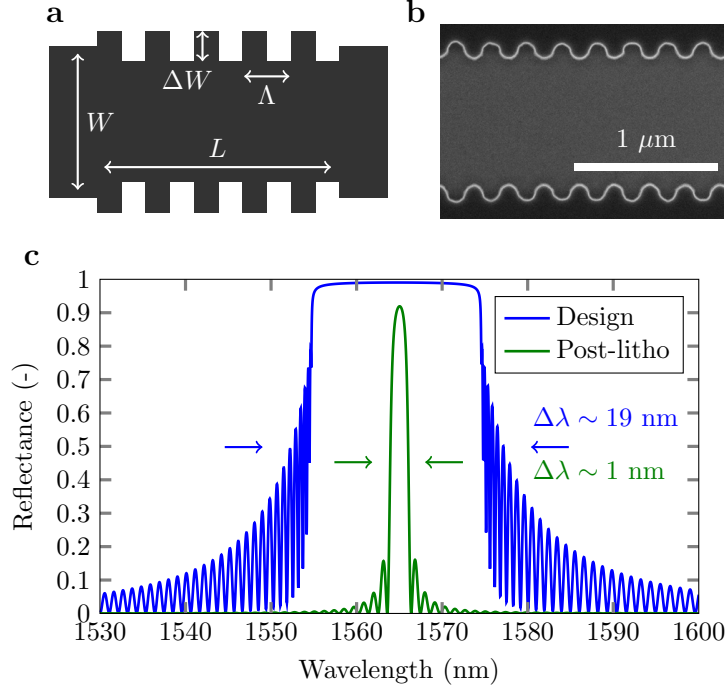


**Figure 5.2:** Sidewall-corrugated silicon grating. (a) Design on the lithographic mask with  $L = 300 \mu\text{m}$ ,  $W = 1 \mu\text{m}$ ,  $\Delta W = 300 \text{ nm}$  and  $\Lambda = 250 \text{ nm}$ . (b) SEM image of the fabricated structure. For clarity the passive InP tuning waveguide is not shown. (c) Simulated reflection spectra for the precompensated design and the fabricated structure (post-litho).

the surrounding cladding layers is not large enough to achieve phase matching between the active InP waveguide mode and the passive InP tuning waveguide mode. Therefore light is immediately coupled from the active InP waveguide to the underlying silicon waveguide. As the optical mode still has an evanescent tail in the passive InP tuning waveguide, the tuning waveguide is tapered down as well in the third section that comes after the phase and Bragg section. Figure 5.3(a) shows the simulated coupling efficiency for the first and second taper section as a function of taper length for different InP taper tip widths. A DVS-BCB bonding layer thickness of 50 nm is assumed. It is clear that for taper lengths above 90  $\mu\text{m}$  the coupling is already adiabatic, with a saturation of the coupling efficiency determined by the width of the InP taper tip. In order to account for some robustness towards a lateral alignment offset between the InP and silicon waveguide (0 – 200 nm) during optical contact lithography, a total taper length of 130  $\mu\text{m}$  is chosen. Figure 5.3(b) shows the influence of the InP

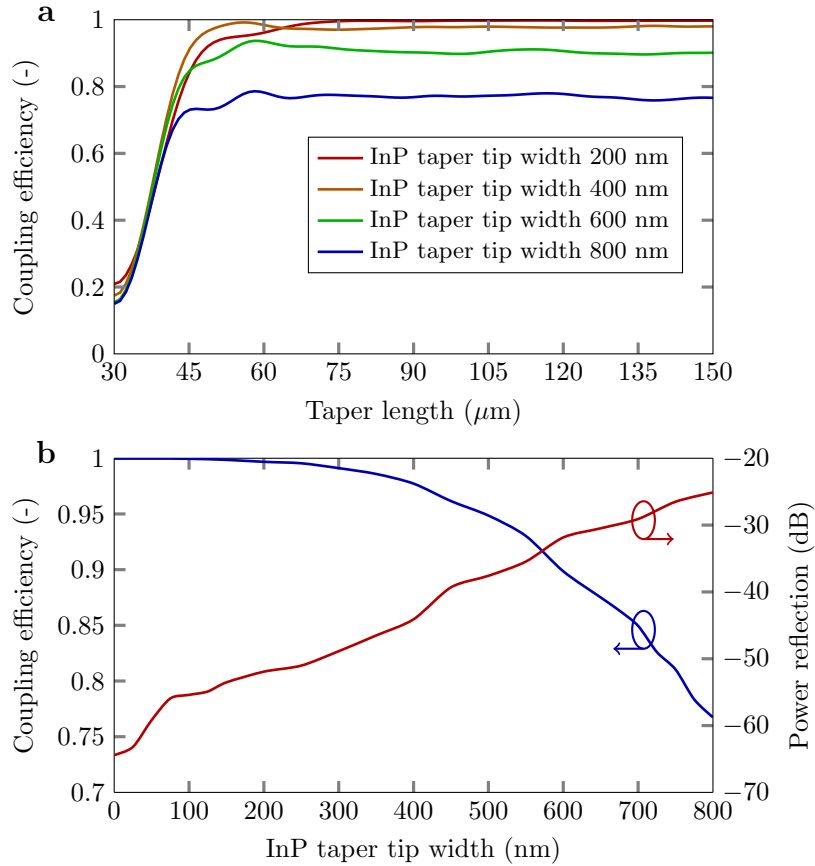


**Figure 5.3:** InP-to-silicon adiabatic tapered coupler. (a) Coupling efficiency for the first and second taper section as a function of taper length. (b) Coupling efficiency and power reflection for the first and second taper section as a function of InP taper tip width for a total taper length of 130  $\mu\text{m}$ .

taper tip width on the coupling efficiency and the power reflection back into the waveguide for the chosen taper length. Although the coupling efficiency stays above 75% for InP taper tips as wide as 800 nm, a InP taper tip of 400 nm or narrower is required to keep the power reflection below  $-40$  dB, which is needed to prevent gaps in the wavelength tuning characteristics [7].

### 5.2.2 Fabrication

Fabrication of the laser devices follows the same procedure as outlined in Chapter 3 and is not further discussed in detail here. We denote that the laser facet is defined by means of a focused ion beam (FIB) cut (see Fig. 5.5)

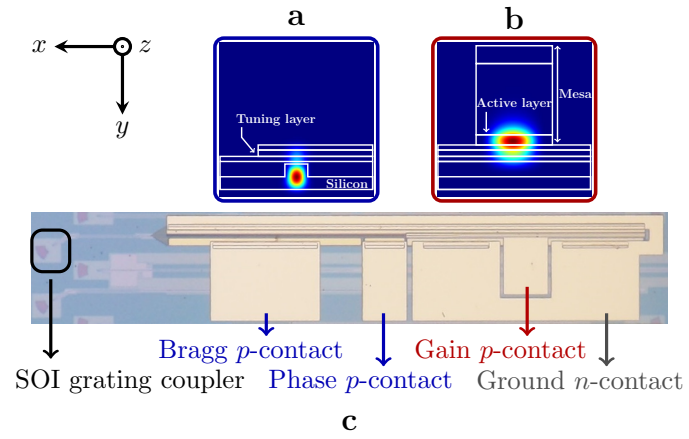


**Figure 5.4:** (a) Optical mode profile in the phase and Bragg section. (b) Optical mode profile in the gain section. (c) Optical microscope image of the fabricated laser device.

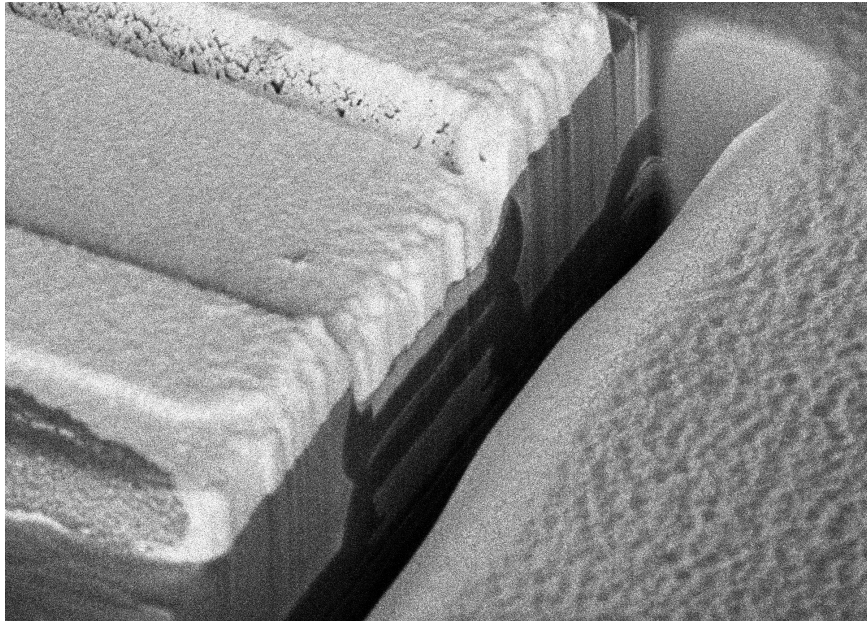


**Figure 5.5:** Facet of a thermally tunable TTG-DBR laser fabricated by means of a FIB cut.

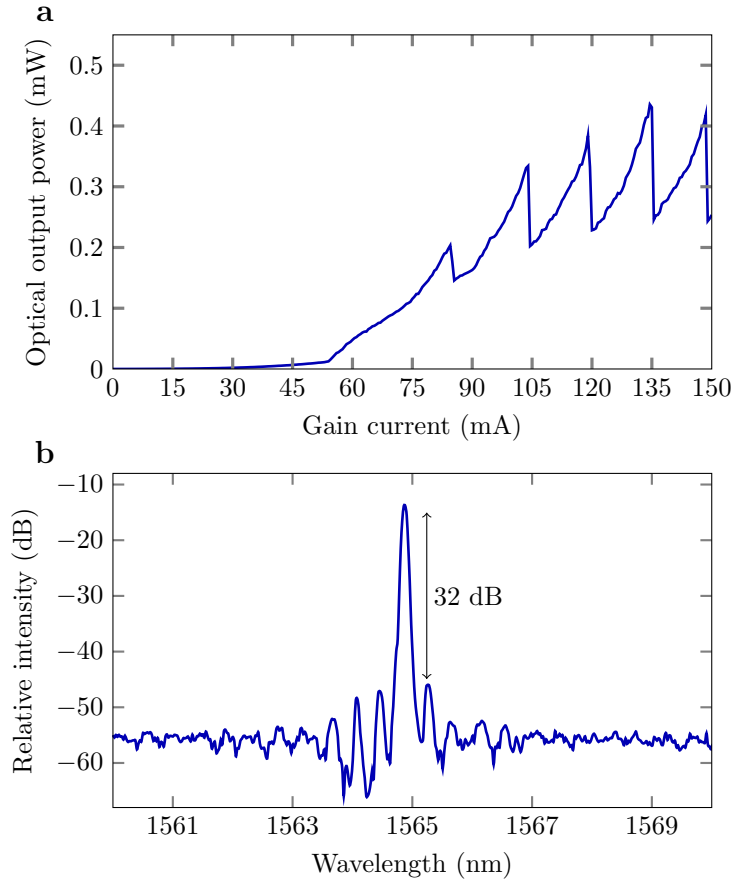


**Figure 5.6:** Static laser characteristics of the thermally tunable TTG-DBR laser. (a) LI characteristic (waveguide-coupled output power); (b) Optical spectrum for a Gain current of 120 mA. In both graphs the Phase and Bragg section are unbiased.

to avoid the need for cleaving and which allows to vary the cavity length from laser to laser. This however does not allow characterizing the laser from the low reflection facet side. An optical microscope image of the fabricated chip is shown in Fig. 5.4(c). The length of the gain (including the coupler), phase and Bragg section is  $650 \mu\text{m}$ ,  $100 \mu\text{m}$  and  $300 \mu\text{m}$  respectively. The optical mode profile in the phase and Bragg section and in the gain section is shown in Figs. 5.4(a) and (b) respectively.

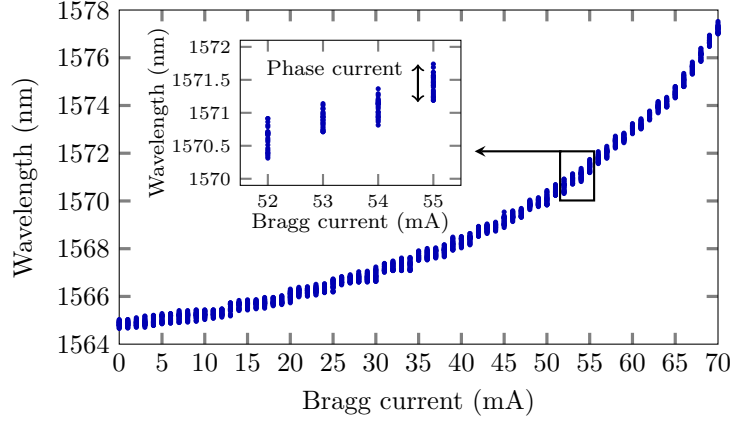


**Figure 5.7:** Laser wavelength as a function of Bragg current at a Gain current of 120 mA. The Phase current is varied between 0 mA and 24 mA. Both currents are swept in steps of 1 mA. The inset shows a close-up around 1571 nm, illustrating the continuous tuning nature.

### 5.2.3 Static laser characteristics

Device characterization is done on a temperature-controlled stage at 10 °C. The DC electrical characteristics are measured with a current source and 4 electrical DC probes. The series resistance ( $dV/dI$ ) in the gain, phase and Bragg section is 4.5  $\Omega$ , 190  $\Omega$  and 85  $\Omega$  respectively. The resistance between the  $p$ -type phase and Bragg contacts is 5.4 k $\Omega$ . The optical properties are measured by coupling light from the chip to a standard single-mode optical fiber (SMF) by means of a reflectionless silicon grating coupler [8]. A power meter is used to measure the fiber-coupled optical output power. The measured fiber-to-chip coupling efficiency at the laser wavelength is -15 dB. Figure 5.6 shows the light-current (LI) characteristic for the DBR laser when the phase and Bragg sections are left unbiased, i.e.  $I_{\text{phase}} = I_{\text{Bragg}} = 0$  mA. The threshold current is 55 mA and the maximum CW on-chip optical output power is 0.4 mW. As expected this value is limited as light is coupled out from the waveguide-grating side, which is designed to exhibit high reflectivity. Also note that facet fabrication is not optimal, which leads to a deterioration of the facet reflectivity and hence of the laser threshold and optical output power. The peaks in the LI characteristic are due to longitudinal mode hopping. The laser spectrum is measured by means of an optical spectrum analyzer at a resolution of 80 pm. The inset of Fig. 5.6 shows the optical spectrum, measured at  $I_{\text{gain}} = 120$  mA. Single-mode laser operation is achieved at 1565 nm with an SMSR of 32 dB. The free spectral range (FSR) of the laser cavity is 0.5 nm. Wavelength tuning is done through carrier injection in the tuning layer of the phase

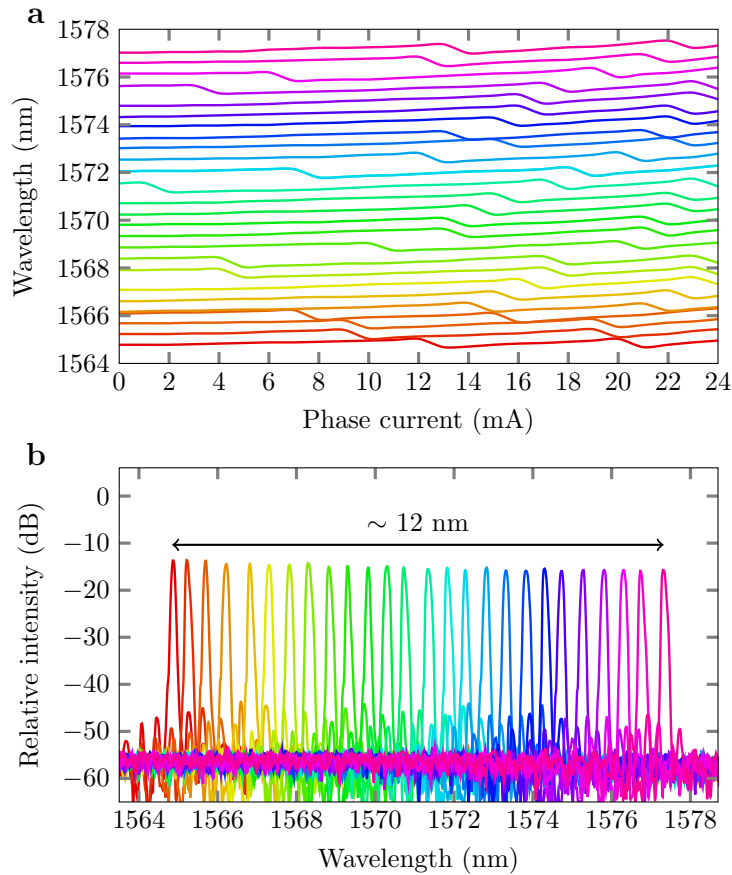


**Figure 5.8:** (a) Laser wavelength as a function of the Phase current. (b) Superimposed laser spectra for different Phase and Bragg currents. In both graphs the Gain current is 120 mA and the Bragg current is varied between 0 mA and 70 mA. The current step is chosen such that the peak wavelength spacing is 0.5 nm (also see Fig. 5.7).

and Bragg section. Figure 5.7 shows the laser wavelength as a function of  $I_{\text{Bragg}}$  when  $I_{\text{phase}}$  is varied between 0 and 24 mA. Clearly all wavelengths between 1565 nm and 1577 nm are accessible and continuous tuning over the 12 nm wavelength range can be achieved through simultaneous adjustment of  $I_{\text{phase}}$  and  $I_{\text{Bragg}}$ . This is also illustrated in Fig. 5.8(a), which shows the laser wavelength as a function of  $I_{\text{phase}}$  for different values of  $I_{\text{Bragg}}$ . When  $I_{\text{Bragg}}$  is kept fixed and  $I_{\text{phase}}$  is varied between 0 and 24 mA at least two mode hops occur, which indicates that a  $2\pi$  phase shift can be achieved such that full wavelength coverage is possible. Figure 5.8(b) shows the superimposed laser spectra across the tuning range. The SMSR remains

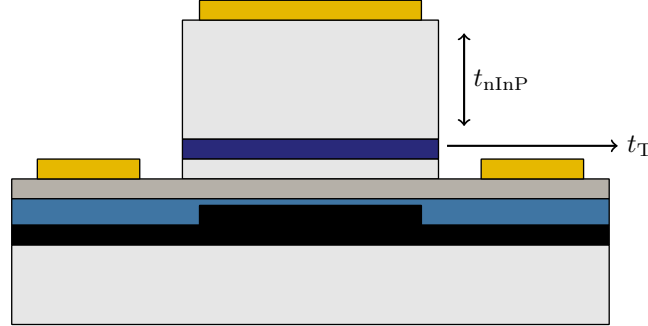


**Figure 5.9:** Cross-sectional view of the improved TTG-DBR laser layout in the phase and Bragg section.

larger than 30 dB and the optical output power only varies within 2 dB over the entire tuning range. The red shift of the laser wavelength with increasing tuning current indicates a dominant heating effect. By improving the heat sinking and through a modification of the epitaxial layer stack in future designs, we expect to significantly increase the optical confinement factor in the tuning layer, resulting in a stronger electronic effect and hence faster tuning ( $\sim$  ns). This forms the basis for the discussion in the next section.

### 5.3 Electronically tunable TTG-DBR laser

In order to enhance the electronic tuning effect in the TTG-DBR laser two significant improvements to the TTG epitaxial layer stack are proposed:

1. The use of a much thicker tuning layer (thickness  $t_T$ ) as to improve the optical confinement factor in the tuning layer.
2. The use of a very thick  $n$ -InP cladding layer (thickness  $t_{n\text{InP}}$ ) such that the  $n$ -type ground contact can be placed on top of the tuning waveguide, thereby allowing for a symmetric structure.

A symmetric structure in the phase and Bragg section has the advantage that the tuning waveguide is well-defined and limited in space, which prevents carrier diffusion in the tuning layer. It also ensures that the modal overlap with the injected carriers is optimum. The use of a thick tuning and  $n$ -InP layer has implications for the coupling coefficient of the grating in the Bragg section. Sidewall-corrugated gratings will lead to too low reflectivities and partially etched gratings as used in the DFB lasers seems an appropriate choice.

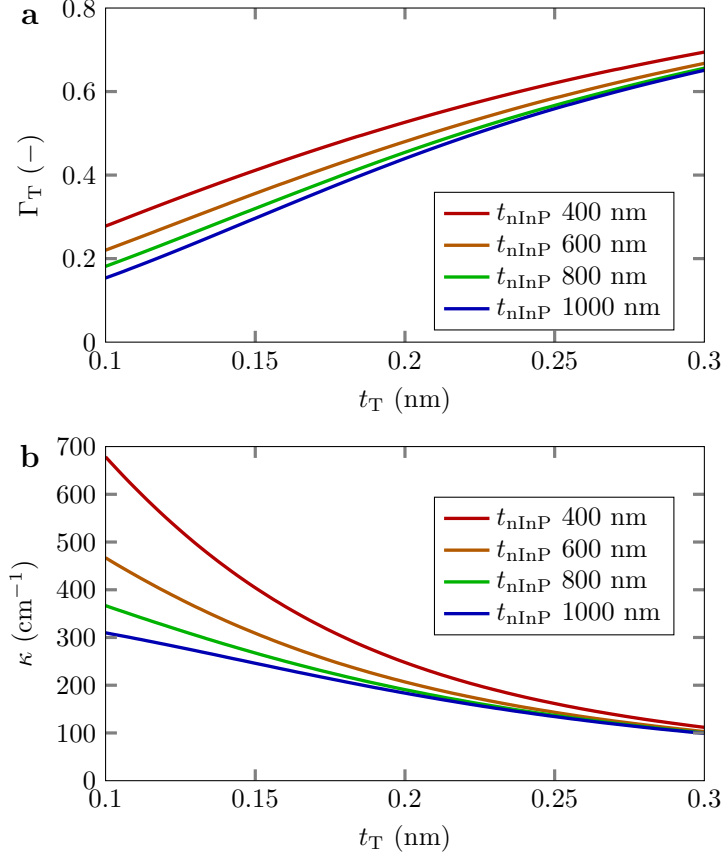


**Figure 5.10:** Optimization of the tuning layer thickness. Influence of  $t_T$  on (a) the confinement factor in the tuning layer  $\Gamma_T$  and on (b) the grating coupling coefficient  $\kappa$ .

### 5.3.1 Laser structure

A cross-sectional view of the improved TTG-DBR laser layout in the phase and Bragg section is shown in Fig. 5.9. Note that the use of such a thick  $n$ -InP layer has important consequences for light coupling between the gain section, the phase and Bragg section and the silicon output waveguide. In Chapter 7 an adiabatic tapered coupler is discussed that could form the basis as coupler for this laser structure.

### 5.3.2 Optimization of the tuning layer thickness

The influence of the tuning layer thickness on the confinement factor in the tuning layer  $\Gamma_T$  and the grating coupling coefficient  $\kappa$  is shown in Fig. 5.10.

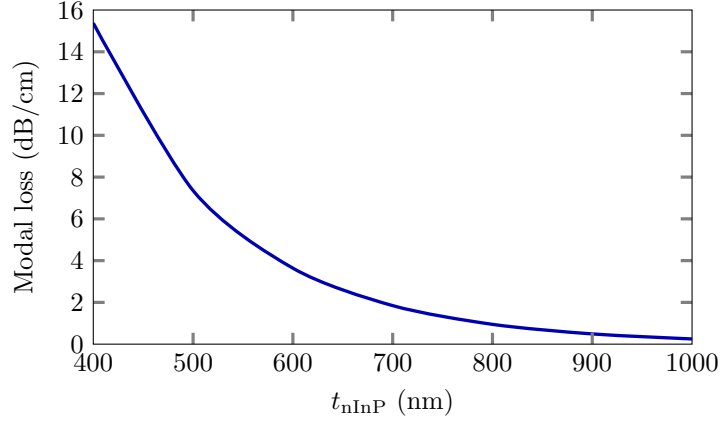


**Figure 5.11:** Optimization of the cladding layer thickness. Influence of  $t_{\text{nInP}}$  on the modal loss, with assumption of a Ni/Ge/Au metallurgy.

Thereby an InGaAsP contact layer thickness  $t_C = 150$  nm and DVS-BCB thickness  $t_{\text{DVS-BCB}} = 50$  nm is assumed. The former is slightly thicker than for TTG-DFB lasers, where a more difficult trade-off between the confinement in the different sections was in place. Clearly  $\Gamma_T$  dramatically increases with increasing  $t_T$ . Furthermore,  $t_{\text{nInP}}$  seems to have little influence on both  $\Gamma_T$  and  $t_T$  for  $t_T > 200$  nm. A tuning layer thickness  $t_T = 225$  nm seems an adequate choice, with  $\Gamma_T \approx 0.4$  and  $\kappa \approx 200 \text{ cm}^{-1}$ .

### 5.3.3 Optimization of the cladding layer thickness

Although the thickness of the  $n$ -InP cladding layer has some influence on  $\Gamma_T$  and  $t_T$ , a more stringent condition is put by the absorption loss when a metal contact is defined on top of the mesa. Fig. 5.11 shows the simulated modal loss versus  $t_{\text{nInP}}$ . Thereby a Ni/Ge/Au metallurgy is assumed. A thickness  $t_{\text{nInP}} > 800$  nm seems a good choice, with a modal loss that drops below 2 dB/cm. Obviously,  $t_{\text{nInP}}$  cannot be chosen too large either, as it would dramatically increase the length of the coupling structure.

### 5.3.4 Mode profiles for the optimized structure

The mode profiles in the gain section and Bragg section for the optimized design with  $t_T = 225$  nm and  $t_{\text{nInP}} = 800$  nm are shown in Fig. 5.12.

## 5.4 Conclusion

In conclusion, two TTG-based heterogeneously integrated three-section DBR lasers have been presented. The first structure utilizes a sidewall-corrugated

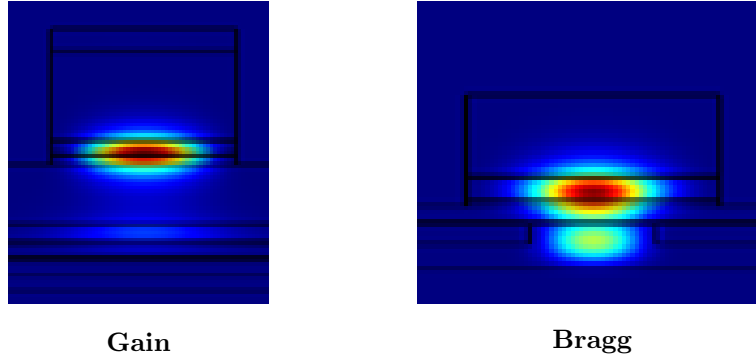


**Figure 5.12:** Illustration of the optical mode profiles in the gain and Bragg section for the optimized TTG-DBR laser design (at 1550 nm, TE polarization).

waveguide grating as wavelength-selective mirror. A flat-band continuous tuning range of more than 12 nm is obtained with an SMSR greater than 30 dB and a maximum CW on-chip optical output power of 0.4 mW. The demonstrated laser device is expected to find application in future advanced optical networks and can be attractive for emerging applications such as LIDAR and CO<sub>2</sub> spectroscopy. The dominant heating effect makes the structure unsuitable for operation in optical packet switching systems. Therefore a new design was proposed, where use is made of TTG stack with thick tuning layer and very thick *n*-type cladding. The redesign should dramatically improve the device performance.

## References

- [1] S. Dhoore, S. Uvin, D. Van Thourhout, G. Morthier, and G. Roelkens, “Novel adiabatic tapered couplers for active III–V/SOI devices fabricated through transfer printing,” *Optics Express* **24**(12), 12,976–12,990 (2016).
- [2] S. Dhoore, G. Roelkens, and G. Morthier, “III-V-on-silicon three-section DBR laser with over 12 nm continuous tuning range,” *Optics Letters* **42**(6), 1121–1124 (2017).
- [3] X. Wang, W. Shi, R. Vafaei, N. A. Jaeger, and L. Chrostowski, “Uniform and sampled Bragg gratings in SOI strip waveguides with sidewall corrugations,” *IEEE Photonics Technology Letters* **23**(5), 290–292 (2011).
- [4] M. Verbist, W. Bogaerts, and D. Van Thourhout, “Design of weak 1-D Bragg grating filters in SOI waveguides using volume holography techniques,” *Journal of Lightwave Technology* **32**(10), 1915–1920 (2014).
- [5] “Lumerical MODE Solutions – comprehensive optical waveguide design environment,” (2017). URL <https://www.lumerical.com/tcad-products/mode/>.
- [6] L. Chrostowski and M. Hochberg, *Silicon photonics design: from devices to systems* (Cambridge University Press, 2015).
- [7] R. Todt and M.-C. Amann, “Influence of facet reflections on monolithic widely tunable laser diodes,” *IEEE Photonics Technology Letters* **17**(12), 2520–2522 (2005).
- [8] D. Vermeulen, Y. De Koninck, Y. Li, E. Lambert, W. Bogaerts, R. Baets, and G. Roelkens, “Reflectionless grating couplers for Silicon-on-Insulator photonic integrated circuits,” *Optics Express* **20**(20), 22,278–22,283 (2012).

# 6

## Discretely tunable lasers on silicon based on filtered optical feedback

**I**N this chapter, a wavelength-selectable laser structure is proposed as an alternative for the wavelength-tunable laser diodes discussed in the previous two chapters. Filtered optical feedback is used as a way to achieve single-mode laser operation and wavelength selectivity. The discussion is based on [1].

### Contents

---

6.1	Introduction . . . . .	121
6.2	Design aspects . . . . .	122
6.3	Fabrication . . . . .	129
6.4	Static laser characteristics . . . . .	129
6.5	Dynamic laser characteristics . . . . .	133
6.6	Conclusion . . . . .	137
	References . . . . .	138

---

### 6.1 Introduction

In order to achieve nanosecond fast wavelength tuning, typically use is made of carrier-injection based *p-i-n* structures [2, 3]. Such tuning schemes have

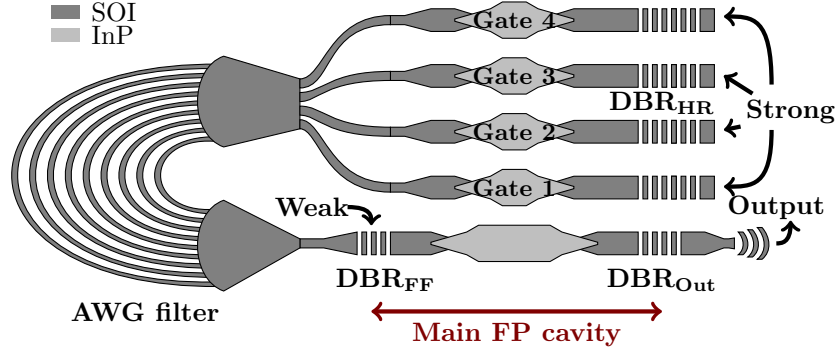


Figure 6.1: Schematic of the filtered feedback tunable laser structure.

the advantage of offering (quasi-) continuous wavelength tunability but tuning speeds and ranges are limited by thermal effects. Indeed, the free-carrier plasma dispersion effect leads to a blueshift of the laser wavelength whereas heating effects lead to a redshift of the laser peak. Filtered optical feedback lasers rely on delayed optical feedback to the main laser cavity. Using such on-chip optical feedback the lasers are less affected by temperature fluctuations caused by tuning (or wavelength-selective) currents, as the tuning sections are located outside the main laser cavity [4–6] in contrast to classic tunable lasers [3, 7]. Initial demonstrations of filtered feedback lasers are based on single-ring [6] and double-ring resonator [4] configurations. In [5] nanosecond fast discrete wavelength tuning was achieved with an InP-based laser and AWG as wavelength filter in the feedback path. Since then, also more complex laser structures using filtered optical feedback have been demonstrated. In [8], a ring laser with two AWGs in the feedback section is investigated, where no cleaved facets or DBR mirrors are needed. Despite the promising properties of filtered feedback wavelength-selectable lasers, so far no demonstration on a silicon photonics platform has been realized. In this chapter the design, fabrication and characterization of a four-channel wavelength-selectable laser on SOI based on filtered optical feedback is presented. As SOI lends itself very well for small bend radii and gratings with large coupling coefficient [9, 10], a laser structure based on an AWG in combination with several DBRs is chosen.

## 6.2 Design aspects

### 6.2.1 Laser structure

The laser structure is schematically shown in Fig 6.1. The laser consists of a main FP cavity with two partially reflective broadband SOI DBR mirrors (denoted as DBR<sub>FF</sub> and DBR<sub>Out</sub>, respectively). At one side of the FP cavity

the light output is coupled to an SOI AWG filter that demultiplexes the light in four different waveguide branches. In each branch an InP-on-silicon semiconductor optical amplifier (SOA) is implemented that can function as optical gate. If the SOA is biased at or above transparency, input light can be efficiently transmitted or even be amplified. When unbiased, all incident light is absorbed in the gate. By making use of a highly reflective SOI DBR mirror at the end of each waveguide branch (denoted as  $\text{DBR}_{\text{HR}}$ ), light can be fed back to the laser. This enables the laser to operate in single-mode regime, close to the wavelength with maximum transmission through the AWG filter [11–13]. Light exiting at the  $\text{DBR}_{\text{Out}}$  side is coupled towards a reflectionless SOI fiber-to-chip grating coupler [14] for characterization of the laser device.

### 6.2.2 SOA design

The SOAs that constitute the main FP cavity and the optical gates are implemented as InP-based *p-i-n* structures on top of SOI waveguides. The standard InP/InGaAsP epitaxial layer stack from Table 2.1 is used. With a 180  $\mu\text{m}$  long double taper structure [15] light is coupled from the SOA to the underlying silicon waveguide. For an InP taper tip width of 400 nm the simulated transition loss is only 0.5 dB. The straight section of the main FP cavity and the gates is kept sufficiently short (240  $\mu\text{m}$  and 40  $\mu\text{m}$ , respectively) to maximize the longitudinal mode spacing and minimize the transparency current, respectively.

### 6.2.3 AWG filter design

The design of the AWG is done by means of the IPKISS spectral toolbox from Lucedá Photonics [16] and follows the approach outlined in [17]. The AWG is implemented on an SOI wafer with a 400 nm thick device layer using a 180 nm etch. The shallow etch depth leads to reduced phase errors [18]. The AWG is acyclic and has  $N = 4$  output channels with a designed channel spacing  $\Delta\lambda_{\text{AWG}} = 4$  nm and free spectral range  $\text{FSR} = \Delta\lambda_{\text{AWG}}(N + 1) = 20$  nm. The free propagation region (FPR) of both star couplers has a length of 71.6  $\mu\text{m}$ , whereas the input and output aperture width is 1.8  $\mu\text{m}$ . At the grating side the apertures are spaced 230 nm apart and 90  $\mu\text{m}$  long linear tapers are used to connect the star coupler apertures with the grating arms. At the input and output side of the AWG the star coupler apertures are connected to the 650 nm wide rib waveguides using 45  $\mu\text{m}$  long linear tapers. The simulated transmission characteristic for the different channels of the AWG is shown in Fig. 6.2(a). The full width at half maximum (FWHM) of the passband of each wavelength channel is 1.2 nm. SEM images of the fabricated AWG structure are shown in Figs. 6.2(b) and 6.2(c). The measured transmission characteristic of the AWG, characterized through a neighboring reference structure after complete laser device processing, is

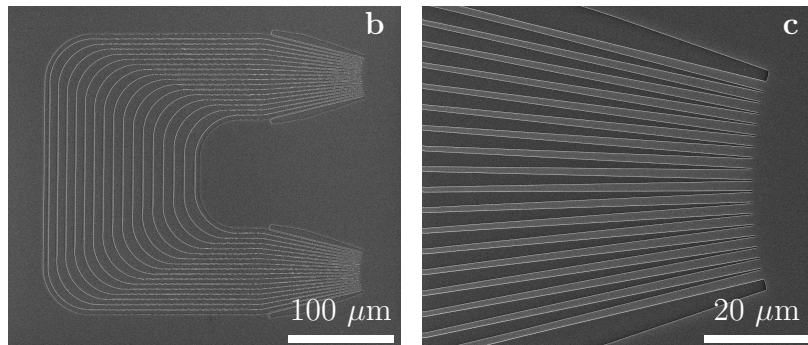
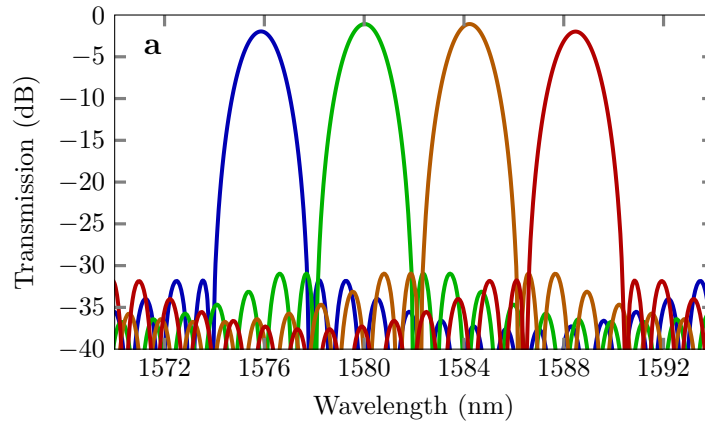


**Figure 6.2:** AWG design. (a) Simulation of the AWG filter transmission; (b) SEM image of the AWG; (c) SEM image of the AWG (zoom on the star coupler region).

shown in Fig. 6.3. The insertion loss is 4 dB and the minimum adjacent cross talk 10 dB. The FWHM of the passband of each wavelength channel is 1.7 nm. For our purpose this is sufficient, since passive filtering of 10 dB is sufficient to obtain single-mode laser operation. The filtered light also passes twice through the AWG before it is coupled back to the main cavity, which provides extra filtering. As a stand-alone AWG, however, the filter does not show sufficient isolation needed for most applications. It is noted that the device was processed in a very early e-beam fabrication run and that there is ample room for design and fabrication optimization in order to reduce the waveguide loss and improve the overall device performance.

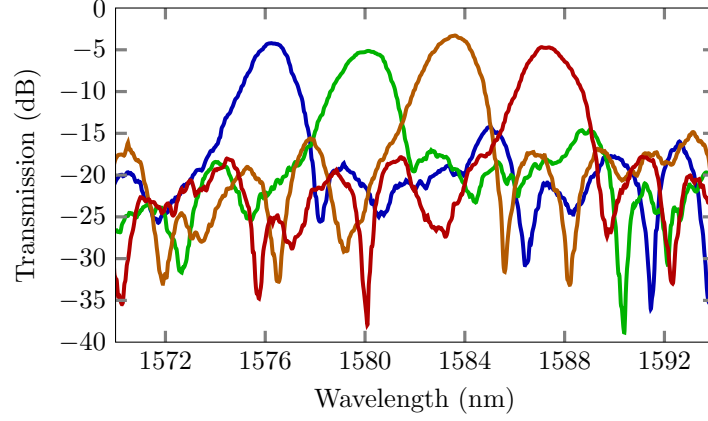


**Figure 6.3:** Characterization of the stand-alone AWG after complete laser device processing.

#### 6.2.4 DBR design

Three distinct DBR grating designs are used in the overall laser structure. One functions as semi-reflective output DBR grating ( $\text{DBR}_{\text{Out}}$ ), one as low-reflective filtered feedback DBR grating ( $\text{DBR}_{\text{FF}}$ ) and four as high-reflective DBR gratings ( $\text{DBR}_{\text{HR}}$ ). In all three designs the DBRs have a silicon waveguide width of  $2 \mu\text{m}$  and are implemented in a  $400 \text{ nm}$  thick device layer with  $180 \text{ nm}$  etch depth. The grating period is  $252 \text{ nm}$  in all DBR designs, which corresponds to a Bragg wavelength of  $1580 \text{ nm}$ , close to the gain peak wavelength of the amplifier epitaxial layer stack. The reflectivity of the DBRs is determined by the number of grating periods, as shown in Fig. 6.4(a). The corresponding reflection spectra for the different DBR designs are shown in Fig. 6.4(b). The reflectivity of  $\text{DBR}_{\text{HR}}$  is larger than 95% whereas  $\text{DBR}_{\text{Out}}$  has a designed reflectivity of 66%, as trade-off between a targeted low threshold current and large output power. The reflectivity of  $\text{DBR}_{\text{FF}}$  controls the filtered feedback strength  $\gamma$  ( $\text{ns}^{-1}$ ), which can phenomenologically be described as [5]

$$\gamma = \frac{1 - R_{\text{DBR}_{\text{FF}}}}{\tau_{\text{in}}} \sqrt{\frac{R_{\text{DBR}_{\text{HR}}}}{R_{\text{DBR}_{\text{FF}}}} (1 - A_{\text{DBR}_{\text{FF}}})^2 T_{\text{AWG}}^2 A_{\text{Gate}}^2}, \quad (6.1)$$

where  $\tau_{\text{in}}$  is the roundtrip time of the main FP cavity,  $R_{\text{DBR}_{\text{FF}}}$  the reflectivity of  $\text{DBR}_{\text{FF}}$ ,  $R_{\text{DBR}_{\text{HR}}}$  the reflectivity of  $\text{DBR}_{\text{HR}}$ ,  $T_{\text{AWG}}$  the transmission of the AWG and  $A_{\text{Gate}}$  the amplification of an SOA gate.  $A_{\text{DBR}_{\text{FF}}}$  is given by  $1 - T_{\text{DBR}_{\text{FF}}}/(1 - R_{\text{DBR}_{\text{FF}}})$  and accounts for scattering losses in  $\text{DBR}_{\text{FF}}$ , whereby it is assumed that  $R_{\text{DBR}_{\text{FF}}} + T_{\text{DBR}_{\text{FF}}} < 1$ . Here we assume  $A_{\text{DBR}_{\text{FF}}} = 0.1$ . Generally, a small  $R_{\text{DBR}_{\text{FF}}}$  leads to a larger  $\gamma$  but increased threshold current and vice versa. In our case  $\tau_{\text{in}} = 2L_{\text{FP}}n_g/c = 16 \text{ ps}$ , with

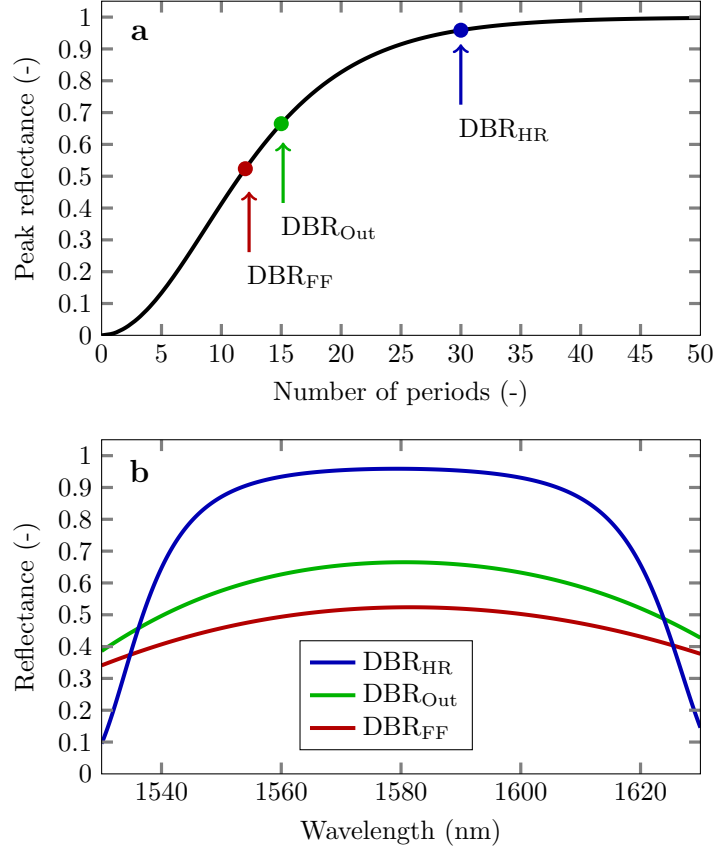


**Figure 6.4:** DBR design. (a) Peak reflectance as a function of number of grating periods ( $\Lambda = 252$  nm, duty cycle = 50%); (b) Reflection spectra for DBR<sub>FF</sub>, DBR<sub>Out</sub> and DBR<sub>HR</sub>.

$L_{\text{FP}} = 600 \mu\text{m}$  the total length of the main FP cavity (i.e. the distance between DBR<sub>FF</sub> and DBR<sub>Out</sub>),  $n_g \approx 4.1$  the group index of the waveguide mode and  $c$  the speed of light. Assuming the gates are pumped to transparency ( $A_{\text{Gate}} = 0$  dB) and with  $T_{\text{AWG}} = 0.4$ ,  $\gamma = 6 \text{ ns}^{-1}$  is obtained. The relationship between  $\gamma$  and  $A_{\text{Gate}}$  is shown in Fig. 6.5, for different values of  $R_{\text{DBR}_{\text{FF}}}$ . The graph shows that with stronger pumping of the gates such that e.g.  $A_{\text{Gate}} = 3$  dB,  $\gamma$  can be increased to a relatively large value of  $23 \text{ ns}^{-1}$ .

### 6.2.5 Simulation of the wavelength switching behavior

In order to gain some more insight into the wavelength switching behavior and how the wavelength switching time is influenced by the different design

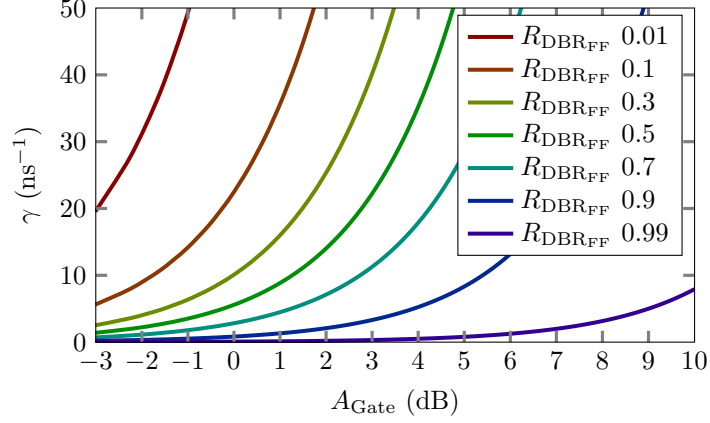


**Figure 6.5:** Relationship between the filtered feedback strength  $\gamma$  and the amplification in the SOA gate  $A_{\text{Gate}}$ , for different values of  $R_{\text{DBR}_{\text{FF}}}$ .

parameters, simulations based on a self-written Matlab code are performed. A similar approach as described in [5] is followed.

### Filtered feedback model

Simulations are based on an extended Lang-Kobayashi model [19, 20]. The model consists of a number of delay differential equations (DDEs) for the complex slowly varying field amplitudes  $E_m$  of each laser mode and the carrier density  $N$  in the FP cavity. In essence, the laser rate equations (2.26) and (2.27) from Chapter 2 are reformulated to include multiple modes and delayed filtered feedback. They are given by:

$$\frac{dN}{dt} = \eta_h \frac{I}{q} - \frac{N}{\tau_n} - g_m (N - N_0) \sum_{m=1}^n \left( \frac{|E_m|^2}{1 + S|E_m|^2 + C \sum_{k \neq m} |E_k|^2} \right) \quad (6.2)$$

$$\frac{dE_m}{dt} = \frac{1}{2} (1 + j\alpha) \left[ \frac{g_m (N - N_0)}{1 + S|E_m|^2 + C \sum_{k \neq m} |E_k|^2} - \frac{1}{\tau_m^{\text{ph}}} \right] E_m + \gamma_m F_m \quad (6.3)$$

$$\frac{dF_m}{dt} = \Lambda E_m(t - \tau) \exp(j\phi_m) + (j\Delta\omega_m - \Lambda) F_m, \quad (6.4)$$

where  $g_m$  and  $\tau_m^{\text{ph}}$  are the differential gain and photon lifetime for mode  $m$ , respectively. For simplicity, equal gain for all modes is assumed (with  $g_m = 1.5 \cdot 10^{-5} \text{ ns}^{-1}$ ).  $S$  and  $C$  are phenomenological parameters that take into account nonlinear saturation processes. We assume  $S = C = 5 \cdot 10^{-7}$ . The linewidth enhancement factor is assumed to be  $\alpha = 5$ . For

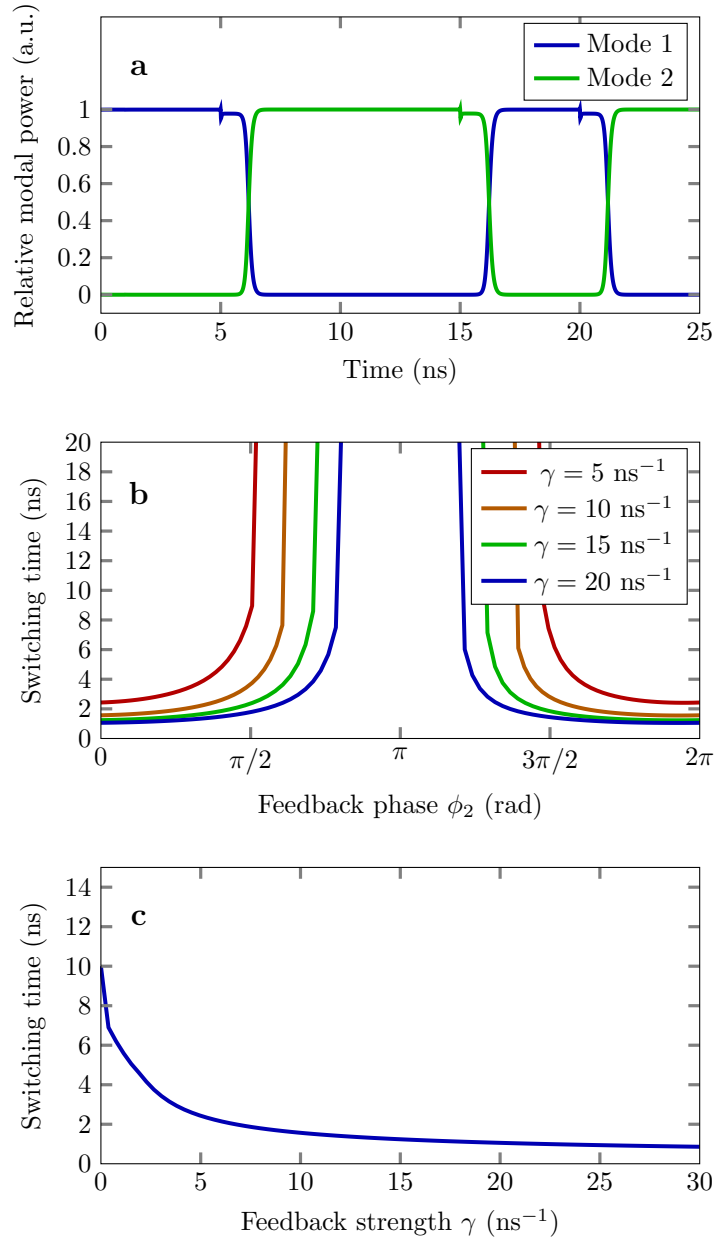


**Figure 6.6:** Simulation of the wavelength switching behavior. (a) Time-domain characteristics when  $\gamma_1$  and  $\gamma_2$  are periodically and complementarily switched between  $0 \text{ ns}^{-1}$  and  $10 \text{ ns}^{-1}$ ; (b) Dependence of the switching time on feedback phase  $\phi_2$  ( $\phi_1 = 0$ ); (c) Dependence of the switching time on the feedback strength  $\gamma$  ( $\phi_1 = \phi_2 = 0$ ).

simplicity we furthermore take  $\eta_i = 1$ , with  $I = 100$  mA.  $\tau_n = 2$  ns is the carrier lifetime. The filtered feedback is described in (6.4) for the auxiliary dynamical variables  $F_m$ , with feedback amplitudes  $\gamma_m$ , phases  $\phi_m$  and delay time  $\tau = 2L_{\text{ext}}n_g/c = 50$  ps, where  $L_{\text{ext}} = 1.85$  mm is the external cavity length. The AWG transmission characteristic is modeled as a Lorentzian with half width at half maximum (HWHM)  $\Lambda = 106$  GHz and detuning  $\Delta\omega_m = 0$ .

### Wavelength switching simulation

The wavelength switching behavior is simulated for the simple case when two laser modes of the FP cavity are in competition, where the feedback strength  $\gamma_1$  and  $\gamma_2$  is periodically and complementary switched between  $0 \text{ ns}^{-1}$  and  $10 \text{ ns}^{-1}$ . This corresponds to the situation where the bias is switched between two SOA gates. The relative power  $|E_1|^2$  and  $|E_2|^2$  for respectively mode 1 and mode 2 is monitored as a function of time. The resulting time domain characteristics are shown in Fig. 6.6(a). Initially the laser operates in single-mode, with gate 1 being forward biased. When the feedback is moved to channel 2 the laser switches to mode 2 as its effective gain is increased. Switching does not occur instantaneously, as the delayed feedback needs to build up. The increasing relative power of mode 2 will quench the gain of mode 1 and eventually lead to single-mode laser operation. From Fig. 6.6(b) it is clear that the feedback phase has a strong influence on the wavelength switching time. Finally Fig. 6.6(c) shows that for sufficiently strong feedback (and with the feedback being in phase with the propagating field) sub-ns wavelength switching times can be achieved.

## 6.3 Fabrication

The SOI structures have a 400 nm thick silicon device layer with a single shallow etch depth of 180 nm and are fabricated in-house by means of electron-beam lithography (EBL) and subsequent reactive ion etching (RIE). The InP-on-silicon integration is based on adhesive divinylsiloxane-bis-benzocyclobutene (DVS-BCB) bonding. Ti/Au *p*-contact and Ni/Ge/Au *n*-contact metallurgies are used for all SOAs. Details of the bonding procedure and InP post processing can for instance be found in [21]. An optical microscope image of the fabricated device with indication of the different metal contact pads is shown in Fig. 6.4.

## 6.4 Static laser characteristics

The laser device is characterized on a temperature-controlled stage. The DC electrical characteristics are measured with two Keithley 2400 current

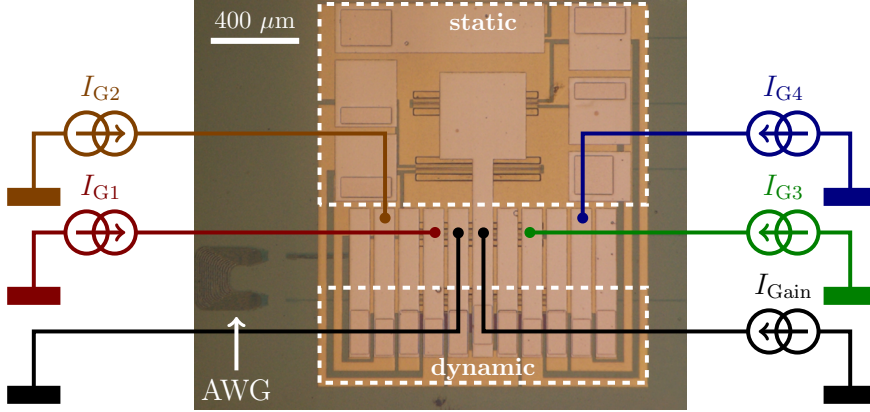


**Figure 6.7:** Optical microscope image of the fabricated device. Naming of the different currents and contact pads for characterization are indicated. The upper contact pads are used for static characterization whereas the lower contact pads are used for dynamic characterization.

sources and three electrical DC probes. The gain current and different gate currents are indicated as  $I_{\text{Gain}}$  and  $I_{G_i}$ , with  $i = 1, \dots, 4$ , respectively. The differential series resistances ( $dV/dI$ ) in the main FP cavity and the optical gates are  $3 \Omega$  and  $5 \Omega$ , respectively. The optical properties are measured by coupling the output light from the chip to a standard single-mode optical fiber (SMF) by means of a reflectionless SOI grating coupler [14] at the  $\text{DBR}_{\text{Out}}$  side. An HP 8153A power meter is used to measure the fiber-coupled optical output power. Figure 6.8(a) shows the light-current (LI) characteristics for the laser at different temperatures when the gates are left unbiased. Continuous-wave (CW) laser operation up to  $65^\circ\text{C}$  is achieved. At room temperature the laser threshold is 20 mA, with a maximum fiber-coupled output power of 0.1 mW. The grating coupler efficiency at the laser wavelength is  $-16$  dB (measured by means of a reference structure neighboring the laser device), which yields a maximum waveguide-coupled output power of 4 mW. The influence of the stage temperature on the laser threshold is shown in Fig. 6.8(b).

Laser spectra are measured with an Anritsu MS9740A optical spectrum analyzer (OSA). The laser spectrum at room temperature for  $I_{\text{Gain}} = 80$  mA with unbiased gates is shown in Fig. 6.9(a). The lack of wavelength selectivity results in a typical Fabry-Pérot spectrum. The total length of the main FP cavity ( $L_{\text{FP}}$ ) is  $600 \mu\text{m}$ , which corresponds to a longitudinal mode spacing  $\Delta\lambda_{\text{FP}} = 0.5$  nm, calculated from [22]

$$\Delta\lambda_{\text{FP}} = \frac{\lambda^2}{2n_g L_{\text{FP}}}, \quad (6.5)$$

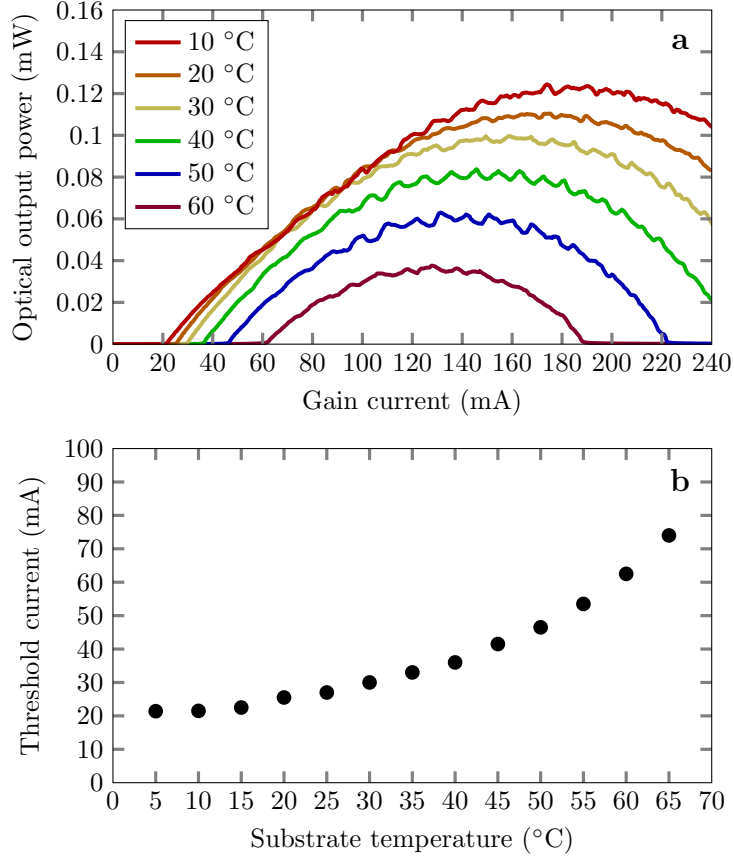


**Figure 6.8:** Static laser characteristics (with unbiased gates). (a) LI curves at different substrate temperatures (fiber-coupled output power); (b) Dependence of the threshold current on the substrate temperature.

with  $\lambda = 1580$  nm the center wavelength. The same longitudinal mode spacing is also obtained from the measured optical spectrum. When one of the SOA gates is biased at or above transparency single-mode laser operation can be achieved because of the filtered feedback, as explained in Section 6.2.5. Figure 6.9(b) shows the laser spectra when the gates are appropriately biased. The transparency current varies between 20 mA and 24 mA for the different gates. Single-mode laser operation is achieved with an SMSR larger than 35 dB for all four wavelength channels. The channel spacing is 4 nm.

Figure 6.9(c) shows the peak laser wavelength versus gate current for the different gates. At low gate currents (below transparency), the laser is not

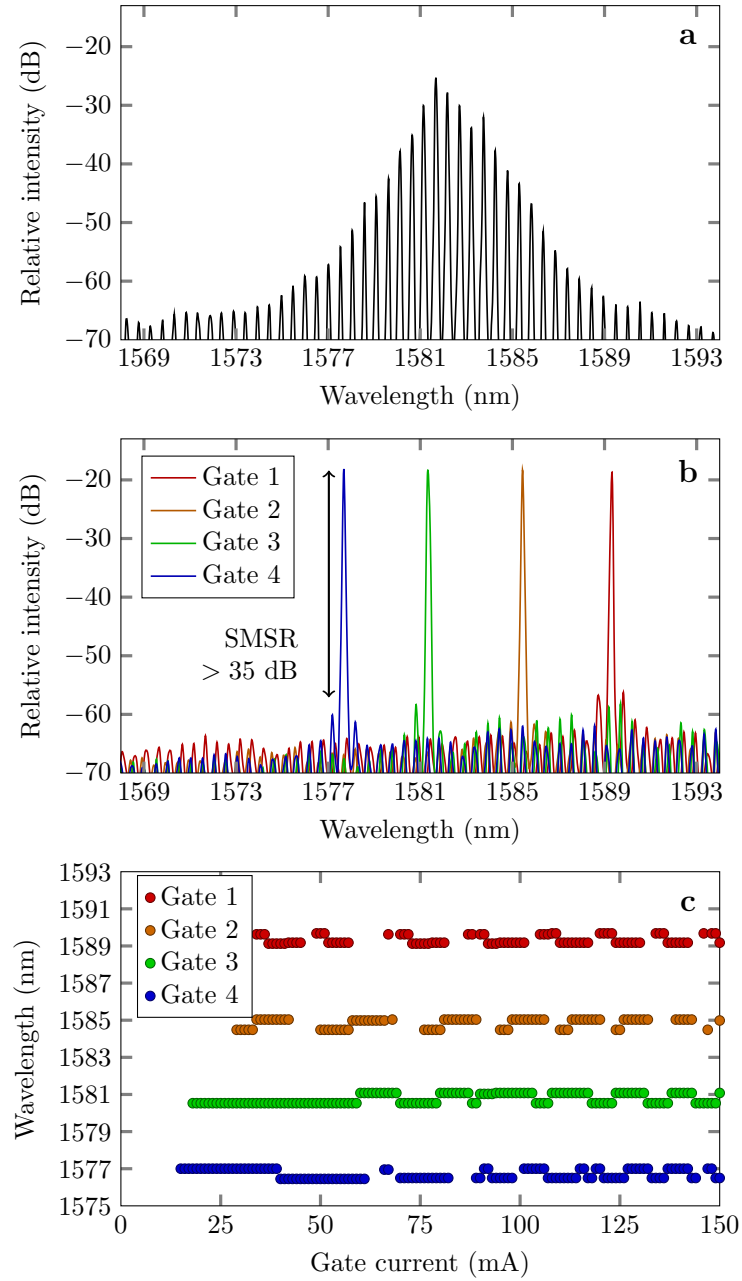


**Figure 6.9:** Static laser characteristics. (a) Laser spectrum when the gates are left unbiased; (b) Superimposed laser spectra when the gates are appropriately biased above transparency; (c) Dependence of the laser wavelength on the gate current (only data points with an SMSR > 35 dB are shown).

single-mode and operates at random wavelengths. Above transparency the laser can operate in single-mode regime. Generally the SMSR is larger than 35 dB. However, for certain gate currents the filtered optical feedback is out of phase with the oscillating laser mode, which effectively impedes single-mode operation. A large gate current leads to a large  $A_{\text{Gate}}$ , which leads to a large  $\gamma$  and which results in a larger SMSR at large gate currents as compared to lower gate currents. The 0.5 nm spaced mode hops are the result of a change in feedback phase and hence a different longitudinal mode selection, when the gate current is changed. In order to provide enhanced control of the feedback phase independently of the filtered feedback strength in future devices, a common phase control section could be added between the main FP cavity and the AWG input [23].

## 6.5 Dynamic laser characteristics

The dynamic characterization results include the small-signal laser characteristics, large-signal laser characteristics and the wavelength switching behavior between the different wavelength channels of the laser device.

### 6.5.1 Small-signal characteristics

Small-signal characterization of the laser is done using a Keysight PNA-X N5247A Microwave Network Analyzer. A small-amplitude radio frequency (RF) signal is combined with a DC  $I_{\text{Gain}}$  bias using a bias-tee. Using a 100  $\mu\text{m}$  pitch high-speed GSG electrical probe the combined signal is connected to the amplifier of the main Fabry-Pérot cavity. One of the gate currents is appropriately biased to achieve single-mode laser operation. The small-signal response is shown in Fig. 6.10(a) for  $I_{\text{Gain}} = 80$  mA and  $I_{\text{G1}} = 28$  mA. A 6 dB bandwidth of 6 GHz is obtained. Similar bandwidths are found when the other wavelength channels are operated. The reason for the limited bandwidth can be attributed to the presence of the external cavity. Indeed, the square of resonance frequency scales with  $L_{\text{FP}} / (L_{\text{FP}} + L_{\text{ext}})$  [24].

### 6.5.2 Large-signal characteristics

For the large-signal characterization of the laser a similar setup as for the small-signal characterization is used. This time a large-amplitude non-return-to-zero on-off-keying (NRZ-OOK) electrical signal is generated by means of a Keysight M8195A arbitrary waveform generator (AWG) at different bitrates. A 3 Vpp RF voltage swing is applied to the laser device with an  $I_{\text{Gain}} = 80$  mA DC bias. Eye diagrams are measured by means of a 40 GHz Discovery Semiconductors *p-i-n* photodiode of which the output is connected to a Keysight DSA-Z63 real-time oscilloscope. Open eye diagrams

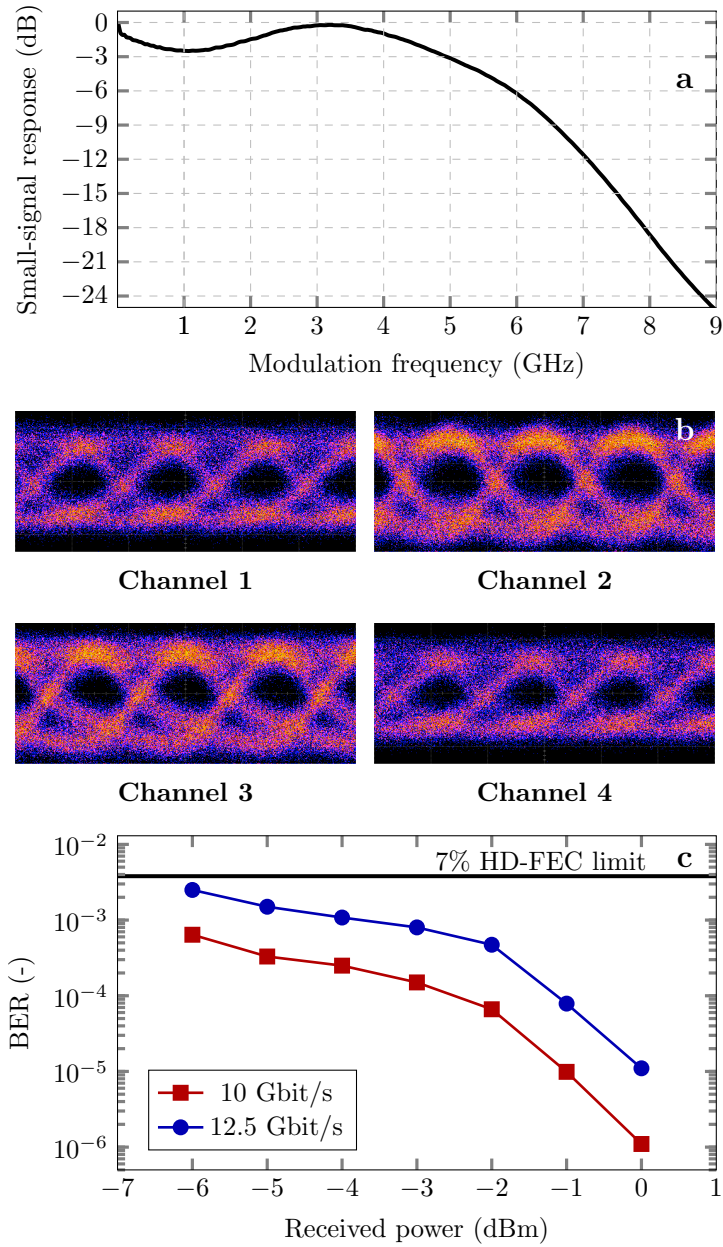


**Figure 6.10:** Dynamic laser characteristics. (a) Small-signal modulation response for  $I_{\text{Gain}} = 80$  mA and  $I_{\text{G1}} = 28$  mA (curve has been smoothed); (b) Eye diagrams for all four different wavelength channels under 12.5 Gbit/s direct modulation (back-to-back); (c) Bit error rate versus received power under 10 Gbit/s and 12.5 Gbit/s direct modulation (Channel 1, back-to-back).

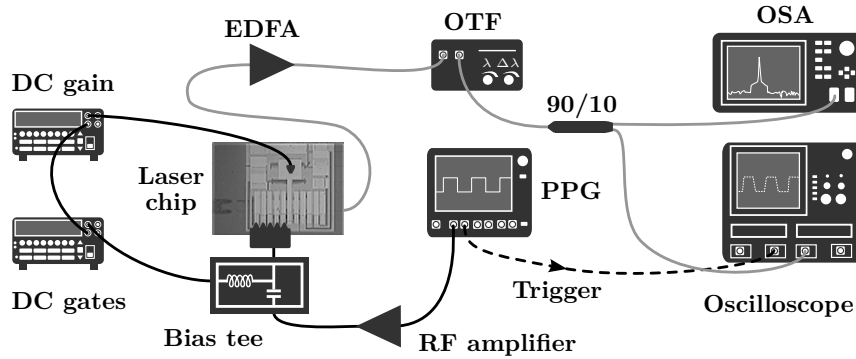


**Figure 6.11:** Schematic of the optical setup to measure the wavelength switching characteristics.

are obtained up to 12.5 Gbit/s for the four different wavelength channels. This is shown in Fig. 6.10(b). Data streams are stored using the real-time oscilloscope and an off-line bit error rate (BER) analysis is performed. The recorded BER versus received optical power is shown in Fig. 6.10(c) for back-to-back operation at both 10 Gbit/s and 12.5 Gbit/s for a pseudorandom binary sequence (PRBS) with a word length of  $2^7 - 1$ . Clearly a BER below  $3.8 \cdot 10^{-3}$  can be obtained, which enables error-free operation assuming 7% overhead hard decision forward error correction (HD-FEC) [25]. At a BER of  $10^{-5}$  the power penalty for increasing the bitrate from 10 Gbit/s to 12.5 Gbit/s is 1 dB. At a BER of  $5 \cdot 10^{-4}$  the power penalty is 3.3 dB, which is significantly larger as modulation is performed at the edge of the device bandwidth. We remark that a further increase of the direct modulation speed can be expected by exploiting the photon-photon resonance effect in the external cavities [26] and by making use of an optimized design with electrically isolated InP-to-silicon taper structures [27].

### 6.5.3 Wavelength switching characteristics

The measurement setup for characterization of the wavelength switching behavior is shown in Fig. 6.11. An Anritsu MP2100A pulse-pattern generator (PPG) and a  $100 \mu\text{m}$  pitch high-speed GSGSG electrical probe are used to differentially drive the bias in two neighboring gates while  $I_{\text{Gain}}$  remains fixed. The light output from the laser device is then amplified by an Erbium-Doped Fiber Amplifier (EDFA) and sent through a Santec OTF-350 tunable bandpass filter. The latter allows to filter out one of the wavelength channels upon switching. A 90/10 splitter is used to couple 90% and 10% of the light to an Anritsu MS9740A OSA and Tektronix DSA 8300 sampling oscilloscope with built-in photodiode, respectively. The OSA monitoring allows to appropriately tune the bandpass filter whereas the time-dependent power

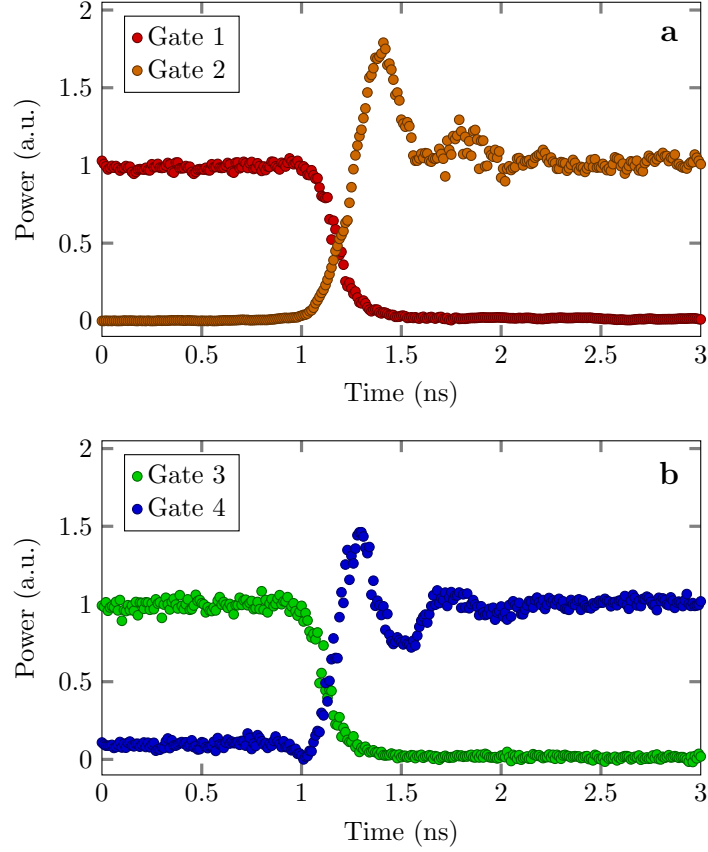


**Figure 6.12:** Wavelength switching characteristics. (a) Switching from Gate 1 to Gate 2; (b) Switching from Gate 3 to Gate 4.

levels in the two wavelength channels are monitored with the oscilloscope. As proof-of-principle wavelength tuning is done by periodically switching the bias between Gate 1 and Gate 2 and between Gate 3 and Gate 4 with a 500 ns periodic rectangular 0.75 V ( $\sim 0$  mA) – 1.1 V (50 mA) pulse train. Similar switching behavior can be expected between non-neighboring wavelength channels. The wavelength switching characteristics are shown in Fig. 6.12(a) and 6.12(b), for switching from Gate 1 to Gate 2 and from Gate 3 to Gate 4, respectively. Clearly, wavelength switching occurs in less than a nanosecond with a rise time of 195 ps and 135 ps, respectively. The fall time is 190 ps and 185 ps, respectively. Hereby rise (fall) time is defined as the time it takes for the response to rise (fall) from 10% (90%) to 90% (10%) of the steady-state response. It is clear that the obtained switching times are much shorter than for the demonstrated TTG-DFB lasers from

Chapter 4. This is because the stimulated emission process reduces the carrier lifetime. This is not the case for carrier injection in the passive tuning layer of the TTG stack.

## 6.6 Conclusion

In this chapter, we have discussed and demonstrated fast wavelength switching with a four-channel InP-on-silicon laser that exploits filtered feedback to achieve single-mode laser operation and tunability. At room temperature the laser has a threshold current of 20 mA with a maximum waveguide-coupled output power of 4 mW. CW operation up to 65°C is achieved. Wavelength switching times are less than 1 ns and each wavelength channel can be directly modulated at 12.5 Gbit/s, making the structure very useful for optical packet or burst switching applications.

## References

- [1] S. Dhoore, A. Rahim, G. Roelkens, and G. Morthier, “12.5 Gbit/s discretely tunable InP-on-silicon filtered feedback laser with sub-nanosecond wavelength switching times,” *Optics Express* **26**(7), 8059–8068 (2018).
- [2] F. Delorme, S. Slempek, P. Gambini, and M. Puleo, “Fast tunable 1.5  $\mu\text{m}$  distributed Bragg reflector laser for optical switching applications,” *Electronics Letters* **29**(1), 41–43 (1993).
- [3] J. Buus, M.-C. Amann, and D. J. Blumenthal, *Tunable laser diodes and related optical sources* (Wiley-Interscience New York, 2005).
- [4] S. Matsuo, T. Segawa, T. Kakitsuka, T. Sato, R. Takahashi, H. Suzuki, B. Docter, F. Karouta, and M. Smit, “Integrated filtered feedback tunable laser using double-ring-resonator-coupled filter,” in *Semiconductor Laser Conference, 2008. ISLC 2008. IEEE 21st International*, pp. 155–156 (IEEE, 2008).
- [5] B. Docter, J. Pozo, S. Beri, I. V. Ermakov, J. Danckaert, M. K. Smit, and F. Karouta, “Discretely tunable laser based on filtered feedback for telecommunication applications,” *IEEE Journal of Selected Topics in Quantum Electronics* **16**(5), 1405–1412 (2010).
- [6] S. Furst, S. Yu, and M. Sorel, “Fast and digitally wavelength-tunable semiconductor ring laser using a monolithically integrated distributed Bragg reflector,” *IEEE Photonics Technology Letters* **20**(23), 1926–1928 (2008).
- [7] L. A. Coldren, G. Fish, Y. Akulova, J. Barton, L. Johansson, and C. Coldren, “Tunable semiconductor lasers: a tutorial,” *Journal of Lightwave Technology* **22**(1), 193 (2004).
- [8] I. V. Ermakov, S. Beri, M. Ashour, J. Danckaert, B. Docter, J. Bolk, X. J. Leijtens, and G. Verschaffelt, “Semiconductor ring laser with on-chip filtered optical feedback for discrete wavelength tuning,” *IEEE Journal of Quantum Electronics* **48**(2), 129–136 (2012).
- [9] P. Dumon, W. Bogaerts, V. Wiaux, J. Wouters, S. Beckx, J. V. Campenhout, D. Taillaert, B. Luyssaert, P. Bienstman, D. V. Thourhout, and R. Baets, “Low-loss SOI photonic wires and ring resonators fabricated with deep UV lithography,” *IEEE Photonics Technology Letters* **16**(5), 1328–1330 (2004).
- [10] L. Chrostowski and M. Hochberg, *Silicon photonics design: from devices to systems* (Cambridge University Press, 2015).

- [11] A. P. Fischer, O. K. Andersen, M. Yousefi, S. Stolte, and D. Lenstra, "Experimental and theoretical study of filtered optical feedback in a semiconductor laser," *IEEE Journal of Quantum Electronics* **36**(3), 375–384 (2000).
- [12] D. M. Kane and K. A. Shore, *Unlocking dynamical diversity: optical feedback effects on semiconductor lasers* (John Wiley & Sons, 2005).
- [13] H. Erzgräber and B. Krauskopf, "Dynamics of a filtered-feedback laser: influence of the filter width," *Optics Letters* **32**(16), 2441–2443 (2007).
- [14] D. Vermeulen, Y. De Koninck, Y. Li, E. Lambert, W. Bogaerts, R. Baets, and G. Roelkens, "Reflectionless grating couplers for Silicon-on-Insulator photonic integrated circuits," *Optics Express* **20**(20), 22,278–22,283 (2012).
- [15] S. Keyvaninia, S. Verstuyft, L. V. Landschoot, F. Lelarge, G.-H. Duan, S. Messaoudene, J. M. Fedeli, T. D. Vries, B. Smalbrugge, E. J. Geluk, J. Bolk, M. Smit, G. Morthier, D. V. Thourhout, and G. Roelkens, "Heterogeneously integrated III-V/silicon distributed feedback lasers," *Optics Letters* **38**(24), 5434–5437 (2013).
- [16] "Luceda Photonics," (2017). URL <https://www.lucedaphotonics.com/en>.
- [17] W. Bogaerts, S. K. Selvaraja, P. Dumon, J. Brouckaert, K. De Vos, D. Van Thourhout, and R. Baets, "Silicon-on-insulator spectral filters fabricated with CMOS technology," *IEEE Journal of Selected Topics in Quantum Electronics* **16**(1), 33–44 (2010).
- [18] P. Dumon, W. Bogaerts, D. Van Thourhout, D. Taillaert, R. Baets, J. Wouters, S. Beckx, and P. Jaenen, "Compact wavelength router based on a silicon-on-insulator arrayed waveguide grating pigtailed to a fiber array," *Optics Express* **14**(2), 664–669 (2006).
- [19] R. Lang and K. Kobayashi, "External optical feedback effects on semiconductor injection laser properties," *IEEE journal of Quantum Electronics* **16**(3), 347–355 (1980).
- [20] M. Yousefi and D. Lenstra, "Dynamical behavior of a semiconductor laser with filtered external optical feedback," *IEEE Journal of Quantum Electronics* **35**(6), 970–976 (1999).
- [21] G. Roelkens, A. Abassi, P. Cardile, U. Dave, A. de Groot, Y. de Koninck, S. Dhoore, X. Fu, A. Gassenq, N. Hattasan, Q. Huang, S. Kumari, S. Keyvaninia, B. Kuyken, L. Li, P. Mechet, M. Muneeb, D. Sanchez, H. Shao, T. Spuesens, A. Z. Subramanian, S. Uvin, M. Tassaert, K. van Gasse, J. Verbist, R. Wang, Z. Wang, J. Zhang, J. van Campenhout,

- X. Yin, J. Bauwelinck, G. Morthier, R. Baets, and D. van Thourhout, “III-V-on-silicon photonic devices for optical communication and sensing,” *Photonics* **2**(3), 969–1004 (2015).
- [22] L. A. Coldren, S. W. Corzine, and M. L. Mashanovitch, *Diode lasers and photonic integrated circuits*, vol. 218 (John Wiley & Sons, 2012).
- [23] B. Docter, J. Pozo, I. Ermakov, X. Leijtens, F. Karouta, S. Beri, J. Danckaert, and M. Smit, “Integrated filtered-feedback tunable laser with enhanced control of feedback phase,” (TNO, 2010).
- [24] G. Sarlet, G. Morthier, and R. Baets, “Control of widely tunable SSG-DBR lasers for dense wavelength division multiplexing,” *Journal of Lightwave Technology* **18**(8), 1128 (2000).
- [25] J. Cho, C. Xie, and P. J. Winzer, “Analysis of soft-decision FEC on non-AWGN channels,” *Optics Express* **20**(7), 7915–7928 (2012).
- [26] G. Morthier, R. Schatz, and O. Kjebon, “Extended modulation bandwidth of DBR and external cavity lasers by utilizing a cavity resonance for equalization,” *IEEE Journal of Quantum Electronics* **36**(12), 1468–1475 (2000).
- [27] A. Abbasi, B. Moeneclaey, J. Verbist, X. Yin, J. Bauwelinck, G.-H. Duan, G. Roelkens, and G. Morthier, “Direct and electroabsorption modulation of a III-V-on-silicon DFB laser at 56 Gb/s,” *IEEE Journal of Selected Topics in Quantum Electronics* **23**(6), 1–7 (2017).

# 7

## Adiabatic tapered coupler for transfer printing

**T**HIS chapter covers the design of an adiabatic tapered coupling structure that is alignment tolerant and compatible with active III-V-on-silicon devices that are fabricated by means of transfer printing. The coupler can also be of interest for implementation in TTG-DBR laser structures.

### Contents

---

<b>7.1</b>	<b>Introduction</b>	<b>141</b>
<b>7.2</b>	<b>Coupler design</b>	<b>144</b>
<b>7.3</b>	<b>Other alignment-tolerant couplers</b>	<b>153</b>
<b>7.4</b>	<b>Conclusion</b>	<b>154</b>
	<b>References</b>	<b>155</b>

---

### 7.1 Introduction

Direct or adhesive bonding approaches are very suited for dense III-V integration on passive SOI waveguide circuits but are less efficient in terms of III-V material usage when a sparse integration of III-V is required [1]. Furthermore, they do not allow prior device testing and are difficult to implement when III-V devices need to be integrated on full platform silicon photonic ICs comprising a thick back-end stack.

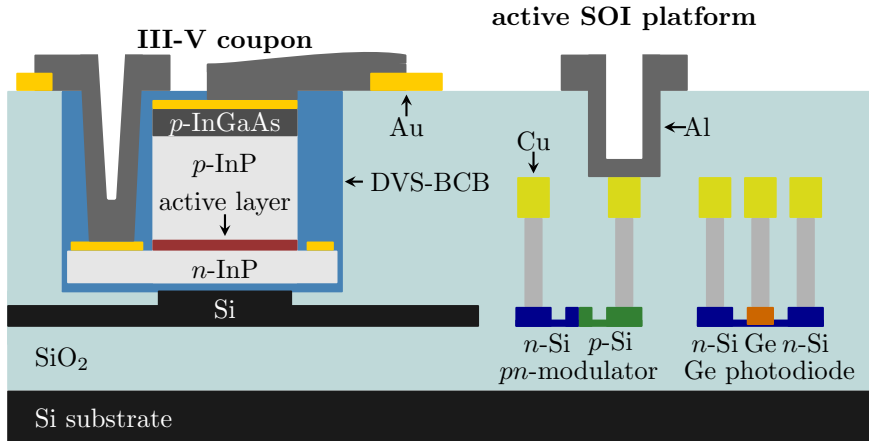


**Figure 7.1:** Illustration of sparse heterogeneous integration through transfer printing. The schematic shows a typical active silicon photonic integration platform. A local opening in the back-end stack contains a processed III-V device coupon.

Micro-transfer printing ( $\mu$ TP or just TP) is a relatively novel technique initially proposed by Rogers *et al.* [2] in 2004 that allows to transfer thin film components from a source to a target substrate. Shortly after its first introduction, several devices were successfully fabricated using the TP technique. Examples include a quantum dots display on glass [3], a stacked nano-membrane laser on silicon [4] and light-emitting diodes on diamond and glass substrates [5]. In the meanwhile, the technique has also been successfully employed to transfer processed III-V membranes such as FP laser devices to a silicon substrate [6]. In TP, a soft elastomeric stamp is used to pick-and-place the desired device structures in a massively parallel fashion. Hence the technique serves as a promising alternative to the bonding approaches for III-V integration on full platform silicon photonic ICs. III-V devices can first be (partially) realized in dense arrays on their native substrate, after which they are released from the substrate and transferred in parallel to the silicon photonic target wafer. Through wafer-scale global wiring the III-V/SOI device contacts are then connected to the metal contact pads. Figure 7.1 shows the layout of a typical active silicon photonic integration platform in which a local opening in the back-end stack is made for the processed III-V device coupon.

### 7.1.1 Process flow for transfer printing

Figure 7.2 shows a schematic of the TP process to integrate a III-V patterned device onto a silicon target substrate [7]. First the III-V device is

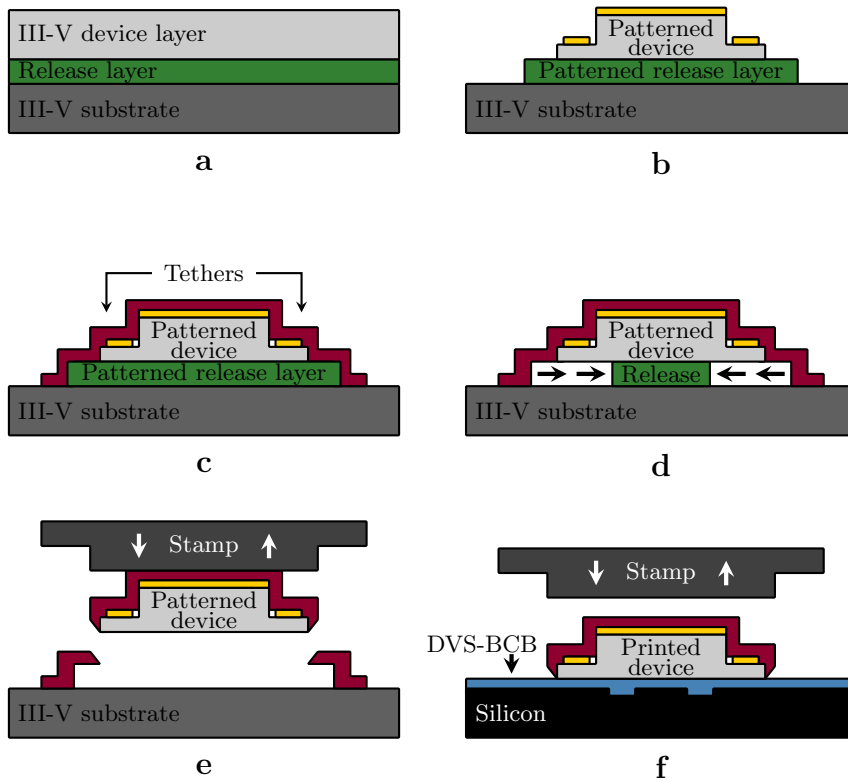


**Figure 7.2:** Process flow for transfer printing a III-V patterned device onto a silicon target substrate. (a) III-V source wafer; (b) Patterning of device and release layer; (c) Definition of tethers for device anchoring; (d) Removal of release layer; (e) Device pick-up from source; (f) Device release on target.

patterned on its native substrate. This comprises typical III-V processing and includes the definition of the metal contacts. Afterwards polymer tethers are defined that anchor the device to the substrate. During subsequent underetching of the release layer the III-V device becomes free-standing, only anchored to the substrate at specific points. During device pickup the tethers easily break at these anchor points. Finally the device is printed on the SOI target substrate. A thin DVS-BCB adhesive layer can be used to planarize the SOI surface, which facilitates the printing process.

### 7.1.2 Adiabatic tapered coupler for transfer printing

In order to efficiently couple light between the III-V waveguide layer and the silicon waveguide layer adiabatic tapered III-V/SOI couplers are commonly employed. Such optical coupling structures can be made highly effi-

cient [8–10] and ultra-compact [11] but typically require a lateral alignment accuracy better than 300 nm [11, 12]. Currently the alignment accuracy in high-throughput TP lies between 500 nm and 1  $\mu\text{m}$  such that those conventional coupling structures are not suited for TP. Here we propose a novel adiabatic tapered coupler that enables alignment-tolerant coupling for active III-V/SOI devices.

## 7.2 Coupler design

In this section we will provide an in-depth discussion of the coupler design together with an analysis of the different parameters that influence the coupling efficiency and alignment tolerance.

### 7.2.1 Technology platforms and simulation tools

We consider *imec*'s active silicon photonic integration platform [13] as the target wafer for the transfer printed devices. The SOI platform comes with a 160 nm thick polycrystalline silicon (*p*-Si) layer on top of a 220 nm thick monocrystalline silicon (*c*-Si) layer. Such a silicon waveguide layer thickness enables efficient light coupling from the III-V to the SOI waveguide in heterogeneously integrated III-V/SOI devices [8]. The silicon substrate and silicon device layer are separated by a 2  $\mu\text{m}$ -thick BOX layer.

For the III-V material an epitaxial layer stack is assumed that matches a typical 1550 nm optical amplifier epitaxial layer stack. The stack consists of an *n*-InP bottom cladding layer (thickness to be optimized, as discussed in the respective design sections), a 300 nm-thick AlGaInAs core layer and a 1.6  $\mu\text{m}$ -thick InP top cladding. The stack is representative for a real active stack containing quantum wells and barriers but the AlGaInAs core and InP top cladding layers can also be considered to be passively regrown such that no electrical pumping of the coupler is required. In that case no *p*-doping of the InP top cladding is required either. The details of the assumed epitaxial layer stack are shown in Table 7.1. Extensive use is made of the commercially available software Fimmwave, an optical mode solver from Photon Design [14]. The Eigenmode Expansion (EME) method [15] is used to simulate the light propagation in the proposed coupling structures. Simulations are carried out for transverse electric (TE)-polarized light at a wavelength of 1550 nm.

### 7.2.2 Coupling mechanism

Just as in many commonly employed coupling structures, the mode conversion from the III-V waveguide to the SOI waveguide is based on adiabatic tapering [16]. By varying the waveguide dimensions along the structure, the

**Table 7.1:** Detailed III-V epitaxial layer stack. The refractive index (RI) values are at 1550 nm.

Layer	Composition	Doping	Thickness (nm)	RI
Cladding	InP	NID	1600	3.169
Quaternary	AlGaInAs	NID	300	3.325
Cladding	InP	$n$	$t_{n-clad}$	3.169

effective indices of the fundamental local modes of the unperturbed waveguides (i.e. the III-V and SOI waveguide) can be increased or decreased. In this way the optical mode is gradually coupled from one waveguide to another. At the intermediate phase-matching point the energy of the optical mode is equally distributed over both waveguides. If the spatial waveguide variations occur gradual enough no light is coupled to higher-order modes and the tapering is said to be adiabatic.

### 7.2.3 Coupling structure

Figures 7.3(a)–7.3(c) show a detailed schematic of the proposed adiabatic tapered coupler. The III-V waveguide structure is assumed to be transfer printed onto the SOI waveguide circuit using a DVS-BCB adhesive bonding layer. A passive regrown III-V stack is assumed in the taper such that no electrical pumping of the coupler is required. The structure comprises three tapered coupling sections that gradually transform the optical mode from the III-V waveguide to the silicon waveguide. The first coupling section consists of a two-step piecewise linear taper that converts the optical mode from the III-V waveguide to an InP rib waveguide implemented in the  $n$ -type contact layer. The InP contact layer is  $n$ -doped and hence propagation losses due to free-carrier absorption are small ( $\alpha$  ( $\text{cm}^{-1}$ )  $\approx 10^{-18}\text{cm}^2 N_D$ , with  $N_D$  the doping ( $\text{cm}^{-3}$ ) of the layer). The bottom slab of the  $n$ -InP rib waveguide is designed to be 300 nm thick, which facilitates the TP pick-up and release process. In the second coupling section a short linear taper increases the width of the  $n$ -InP waveguide to broaden the optical mode. This enhances the tolerance of the structure with respect to lateral misalignment of the III-V and the underlying silicon waveguide introduced by the TP process. In the third coupling section another two-step piecewise linear taper (defined in silicon) is used to eventually couple the light to the silicon output waveguide. Finally the  $n$ -InP rib waveguide is tapered down to minimize reflections at the end of the coupling structure.

### 7.2.4 Optimization of Coupling Section 1

The details of Coupling Section 1 are shown in Fig. 7.4(a). The optical mode initially resides in the III-V waveguide, which is assumed to be 3  $\mu\text{m}$  wide. A

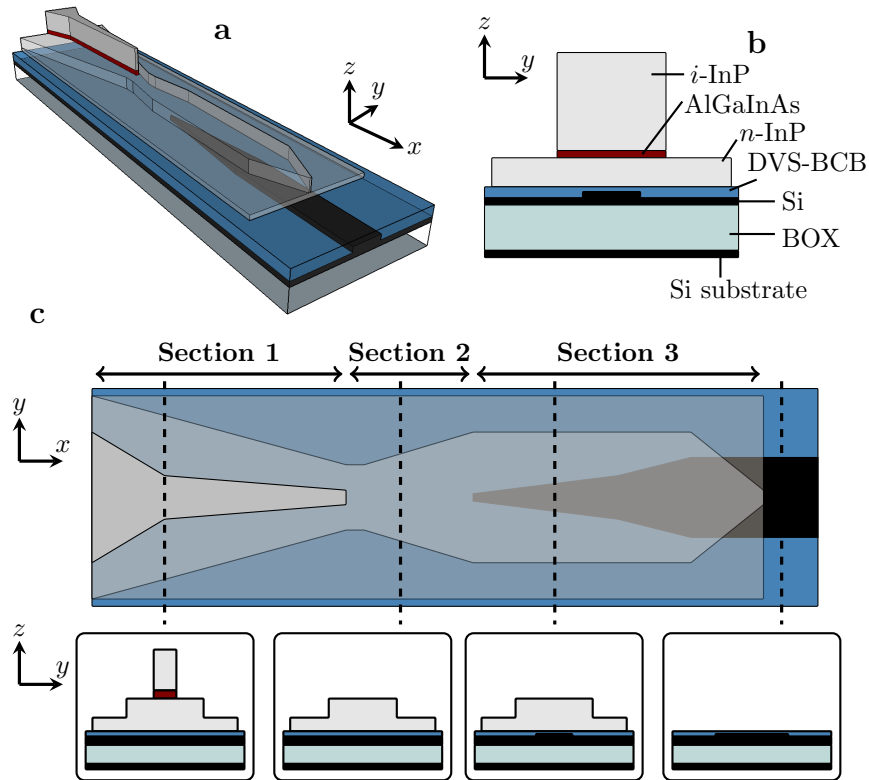


**Figure 7.3:** Schematic of the adiabatic tapered coupler. (a) 3D view; (b) Projected cross-sectional view with indication of the different layers; (c) Top view with cross-sectional views along the coupling structure.

two-step piecewise linear taper is used to gradually decrease the waveguide width such that the optical mode is adiabatically coupled to the  $n$ -InP rib waveguide. The intermediate waveguide width is chosen to be  $1\ \mu\text{m}$ . The length of the first taper part can be chosen as short as  $50\ \mu\text{m}$ . In the second part the actual coupling to the  $n$ -InP rib waveguide occurs, leading to a larger length of the second part of the taper. The coupling efficiency strongly depends on the dimensions of the  $n$ -InP rib waveguide and the achievable width of the III-V taper tip ( $w_{\text{III-V tip}}$ ). Both dependencies are discussed below.

#### Choice of the $n$ -InP cladding layer thickness

Figure 7.4(c) shows the coupling efficiency of the fundamental TE-mode of the III-V waveguide to the fundamental TE-mode of the butt-coupled

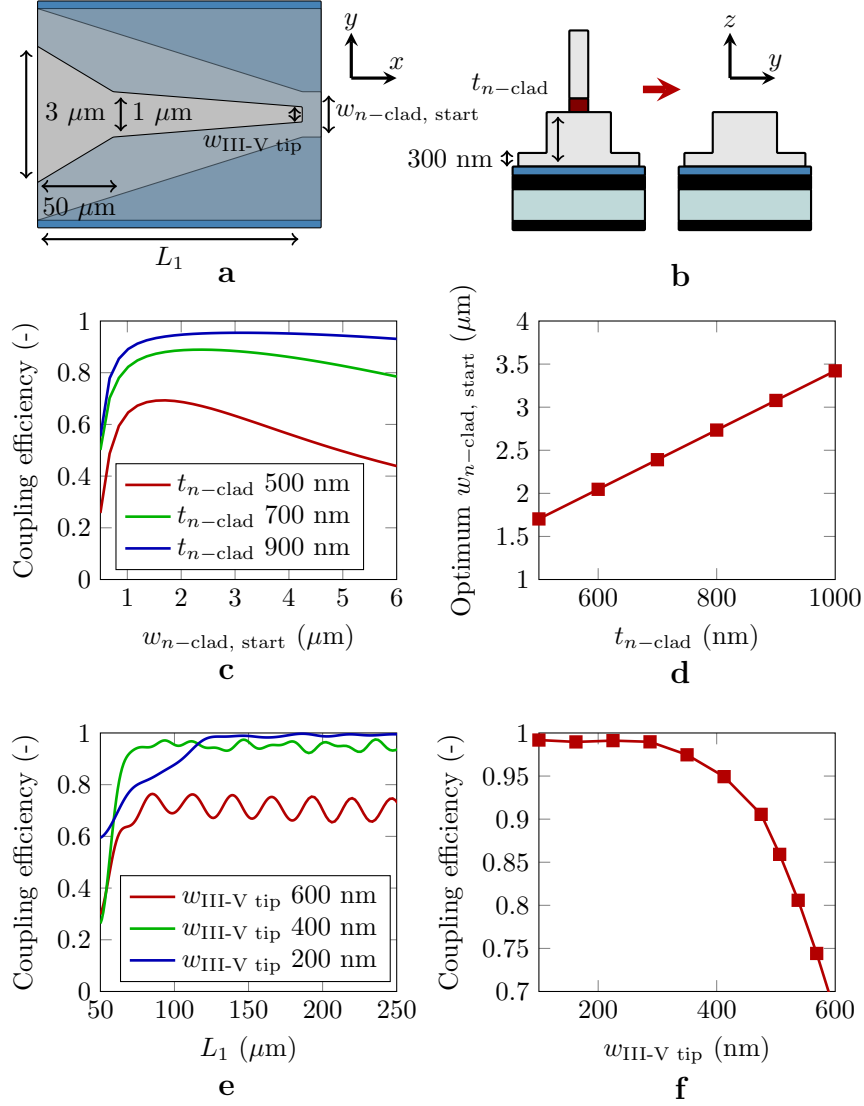


**Figure 7.4:** Optimization of Coupling Section 1. (a) Schematic of Coupling Section 1; (b) Schematic of the interface at the end of Coupling Section 1; (c) Transmission at the interface at the end of Coupling Section 1 versus width of the  $n$ -InP rib waveguide for different thicknesses of the  $n$ -InP bottom cladding,  $w_{\text{III-V tip}} = 400 \text{ nm}$ ; (d) Optimum choice of the  $n$ -InP rib waveguide width versus length; (e) Taper coupling efficiency versus taper length for different values of the III-V taper tip width,  $t_{n\text{-clad}} = 900 \text{ nm}$  and  $w_{n\text{-clad, start}} = 3 \mu\text{m}$ ; (f) Taper coupling efficiency versus III-V taper tip width for  $L_1 = 150 \mu\text{m}$ ,  $t_{n\text{-clad}} = 900 \text{ nm}$  and  $w_{n\text{-clad, start}} = 3 \mu\text{m}$ .

$n$ -InP rib waveguide versus width of the  $n$ -InP waveguide ( $w_{n\text{-clad, start}}$ ), for different thicknesses of the  $n$ -InP cladding layer ( $t_{n\text{-clad}}$ ). A schematic of the considered interface is shown in Fig. 7.4(b). A III-V taper tip width of 400 nm is assumed. As expected the transmission at the interface increases with increasing thickness of the  $n$ -InP cladding layer. Furthermore, for a given  $n$ -InP thickness an optimum width of the  $n$ -InP waveguide can be chosen for maximal transmission. This is because for a narrow ( $< 1 \mu\text{m}$ )  $n$ -InP waveguide the finite extent of the III-V taper tip prevents a high coupling efficiency whereas for very wide  $n$ -InP waveguides the mode mismatch at the interface increases, such that the coupling efficiency drops. Figure 7.4(d) shows the optimum  $n$ -InP waveguide width versus  $n$ -InP thickness. An  $n$ -InP thickness of 900 nm is chosen with a corresponding optimum  $n$ -InP waveguide width of  $3 \mu\text{m}$ .

### Influence of III-V taper tip width

The coupling efficiency is substantially influenced by the width of the III-V taper tip. Figure 7.4(e) shows the taper coupling efficiency versus taper length ( $L_1$ ), for different III-V taper tip widths. The simulations are performed assuming the optimum dimensions obtained before. The coupling efficiency saturates at a value determined by the butt-coupling of both waveguides. For taper tips narrower than 200 nm coupling is near to ideal. In practice III-V taper tip widths smaller than 400 nm are possible to obtain with standard optical lithography and subsequent lateral underetching of the passive quaternary layer, as demonstrated in [17]. This yields a coupling efficiency of more than 96% for a taper length of  $150 \mu\text{m}$ . Figure 7.4(f) shows the coupling efficiency versus III-V taper tip width for a fixed taper length of  $150 \mu\text{m}$ . For taper tips wider than 500 nm the coupling efficiency already drops below 85%.

### 7.2.5 Optimization of Coupling Section 2

The details of Coupling Section 2 are shown in Fig. 7.5(a). The coupling section consists of a linear taper and serves to broaden the optical mode as to improve the alignment tolerance of the coupling structure. Based on the simulation results from Section 7.2.4 the starting width of the  $n$ -InP waveguide is assumed to be  $3 \mu\text{m}$ . The choice of the width of the  $n$ -InP end waveguide ( $w_{n\text{-clad, end}}$ ) depends on the imposed alignment tolerance requirements. In general tapering to a wider  $n$ -InP rib waveguide will increase the alignment tolerance, at the expense of a slightly longer taper. In any case the length of Coupling Section 2 can be chosen very short, as is clear from Fig. 7.5(b). A taper length of  $30 \mu\text{m}$  already suffices to achieve over 99% coupling efficiency for a width of the  $n$ -InP end waveguide of  $4 \mu\text{m}$ . A  $4 \mu\text{m}$  waveguide width is also assumed in the remainder of the manuscript. Note that the values for the coupling efficiencies at  $L_2 = 0 \mu\text{m}$

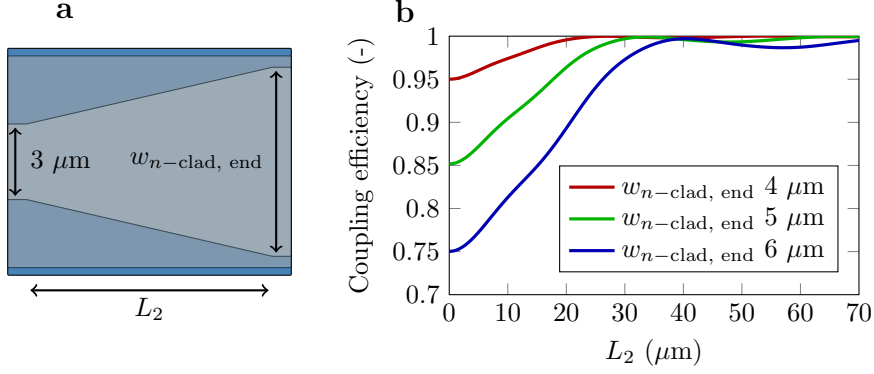


**Figure 7.5:** Optimization of Coupling Section 2. (a) Schematic of Coupling Section 2; (b) Taper coupling efficiency versus taper length for different values of the InP waveguide end width.

correspond with the coupling efficiencies for the  $3 \mu\text{m}$  wide  $n$ -InP waveguide butt-coupled to the  $w_{n\text{-clad, end}}$  wide  $n$ -InP waveguide.

### 7.2.6 Optimization of Coupling Section 3

In Coupling Section 3 light is converted from the broad  $n$ -InP rib waveguide to the underlying silicon device layer. A schematic of Coupling Section 3 is shown in Fig. 7.6(a). A two-step piecewise linear silicon taper is used. At the end of the coupling structure the III-V waveguide is tapered down to enhance the coupling efficiency and to minimize reflections. This tapered section can be very short: a length of  $30 \mu\text{m}$  suffices to achieve a good coupling efficiency. The coupling efficiency of Coupling Section 3 is greatly influenced by the III-V/silicon spacing (i.e. the thickness of the DVS-BCB adhesive layer) and the width of the silicon waveguide. The influence of both parameters is discussed below.

Figures 7.6(c) and 7.6(d) show the coupling efficiency of the fundamental TE-mode of the  $n$ -InP waveguide to the fundamental TE-mode of the silicon waveguide at the end of Coupling Section 3 versus silicon waveguide width, for different values of the III-V taper tip width and the DVS-BCB thickness. A schematic of the considered interface is shown in Fig. 7.6(b). As expected the coupling efficiency increases with increasing silicon waveguide width, as the mode becomes much stronger confined to the silicon waveguide. Figure 7.6(e) shows the coupling efficiency versus III-V taper tip width for different values of the DVS-BCB thickness. As the spacing between the III-V and silicon waveguide increases both waveguides are stronger decoupled

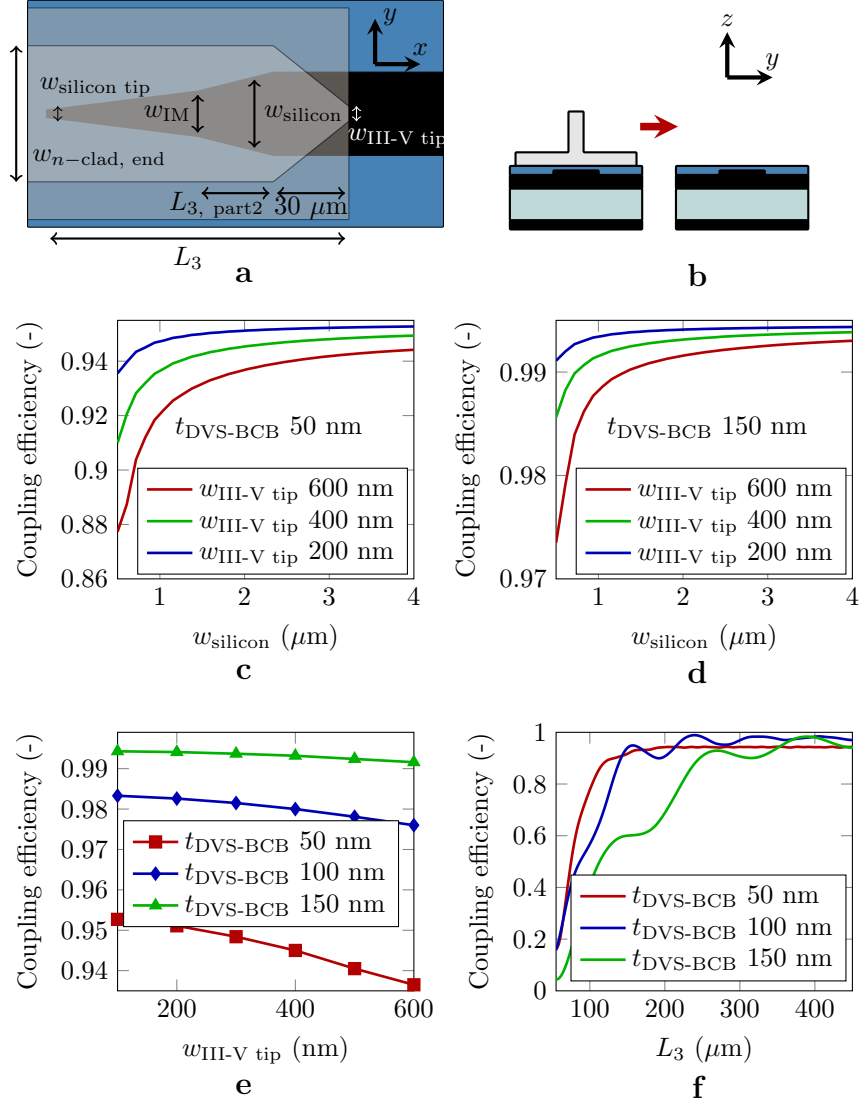


**Figure 7.6:** Optimization of Coupling Section 3. (a) Schematic of Coupling Section 3; (b) Schematic of interface at the end of Coupling Section 3; (c) Transmission at the interface at the end of Coupling Section 3 versus width of the silicon waveguide for different values of the III-V taper tip width,  $t_{\text{DVS-BCB}} = 50$  nm; (d) Transmission at the interface at the end of Coupling Section 3 versus width of the silicon waveguide for different values of the III-V taper tip width,  $t_{\text{DVS-BCB}} = 150$  nm; (e) Transmission at the interface at the end of Coupling Section 3 versus III-V taper tip width for different values of the DVS-BCB thickness,  $w_{\text{silicon}} = 2 \mu\text{m}$ ; (f) Taper coupling efficiency versus taper length for different values of the DVS-BCB thickness,  $w_{\text{silicon}} = 2 \mu\text{m}$ ,  $w_{\text{IM}} = 1.1 \mu\text{m}$ .

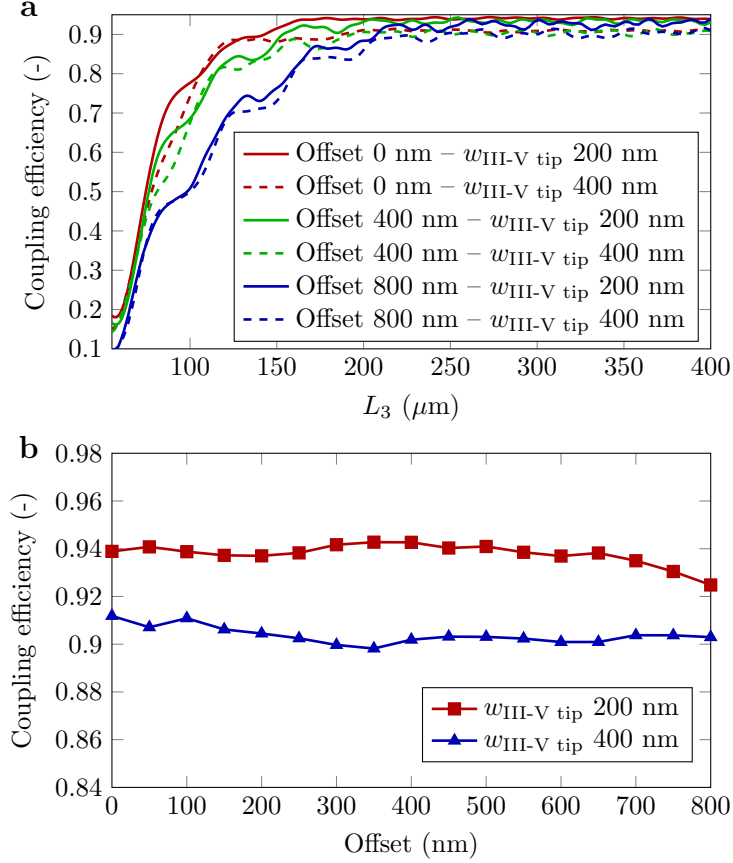


**Figure 7.7:** Overall coupling structure. (a) Coupling efficiency versus length of Coupling Section 3 ( $L_3$ ) for different lateral alignment offsets and values of the III-V taper tip width; (b) Coupling efficiency versus lateral alignment offset for different values of the III-V taper tip width,  $L_3 = 255 \mu\text{m}$ .

and the coupling efficiency increases. Obviously a larger III-V/silicon spacing will also increase the taper length, which is not desired. The width of the silicon taper tip ( $w_{\text{silicon tip}}$ ) is assumed to be 150 nm. This corresponds with the minimum reproducible dimension obtainable in a typical *imec* SOI run and only slightly influences the coupling efficiency. Simulations indicate that for silicon taper tip widths below 200 nm the coupling efficiency stays above 98%. Figure 7.6(f) shows the coupling efficiency versus taper length for different values of the DVS-BCB thickness.  $w_{\text{IM}}$  is chosen to be 1.1  $\mu\text{m}$ , which is beyond the phase-matching point such that the mode is already well confined to the silicon waveguide at this point along the coupler.  $L_{3, \text{ part 2}}$  can therefore be chosen as short as 25  $\mu\text{m}$ . For modest DVS-BCB

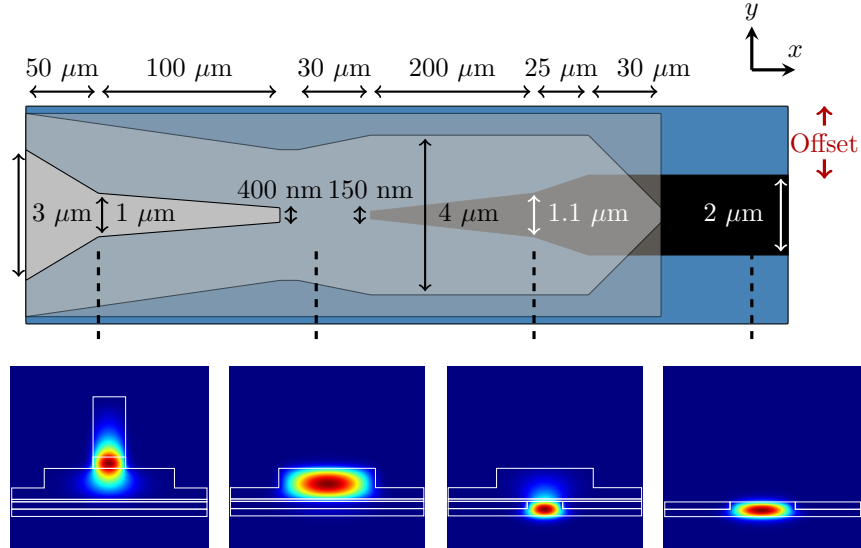


**Figure 7.8:** Overall coupling structure. Light propagation from the III-V waveguide to the SOI waveguide in the overall coupling structure for  $w_{\text{III-V tip}} = 400$  nm. Mode profiles along the coupler are indicated as well.

thicknesses ( $< 100$  nm) and a silicon waveguide width of  $2 \mu\text{m}$  a coupling efficiency of 94% is retrieved assuming a III-V taper tip width of 400 nm and a taper length ( $L_3$ ) of  $250 \mu\text{m}$ .

### 7.2.7 Overall coupling structure – lateral misalignment tolerance

Figure 7.7(a) shows the overall taper coupling efficiency versus taper length  $L_3$  for different lateral alignment offsets ( $y$ -direction) of the silicon waveguide with respect to the III-V waveguide, simulated for a III-V taper tip width of 200 nm and 400 nm. A DVS-BCB thickness of 50 nm is assumed. It is clear that for a given coupling efficiency a longer taper length is needed for a larger lateral alignment offset. However, at a taper length  $L_3$  of  $255 \mu\text{m}$  the coupling efficiency reaches values above 90%, even for a very large lateral alignment offset of 800 nm. This is a significant improvement as compared to previously reported coupling structures, which typically require a lateral alignment accuracy better than 300 nm. In Fig. 7.7(b) the coupling efficiency is shown versus lateral alignment offset for  $L_3 = 255 \mu\text{m}$ . A very robust performance is achieved with a coupling efficiency varying only a few percent with varying lateral alignment offset. Coupling to higher order

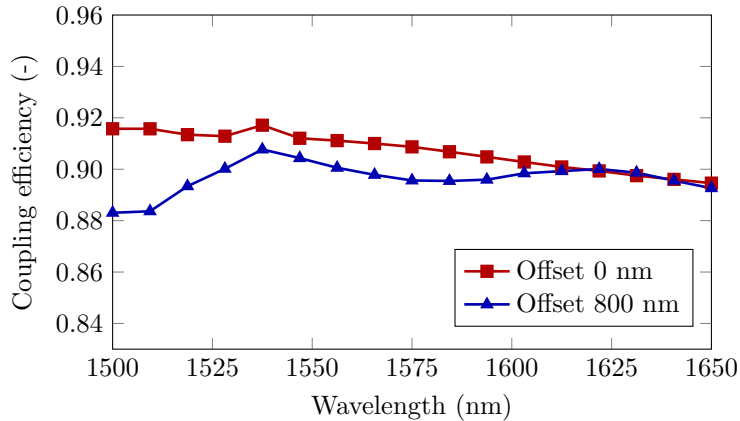


**Figure 7.9:** Wavelength dependence of the coupler efficiency for the overall optimized coupling structure with  $n$ -InP intermediate waveguide,  $w_{\text{III-V tip}} = 400$  nm.

modes remains below 1%, even for large lateral alignment offsets. Furthermore, by tapering down the silicon waveguide, the waveguide can be made single-mode such that guided higher-order modes will eventually radiate out and will not be present in the remaining optical circuit. Figure 7.8 shows the overall optimized coupling structure, assuming a III-V taper tip width of 400 nm. Mode profiles along the coupler show the adiabatic mode transformation from the III-V to the SOI waveguide. Finally Figure 7.9 shows the wavelength dependence of the coupler performance, both for a 0 nm and 800 nm lateral alignment offset. The simulations indicate that the coupling efficiency varies less than 5% over a broad wavelength range covering the C and L band. Finally the back reflections in the coupling structure are assessed. For taper tip widths between 200 nm and 400 nm and lateral alignment offsets between 0 nm and 800 nm the simulated back reflection remains smaller than -26 dB, which is adequate for most applications.

### 7.3 Other alignment-tolerant couplers

Also other structures have been proposed that can provide alignment-tolerant coupling in heterogeneously integrated devices. An example of such a coupler is presented in [18] and does not require tapers to be etched in the III-V waveguide. The advantage is that no long coupling structures are present in the III-V material such that regrowth of a passive layer stack can be avoided. Instead, use is made of an approach where the III-V waveguide is butt-coupled into a polymer waveguide with low refractive index ( $n = 1.69$ ). The mode in the polymer waveguide structure is then coupled to the underlying silicon waveguide using an inverted taper structure. A

very robust coupling performance with respect to lateral misalignment can be expected from simulations across the entire C and L band. The alternative coupling structure is, however, not compatible with the TTG-DBR laser design and mainly suited for heterogeneously integrated amplifiers and fixed-wavelength DFB lasers.

## 7.4 Conclusion

In this chapter a novel tapered coupler for adiabatic mode conversion in active III-V/SOI devices has been presented. The coupler makes use of a broad and thick  $n$ -InP waveguide to which light is coupled as an intermediate step. This greatly enhances the misalignment tolerance, which is needed to comply with the current requirements for high-throughput TP. The proposed coupler is expected to facilitate transfer-printing based heterogeneous integration of processed active III-V membrane devices on both passive and active SOI platforms.

## References

- [1] Z. Wang, A. Abbasi, U. Dave, A. Groote, S. Kumari, B. Kunert, C. Merckling, M. Pantouvaki, Y. Shi, B. Tian, K. Gasse, J. Verbist, R. Wang, W. Xie, J. Zhang, Y. Zhu, J. Bauwelinck, X. Yin, Z. Hens, J. Campenhout, B. Kuyken, R. Baets, G. Morthier, D. Thourhout, and G. Roelkens, “Novel light source integration approaches for silicon photonics,” *Laser & Photonics Reviews* **11**(4), 1700,063 (2017).
- [2] E. Menard, K. Lee, D.-Y. Khang, R. Nuzzo, and J. Rogers, “A printable form of silicon for high performance thin film transistors on plastic substrates,” *Applied Physics Letters* **84**(26), 5398–5400 (2004).
- [3] T.-H. Kim, K.-S. Cho, E. K. Lee, S. J. Lee, J. Chae, J. W. Kim, D. H. Kim, J.-Y. Kwon, G. Amaratunga, S. Y. Lee, B. L. Choi, Y. Kuk, J. M. Kim, and K. Kim, “Full-colour quantum dot displays fabricated by transfer printing,” *Nature Photonics* **5**, 176–182 (2011).
- [4] H. Yang, D. Zhao, S. Chuwongin, J.-H. Seo, W. Yang, Y. Shuai, J. Berggren, M. Hammar, Z. Ma, and W. Zhou, “Transfer-printed stacked nanomembrane lasers on silicon,” *Nature Photonics* **6**(9), 615 (2012).
- [5] A. Trindade, B. Guilhabert, D. Massoubre, D. Zhu, N. Laurand, E. Gu, I. Watson, C. J. Humphreys, and M. Dawson, “Nanoscale-accuracy transfer printing of ultra-thin AlInGaN light-emitting diodes onto mechanically flexible substrates,” *Applied Physics Letters* **103**(25), 239\_1 (2013).
- [6] J. Justice, C. Bower, M. Meitl, M. B. Mooney, M. A. Gubbins, and B. Corbett, “Wafer-scale integration of group III–V lasers on silicon using transfer printing of epitaxial layers,” *Nature Photonics* **6**(9), 610 (2012).
- [7] “X-Celeprint,” (2017). URL <https://x-celeprint.com/>.
- [8] M. Lamponi, S. Keyvaninia, C. Jany, F. Poingt, F. Lelarge, G. de Valicourt, G. Roelkens, D. V. Thourhout, S. Messaoudene, J.-M. Fedeli, and G. H. Duan, “Low-threshold heterogeneously integrated InP/SOI lasers with a double adiabatic taper coupler,” *IEEE Photonics Technology Letters* **24**(1), 76–78 (2012).
- [9] S. Keyvaninia, G. Roelkens, D. V. Thourhout, C. Jany, M. Lamponi, A. L. Liepvre, F. Lelarge, D. Make, G.-H. Duan, D. Bordel, and J.-M. Fedeli, “Demonstration of a heterogeneously integrated III-V/SOI single wavelength tunable laser,” *Optics Express* **21**(3), 3784–3792 (2013).

- 
- [10] G. Kurczveil, P. Pintus, M. J. Heck, J. D. Peters, and J. E. Bowers, “Characterization of insertion loss and back reflection in passive hybrid silicon tapers,” *IEEE Photonics Journal* **5**(2), 6600,410–6600,410 (2013).
- [11] Q. Huang, J. Cheng, L. Liu, Y. Tang, and S. He, “Ultracompact tapered coupler for the Si/III–V heterogeneous integration,” *Applied Optics* **54**(14), 4327–4332 (2015).
- [12] D. Van Thourhout, S. Keyvaninia, G. Roelkens, M. Lamponi, F. Lelarge, J. Fedeli, S. Messaoudene, and G. Duan, “Optimization of taper structures for III-V silicon lasers,” in *2012 International Conference on Solid State Devices and Materials (SSDMS-2012)*, pp. 524–525 (2012).
- [13] “imec iSIPP50G silicon photonics technology,” (2017). URL [http://www.europractice-ic.com/SiPhotonics\\_technology\\_imec\\_ISIPP50G.php](http://www.europractice-ic.com/SiPhotonics_technology_imec_ISIPP50G.php).
- [14] “Fimmwave: a powerful waveguide mode solver,” (2017). URL <https://www.photond.com/>.
- [15] D. F. Gallagher and T. P. Felici, “Eigenmode expansion methods for simulation of optical propagation in photonics: pros and cons,” in *Integrated Optics: Devices, Materials, and Technologies VII*, vol. 4987, pp. 69–83 (International Society for Optics and Photonics, 2003).
- [16] X. Sun and A. Yariv, “Engineering supermode silicon/III-V hybrid waveguides for laser oscillation,” *Journal of the Optical Society of America B* **25**(6), 923–926 (2008).
- [17] X. Fu, J. Cheng, Q. Huang, Y. Hu, W. Xie, M. Tassaert, J. Verbist, K. Ma, J. Zhang, K. Chen, C. Zhang, Y. Shi, J. Bauwelinck, G. Roelkens, L. Liu, and S. He, “5 x 20 Gb/s heterogeneously integrated III-V on silicon electro-absorption modulator array with arrayed waveguide grating multiplexer,” *Optics Express* **23**(14), 18,686–18,693 (2015).
- [18] S. Dhoore, S. Uvin, D. Van Thourhout, G. Morthier, and G. Roelkens, “Novel adiabatic tapered couplers for active III–V/SOI devices fabricated through transfer printing,” *Optics Express* **24**(12), 12,976–12,990 (2016).

# 8

## Conclusion and prospects

### 8.1 Conclusion

As outlined in the introduction chapter, heterogeneously integrated fast tunable lasers are expected to become key components for optical packet switching systems in future data center networks. They can also be useful for spectroscopy and other emerging applications such as LIDAR in autonomous vehicles. In this work, we have proposed and realized several InP-on-silicon electronically tunable laser diodes that could fulfill these roles to a certain extent. The main approach to reach this target originates from the use of an InP/InGaAsP tunable twin-guide (TTG) epitaxial layer stack, where carrier injection into the InGaAsP tuning layer allows for nanosecond fast tuning of the laser wavelength. This is highly facilitated by the very strong free-carrier plasma dispersion effect in InGaAsP, which yields tuning efficiencies and tuning ranges for which related methods based on carrier-depletion or tuning in silicon stand no chance to reach comparable characteristics. Good single-mode laser operation and a 2 nm continuous wavelength tuning range with a DFB structure have readily been achieved. Direct modulation at 12.5 Gbit/s is demonstrated and dynamic wavelength modulation experiments indicate wavelength switching times around 3 ns. The more advanced sampled grating (SG-) TTG-DFB laser shows promising characteristics too, but requires an optimized epitaxial layer stack growth process to reach broadband gain and wide tunability. Therefore, also effort has been put into the investigation of alternative laser structures based on the more standard InP/InGaAsP amplifier stack. A sampled grating DFB

laser with wide discrete wavelength tuning over 55 nm has been successfully demonstrated and only requires two injection currents for laser operation and tuning. Likewise, promising behavior stems from the four-channel wavelength-selectable AWG-based filtered feedback laser characterization results. With the laser device direct modulation up to 12.5 Gbit/s and sub-nanosecond switching times between the different wavelength channels have been achieved. The structure is of particular interest as the design can easily be matched with the AWG grid of the deployed passive filter in the routing network.

## 8.2 Prospects

Although the presented laser devices form a good first step towards the realization of transmitters that are compatible with optical packet switching, there is still ample room for improvement and further elaboration on the chosen paths presented in this work. Clearly the use of a TTG epitaxial layer stack highly complicates the laser design and yields additional complexity in epitaxial growth and laser fabrication. However, we believe there is good reason to continue the research on this subject. The following TTG-based laser structures could be of particular interest:

**TTG-DBR laser** The design of a TTG-DBR laser with thick tuning layer and  $n$ -InP layer has been thoroughly presented in Chapter 5. It is expected that such a laser could achieve a wide wavelength tuning range in combination with nanosecond fast tuning speeds. The proposed TTG-DBR laser is relatively long as compared to the TTG-DFB laser and therefore not very suited for direct modulation at high speed. Therefore an approach where uses is made of an integrated external modulator seems the way to go.

**TTG-SG-DFB laser** In Chapter 4 some characterization results on TTG-SG-DFB lasers have been presented. Although single-mode laser operation was achieved, the laser threshold was rather high and the wavelength tuning range limited, with only a few supermodes that could be addressed upon tuning. A first step to improve the laser characteristics would involve optimization of the TTG epitaxial layer growth process, but also optimization of the laser structure in terms of heat dissipation is required to reduce the optical loss and to achieve wider tuning ranges.

**TTG double-ring laser** One problem with sampled gratings is the non-flatness of the spectral envelope in the reflection characteristics. This makes it relatively hard to achieve wide tuning ranges or constant output powers across the tuning range. Ring resonators have an inherently flat spectral response and could therefore be used to realize a fast and widely tunable

laser on silicon. In a double-ring configuration a III-V microdisk could be integrated on top of the rings to allow for carrier-injection-based tuning of the rings. In the gain section the tuning layer is left unbiased, similarly as for the other TTG-DBR laser approaches.

The alternative AWG-based filtered feedback tunable laser presented in Chapter 6 does not involve a complex TTG stack and is interesting as wavelength-selectable laser. Obviously, also the laser structure can be further improved to push the optical output power and direct modulation bandwidth further.

Finally, transfer printing is envisioned as a promising technique to realize the presented tunable laser devices on an active SOI platform. The technology also seems to become an enabler for the realization of heterogeneously integrated devices in a massively parallel fashion.



